The Atomic Point Contact as a Detector of Nanomechanical Motion

by

Nathan Edward Flowers-Jacobs

B.S., California Institute of Technology, 2001

A thesis submitted to the

Faculty of the Graduate School of the

University of Colorado in partial fulfillment

of the requirements for the degree of

Doctor of Philosophy

Department of Physics

2010

This thesis entitled:
The Atomic Point Contact as a Detector of Nanomechanical Motion
written by Nathan Edward Flowers-Jacobs
has been approved for the Department of Physics

Prof. Konrad W. Lehnert

Prof. Charles T. Rogers

Date

The final copy of this thesis has been examined by the signatories, and we find that both the content and the form meet acceptable presentation standards of scholarly work in the above mentioned discipline.

Flowers-Jacobs, Nathan Edward (Ph.D., Physics)

The Atomic Point Contact as a Detector of Nanomechanical Motion

Thesis directed by Prof. Konrad W. Lehnert

I experimentally demonstrate that an atomic point contact (APC) is a sensitive detector of nanomechanical motion. With a microwave technique, I increase the measurement speed of APCs by a factor of 500. This measurement is fast enough to detect the resonant motion of nanomechanical structures at frequencies up to 150 MHz. I measure displacement with a shot-noise limited imprecision of $\sqrt{S_x} = 0.29$ fm$/\sqrt{\text{Hz}}$ and simultaneously observe a $\sqrt{S_F} = 61$ aN$/\sqrt{\text{Hz}}$ backaction force. A quantum limited detector would operate at the limit imposed by the Heisenberg uncertainty principle, $\sqrt{S_x S_F} \geq \hbar$; for this APC detector $\sqrt{S_x S_F} = 168\hbar$. Because the measurement noise is dominated by the shot noise of tunneling electrons, the non-ideality of the APC detector is likely due to a backaction force in excess of that required by quantum mechanics. Although I cannot unambiguously determine the origin of this excess backaction force, I am able to eliminate certain possible origins. For example, the observed linear dependence of the backaction force S_F on APC current is inconsistent with a noisy electrostatic attraction mediated by the mutual capacitance between the APC electrodes. In contrast, a model of the backaction force that invokes a momentum impulse delivered by each tunneling electron correctly accounts for the observed scaling. However, each electron would have to deliver a momentum impulse greater than 20 times the Fermi momentum which seems implausibly large. I also observe the signs of molecular vibrations in the APC using inelastic electron tunneling spectroscopy. At the bias energy associated with vibrations I measure a resonant increase in the backaction force. This observation suggests that the excess backaction may arise from the interaction of tunneling electrons and molecular vibrations.

Acknowledgements

I would first like to acknowledge and thank my thesis advisor, Prof. Konrad W. Lehnert. Konrad was willing to spend an enormous amount of time introducing me to cryogenic/microwave techniques and physics as a profession, working beside me during long nights and providing a constant source of motivation and intellectual stimulation. I am tremendously grateful.

I first started working in Konrad's lab with Dan Schmidt, a post-doc, and Manuel Castellanos-Beltran. I am thankful that Dan was always willing to provide advice when I knew, basically, nothing. I have always appreciated having Manuel across the room; having someone who shared a similar perspective to talk physics, and gossip, with was invaluable.

Similarly, I am glad that I was able to interact with the members of the opto-mechanics experiment in the Lehnert Lab: Cindy Regal, John Teufel, Jennifer Harlow, Tobias Donner. It was a pleasure to have another group of people readily available with whom I could discuss the details of cryogenic nanomechanical fabrication and measurement. I also acknowledge and appreciate conversations with professors Aash Clerk, Steve Girvin, John Price, and Chuck Rogers.

The support staff at JILA are amazing. I would especially like to thank David Alchenberger who made it possible to perform nano-fabrication at JILA; the wonderful JILA instrument shop people who were always willing to provide advice on (among other things) how not to kill yourself while dealing with heavy loads and spinning blades , in

particular Tracy Keep for designing and machining the bending apparatus used in this experiment; the electronics shop for advice on microwave (and low frequency) electronics and for allowing me to almost permanently "borrow" spectrum analyzers and network analyzers; and finally, the computing team and supply office for quickly dealing with my frantic queries.

On a more personal note, I also immensely appreciate how my partner Celeste Yang, my friends in Colorado (including Bryan Eastin, Matt Reese, and Samantha Bench Reese who likes getting her name in theses), and my family have supported me emotionally and physically. I am in their debt, most recently for their willingness to put up with me during the thesis writing process.

Contents

Chapter

Chapter 1

Introduction

The goals of the experiments described in this thesis were to create and evaluate the atomic point contact (APC) as a detector of nanomechanical motion. The first step towards these goals was to couple the APC, a mesoscopic device, to the dynamics of mechanical displacement. By making the relative position of the APC atoms a dynamical variable, I hoped to extend the field of mesoscopic electronics to mesoscopic electromechanics. The second step was to increase the speed of APC measurements so that the APC can be used to sensitively observe nanomechanical motion at frequencies between 10 MHz and 150 MHz. The final step was to measure both the APC's displacement sensitivity and the backaction force created by the APC detector. These measurements were used to evaluate theoretical claims that the APC detector can be a quantum-limited displacement detector.

An APC is formed by locating an atomically sharp metal tip near another conducting mass (figure 1.1), as in a scanning tunneling microscope (STM). When the vacuum gap between the tip and the mass is on the order of a nanometer, electrons incident on the APC can quantum-mechanically tunnel across the gap between atoms in the APC. The probability that an electron will tunnel and be transmitted across the gap, instead of reflecting off of the gap, is exponentially dependent on the width of the gap. In most metals, including the gold APCs used in this thesis, the length scale λ that controls the exponential dependence is approximately $\lambda \approx 100$ pm. A voltage applied

across the gap (figure 1.1) creates a difference in chemical potential for electrons in the two electrodes. The flow of electrons that results from the chemical potential difference is an electrical current which is extremely sensitive to the size of the separation between the mass and the point. If the mass is attached to a spring (figure 1.1), then the measured changes in the current through the APC is a sensitive measurement of the displacement of the mass-on-a-spring harmonic oscillator.

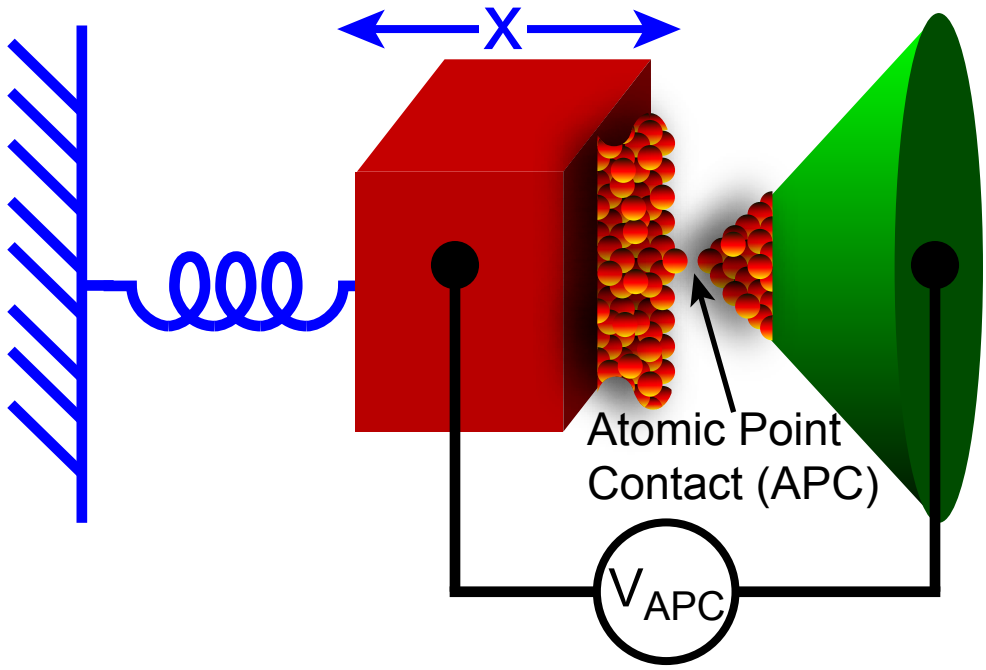

Figure 1.1: A conceptual diagram of an APC displacement detector. A metal mass (red box) is placed about one nanometer away from an atomically sharp, metal tip (green pyramid). The atomic point contact is formed between two atoms (orange circles). A voltage bias V_{APC} will cause electrons to tunnel across the APC and the tunneling current is a sensitive measurement of the displacement x of the metal mass. If the metal mass is attached to a spring (blue), then the APC displacement detector measures the displacement of the resulting harmonic oscillator.

There were three main goals behind this investigation of the APC displacement detector. First, I wanted to expand the field of mesoscopic electronics to mesoscopic electromechanics by using the APC, a mesoscopic device, to sense the dynamical motion of a nanomechanical structure instead of the static position of atoms. Mesoscopic elec-

tronic devices are those devices in which the discrete charge, spin, or quantum phase of electrons is manifest in the device behavior. The current in mesoscopic devices cannot be modeled as the flow of a classical charged fluid. The APC is a mesoscopic device where the discreteness of electrons is manifest because electrons pass across the APC by tunneling through a barrier. The probabilistic nature of discrete electrons tunneling across the barrier creates shot noise; in comparison, a resistance which reduces the flow of a charged fluid would not create shot noise. The devices I study as part of my thesis will couple the discreteness of charge to a mechanical oscillator.

APCs are widely used as atomic-scale mesoscopic sensors. The atomic resolution in a STM is provided by the APC formed between the STM's atomically sharp tip and the substrate. APCs are used in mechanically controllable break junctions to study how metals fracture and flow at the atomic scale. They are also used to electrically contact single molecules. In each of these examples, the APC combines the mesoscopic effects associated with the discreteness of charge with a sensitivity to the static position of atoms. This thesis was motivated by the possibility of using this sensitivity to detect the dynamic motion of nanomechanical structures.

Experimentally, the first step in achieving this goal was creating the APC *in situ* as part of a nanomechanical structure (figure 1.2, for example). The frequency of the nanostructure's fundamental mode is between 10 MHz and 100 MHz. The APC is created in the ultra-high vacuum environment provided by a 4 K cryogenic system using either electromigration or a mechanically controllable strain. The displacement of the nanostructure strains the APC and changes the width of the APC gap, so the APC displacement detector can sensitively measure the harmonic motion of the nanostructure.

The final step towards sensitively detecting nanomechanical displacement, and the second goal of this project, was the development of a high bandwidth readout of an APC. In the past, only about 100 kHz of an APC's intrinsically large bandwidth is usually realized because the APC, which is necessarily high-impedance $R_{APC} > 20\,\mathrm{k}\Omega$, is

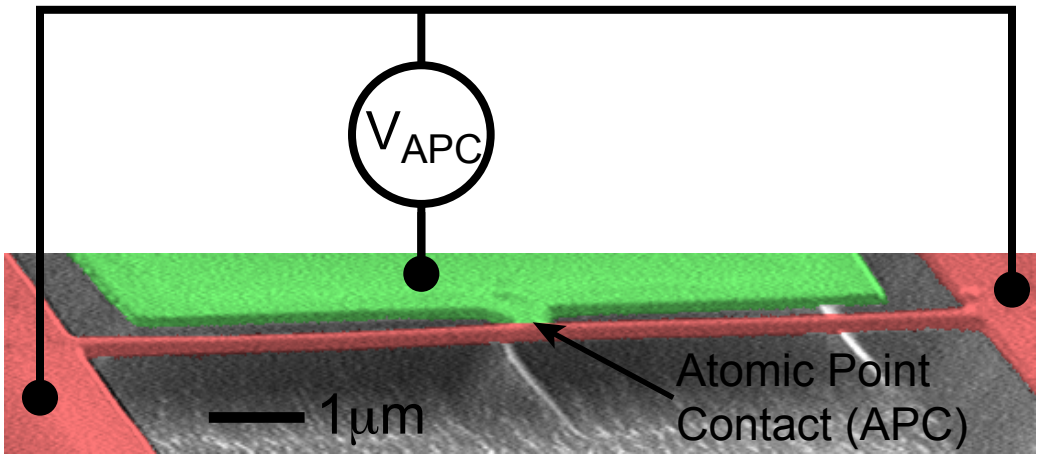

Figure 1.2: A scanning electron micrograph of a nanostructure prior to APC creation. The APC will be created at the constriction between the stationary electrode (green) and nanomechanical beam (red); the entire structure (red and green) is made entirely out of gold. A voltage bias V_{APC} applied between the electrode and the nanomechanical supports will cause electrons to tunnel across the APC and is used to measure the displacement of the nanomechanical beam.

shunted by the large cable capacitance between the device and the remote measurement electronics. I overcame this limitation by embedding the high-impedance device in a LC resonant circuit; this is the same microwave technique that was used to create the radio frequency single electron transistor (RF-SET). This microwave APC measurement has a bandwidth that is controlled by the quality factor of the resonant circuit which, in this case, is greater than 30 MHz [11].

The final goal of this project was to evaluate theoretical claims that the APC can be a quantum-limited displacement detector. The noise in any displacement detector will result in an imprecise measurement of displacement; the imprecision can be expressed as a displacement noise spectral density S_x. The detector will also effect the mechanical system that is being measured and create a noisy backaction force with a spectral density S_F. A continuous linear measurement of position is subject to the Heisenberg constraint $\sqrt{S_x S_F} \geq \hbar$. When the detector is measuring the displacement of a harmonic oscillator, this quantum-mechanical constraint also limits the total uncer-

tainty in the displacement measurement due to the sum of the measurement imprecision and the random motion created by the backaction force. The point of minimum total uncertainty is called the standard quantum limit and occurs, on-resonance, at an imprecision $S_{xSQL} = \hbar/m\gamma\omega_0$ and backaction $S_{FSQL} = \hbar m\gamma\omega_0$ where m is the mass of the oscillator, γ is the damping, and ω_0 is the resonance frequency.

In a basic phenomenological model of an APC displacement detector at the quantum limit, the imprecision S_x is due to the shot noise of tunneling electrons and the backaction S_F is due to the random momentum kick imparted by each tunneling electron. Unlike many other mesoscopic detectors, the large 5 eV energy scale of the APC barrier allows a large voltage bias (50 mV in this experiment) to be applied across the contact without significantly affecting the mesoscopic properties of the detector. Because I use both a large voltage bias and the microwave measurement technique mentioned earlier, I can make a displacement measurement whose noise is dominated by the fundamental shot noise of tunneling electrons instead of the other, less interesting, sources of noise such as the noise of following amplifiers. This is important because it is a prerequisite for making quantum-limited displacement measurements. Experimentally, I use the APC detector to measure nanomechanical motion with a shot-noise limited imprecision $S_x = 0.08$ fm^2/Hz $= 20S_{xSQL}$.

I also measure the noisy backaction force created by the detection process. Since $S_x > S_{xSQL}$, if this APC detector was operating at the quantum limit then $S_F < S_{FSQL}$. Instead, I measure a backaction force with a spectral density $S_F = 3750$ aN^2/Hz $= 1400S_{FSQL}$ and an imprecision-backaction product $\sqrt{S_x S_F} = 168\hbar$ which is 168 times larger than required by quantum mechanics. The total imprecision on-resonance $S_x + S_F H(\omega_0)$, where $H(\omega)$ is the harmonic oscillator response function, is 730 times the total imprecision at the standard quantum limit.

Since the imprecision is shot-noise limited, I conclude that the likely source of non-ideality in the APC displacement detector is a backaction force in excess of that

required by quantum mechanics. If the entire backaction force is due to the momentum kicks of tunneling electrons, each electron would have to deliver a momentum equal to 23 times the Fermi momentum p_F. Since an electron with an energy equal to the height of the tunnel barrier would only have a momentum equal to about $2p_F$, the electron momentum required to account for the observed backaction is implausibly large.

The momentum kicks from tunneling electrons would result in a backaction force proportional to the current I_{APC} through the APC, but there are also other possible sources of detector backaction which depend on the voltage V_{APC} across the APC. The capacitance of the APC changes as the width of the gap changes, creating an electrostatic backaction force proportional to V_{APC}^2. The presence of trapped charges near the APC would result in a backaction force proportional to V_{APC}. Finally, the power V_{APC}^2/R_{APC} dissipated near the APC could effectively create a backaction force by increasing the temperature of the nanostructure.

I have attempted to determine the origin of the backaction force using four different approaches. While all of the results are consistent with a backaction force created by momentum kicks from tunneling electrons, further work is required to both conclusively demonstrate the origin of the backaction and understand the physical mechanism.

First, the simplest approach is to measure multiple devices in different configurations. I have measured the random backaction force of three different devices using two different nanostructure geometries and APC creation techniques. In all three cases, the random backaction force is consistent with each tunneling electron delivering a momentum between $20p_F$ and $35p_F$; the factor of two difference is contained within the large systematic error caused by my poor knowledge of the shape of the nanomechanical modes. Although the origin of the backaction force remains unknown, these measurement do allow me to determine that the size of this random force S_F is linearly proportional to the current or voltage across the APC. This observation is inconsistent with a random force which arises from the potential fluctuations across the mutual

capacitance between the APC electrodes.

Second, I use an unintentional feedback loop created by the APC measurement to determine that the backaction force is more consistent with a force proportional to I_{APC}, such as the momentum kicks of tunneling electrons, than with a force proportional to V_{APC}, such as a force created by the presence of trapped charges. The feedback loop is unintentional because I do not measure displacement and then create a force proportional to the measured displacement. Instead, the feedback loop is caused by the motion of the nanostructure changing the current or voltage across the APC and thus changing the backaction force. The magnitude of the feedback depends upon both the origin of the backaction force and the electrical circuit surrounding the APC. As an example, if the APC is voltage biased then the voltage V_{APC} does not depend on R_{APC} and only a backaction force proportional to current I_{APC} would result in feedback. I observe a feedback force which is more consistent with a backaction force proportional to current. The observed feedback cannot be used to determine the physical origin of the backaction force, but if the backaction force is due to the momentum kicks of tunneling electrons then each electron would have to deliver a momentum kick between p_F and $40p_F$.

Third, I attempt to determine whether the observed backaction force is correlated with the shot noise of tunneling electrons. If the backaction force is caused by heating due to electrical power dissipation, then it would not be correlated with the shot noise. On the other hand, a backaction force caused by the fluctuating V_{APC} or I_{APC} would be correlated with the shot noise. The correlation measurement is plagued by the noise added by the first amplifier in the measurement circuit; I am only able to determine that the observed signal is consistent with an electron momentum $< 50p_F$. An amplifier with less noise would be required to better determine the correlations between electrical shot noise and the observed backaction force.

Finally, I simultaneously measure the backaction force and differential resistance

R_{APC} of the APC as a function of the dc voltage across the APC. This type of tunneling spectroscopy has been used in other experiments to investigate the vibrational modes of molecules trapped in the APC. I sometimes observe features in the differential resistance as a function of voltage that are similar to the vibrational features observed in other experiments. At the same dc APC voltage where I observe these features, I also observe an large increase ($> \times 2$) in the backaction force. This opens the possibility that the vibration of nearby atoms or molecules could play a role in the large backaction force.

This thesis is organized into four broad sections: background, theory, experimental techniques, and results. In the next chapter (chapter 2), I discuss in more detail the past work involving nanomechanics and atomic point contacts that is relevant to and helped motivate this thesis. I then explain the necessary theoretical background in chapter 3. The experimental techniques used to create an APC coupled to a nanomechanical structure and perform the fast, shot-noise limited measurement of the APC are described in chapters 4 and 5, respectively. In chapters 6 and 7 I present in detail the experimental results of my evaluation of the APC as a displacement detector; these results are briefly summarized in this introduction. Finally, I conclude this thesis in chapter 8 and discuss some possible directions for further research.

Chapter 2

Background: Mechanics Coupled to Mesoscopics

This thesis describes an experiment that combines the fields of nanomechanics and mesoscopics, using the mesoscopic physics of tunneling electrons to create a sensor of nanomechanical motion: the atomic point contact (APC) displacement detector. Both of these fields spring from the idea of nanotechnology [12,13]: that shrinking the overall size of systems to the nanometer scale and beyond can lead to new and interesting physics and applications. Nanomechanics is the the study of mechanical systems on the nanometer (or 100s of nanometers) scale [14–16]. Mesoscopic physics usually involves studying electrical systems created using physical structures on a similar scale, however the important feature of mesoscopic systems is that the flow of electrical current can no longer be described by the flow of a charged fluid. Instead, the discreteness of an electron becomes important [17–20].

In this chapter I am going to summarize the work in nanomechanics and mesoscopics that has motivated and influenced this thesis. Starting with the broad motivation for interest in nanomechanics, I will describe the important role nanomechanical systems play in nanoscale probes and other sensors [21–23]. More specifically, the desire to create a gravitational wave detector twenty years ago led to the first investigations into how mesoscopic physics could be used to sensitively detect nanomechanical motion [24–28]. In the past ten years that interest has shifted towards using nanomechanical systems to demonstrate quantum limited measurements of nanomechanical modes and observing

quantum mechanical effects in a macroscopic degree of freedom [3–5, 29–34].

After covering this background on nanomechanics, I will focus on how four mesoscopic systems have been coupled to nanomechanical motion in attempts to make quantum limited measurements. The first technique is to use a single electron transistor (SET) which is capacitively coupled to the nanomechanical device [3, 31, 32]. The effect that the SET displacement detector has on the system being measured, that is, the SET's backaction, has been measured [31]. This is a prerequisite for quantum limited detector, though in the case of the SET experiment the backaction was twenty times larger than theoretically predicted. A second technique involves magnetically coupling a superconducting quantum interference devices (SQUIDs) to a nanomechanical beam. As a third example, I will describe how nanomechanical motion has been coupled to quantum point contacts (QPCs) using both piezoelectricity [33] and capacitance [5]. This technique using QPCs is especially interesting because the APC and the QPC measurements are theoretically similar and have the same tunneling Hamiltonian. I will then briefly discuss how the nanomechanical motion of carbon nanotubes can be measured using the transistor properties of semi-conducting carbon nanotubes [6,35–37].

I also describe previous work using atomic point contacts (APCs). APCs have been widely used as detectors of static changes in position, since they provide the atomic resolution for imaging and manipulation in scanning tunneling microscopes (STMs) [7, 38, 39]. STMs have a large mechanical support structure to allow the tip to scan over a large three dimensional area; however, APCs have also been fabricated as part of a stiffer, more compact nanostructure. The experiments in this thesis build on these fabrication techniques, where the APC is formed from a constriction in the nanostructure either by passing a large current through the constriction thus creating an APC using electromigration [40–43] or by stretching the constriction to form a mechanically controllable break junction (MCBJ) [8, 44–48]. In the past these techniques have been used to measure static properties of the contact and study how metals fracture and flow

at the nanoscale (summarized in [8]) as well as the electrical properties of molecules trapped in the contact [40, 49–57].

Finally, I will discuss theoretical proposals and evaluations of the APC displacement detectors. In the late 1980s and early 1990s the APC displacement detector was proposed as a possible means to detect the strain created by gravitational waves [58–63]. At the time, the APC displacement detector was evaluated theoretically and predicted to be a quantum-limited detector [64–66]. Since 2002 there has been renewed theoretical interest in the APC displacement detector in the context of quantum-limited measurement [67–77].

2.1 Nanomechanics

Research into new detectors of nanomechanical motion, such as the research described in this thesis, is partially motivated by the wide use of nanomechanical motion in other sensors. This motivation comes from the possibility that a new detector of nanomechanical motion will result in better sensors, either because the new detector has a better absolute sensitivity or because the change in constraints on the sensor due to the change in detection method results in a better sensor. I am therefore going to emphasize the importance of nanomechanics by describing two ways in which nanomechanical devices are used to probe the nanoscale world, atomic force microscopy (AFM) and magnetic resonance force microscopy (MRFM), as well as some other applications of nanomechanical devices.

The other motivation for research into new detectors of nanomechanical motion is the desire to measure the quantum behavior of a macroscopic degree of freedom. The initial interest in the quantum limits of position detection revolved around interest in designing gravity wave detectors. However most current gravity wave detectors use optical interferometry, and mesoscopic experiments have moved away from this focus on gravity wave detection. Instead, more recent mesoscopic experiments have focused on

two goals: detecting nanomechanical motion with an imprecision at the quantum limit and cooling a nanomechanical mode to the ground state defined by quantum mechanics. I will end this section (section 2.1) by discussing both of these goals in the context of nanomechanical motion; in the next section (section 2.2) I will describe a number of mesoscopic experiments aimed at creating a quantum-limited position detector.

2.1.1 Nanomechanics as a gentle probe of the nanoworld

Two different techniques use the exquisite force sensitivity of nanomechanical oscillators to create images with atomic-scale resolution. In magnetic resonance force microscopy (MRFM, figure 2.1), a nanomechanical oscillator is used to sense the force due to spins rotated by an oscillating microwave field in a static magnetic field with a large magnetic field gradient [78–80]. The combination of the microwave field at frequency ω_0 and static magnetic field with a large gradient $B_z(y)$ results in the resonant excitation of spins in a thin slice of the sample where $B_z(y) = \omega_0/\gamma$ (γ is the gyromagnetic ratio of the sample). The frequency of the microwave field is usually modulated slightly around ω_0, causing the spins to Rabi flop and creating a magnetic moment in the $\hat{z}$ direction $m_z(t)$ with a sinusoidal time dependence [1, 78, 81–88]. Since this magnetic moment is in a static magnetic field gradient $\partial B_z/\partial y$, there is a force on the cantilever due to the precession of the spins

$$F_y(t) = m_z(t)\frac{\partial B_z}{\partial y} \tag{2.1}$$

The frequency of the force can be matched to the < 10 kHz nanomechanical resonance frequency, where the nanomechanical system has the best force sensitivity, by matching the mechanical resonance frequency to the rate at which the spins flip. This rate is controlled by the frequency of the modulations to the frequency of the microwave field.

The location of the resonant slice can be moved by changing the location of the sample in the magnetic field. Since this slice can be as thin as a few nanometers, the

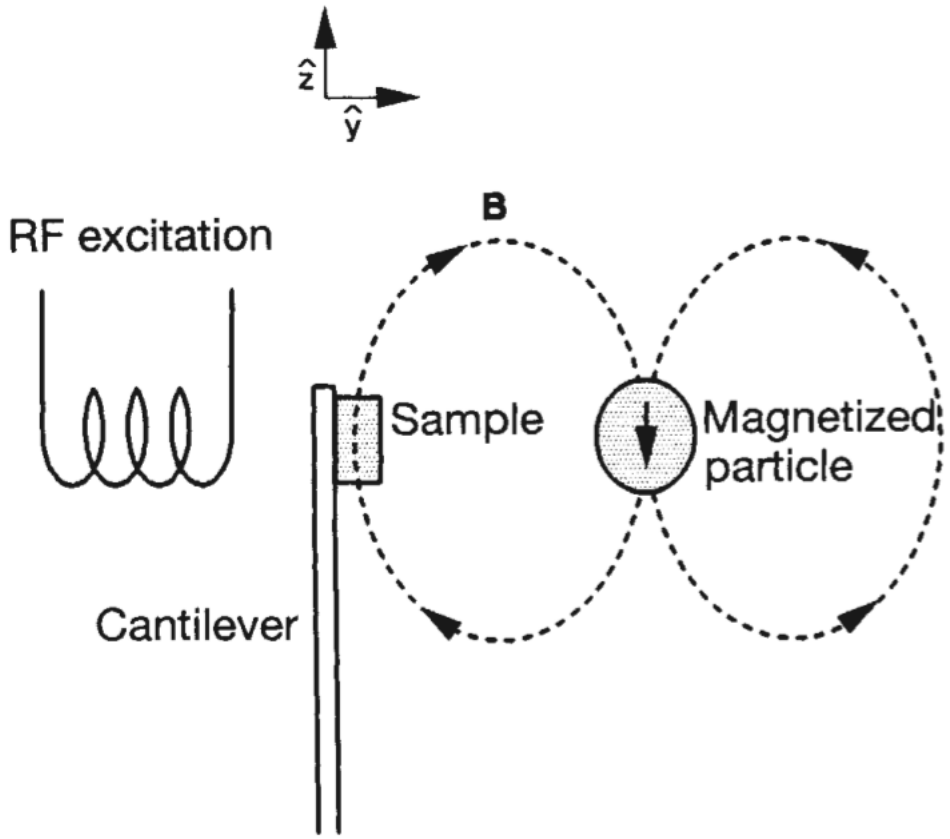

Figure 2.1: Basic diagram of Magnetic Resonance Force Microscopy (MRFM), figure from reference [1].

MRFM resolution is on the nanometer scale [81]. By sensitively detecting the force on the cantilever as the resonant slice is moved through the sample it is possible, for example, to determine the location of a single electron spin [78] or image a tobacco mosaic virus [81].

One future direction of MRFM research is pushing the observation frequency to the Larmor frequency ω_0 which is usually in the MHz to GHz regime. This increase in frequency could be helped by new types of detectors designed to monitor smaller, higher frequency nanomechanical resonators. The optical interferometer technique currently used to detect cantilever motion works best with large, and thus low frequency, cantilevers.

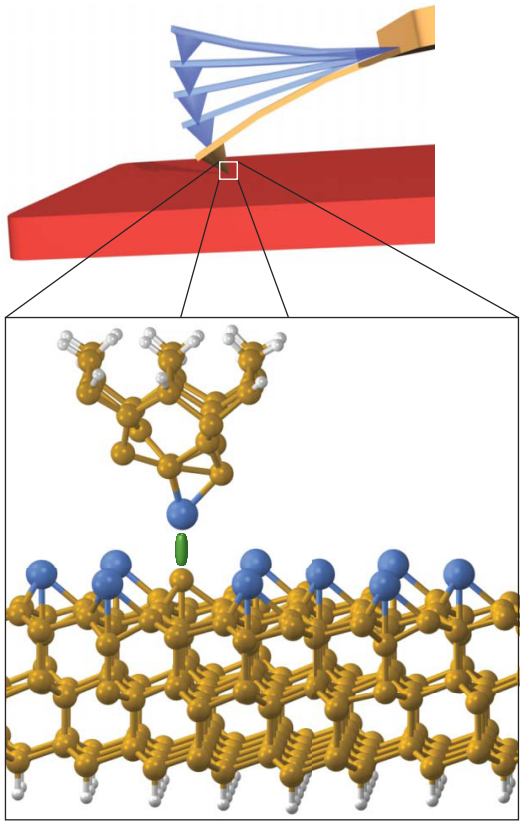

Figure 2.2: Basic diagram of an Atomic Force Microscope (AFM), figure from reference [2]. The surface is imaged by measuring the force between the tip of the cantilever and the surface as the tip is scanned over the surface.

In atomic force microscopy (AFM), a surface is imaged by measuring the force between a sharp tip attached to a lever and the surface as the tip is moved over the surface (figure 2.2). In general, the force is larger when the gap between the tip and the surface is smaller. This map of force versus tip position can be used to infer the three-dimensional surface topology [21–23]). If the tip is atomically sharp then it is possible to image the surface with atomic resolution [21, 89–92].

In the twenty five years since the first AFM experiments, this technique has progressed from it's origin as a method to measure forces in an scanning tunneling microscope (STM) to it's current place as a widely used tool for imaging nanostruc-

tures and measuring force in both biological and material sciences. The initial AFM measurements where taken using a diamond STM tip which was attached to the free end of a macroscopic singly-clamped beam, a 0.8 mm long by 0.25 mm wide by 25 μm thick piece of gold foil. The force on the beam was then detected by measuring the beam's 5.8 kHz resonant motion using the STM's tunneling current between the tip and the sample [23]. However, in modern AFM measurements a smaller beam with micron-scale dimensions and an optical readout is usually used and changes in force are usually detected by measuring changes in the beam's resonance frequency [21]. AFMs have become important and common laboratory instruments, commercially produced for general surface characterization and imaging. AFMs are also the key measurement tool in continuing research into understanding nanoscale forces, macromolecules, and biological materials [21, 22].

2.1.2 Applications of nanomechanical oscillators

Nanomechanical oscillators are not only used to probe the nanoscale world, but they also play a role in other sensors both in a research setting and commercially. Two examples of the role of nanomechanical sensors in current research are in sensitive detectors of mass [93–96] and in the related area of detecting the presence of molecules for biological applications [97–101].

In general, mechanical oscillators can be used to detect mass by measuring the effect on the oscillator's resonance frequency of placing mass on the oscillator. The deposition of a small amount of mass causes a measurable change in the resonance frequency of a nanomechanical oscillator [95, 96] because, compared to large oscillators, nanomechanical oscillators have a low total mass. To be more quantitative, recent experiments with nanomechanical systems have demonstrated a mass sensitivity of about 10^{-23} kg/$\sqrt{\text{Hz}}$ using a doubly clamped SiC beam which is 2 μm long by 150 nm wide by 100 nm thick and has a resonance frequency of about 150 MHz with a quality factor of

5000 [94]. Further improvements in sensitivity, to about 10^{-25} kg/$\sqrt{\text{Hz}}$, have been made by using a singly-clamped carbon nanotube to make a lighter mechanical resonator [93].

Nanomechanical oscillators are also promising sensors of biological molecules. The standard approach combines the mass sensitivity described in the previous paragraph with the application of a molecular coating to the nanomechanical oscillator which selectively binds the molecule of interest [100,102–104]. The presence and concentration of the molecule of interest can then be deduced by measuring the changes in the mass of the nanomechanical oscillator. In general, it is desirable to operate the mass sensor in a room temperature and pressure environment (or in a fluid) which has the effect of lowering the mechanical quality factors and complicating the entire measurement; this has led to some novel approaches such as flowing solvents through, instead of around, a micron-scale mechanical oscillator [102]. Sensors based on this technique are being developed [99, 101]. There is also research into using the mass sensitivity of a nanomechanical oscillator to effectively create a mass spectrometer, determining the identity of an absorbed macromolecule based purely on the detected mass of the molecule [97].

Finally, nanomechanical and micromechanical oscillators also have many commercial applications [105–114], including as inertial sensors for automotive and navigation applications [109, 114] and in analog signal processing [109, 112]. While I am not going to describe these devices in detail, in general the use of micromechanical oscillators allows an intertial sensor to be compact, low power, and cheap without losing sensitivity [114]. In the realm of analog signal processing, the mechanical oscillator's motion at it's resonance frequency can be used as an electrical filter with a high quality factor. In comparison with a filter built from discrete inductors and capacitors, the mechanical oscillator is both high-Q and compact. The frequency of the mechanical resonance can also be tuned over a wide range in frequency and dissipates very little power during operation [112]. This combination makes electrical filters created from micromechanical

oscillators ideal for many different applications, particularly for wireless communication [109].

2.1.3 Quantum behavior of macroscopic degree of freedom

The initial interest in quantum limited position detection in the 1970s, 1980s, and 1990s was motivated by a desire to detect gravitational waves. Gravitational waves effectively create a classical force on a mechanical oscillator. Therefore there was a large amount of theoretical interest in the limits imposed by quantum mechanics on the detection of classical forces [24, 34] as well as in general limits on measurement precision [115, 116].

At the most basic theoretical level, the quantum limit on a measurement is described by the Heisenberg Uncertainty principle. For a measurement of the position of a particle, the quantum limit is $\Delta x \Delta p \geq \hbar/2$ where Δx is the uncertainty in the position measurement and Δp is the uncertainty in the momentum of particle due to the measurement [115, 117, 118]. This formula describes the effect of a single measurement, however from the perspective of force detection a more interesting case is the continuous measurement of position. In this case, the quantum limit on a continuous measurement is $S_x S_F \geq \hbar^2$ (see chapter 3 for more details), where S_x is the spectral density of the displacement imprecision and S_F is the spectral density of the random force caused by the detector, that is, the backaction of the detector [72, 115, 116]. This thesis focuses on evaluating a specific detector, the atomic point contact (APC) displacement detector, in the context of this quantum limit.

Accompanying these theoretical discussions of the quantum limit were proposals describing detectors which could approach these limits. Many different types of detectors where considered [24,25,34,115], including optical interferometers, Weber-type resonant bars coupled to SQUID amplifiers, and detectors using electron tunneling in atomic point contacts. The most sensitive gravitational wave detectors in use today employ

optical interferometers [119, 120], however Weber-type resonant bar detectors are still being used [121–126] and in active development [127]. Gravitational wave detectors that used electron tunneling were never implemented, though the analysis provided in the proposals, which will be discussed in more detail in section 2.3.2, helped motivate the research in this thesis.

Since 2000, interest in mesoscopic detectors at the quantum limit has largely shifted from a desire to detect gravitational waves towards the dual goal of demonstrating a quantum limited detector and then detecting the quantum behavior of a macroscopic degree of freedom [29,30]. This has resulted in a change in focus, from detecting the motion of large masses which are better coupled to gravity waves to detecting the motion of nanomechanical objects which are easily integrated with mesoscopic detectors and are both higher frequency and lower mass [3–5,11,31–33]. The move towards higher frequencies is important in the context of the second goal, because the first step towards detecting quantum behavior is usually the ability to cool the oscillator to it's quantum mechanical ground state $T_{osc} \approx \hbar\omega_0/2$, where ω_0 is the frequency of the mechanical oscillator. Making lighter oscillators is also important because it implies larger, more easily detectable, motion when the oscillator is in the ground state in comparison with more massive oscillators that have the same resonance frequency.

2.2 Mesoscopic Amplifiers Coupled to Nanomechanical Oscillators

Having discussed some of the motivations for sensing nanomechanical motion, I now describe four different types of mesoscopic position detectors. The first type of detector capacitively couples a nanomechanical beam to a single electron transistor (SET) and uses the mesoscopic physics of electrons tunneling through multiple Josephson junctions to sensitively detect the change in capacitance due to motion of the nanomechanical beam [3, 31, 32]. The second type of detector also uses Josephson junctions, but in this case the junctions are used to form a superconducting quantum interference device

(SQUID) which is inductively coupled to a nanomechanical beam [4]. The third type of detector couples nanomechanical motion to a quantum point contact (QPC), and nanomechanical motion changes the probability of electrons tunneling through a barrier in a two-dimensional electron gas [5, 33]. While physically different from the detector described in this thesis, which involves electrons tunneling through a vacuum gap between atoms, the theoretical descriptions of the APC and QPC detectors are equivalent. I will finally describe how the motion of carbon nanotubes results in a change in the electrical properties of the nanotube, thus creating a sensor of motion that uses the mesoscopic properties of the nanotube [6, 35–37].

2.2.1 SET nanomechanical displacement detector

The displacement detectors based on single electron transistors (SETs) leverage the extraordinary charge sensitivity of the radio frequency SET (RF-SET, [128]) to detect the motion of a charged nanomechanical beam [3,31,32]. One type of single electron transistor is composed of a conducting metal wire interrupted by two barriers of thin insulating material placed in series; the island between the two barriers is capacitively coupled to a gate electrode [129, 130]. Each insulating barrier is a capacitively-shunted tunnel junction: the metallic leads separated by an insulating layer forms a capacitor and the insulating layer is thin enough that electrons can tunnel across the gap. In comparison to an APC or QPC, the tunnel junctions in an SET have a large number of channels through which electrons can tunnel, though each channel has a much smaller transmission probability. A voltage bias is applied across the junction-island-junction circuit (effectively the drain-source voltage, see figure 2.3b), and current flows when an electron sequentially tunnels across the first barrier and then the second barrier.

If the drain-source voltage is small compared to the voltage needed to charge all the capacitances in the SET with one electron, then the mesoscopic physics of Coulomb blockade makes the current through the junctions very dependent on the SET gate

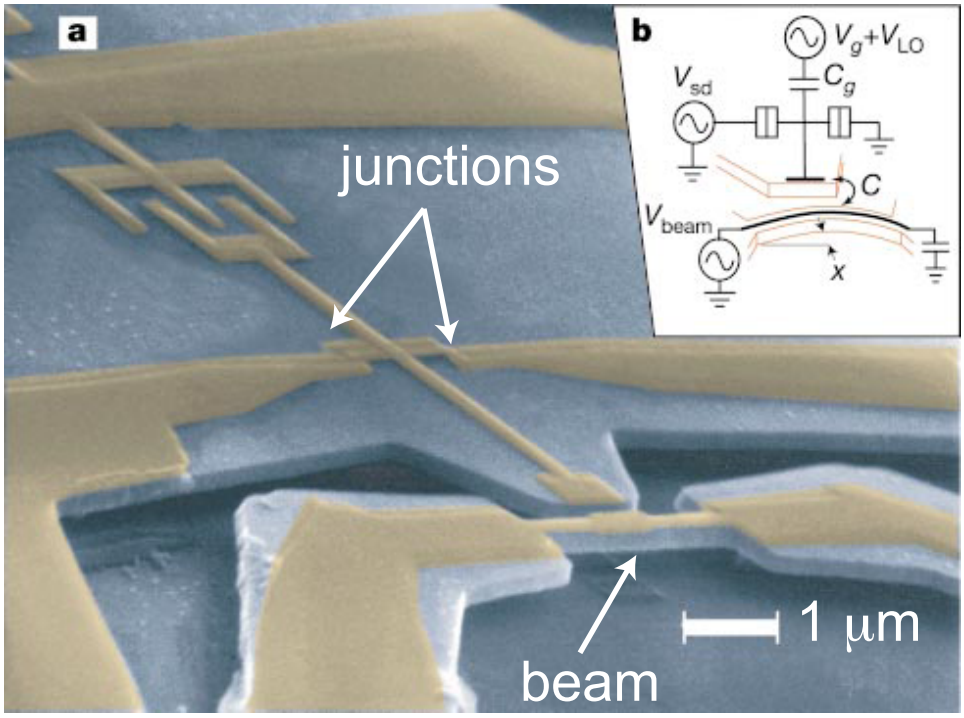

Figure 2.3: SET detector of nanomechanical motion, figure from reference [3]

voltage. If the voltage on the gate is such that there is an integer number of electrons on the island, then it is energetically unfavorable for electrons to tunnel on or off of the island and current does not flow. However, if the voltage on the gate is such that the charge on the island is equivalent to half of an integer number of electrons then current will flow and, by appropriately biasing between these two extremes, the SET drain-source current is a sensitive measurement of the charge on the gate [130]. The SET displacement detector is created by capacitively coupling the nanomechanical beam to the SET island, that is, the beam is an SET gate. When the beam is held at the correct, usually large, potential compared to to the SET island, the drain-source current of the SET is modulated by the nanomechanical motion and can be used to sensitively infer the displacement of the beam.

One problem with SET measurements is that SETs, like the atomic point contacts

(APCs) described in this thesis, are intrinsically high impedance devices $R_{SET} > 26$ kΩ which makes the fast measurements required to detect the 10s of MHz nanomechanical resonance frequencies more difficult. In general, the stray capacitance to ground of the leads to the SET and the high impedance of the SET limit the typical bandwidth of the measurement to less than 1 MHz. However, Schoelkopf *et al* demonstrated a technique that increased the bandwidth of the SET to more than 100 MHz by using a microwave matching circuit to create the radio frequency SET (RF-SET, [128]). Experimentally, RF-SETs are used to detect nanomechanical motion [3, 31, 32], and I use this same microwave technique to greatly increase the bandwidth of APC measurements (see chapter 5, [11]).

The other problem with SET measurements is that the intrinsically near-quantum limited performance of an SET amplifier is not realized in practice. In an SET, as in an atomic point contact, the fundamental source of noise is the shot noise of electrons tunneling through the insulating gaps in the junctions. Ideally, this noise source should dominate the noise in the measurement system. However, if the shot noise of tunneling electrons is small, because the current through the junctions is small, then the system noise is dominated by the added noise of the measurement amplifiers that follow the SET and it is not possible to make a quantum limited measurement. In an SET it is difficult to pass a large current through the junctions because the maximum voltage across the junctions is limited by the physics of the Coloumb blockade. Therefore in the experiments that have used an SET to detect nanomechanical motion the displacement imprecision was dominated by the noise of following amplifiers and the measurement was not quantum limited [3, 31, 32].

The first experiments using an SET to detect nanomechanical motion were made by Knobel and Cleland [3] in 2003 and by LaHaye *et al* in 2004 [32]. Knobel measured the 117 MHz, $Q = 1700$, fundamental mode of a doubly-clamped nanomechanical beam that was 3 μm long by 250 nm wide by 200 nm thick. The beam was made from a

GaAs heterostructure and topped with a thin layer of aluminum. They calibrated their experiment using a magnetomotive measurement, and determined that the SET measurement had an imprecision of 2 fm/$\sqrt{\text{Hz}}$. A good way of determining the significance of the measurement precision is by comparing the precision to the zero-point motion of the nanomechanical system which is closely related to the standard quantum limit [29]. In this case, the imprecision is 180 times the zero-point motion of the nanomechanical beam. LaHaye measured the 19.7 MHz, $Q \approx 40 \times 10^3$, fundamental mode of a doubly-clamped nanomechanical beam that was 8 μm long by 200 nm wide by 100 nm thick. It was made from a SiN membrane and topped with a 20 nm layer of gold. The imprecision of this SET detector was calibrated using the thermal motion of the beam between 100 mK and 600 mK and they determined that the SET measurement had an imprecision of 3.8 fm/$\sqrt{\text{Hz}}$ which is 5.4 times the zero-point motion of the nanomechanical beam when comparing the imprecisions in units of m/$\sqrt{\text{Hz}}$.

More recently, in 2006 Naik *et al* [31] measured the classical backaction of a SET, that is, the effect of the SET measurement on the nanomechanical beam. This backaction force is caused by the electrical potential of the SET island which creates an electrostatic force on the nanomechanical beam through the dependence of the island-beam capacitance on the position of the beam. Niak measured the backaction of a superconducting SET near a bias point where there is resonant transport of electrons through the SET. In this case, the backaction can effect the mechanical resonance frequency and quality factor. They measured a backaction force twenty times larger than theoretically expected and used this backaction to change the mechanical damping. This additional damping cooled the temperature of a mode of the nanomechanical beam by about a factor of two.

2.2.2 SQUID nanomechanical displacement detector

A recent experiment by Etaki *et al* [4] in 2008 demonstrated the direct coupling of a nanomechanical beam to a dc superconducting quantum interference device (dc SQUID). A dc SQUID is a sensitive magnetometer composed of a pair of Josephson junctions: thin, electrically insulating barriers across which both electrons and Cooper pairs can tunnel. The junctions are connected in parallel and form a loop with an input and an output (see figure 2.4). In this experiment, the SQUID is current biased with a current that is greater than the critical current of the SQUID, that is, current biased so that a voltage has developed across the superconducting loop due to the presence of the Josephson junctions. Since the loop is superconducting, a screening current will develop in the loop which ensures that the flux through the loop is an integer number of flux quanta, $\Phi = Nh/2e$. This screening current changes the current through each Josephson junction, changing the voltage across the SQUID. Small changes in the flux through the loop will therefore cause changes in the voltage across the SQUID, thus the SQUID can be used to create a sensitive magnetometer [131].

Nanomechanical motion is coupled to a SQUID by designing a nanostructure where the motion of a nanomechanical element changes the magnetic flux through the SQUID loop. Etaki coupled the nanomechanical beam to the SQUID by suspending one arm of the SQUID loop, creating a nanomechanical beam whose motion will change the area of the SQUID loop (figure 2.4). The device was placed in a magnetic field and changes in the size of the SQUID loop due to nanomechanical motion will change the flux through the loop. Nanomechanical motion is detected by monitoring the voltage across the SQUID loop. While SQUID amplifiers have a long history of use in attempts to detect gravitational waves by measuring the vibrations of large metal masses [26, 121–127, 132], in these earlier experiments the mechanical system was macroscopic rather than nanoscale. Also, mechanical motion was not directly coupled to the SQUID but

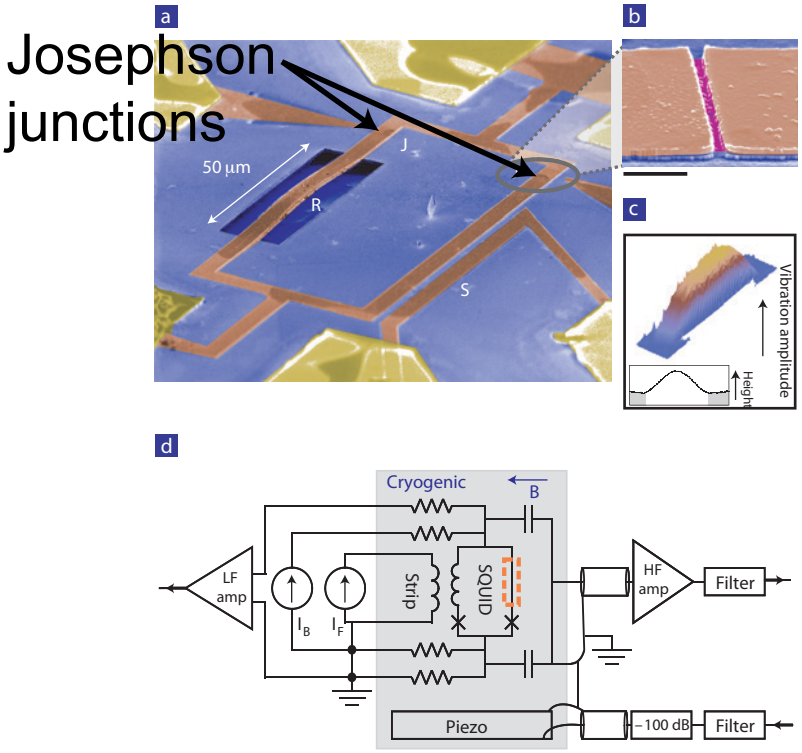

Figure 2.4: SQUID detector of nanomechanical motion, figure from reference [4]

instead was capacitively or inductively coupled to the SQUID through superconducting circuits.

Theoretical investigations have suggested that this SQUID displacement detector can be quantum limited [133, 134], with an imprecision that is set by the shot noise of electrons and Cooper pairs tunneling through the Josephson junctions and a backaction due to the Lorentz force from a noisy current passing through the beam in a magnetic field. In the experiment described by Etaki *et al*, the imprecision was limited by conventional electronics to $S_x = 10$ fm/$\sqrt{\text{Hz}}$, which is 50 times the zero-point motion of the 2 MHz, 6.1×10^{-13} kg, doubly-clamped beam. The measurement was not sensitive enough to detect the SQUID backaction.

2.2.3 QPC nanomechanical displacement detector

In a quantum point contact (QPC) displacement detector, nanomechanical motion changes the transmission through a weak link in a two-dimensional electron gas. In general, a quantum point contact is formed in a conductor by creating a constriction with a width that is comparable to the Fermi wavelength [135]. This constriction effectively creates an electron waveguide with a small number of conducting channels; each fully conducting channel has a conductance $G_q = 2e^2/h$ (the factor of two comes from spin degeneracy) because of the small number of modes, or channels, in the waveguide compared to the large number in the surrounding conductor.

Experimentally, a quantum point contact is usually formed by restricting the region through which electrons flow in a 2-Dimensional Electron Gas (2DEG) [135]. The 2DEG is formed at the interface between two different layers of material, often the interface of a GaAs-AlGaAs heterostructure created on top of a GaAs substrate using molecular beam epitaxy. The flow of electrons in the 2DEG is constricted forming a QPC by applying a potential between gates on top of the heterostructure and the 2DEG (figure 2.5c, for example) which locally depletes the electron gas. The conductance of the QPC is controlled by controlling the voltage on the gates.

The conductance of the QPC is a step-like function of the gate voltage. The size of the constriction is a continuous function of the gate voltage, but the number of conducting channels is an integer quantity. As electrons are allowed to flow through a new channel, the conductance increases in steps of $G_q = 2e^2/h$. This step is smeared out by thermal energy allowing access to otherwise closed modes and by electrons tunneling through partially closed modes. The abrupt change in conductance as a function of voltage is used to sensitively detect changes in the gate voltage and create, for example, charge detectors to investigate quantum dephasing [136] or detectors of nanomechanical motion [5, 33].

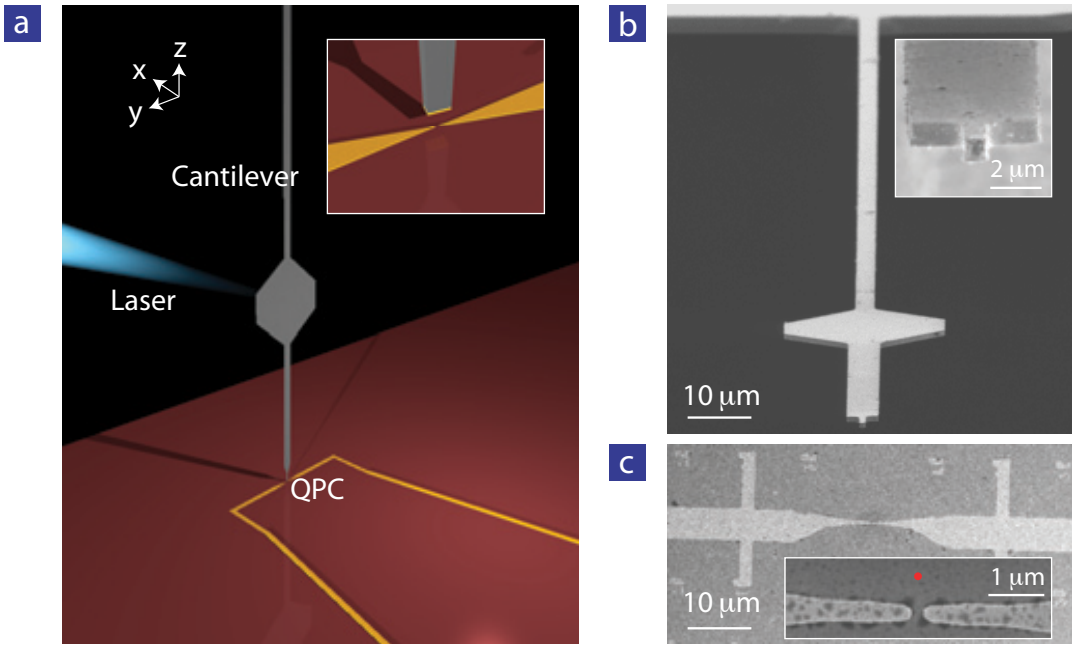

Figure 2.5: QPC detector of nanomechanical motion, figure from reference [5]

The theoretical descriptions of the QPC displacement detector and the atomic point contact (APC) displacement detector are very similar. In both detectors, nanomechanical motion is detected by measuring changes in the transmission of electrons through a barrier. Using this simple description, both detectors are described by the same Hamiltonian (see [75] and section 2.3.2).

Cleland [33] used the peizoelectric effect in GaAs to couple nanomechanical motion to the conductance of a QPC. The 2DEG was fabricated as part of the layered GaAs-AlGaAs-GaAs nanomechanical structure: a beam that was 680 nm thick by 4 μm wide by 13 μm long. The QPC gates were fabricated on top of the nanostructure. This fabrication procedure significantly degraded the quality of the 2DEG which hurt the displacement sensitivity. Out-of-plane nanomechanical motion effectively lengthens the beam, stressing the GaAs and creating out-of-plane peizoelectric fields. These fields also deplete the 2DEG, creating a change in the QPC conductance. The nanomechanical

motion is detected by measuring the small changes in QPC conductance. In this experiment, the QPC displacement detector was able to detect nanomechanical motion with an imprecision of 3 pm/$\sqrt{\text{Hz}}$ which was limited by the voltage noise of the amplifier used to measure the QPC conductance.

More recently, Poggio [5] used a QPC to detect the motion of a micron-scale cantilever by capacitively coupling the cantilever to the QPC (figure 2.5). In this case, the QPC and the cantilever were fabricated separately which simplified the fabrication of the QPC and improved the quality of the 2DEG. The cantilever was 350 μm long by 3 μm wide by 1 μm thick and was made out of single-crystal silicon with a gold tip and a platinum coating. After placing both the QPC and the cryostat in a 4 K cryostat, the end of the cantilever was positioned 70 nm above the QPC. Because the tip was close to the QPC, the tip was capacitively coupled to the QPC and acted as another, moveable QPC gate. The x-y position of the tip was also optimized for maximum coupling between the movement of the cantilever and the QPC conductance. The minimum imprecision of this QPC displacement detector was 1 pm/$\sqrt{\text{Hz}}$ and was limited by the noise caused by charges fluctuating near the QPC.

2.2.4 Carbon nanotube displacement detector

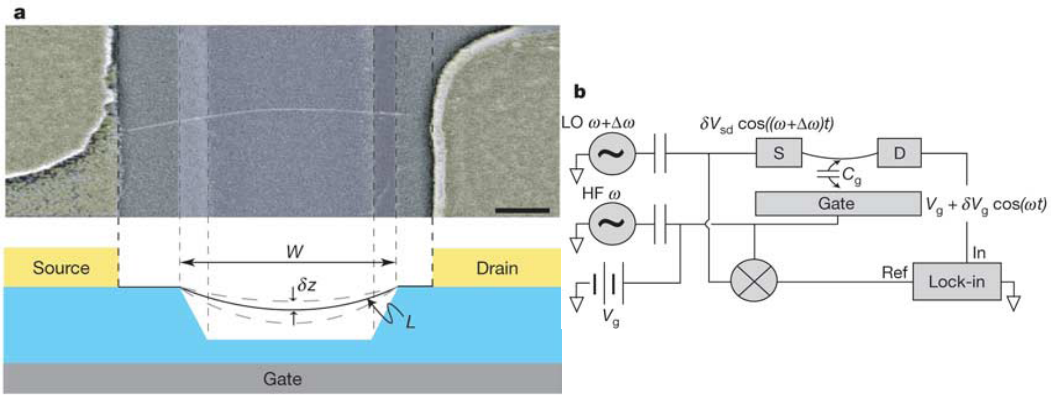

Figure 2.6: Carbon nanotube displacement detector, figure from reference [6]

The nanomechanical motion of carbon nanotubes has been measured using the carbon nanotube as both the sensing element and the mechanical oscillator [6, 35–37]. The resistance of the nanotube is effected by the charge induced on the nanotube. This effect is used to detect mechanical motion by voltage biasing a nearby gate electrode that is capacitively coupled to the nanotube (figure 2.6) and measuring changes in nanotube resistance. Mechanical motion changes the nanotube-gate capacitance; the resulting change in the charge induced on the nanotube creates a detectable shift in the resistance of the nanotube. The nanomechanical motion of nanotubes and larger silicon nanopillars has also been detected using the field emission of electrons from the tip of the nanotube or pillar [137–139].

2.3 The Atomic Point Contact as a Mesoscopic Detector

In this section, I briefly review the use of atomic point contacts (APCs) as mesoscopic detectors and the theoretical descriptions of APC displacement detectors. The APC has been widely used to detect the position of atoms in scanning tunneling microscopes (STMs) and to investigate both mechanical and electrical properties on the atomic scale. In this thesis, I combine the displacement sensitivity of the APC with a fast measurement technique to detect nanomechanical displacement and evaluate the performance of the APC as a detector of displacement. Theoretical descriptions of this type of APC detector indicate that it is possible for the APC to be used to detect motion at the limits imposed by quantum mechanics.

2.3.1 APC as a widely used detector of static displacements

Broadly speaking, the use of APCs as detectors of static displacement can be divided into two categories. The first category contains STMs where the APC is created by bringing an atomically sharp tip close to another surface. The position of the tip can be scanned over the surface and controlled in three-dimensions, creating a versatile tool

for investigating mesoscopic phenomenon. Second, the APC can be created *in situ* from a constriction composed of more than 10^6 atoms either using electromigration or by straining the constriction; the constriction is often part of a suspended nanostructure. This second type of APC trades the ability to scan the tip for simplicity and stability. Usually the mechanical circuit is entirely on-chip resulting in a much stiffer support structure than can be obtained in a STM. Experiments that investigate how metals fracture and flow on the atomic scale and the electrical properties of single atoms and molecules can be carried out using either type of detector, but benefit from the improved stability of the second category of APCs which are supported by a nanostructure.

APCs provide the atomic resolution in STMs [7, 22, 38, 39]. As implied by the name "scanning tunneling microscope", an STM scans a tunneling probe, i.e., APC, over a surface and uses the changes in the probability that an electron tunnels to create a topographic image of the surface (figure 2.7). The probability that an electron will tunnel is exponentially sensitive to the size x of the gap and so the resistance of the APC is $R_{APC} = R_0 \exp[2x/\lambda]$. The length scale λ that controls the probability of electrons tunneling is determined by the height of the energy barrier through which the electrons tunnel. The energy barrier is usually set by the work function ϕ of the material; in most metals, ϕ is on the order of 5 eV resulting in a length scale $\lambda \approx 0.1$ nm. The exponential dependence of the APC resistance on a sub-atomic length scale allows an STM to image the surface of a pure material with atomic resolution. Experimentally, the gap x is determined by applying a voltage V_{APC} across the APC and measuring the tunneling current $I_{APC} = V_{APC}/R_{APC}$ as the tip of the APC is swept over a surface (figure 2.7).

The high-impedance nature of the APC limits the speed, or bandwidth, of the position measurement. STMs are usually operated with APC gaps > 1 nm and $R_{APC} > 1$ MΩ. There is also capacitance in parallel with the APC resistance (figure 2.7); this stray capacitance C_s is usually dominated by the electrical wiring connecting the APC to

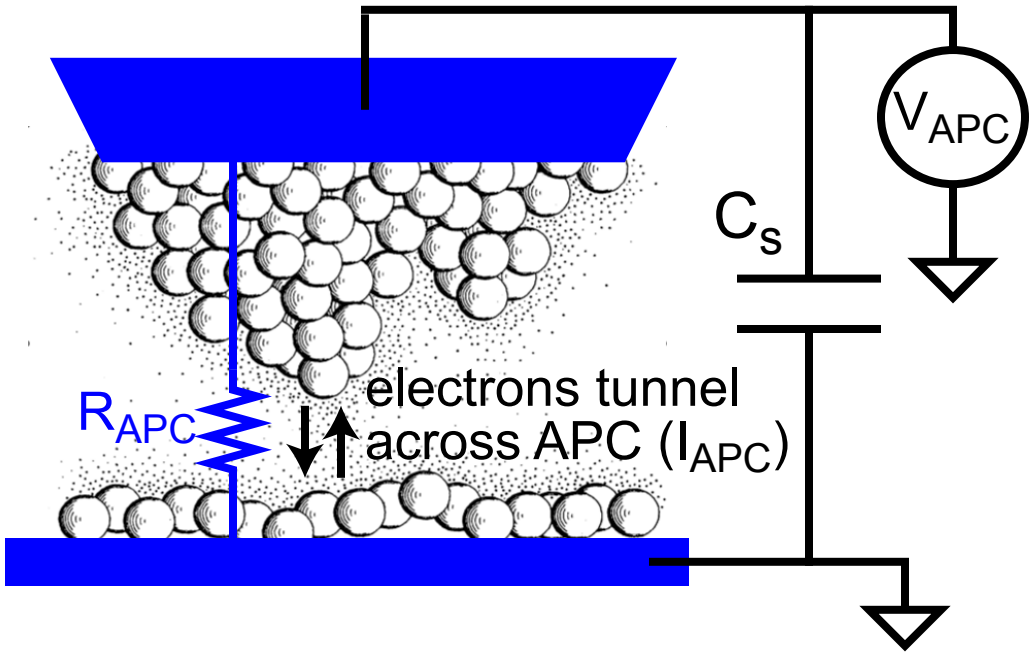

Figure 2.7: Basic diagram of Scanning Tunneling Microscope (STM), figure adapted from reference [7]. The topography of the surface is determined by scanning the tip (triangular arrangement of atoms) over the surface and determining the relative change in the probability of electrons tunneling from the tip. The tip is voltage biased V_{APC}, and measured changes in the tunneling current $I_{APC} = V_{APC}/R_{APC}$ are used to infer the probability of electron tunneling.

external amplifiers. The APC resistance $R_{APC} > 1$ MΩ and stray capacitance $C_s > 1$ fF form a low-pass RC filter with a resonance frequency less than 100 kHz [11, 140]. Any signal at frequencies above 100 kHz will be attenuated by this unintentional RC filter, limiting the bandwidth of the resistance measurement.

There have been a number of attempts to overcome this bandwidth limitation. Standard STMs have been improved to the point where the bandwidth of the electrical measurement is on the order of 500 kHz [141, 142]; in these experiments, the focus is often on improving the speed with which the APC can be scanned over a surface. There have also been attempts to directly measure radio-frequency spin precession [143, 144] using an STM tip. The sample is placed in a static magnetic field and the STM tip is

located near a spin center. The spin precesses at the Larmor frequency (500-800 MHz in these experiments). The changing magnetic moment couples to the tunneling electrons, causing modulations at the Larmor frequency in the probability of electrons tunneling. This signal frequency is significantly higher than the frequency of the unintentional low pass filter, so the signal should be significantly attenuated. These experiments did not focus on improving the bandwidth of the STM, but instead simply increasing the tunneling current until the 500-800 MHz signal could be detected despite the attenuation [144].

Ekinci [140], following the work described in this thesis [11], recently used a microwave technique to increase the STM bandwidth and create the RF-STM. This technique involves creating an LC matching circuit with a bandwidth > 10 MHz and will be described in detail in chapter 5. It was first used in mesoscopic physics by Schoelkopf [128] to increase the bandwidth of another high-impedance device, the SET, and create the RF-SET. Using this technique, Ekinci demonstrated an RF-STM with a bandwidth of 10 MHz [140]. Ekinci also measured the motion of a 65 μm by 70 μm by 40 nm silicon nitride membrane coated with 20 nm of gold. The best imprecision obtained in this measurement was 15 fm/$\sqrt{\text{Hz}}$ and was limited by amplifier noise, not the smaller fundamental noise due to the shot noise of tunneling electrons.

STMs are not only used to create topographic images, but also to probe the mechanical and electrical properties of small numbers of atoms and molecules. In fact, the initial motivation behind the STM was to create a local spectroscopic probe [7]. Electrical properties of samples are determined by measuring the dependance of the tunneling current I_{APC} on the voltage V_{APC} across the APC. In the simple tunneling picture, the tunneling current is proportional to voltage $R_{APC} = V_{APC}/I_{APC}$ when $eV_{APC} \ll \phi$. However, changes in the local density of states due, for example, to deviations in the tunneling barrier from a rectangular barrier or the presence of vibrational energy levels will result in a voltage-dependent tunneling current and resistance

$d^2R_{APC}/dV_{APC}^2 \neq 0$ [145]. This spectroscopic technique has been widely used to investigate the electrical properties of everything from high temperature superconductors to graphene [146]. I will discuss the voltage dependence of the tunneling current in chapter 3 and the effect of vibrational levels in chapters 3 and 7.

STMs are used to probe mechanical characteristics on the atomic scale in two different ways. First, the STM can be combined with an atomic force microscope (AFM) to measure the force required to change the size of the APC gap [147, 148]. This can be used to understand how metals fracture and flow on the atomic scale. Second, the interaction between the STM tip and the surface atoms can be used to manipulate the position of atoms and understand how atoms slide over surfaces [149, 150].

The second, different, way in which APCs are often created is by fabricating a thin, narrow section of material and removing atoms *in situ* until electron transport across the junction is due to tunneling between two atoms: an APC. The thin, narrow section of material is usually a constriction in a larger nanostructure created on-chip using the tools of nanolithography (for example, figure 2.8). The micron-scale support structure is both simpler and stiffer than the cm-scale structure used to support and scan the APC in an STM.

Two different techniques are commonly used to remove atoms from the constriction and create an APC. First, a large current can be passed through the constriction. In a process called electromigration, atoms will move from regions of high current density to low current density eventually forming an APC. Second, the constriction can be strained by increasing the distance between the supports (figure 2.8); under strain, constriction will flow, reducing the cross-section and eventually fracturing forming an APC. This type of junction is called a mechanically controllable break junction (MCBJ). Unlike an electromigrated APC, the resistance of a MCBJ can be controlled and cycled between completely closed, with $> 10^3$ atoms separated by < 0.1 nm, and open with the resistance controlled by the > 100 nm separation between two atoms.

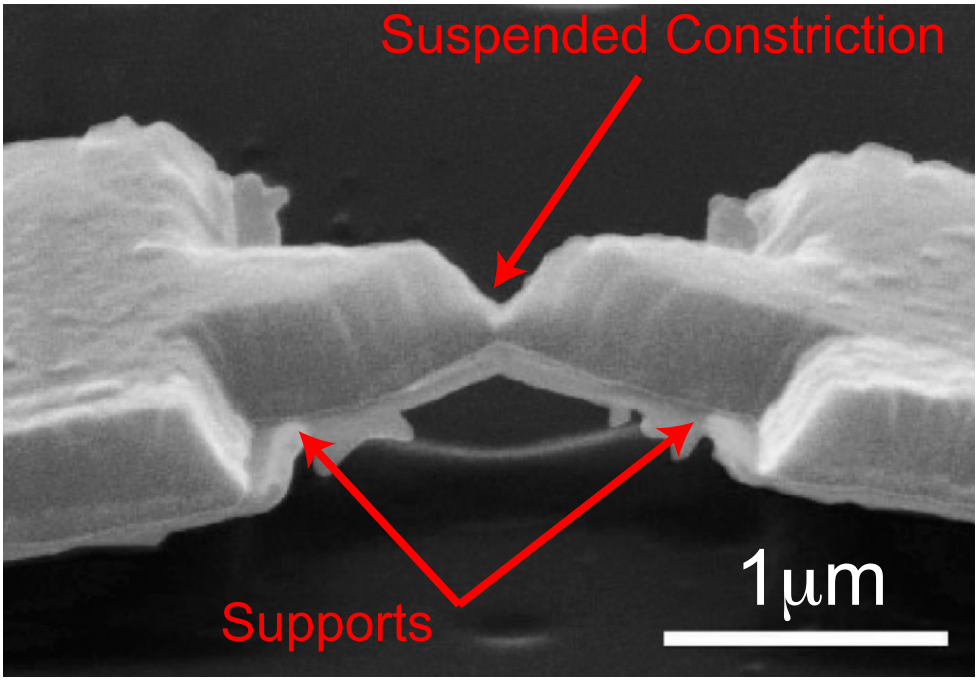

Figure 2.8: Example of the nanostructure used in a mechanically controllable break junction (MCBJ), figure adapted from reference [8]. In this isometric scanning electron micrograph, the constriction is suspended above the substrate over a length of 1 μm by two supporting electrodes.

The experiments described in this thesis have used both electromigrated APCs and APCs created by applying mechanical strain. The creation of these APCs is discussed in detail in chapter 4. A more detailed review of the creation and properties (which are briefly discussed below) of such atomic-sized conductors is also given in reference [8].

MCBJs have been used to study the fracture and flow of metals at the atomic scale [8]. In one technique, the resistance of the MCBJ is cycled between closed and open and hysteretic patterns in the resistance as a function of strain are observed due to atom rearrangement. This hysteretic behavior has, for example, been used to study how chains of gold atoms form and break under strain [151]. Repeatable hysteretic loops in gold APCs have also been used to determine the adhesion between the two atoms that form a gold APC. The data is explained by a simple elastic model of a gold

dimer attached to elastic electrodes; the electrodes are modeled as springs with a spring constant between 5 N/m and 32 N/m [9].

A similar technique has also been used to investigate how the electrical properties of the junction change as the junction fractures. Instead of analyzing just a single cycle between closed and open, thousands of cycles are averaged in a histogram. It is hoped that using many cycles averages over mechanical effects due to the position of atoms and reveals the preferred values of the electronic system [8]. In gold, these histograms generally show a clear peak at the quantum of resistance, $R_Q = h/2e^2 = 12.9$ kΩ and smaller, less pronounced peaks at $R_Q/2$ and $R_Q/3$. This technique has also been used to investigate the change in the electrical properties of the APC created by the presence of other atoms or molecules in the junction [8, 54].

APCs created using both electromigration and mechanical strain have been used to electrically contact and study single molecules [8]. These experiments usually use gold or platinum contacts which are inert and easy to clean. The molecules are incorporated into the APC using two different techniques. First, after the APC has been created a gas of molecules can be added to the APC environment [49, 50, 54]. One (or more) molecule condenses on the APC, changing the electrical and mechanical properties of the APC. Second, molecules can be placed on the surface of the nanostructure prior to APC creation, usually by placing the nanostructure in a dilute solution that includes the molecule of interest. The APC is then created using either electromigration (for example, [40, 52, 56]) or mechanical strain (for example, [51, 53, 57, 152]). In a fraction (usually $> 10\%$) of the APCs there is a molecule trapped in the middle of the APC. The presence of the molecule is confirmed based on the mechanical and electrical properties of the APC.

As with the STM, the electrical properties of samples are determined by measuring the dependance of the tunneling current I_{APC} on the voltage V_{APC} across the APC. This has been used to study molecular conductance and APC-molecule coupling [54, 57]

as well as, more specifically, the Kondo effect [51, 56] and Coloumb blockade physics in molecules (which also requires a nearby capacitive gate) [40, 52, 53, 56]. This spectroscopic measurement has also been used to study the conformational changes [49] and vibration [10, 40, 50, 52, 54] of molecules attached to the APC. A static change in the orientation of the molecule in the junction shifts the resistance of the APC. The coupling between electron tunneling and molecular vibration causes a change in the resistance of the APC at a voltage V_{APC} where the energy of the electron eV_{APC} is large enough to excite the molecular vibration $\hbar\omega_m$. This is discussed in more detail in chapters 3 and 7 and references [8, 10]. The same procedure has also been used to study the vibration of chains of gold atoms created using mechanical strain [152].

2.3.2 APC as a quantum-limited displacement detector

In this thesis, I combine the displacement sensitivity of the APC with a fast measurement scheme and implement an APC displacement detector. The APC displacement detector has two main advantages over optical displacement detectors and other mesoscopic displacement detectors: it is inherently a nanoscale detector, and, unlike many other mesoscopic detectors, the measurement imprecision can be limited by the the shot noise of tunneling electrons which is the fundamental source of noise in an APC. This idea is not new; the use of an APC to detect the vibration of micron and nano-scale mechanical structures was proposed in the late 1980s and early 1990s in the context of gravitational wave detection [58–63]. At the time, theoretical evaluations of the APC detector based on an analysis of electron tunneling through a barrier indicated that an APC detector could be quantum limited [64–66]. Starting in 2002 there has been renewed theoretical interest in the APC displacement detector in the context of quantum-limited measurement [67–77].

In 2007 I demonstrated an APC measurement with a 30 MHz bandwidth [11] using the same microwave technique that was used by Schoelkopf in creating the RF-

SET [128]. This increased bandwidth adds a dynamic component to a previously static measurement of APC resistance. Instead of just measuring the average resistance of the APC, I can measure the fast modulation in resistance caused by nanomechanical motion. In comparison, previous measurements of displacement due to molecular vibrations were only able to measure the indirect effect of molecular vibration energy levels on the average resistance. I not only detect nanomechanical motion, but the noise in the measurement is also dominated by the shot noise of tunneling electrons (see chapter 5). This is important, because it is the fundamental source of noise in the APC detector.

In detecting nanomechanical motion, the APC detector has a number of advantages over both optical detectors and other mesoscopic detectors. First, unlike the other detectors it is inherently a detector of atomic-scale motion. The optical detectors are not sensitive to the motion of objects that are much smaller than the wavelength of the light used in the detector. Most other mesoscopic detectors either rely on capacitive coupling between the nanostructure and the detector or measure the total strain created by nanomechanical motion. In both cases, the coupling becomes smaller as the dimensions of the nanostructure are decreased. On the other hand, the APC detector measures the change in the relative position of two atoms. The coupling between that atomic gap and motion of the surrounding nanostructure is not inherently decreased by shrinking the size of the nanostructure.

Second, as mentioned above, the noise in the APC displacement measurement can be dominated by the shot noise of tunneling electrons. This is important because in an APC detector and many other mesoscopic detectors the fundamental source of noise is shot noise. Additional sources of noise such as external amplifiers can also contribute to the total measurement noise, however these sources of noise are not a fundamental part of the measurement. Achieving a quantum limited measurement requires that the additional sources of noise are negligible compared to the fundamental noise, that is, the shot noise. Two approaches are used to minimize the additional noise in comparison

to the shot noise. First, the additional noise is made as small as possible using carefully designed electrical circuits and low-noise cryogenic amplifiers (see chapter 5). Second, the shot-noise is made as large as possible. This is somewhat counter-intuitive, since it increases the total noise in the measurement. However, the size of the signal due to mechanical motion (in displacement units) is linearly proportional to the current while the shot noise is proportional to the square root of the current. Increasing the shot noise therefore results in a more precise measurement of displacement and decreases the displacement noise added by the additional, non-fundamental noise sources.

In this context, the APC has an advantage over other mesoscopic detectors because it can be used to create larger shot noise. The maximum voltage that can be applied to the APC is determined by the height of the tunneling barrier. In most metals, the height of the barrier is about 5 eV; the effective barrier in most other mesoscopic devices is much smaller. This comparatively large energy scale implies that a large voltage can be applied to the APC resulting in a large tunneling current and large shot noise. In other words, the APC can have much larger gain than other mesoscopic detectors. Given the magnitude of additional noise added by commercial low-noise amplifiers, APC displacement measurements can be limited by shot noise while displacement measurements made using other mesoscopic detectors, such as SETs, have been limited by the additional noise of amplifiers. It is relatively easy to use an optical detector to make displacement measurements which are limited by photon shot noise.

One disadvantage of the APC detector is that atomic-scale contamination and mesoscopic effects will affect the displacement measurement. In STMs at resistances > 10 MΩ the tunneling barrier appears consistent with a simple rectangular barrier. However, at low resistances and in the presence of contaminant atoms or molecules the mesoscopic physics becomes more complicated. This physics will effect the displacement measurement and is generally expected to reduce the measurement precision (that is, *increase* the measurement imprecision). Atomic rearrangements also alter the mechanical

resonance frequency and dissipation rate. When the APC is unstable, the mechanical resonance is unstable; it is then not possible to determine the properties of the APC displacement detector.

The idea of using an APC to directly detect mechanical motion near the quantum limit is not new; in 1988 Niksch and Binnig proposed that an APC could be used to create a broadband detector of gravitational waves [63]. This proposal was expanded upon by Bocko, Stephenson, and Koch over the next three years [58, 59, 61, 62]. They evaluated the detector from an experimental perspective, including a generic amplifier, and estimated that the displacement detector could operate at the limit imposed by the Heisenberg uncertainty principle $S_x S_F \geq \hbar^2$.

The spectral density S_F of the backaction force noise is estimated using a simple model where each tunneling electron delivers a momentum kick to the mechanical structure. The average momentum that each electron delivers is assumed to be about equal to the Fermi momentum p_F. Because there is shot noise with spectral density $S_I = 2eI_{APC}$ in the current I_{APC} through the APC, the average momentum delivered by each electron creates a noisy backaction force with spectral density $S_{Fcorr} = 2p_F^2 I_{APC}/e$. This force is correlated with the electron shot noise, so it is theoretically possible to apply a force to the nanostructure proportional to the shot noise and cancel the effect of S_{Fcorr}. Therefore this component of the backaction force is not fundamental and is not included in the comparison of the APC to the Heisenberg limit.

The variance in the size of the momentum kick that is delivered by each electron also causes a backaction force. This backaction force is not correlated with the electron shot noise and enforces the Heisenberg limit. Bocko, Stephenson, and Koch assume that the act of tunneling effectively "measures" the location of the electron with an uncertainty $\Delta x \approx \lambda/2$ where λ is the length scale that controls the probability of electron tunneling. Using the uncertainty relationship $\Delta x \Delta p \geq \hbar/2$, the uncertainty in each electron's momentum is at least $\Delta p = \hbar/\lambda$. A current I_{APC} through the APC will

therefore create a noisy backaction force with a spectral density $S_F = (\hbar/\lambda)^2(I_{APC}/2e)$. The estimated spectral density of the displacement noise due to the shot noise of tunneling electrons is $S_x = \lambda^2/2eI_{APC}$. This simple estimate of the backaction force and displacement imprecision of an APC detector predicts that the product of the backaction and imprecision is equal to the limit imposed by quantum mechanics $S_x S_F = \hbar^2$.

More careful theoretical evaluations of the APC displacement detector in the early 1990s also predicted that the detector could be used to make a quantum limited measurement of position [64–66]. They model the APC as an arbitrary one-dimensional tunnel barrier. A fraction of the electrons incident on the barrier tunnel through the barrier, creating a current of tunneling electrons. The average fraction of electrons that tunnel can be used to measure the width of the barrier; this is a familiar problem used in basic quantum mechanics courses. The uncertainty in the fraction of tunneling electrons, that is, the shot noise, determines the imprecision Δx in the measurement of the width of the barrier. They also calculate the momentum transported across the barrier, and determine the uncertainty in the momentum Δp which is not correlated with the imprecision. For a rectangular barrier, they determine that a quantum limited uncertainty product $\Delta x \Delta p = \hbar/2$ can be achieved.

The APC displacement detector attracted more theoretical interest after 2002 in the context of quantum-limited measurements [67–77]. In comparison to the early 1990s, these theoreticians take a different approach to calculating the effect of the measurement on the mechanical oscillator. In general, they calculate the effect of mechanical displacement on the tunneling current and the backaction of the tunneling current on the mechanical oscillator by describing the detector using a tunnel Hamiltonian with a small linear coupling to displacement. For example, reference [75] uses the detector Hamiltonian

$$H_{det} = \left[\frac{\tau_0 + e^{i\nu}\tau' \hat{x}}{2\pi\Lambda} \sum_{k,k'} \left(Y^\dagger c^\dagger_{R,k} c_{L,k'} + \text{H. C.} \right) \right] - eV(t)\hat{m} \tag{2.2}$$

where $\hat{m}$ denotes the number of electrons that have tunneled, the operator $Y^{\dagger}$ increases $\hat{m}$ by one, the operators $c_{R,k}$ and $c_{L,k}$ destroy an electron state on the right and left side of the APC respectively, τ_0 is the displacement-independent tunneling amplitude, and Λ is the conduction-electron density of states. Displacement $\hat{x}$ is linearly coupled to the tunneling amplitude with a proportionality constant τ' and relative phase ν. It is assumed that the displacement will only create small changes in the tunneling amplitude $\tau_0 \gg \tau' x$. The state of the oscillator x and current m is described using a reduced density matrix. The time evolution of the reduced density matrix is used to determine the full counting statistics of the tunneling electrons m and the effect of displacement x. It is generally found that the detector will create a backaction force. In qualitative agreement with earlier theoretical work, part of the force is correlated with the shot noise of tunneling electrons and part is uncorrelated. Unlike early work, the detector is also predicted to modify the intrinsic dissipation of the mechanical system $\gamma_{tot} = \gamma_{intrinsic} + \gamma_{det}$. The fluctuating force created by the detector can be described by an effective temperature $T_{eff} = eV_{APC}/2$ and damping constant γ_{det} which depends on the strength of the position measurement.

In this thesis, I will evaluate the APC displacement detector in the context of the phenomenological model described by Bocko, Stephenson, and Koch [58, 59, 61, 62] (see chapter 3 for details). The precision of the measurement and the strength of the coupling between displacement and tunneling are not large enough to be able to distinguish between this phenomenological model and the more detailed expectations of the other more complicated models. In addition, even though the theoretical models make a distinction between the backaction forces that are correlated and uncorrelated with the shot noise, in this experiment it is not possible to separate the two types of forces. Finally, it is difficult to extract detailed information about the backaction force because it is obscured by the larger 4 K thermal force on the nanostructure.

Chapter 3

The Theory of an Atomic Point Contact Coupled to a Nanomechanical Oscillator

In this chapter, I start by considering the physics of an electron incident on an atomic point contact (APC). Even if there is no scattering, that is, no tunnel barrier, the junction is still resistive because there are only a limited number of channels for electrons to flow through the junction. In an atomic point contact composed of two atoms with no tunnel barrier, there is one spin-degenerate channel and the resistance $R_{APC} = h/2e^2$. When electrons scatter with a transmission probability D, $R_{APC} = h/2e^2D$ and there will be shot noise in the tunneling current. In the limit where $D \ll 1$ and the temperature is zero, the noise is Poissonian and results in a voltage noise with spectral density $S_V = 2eV_{APC}R_{APC}$. The probability D that an incident electron will tunnel through a vacuum gap is calculated using the Wentzel-Kramers-Brillouin (WKB) method and is approximately equal to $D = \exp[-2x/\lambda]$ where x is the width of the tunneling gap and λ is the length scale that controls the probability of electron tunneling (in gold, $\lambda \approx 90$ pm).

I also compare the APC displacement detector, as described by a phenomenological model, to a quantum-limited detector. The imprecision-backaction product of a continuous, linear quantum-limited detector with uncorrelated backaction S_F and imprecision S_x is equal to the minimum allowed by the Heisenberg uncertainty constraint $S_xS_F \leq \hbar^2$. Using a phenomenological model of the APC detector where the impreci-

sion is caused by the shot noise of tunneling electrons and the backaction is caused by the momentum kicks of tunneling electrons, I estimate that the APC detector can be quantum-limited.

Finally, I describe the flexural motion of a nanomechanical beam and the effect of an APC on the mechanical structure. The vibration of the structure is described using a set of orthogonal modes; each mode has an eigenfrequency and can be thought of as a simple harmonic oscillator. The thermal motion of a single eigenmode at a known temperature can be used to calibrate a displacement measurement [11].

3.1 Electron Tunneling Across an Atomic Point Contact

In this thesis, I generally assume that a small change δx in the size of the APC gap causes an exponential change in the resistance R_{APC} of the APC. In this section I justify this assumption that $R_{APC} = R_0 \exp(2\delta x/\lambda)$. I start by calculating the conductance of a junction where electrons flow through a single channel without scattering, that is, without a gap and with a transmission probability $D = 1$. This is also called ballistic transport and occurs, for example, in a chain of gold atoms. The resistance of a ballistic junction, including spin degeneracy, is equal to half the quantum of resistance $R = h/2e^2$. The quantum of resistance sets the scale of the tunneling resistance. When electrons scatter off of, for example, a potential barrier with a transmission probability D then the resistance of the junction is $R_{APC} = h/2e^2D$. I also describe how the probabilistic nature of electron tunneling causes shot noise in the current passing through the tunnel barrier. Finally, I calculate the probability $D(x)$ that an electron will tunnel through a barrier of width x concentrating on the experimentally relevant case of a rectangular barrier and a small applied voltage bias.

3.1.1 Nano-scale ballistic contact

While the conductance of macroscopic systems $G = \sigma(A/L)$ simply scales with the cross-sectional area A and length L of the conductor, this scaling breaks down when considering nano-scale junctions. At small scales the quantization in the directions perpendicular to L, that is, the transverse directions, becomes important. In this thesis, quantization becomes important when the transverse dimensions are on the atomic scale, though, depending on the material, quantization can effect devices with transverse dimensions up to hundreds of nanometers. The quantization of the transverse momentum limits the number of available incoming and outgoing modes in the junction and the resistance of the junction is due to the transition between the small number of modes in the junction and the large number of modes in the surrounding contacts. This description follows the derivations in references [17, 18, 20, 153].

I will consider the conductance of a ballistic junction between two contacts (figure 3.1). To simplify the discussion below, I assume that the junction is a thin, narrow rectangular conductor. An external potential is applied between the two contacts causing electrons to flow through the junction. Since there is no scattering, the current through the junction and the resistance of the junction are determined by the number of accessible momentum states in the direction perpendicular to the electron flow. In other words, the resistance depends on the number of transverse modes or channels.

The different transverse modes, which are similar to the modes traveling down a waveguide, are well-defined with distinct energy levels. These are the modes of a junction which is a conductor (figure 3.1) with length L in the $\hat{x}$ direction, width W in the $\hat{y}$ direction, and a height Z in the $\hat{z}$ direction where $Z \ll W$ so the junction is effectively two dimensional. There is also a confining potential $U(y)$. Under these conditions, the motion of the electrons (in the absence of a magnetic field) is described

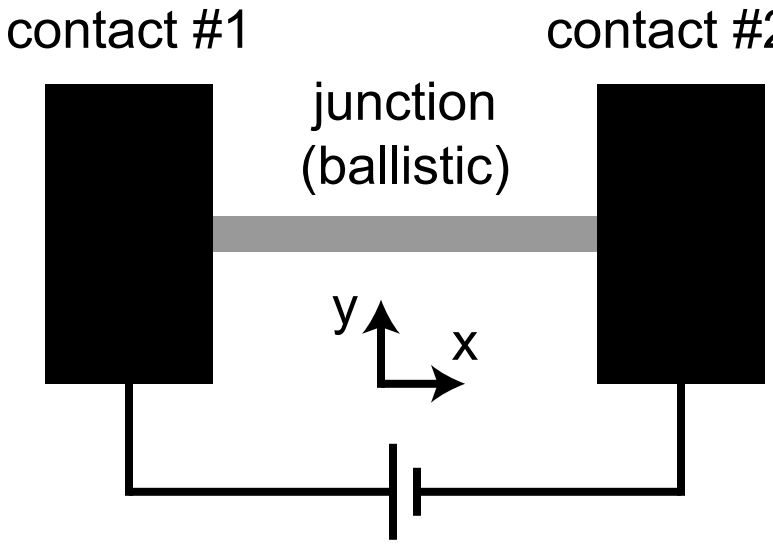

Figure 3.1: A thin, narrow ballistic junction (grey) is attached to large contacts (black). Even though electrons do not scatter in the junction, the transition from large contacts to a small junction creates resistance.

by

$$\left[E_s + \frac{p_x^2}{2m} + \frac{p_y^2}{2m} + U(y)\right]\Psi(x,y) = E\Psi(x,y) \tag{3.1}$$

Expressing Ψ in the form of plane waves traveling through the junction and assuming that $U(y)$ is a parabolic confining potential $U(y) = m\omega_y^2 y^2/2$, which is a good approximation for electron waveguides,

$$\Psi(x,y) = \frac{1}{\sqrt{L}}\exp\left[ik_x x\right]\phi(y) \tag{3.2}$$

$$\left[E_s + \frac{(\hbar k_x)^2}{2m} + \frac{p_y^2}{2m} + \frac{1}{2}m\omega_y^2 y^2\right]\phi(y) = E\phi(y) \tag{3.3}$$

The electron eigenenergies are

$$E(k_x, n_y) = E_s + \frac{(\hbar k_x)^2}{2m} + \left(n_y + \frac{1}{2}\right)\hbar\omega_y, \quad n_y = 0, 1, 2, \ldots \tag{3.4}$$

The use of a parabolic potential is convenient, but not necessary; the important feature of this equation is the discrete energy levels due to confinement in the $\hat{y}$ direction.

For a given electron energy E_e and momentum k_x, the number of available modes is determined by the width of the conductor. For a wide conductor, such as the region contacting the junction, the confining potential is weak and the frequency ω_y is small (compared to a narrow conductor). The eigenergies $E(k_x, n_y)$ of the wide conductor are more tightly spaced, so the number of available modes with an eigenergy less than E_e is much larger than for a narrow conductor. In a narrow conductor, such as the junction, the electrons are tightly confined by a potential with a larger frequency ω_y. The resulting eigenergies are more widely spaced, resulting in fewer available modes. When the narrow junction is connected to wide contacts (figure 3.1), there is a transition between the large number of transverse modes in the contacts to the small number of transverse modes in the junction.

The change in the number of transverse modes results in an effective resistance that is inherent to any mesoscopic system and is not due to quantum interference or uncertainty. In calculating the resistance, I start with a ballistic conductor, as described above, which is connected to two reflectionless contacts (figure 3.1). Since electrons do not reflect of off the contacts, all of the k_+ modes which contribute to the current in the positive $\hat{x}$ direction are due to excitations in contact #1 (left, figure 3.1) and all of the k_- modes which contribute to the current in the negative $\hat{x}$ direction are due to excitations in contact #2 (right, figure 3.1). There will not be any mixing caused by internal reflection off of the contact/conductor interfaces. In other words, the occupation of the k_+ modes is purely a result of the chemical potential μ_1 of contact #1 and the occupation of the k_- modes is purely a result of the chemical potential μ_2 of contact #2.

The current through the junction due to an applied bias V_{APC} is found by summing the electron transport due to all of the occupied modes. The probability that a mode with energy E in contact #1 and contact #2 is occupied is given by the Fermi function $f_1(E)$ and $f_2(E)$ respectively. The total current from contact #1 to contact

#2 is the sum of the current $-ev_k/L$ due to each available mode weighted by the Fermi function

$$I = \sum_{k_x,n_y} \frac{ev_{k_x}}{L} \left[f_2(E_{k_x,n_y}) - f_1(E_{k_x,n_y})\right] \tag{3.5}$$

$$I = \frac{e}{\hbar} \sum_{n_y} \int \frac{\partial E_{k_x,n_y}}{\partial k_x} \left[f_2(E_{k_x,n_y}) - f_1(E_{k_x,n_y})\right] D_{k_x} dk_x \tag{3.6}$$

where $\hbar v_k = \partial E_{k_x,n_y}/\partial k_x$ and D_{k_x} is the one-dimensional density of states. A voltage V applied to contact #1 will change the chemical potential $\mu_1 = \mu - eV$ of contact #1 in comparison to $\mu_2 = \mu$ for contact #2. At low temperatures the Fermi functions are $f_m(E) = \theta(\mu_m - E)$. Since only available modes with an eigenergy $E(k_x = 0, n_y)$ less than the electron energy contribute to the current, the total current is

$$I = \frac{e}{2\pi\hbar} \sum_{n_y} \int_{E(k_x=0,n_y)}^{\infty} dE \left[\theta(\mu - E) - \theta(\mu - eV - E))\right] \tag{3.7}$$

$$I \approx \frac{e^2}{h} V \sum_{n_y} \theta(\mu - E(k_x = 0, n_y)) = N \frac{e^2}{h} V \tag{3.8}$$

where N is the number of occupied modes. The conductance of the junction is equal to the quantum of conductance e^2/h per mode. In an atomic point contact, the two states of the electron spin are degenerate and the total resistance is

$$R_{APC} = \frac{h}{2e^2} \frac{1}{N'} \tag{3.9}$$

where N' is the number of available spin-degenerate channels. For a more detailed discussion of the resistance of atomic point contacts see reference [8].

Electron scattering due, for example, to the presence of a vacuum gap will increase the resistance of a junction. Instead of assuming that the junction is a ballistic conductor, I include the possibility that an electron will scatter. The junction is effectively composed of three parts (figure 3.2): ballistic lead #1 connects contact #1 to the second part, a set of scatterers, which are then connected by ballistic lead #2 to contact #2. Because of the scatterers, an electron in mode n will scatter and transmit with a probability D_n or reflect with probability $1 - D_n$.

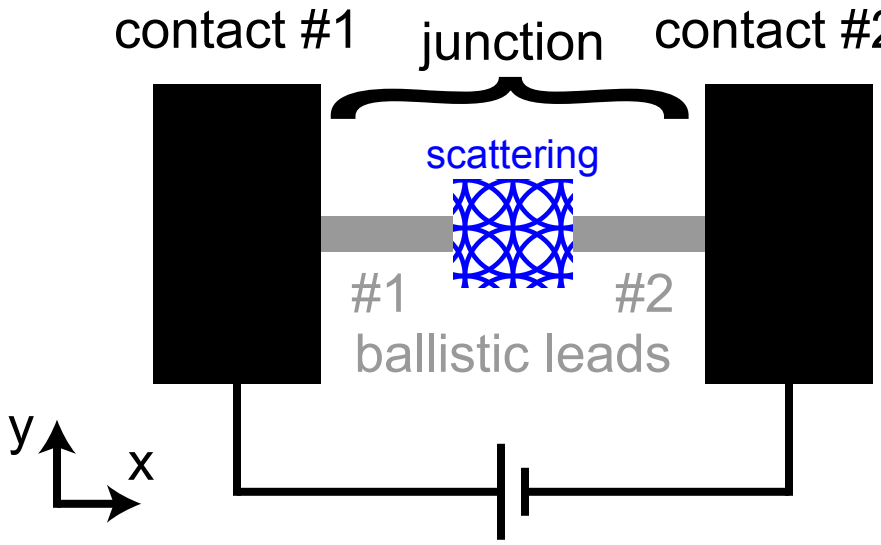

Figure 3.2: A junction is composed of scatterers (blue) and thin, narrow ballistic leads (grey) which are attached to large contacts. The resistance of the junction is increased by the presence of scatterers in comparison with a ballistic junction.

The total current through the junction is equal to the sum of the incident and reflected current as well as the transmitted current. The magnitude of the current incident on the scatterers from ballistic lead #1 due to a voltage V is equal to the current in a ballistic conductor (equation 3.7). For each mode, a fraction $1 - D_n$ of the incident electrons are reflected and a fraction D_n are transmitted into ballistic lead #2 so the total current I flowing through the junction is

$$I = \left(\sum_{n=1}^{N'} \frac{2e^2}{h} V\right) - \left(\sum_{n=1}^{N'} (1 - D_n) \frac{2e^2}{h} V\right) = \sum_{n=1}^{N'} D_n \frac{2e^2}{h} V \tag{3.10}$$

The resistance of this junction is

$$R = \left(\sum_{n=1}^{N'} D_n \frac{2e^2}{h}\right)^{-1} \tag{3.11}$$

and the expected resistance of a ballistic junction is recovered by setting $D_n = 1$ (all of the electrons are transmitted).

3.1.2 Electron shot noise

The discreteness of electrons and the probabilistic nature of electron tunneling creates shot noise in the tunneling current. The shot noise of tunneling electrons is the fundamental source of noise in mesoscopic measurements that use tunnel junctions, such as the APC displacement detector. The shot noise in mesoscopic junctions has been reviewed in detail in references [8, 19, 154, 155]. The current noise spectral density $S_I(\omega)$ is equal to the Fourier transform of the correlation function

$$S_I = 2\int_{-\infty}^{\infty} dt e^{i\omega t}\langle \Delta\hat{I}(t)\Delta\hat{I}(0)\rangle \tag{3.12}$$

where $\Delta\hat{I}(t) = \hat{I}(t) - \langle\hat{I}(t)\rangle$ and the factor of two is included because I use a single-sided spectral density which is only defined for positive frequencies.

I will briefly sketch the calculation of shot noise described in detail in references [8] and [19]. The current operator $\hat{I}(t)$ is defined in terms of electron annihilation and creation operators. The operators (α =1 or 2, figure 3.2) $\hat{a}_{\alpha n}(E)$ and $\hat{a}^{\dagger}_{\alpha n}(E)$ annihilate and create incoming electrons with energy E in channel n of contact $\#\alpha$; similarly, $\hat{b}_{\alpha n}(E)$ and $\hat{b}^{\dagger}_{\alpha n}(E)$ annihilate and create outgoing electrons. The occupation of the incoming modes is determined by

$$\langle \hat{a}^{\dagger}_{\alpha n}(E)\hat{a}_{\beta m}(E')\rangle = \delta_{\alpha\beta}\delta_{mn}\delta(E-E')f_{\alpha}(E) \tag{3.13}$$

where $f_\alpha(E)$ is the Fermi function in contact α. The outgoing modes are related to the incoming modes by the scattering matrix which also determines the transmission probabilities D_n and reflection probabilities $1 - D_n$. The current operator in contact $\#\alpha$ is

$$\hat{I}_{\alpha}(t) = \frac{2e^2}{h}\sum_{n=1}^{N'}\int dE dE' e^{i(E-E')t/\hbar}\left[\hat{a}^{\dagger}_{\alpha n}(E)\hat{a}_{\alpha n}(E') - \hat{b}^{\dagger}_{\alpha n}(E)\hat{b}_{\alpha n}(E')\right] \tag{3.14}$$

and the expectation value $\langle\hat{I}_\alpha(t)\rangle$ is, as expected, equal to the average current calculated earlier using a different approach (equations 3.6, 3.7, 3.10).

Calculating the shot noise (equation 3.12) involves finding the expectation value of products of two creation and two annihilation operators. After performing the necessary algebra, the shot noise in the two contacts is

$$S_I = 2\frac{2e^2}{h}\sum_{n=1}^{N'}\int dE\big[D_n^2(f_1(1-f_1)+f_2(1-f_2))+ \\ D_n(1-D_n)(f_1(1-f_2)+f_2(1-f_1))\big] \tag{3.15}$$

where the transmission probability D_n and the Fermi distributions f_1 and f_2 are all energy E dependent. In this equation, the terms on the top line correspond to the thermal noise and disappear at zero temperature while the terms on the bottom line correspond to the shot noise contribution. The derivation of this equation also assumes that the measurement frequency ω and energy $\hbar\omega$ are much smaller than the other frequencies and energies in the problem.

Equation 3.15 is simplified by assuming that the applied voltage is significantly smaller than the Fermi energy. In this case, only electrons which have an energy close to the Fermi energy contribute to the net current, so the transmission probability is equal to the probability at the Fermi energy and is approximately constant. Using this assumption, the shot noise spectral density is

$$S_I = 2\frac{2e^2}{h}\sum_{n=1}^{N'}\left[2k_BT_{cryo}D_n^2 + D_n(1-D_n)eV\coth\left(\frac{eV}{2k_BT_{cryo}}\right)\right] \tag{3.16}$$

where T_{cryo} is the temperature of the junction. At low temperatures $T_{cryo}\to 0$

$$S_I = 2eV\frac{2e^2}{h}\sum_{n=1}^{N'}[D_n(1-D_n)] \tag{3.17}$$

The expected result for a Poisson process is recovered when there is only a small probability of electron tunneling $D_n \ll 1$

$$S_I = 2e\sum_{n=1}^{N'}D_n\frac{2e^2}{h}V = 2eI \tag{3.18}$$

The expected magnitude of the shot noise in this thesis is determined from equation 3.16. The shot noise is the fundamental source of noise in the measurement. The

measured shot noise is caused by electrons tunneling across a gold atomic point contact (APC). The APCs used to detect nanomechanical motion in this thesis are usually composed of a single spin-degenerate channel $N' = 1$ so $R_{APC} = h/(2e^2 D)$ and

$$S_I = 2\frac{2e^2}{h}\left[2k_B T_{cryo} D^2 + D(1-D)eV \coth\left(\frac{eV}{2k_B T_{cryo}}\right)\right] \tag{3.19}$$

In order to maximize the measured signal I usually apply a voltage $V \gg k_B T_{cryo}/e$ where $T_{cryo} \leq 10$ K. At these large voltages,

$$S_I = 2\frac{2e^2}{h} D(1-D)eV \tag{3.20}$$

Finally, when analyzing the noise in a circuit it is often more convenient to express the shot noise contribution as a voltage noise source in series with the junction. The voltage noise has a spectral density

$$S_V = S_I R_{APC}^2 = 2eV R_{APC}(1-D) \tag{3.21}$$

3.1.3 Tunneling probability

In a gold atomic point contact, the connection between two atoms can be thought of as a single, spin-degenerate conducting channel. A gap between the two atoms will scatter the incident electrons and, at the experimentally relevant voltages, electrons will either reflect off of the barrier created by the vacuum gap or tunnel through the gap. In this section I calculate the the transmission probability D as a function of the gap width x. As will be shown below, the transmission probability D is exponentially sensitive to the size of the gap with a length scale, in gold, of about 0.1 nm. Because this length scale is smaller than the atomic radius, the conductance of an atomic point contact is usually dominated by the least resistive channels: either a sum of ballistic channels where $D_n = 1$ or, if there are no ballistic channels, a single channel m with $D_m = D \gg D_n,\ n \neq m$. The atomic-scale roughness implies that the channel between the two atoms with the smallest separation will dominate the conductance.

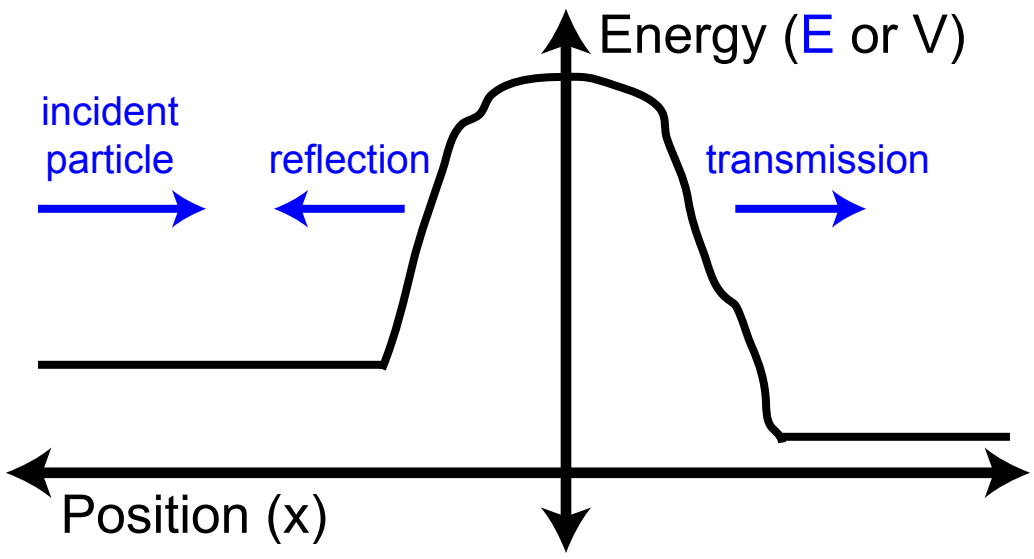

Figure 3.3: A particle (blue) incident from the left will scatter off of a potential barrier (black) and will either be reflected or tunnel through the barrier and be transmitted.

I calculate the transmission probability by modeling the vacuum gap as a one-dimensional barrier $V(x)$ and using the Wentzel-Kramers-Brillouin (WKB) method to calculate the approximate probability D that an incident particle (an electron) with energy E and mass m will tunnel through the barrier (figure 3.3). The WKB method is described in most quantum mechanics textbooks, for example references [156, 157].

The goal of the WKB method is to determine the particle's wave function $\psi(x)$ from the Schrodinger equation

$$\frac{\hbar^2}{2m}\frac{d^2\psi}{dx^2} + V(x)\psi = E\psi \tag{3.22}$$

The WKB method uses a trial wave function $\psi(x) = \exp[u(x)]$ and then finds a solution for $u(x)$. For an arbitrary barrier $V(x)$ there is not an analytic solution for $u(x)$. However, if $V(x) = V_0$ is constant for $-l < x < l$ then over that range $u(x)$ is constant and the wave function is

$$\psi(x) = A\exp[ikx] + B\exp[-ikx] \tag{3.23}$$

where $k = \sqrt{2m[E - V_0]/\hbar^2}$ if $E > V(x)$ or else

$$\psi(x) = C\exp[\kappa x] + D\exp[-\kappa x] \tag{3.24}$$

where $\kappa = \sqrt{2m[V_0 - E]/\hbar^2} = ik$ if $E < V(x)$.

The WKB method extends this solution to potential barriers $V(x)$ that change slowly, that is, where $|k'(x)| \ll |k^2(x)|$. Substituting $\psi(x) = \exp[u(x)]$ into the Schrodinger equation and

$$i\frac{d^2u}{dx^2} - \left(\frac{du}{dx}\right)^2 + k(x)^2 = 0 \tag{3.25}$$

where $k(x) = \sqrt{2m[E - V(x)]/\hbar^2}$. An approximate solution for $u(x)$ is obtained when d^2u/dx^2 is small, as is the case for a free particle, using an iterative approach. The initial approximation

$$u_0(x) = \pm\int^x k(x)dx + c \tag{3.26}$$

assumes that $d^2u/dx^2 = 0$. More accurate approximations are found iteratively by solving

$$\left(\frac{du_n}{dx}\right)^2 = i\frac{d^2u_{n-1}}{dx^2} + k(x)^2 \tag{3.27}$$

The approximate WKB wave functions $\psi(x) = \exp[u_1(x)]$ are found by solving the above equation for $n = 1$

$$\psi(x) \approx \frac{A}{\sqrt{k(x)}}\exp\left[+i\int^x k(x)dx\right] + \frac{B}{\sqrt{k(x)}}\exp\left[-i\int^x k(x)dx\right] \tag{3.28}$$

for $E > V(x)$ and

$$\psi(x) \approx \frac{C}{\sqrt{\kappa(x)}}\exp\left[+\int^x \kappa(x)dx\right] + \frac{D}{\sqrt{\kappa(x)}}\exp\left[-\int^x \kappa(x)dx\right] \tag{3.29}$$

for $E < V(x)$.

This approximation is only valid in the region where $|k'(x)| \ll |k^2(x)|$ which implies that these approximate WKB wave functions are inaccurate in the region where

E is close to $V(x)$. It is necessary to use a different approximations to connect the solutions for $E < V(x)$ to the solutions for $E > V(x)$, or, in terms of equations 3.28 and 3.29, express C and D in terms of A and B. One method, which is appropriate for the potential barriers considered in this thesis, is to use a linear approximation for the barrier near the point where $E = V(x)$. That is, if $E = V(a)$, then near $x = a$ the potential is approximated by $V(x) - E = gx - ga$. Using this approximation, the solutions to the Schrodinger equation are Airy functions $Ai\left[\cdots\right]$ and $Bi\left[\cdots\right]$

$$\psi(x) \approx aAi\left[\left(\frac{2mg}{\hbar^2}\right)(x-a)\right] + bBi\left[\left(\frac{2mg}{\hbar^2}\right)(x-a)\right] \tag{3.30}$$

The Airy functions provide the desired connection between the approximate WKB waveforms for $E > V(x)$ and $E < V(x)$. The asymptotic expressions for the Airy functions can be expressed in terms of the approximate WKB wave functions by appropriately choosing A and B for $E > V(x)$ (equation 3.28) and C and D for $E < V(x)$ (equation 3.29). Explicitly, for a turning point at $x = a$ where $E > V(x)$ when $x < a$ and $E < V(x)$ when $x > a$ (figure 3.4a)

$$\psi(x)|_{x \ll a} \approx \frac{A}{\sqrt{k(x)}} \exp\left[i\int^x k(x)dx\right] + \frac{B}{\sqrt{k(x)}} \exp\left[-i\int^x k(x)dx\right] \tag{3.31}$$

$$\psi(x)|_{x \gg a} \approx \frac{-iA+B}{2\sqrt{-i\kappa(x)}} \exp\left[-\int^x \kappa(x)dx\right] + \frac{A-iB}{\sqrt{-i\kappa(x)}} \exp\left[\int^x \kappa(x)dx\right] \tag{3.32}$$

and for a turning point at $x = b$ where $E < V(x)$ when $x < b$ and $E > V(x)$ when $x > b$ (figure 3.4b)

$$\psi(x)|_{x \ll b} \approx \frac{C}{\sqrt{\kappa(x)}} \exp\left[-\int^x \kappa(x)dx\right] + \frac{D}{\sqrt{\kappa(x)}} \exp\left[\int^x \kappa(x)dx\right] \tag{3.33}$$

$$\psi(x)|_{x \gg b} \approx \frac{C - \frac{iD}{2}}{\sqrt{-ik(x)}} \exp\left[i\int^x k(x)dx\right] + \frac{-iC + \frac{D}{2}}{\sqrt{-ik(x)}} \exp\left[-i\int^x k(x)dx\right] \tag{3.34}$$

I apply the WKB approximation to a simple high potential barrier $V(x)$ (figure 3.4c) where $V(x) < E$ for $x < a$ or $x > b$ and $V(x) > E$ for $a < x < b$. The solution to

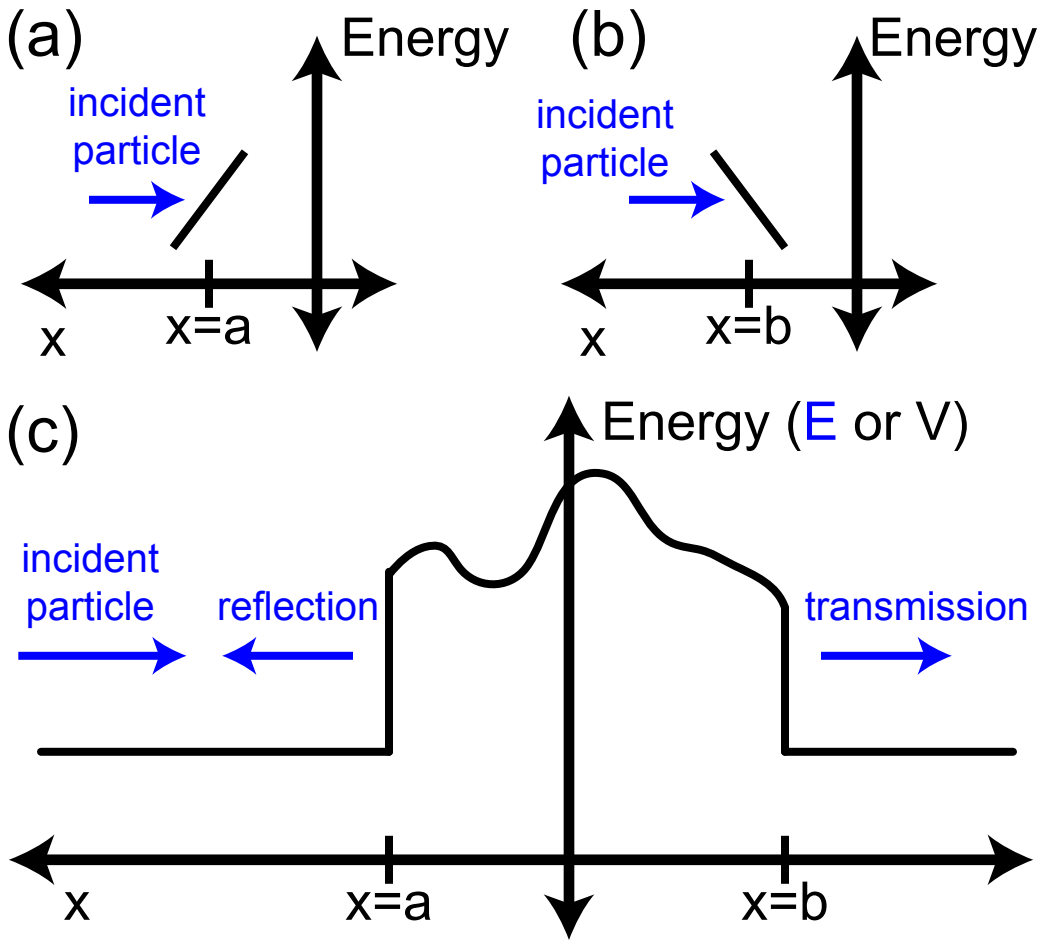

Figure 3.4: (a & b) Diagrams of the WKB turning points. (a) In the vicinity of $x = a$, the energy of the particle (blue) is greater than the potential of the barrier (black) when $x < a$. (b) In the vicinity of $x = b$, the energy of the particle (blue) is greater than the potential of the barrier (black) when $x > b$. (c) Particles (blue) with energy E are incident from the left on a potential $V(x)$ where $V(x) > E$ when $a < x < b$.

the Schrodinger equation with particles incident from the left (from $-\infty$) is

$$\psi(x)|_{x<a} = \frac{A}{\sqrt{k(x)}} \exp\left[+i\int_a^x k(x)dx\right] + \frac{B}{\sqrt{k(x)}} \exp\left[-i\int_a^x k(x)dx\right] \tag{3.35}$$

$$\psi(x)|_{a<x<b} = \frac{C}{\sqrt{\kappa(x)}} \exp\left[-\int_a^x \kappa(x)dx\right] + \frac{D}{\sqrt{\kappa(x)}} \exp\left[\int_a^x \kappa(x)dx\right] \tag{3.36}$$

$$\psi(x)|_{x>b} = \frac{F}{\sqrt{k(x)}} \exp\left[+i\int_b^x k(x)dx\right] \tag{3.37}$$

Using the connection formulas above, I solve for the transmission probability $D = |F/A|^2$

$$D = \exp\left[-2\int_a^b \kappa(x)dx\right]\left(1+\frac{1}{4}\exp\left[-2\int_a^b \kappa(x)dx\right]\right)^{-2} \tag{3.38}$$

A model for the barrier of caused by a vacuum gap of length $L = b - a$ in an atomic point contact (APC) is shown in figure 3.5. When there is no applied voltage, the barrier is rectangular and, at zero temperature, the electron states with energies less than the Fermi energy E_F will be filled on both sides of the barrier. The height of the barrier is equal to the Fermi energy plus the work function of the material $E_F + \phi$. Since there are no states which are filled on one side of the barrier and empty on the other side of the barrier, there will be no tunneling. When a bias voltage V_{APC} is applied to the contact on the left then the height of the barrier on the left will increase to $E_F + \phi + eV_{APC}$ and electron states with an energy up to $E_F + eV_{APC}$ will be filled.

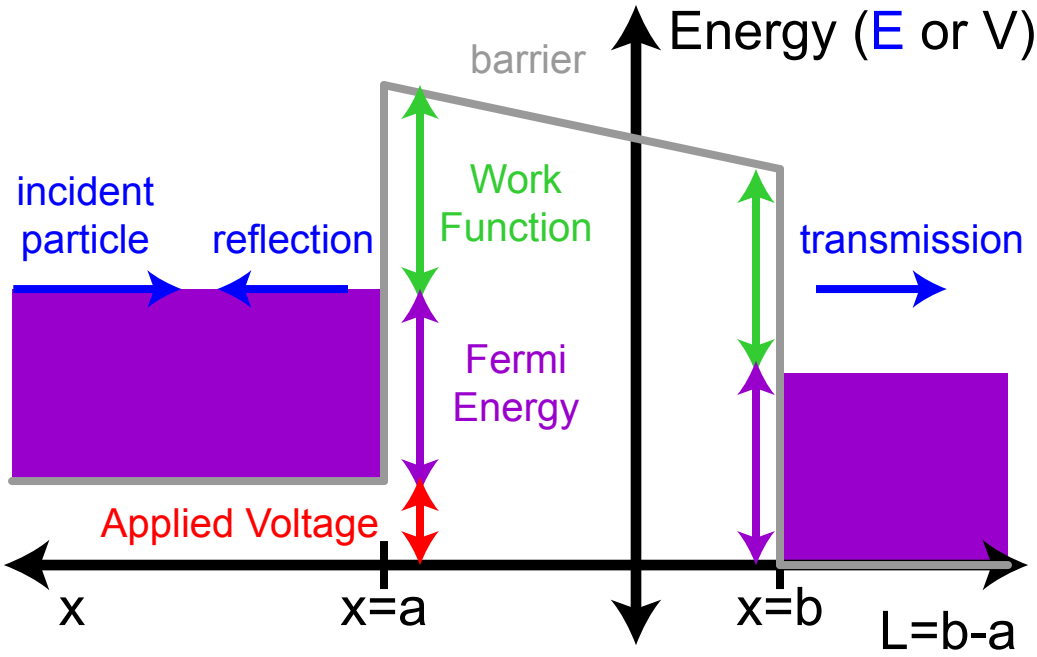

Figure 3.5: Electron tunneling across an APC. When the tunneling probability $D \ll 1$, the height of the potential barrier (grey) above the Fermi energy (purple) is approximately equal to the work function of the material (green). Incident electrons (blue) can tunnel across the potential barrier from filled states (purple) to empty states (white). An applied voltage (red) raises the potential on the left side of the barrier.

The barrier height decreases linearly to $E_F + \phi$ on the right side of the barrier, and the electron states on the right side will still only be filled up to the Fermi energy E_F. Electrons with an energy between E_F and $E_F + eV_{APC}$ can therefore tunnel from filled states on the left hand side of the barrier to empty states on the right hand side of the barrier.

The voltage dependence of the tunneling barrier and available electron energies implies that the APC resistance $R_{APC} = h/(2e^2\langle D\rangle)$ is also dependent on V_{APC}. In figure 3.6a I plot R_{APC} as a function of V_{APC} for APCs with various gap sizes L. I assume typical values for the work function $\phi = 5.1$ eV and Fermi energy $E_F = 5.5$ eV in gold. As seen in figure 3.6a, a voltage $|V_{APC}| > 1$ V is required to significantly modify the tunneling resistance.

Over the experimentally relevant voltages $|V_{APC}| < 50$ mV$\ll \phi/e \approx E_F/e$ the barrier can be modeled as a rectangular barrier with height $E_F + \phi$ and the electron energy is approximately equal to the Fermi energy E_F. Experimentally, the transmission probability is approximately

$$D = \exp\left[-2L/\lambda\right]\left(1 + \frac{1}{4}\exp\left[-2L/\lambda\right]\right)^{-2} \tag{3.39}$$

where $\lambda = \sqrt{\hbar^2/(2m\phi)} = 1/\kappa$ is the length scale that controls the probability of electron tunneling (figure 3.6a, black lines). In gold, $\lambda \approx 86$ pm. Experimentally, the resistance of the APC is approximately

$$R_{APC} = \frac{h}{2e^2}\exp\left[2L/\lambda\right]\left(1 + \frac{1}{4}\exp\left[-2L/\lambda\right]\right)^{2} \tag{3.40}$$

I plot the resistance R_{APC} of the APC versus L/λ in figure 3.6b. When $L/\lambda > 1$ the resistance of the APC is exponentially dependent on the width of the gap L

$$R_{APC} = \frac{h}{2e^2}\exp\left[2L/\lambda\right] \tag{3.41}$$

(figure 3.6b, black lines).

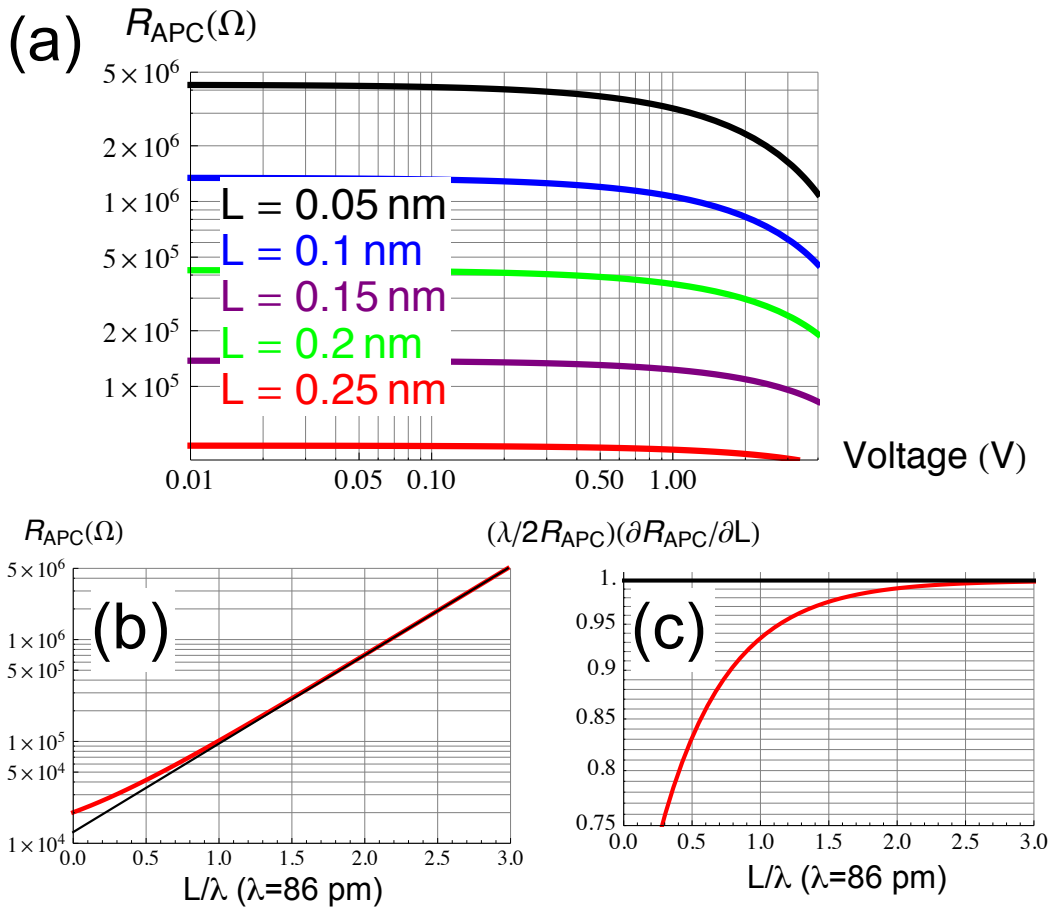

Figure 3.6: (a) APC resistance R_{APC} as a function of bias voltage V across the APC for various barrier widths L, assuming an ideal gold junction. At voltages $V > \phi/10 =$ 500 mV, the effect of the applied voltage on the barrier is noticeable; $\phi = 5.1$ eV is the work function of gold. (b) APC resistance R_{APC} as a function of the width of the junction L. The resistance is calculated assuming a bias voltage $V \ll \phi$ and using the WKB method (red) and assuming an exponential dependence (black). The WKB result deviates from an exponential dependence when the width is small $L < \lambda$. (c) The effective length scale $(1/2R_{APC})(\partial R_{APC}/\partial L)$ as a function of the width of the junction L. When $L > 0.8\lambda$, the difference between the effective length scale calculated using the WKB method (red) and calculated assuming an exponential dependence (black) is less than 10%.

The length scale λ also determines the sensitivity of the resistance R_{APC} to small changes δL in the the width of the gap. From equation 3.40, a small change in the width $L \to L + \delta L$ creates a change in resistance $R_{APC} \to R_{APC} + \delta R$

$$\delta R = \delta L \frac{\lambda}{2R_{APC}} \left(\frac{4 \exp\left[2L/\lambda\right] - 1}{4 \exp\left[2L/\lambda\right] + 1} \right) \tag{3.42}$$

The quantity $\lambda \left(4 \exp\left[2L/\lambda\right] - 1\right) / \left(4 \exp\left[2L/\lambda\right] + 1\right)$ is an effective length scale that controls the probability of electron tunneling. In figure 3.6c I plot this length scale (red line) as a function of L/λ. The difference between this length scale and λ (black line) is less than 10% when $L/\lambda > 0.8$. In this thesis I generally assume that

$$\delta R = \delta L \frac{\lambda}{2R_{APC}} \tag{3.43}$$

and that λ can depend weakly on the resistance of the APC as in figure 3.6c (red line). Deviations of the barrier potential from a rectangular barrier will also cause λ to change with resistance; these deviations are expected to have a larger effect when the size of the gap $L/\lambda < 1$.

3.2 APC as a Quantum-Limited Displacement Detector

The atomic point contact (APC) displacement detector uses the exponential dependence of the APC resistance R_{APC} on the width of the gap between atoms in the APC to sensitively detect nanomechanical motion. This detector has been theoretically predicted to be a quantum-limited detector [65–67, 69, 71, 72, 75, 77]. Near the quantum limit, the displacement imprecision is due to the shot noise of tunneling electrons and the detector backaction is caused by the momentum kicks due to tunneling electrons [58–62]. I use this phenomenological model of the APC backaction to compare the APC detector to a quantum-limited detector.

3.2.1 The standard quantum limit

The Heisenberg uncertainty relationship places a limit on the minimum imprecision-backaction product of a displacement detector. A quantum-limited displacement detector operates at this minimum. The uncertainty relationship in the simple case of a single strong measurement of the position of a particle is calculated in most quantum mechanics textbooks [156–158]. The measurement of position has an uncertainty $\Delta x^2 = \langle(\hat{x} - \langle\hat{x}\rangle)^2\rangle = \langle\hat{x}^2\rangle - \langle\hat{x}\rangle^2$. This measurement of position necessarily effects the state of the particle; this backaction effects the momentum of the particle with an uncertainty $\Delta p^2 = \langle(\hat{p} - \langle\hat{p}\rangle)^2\rangle = \langle\hat{p}^2\rangle - \langle\hat{p}\rangle^2$. For any two operators $\hat{A}$ and $\hat{B}$

$$\Delta A^2 \Delta B^2 \geq \left|\left\langle\left(\hat{A} - \langle\hat{A}\rangle\right)\left(\hat{B} - \langle\hat{B}\rangle\right)\right\rangle\right|^2 = \frac{1}{4}\left|\langle[A,B]\rangle\right|^2 + \frac{1}{4}\left|\langle\{A,B\}\rangle\right|^2 \tag{3.44}$$

Since $\hat{x}$ and $\hat{p}$ do not commute $[\hat{x},\hat{p}] = i\hbar$, the product of the uncertainty in the position measurement Δx and the uncertainty in the detector backaction Δp has a lower bound

$$\Delta x \Delta p \geq \frac{\hbar}{2} \tag{3.45}$$

The APC displacement measurements performed in this thesis are not strong, single-shot position measurements but instead are weak, continuous position measurements. A qualitative understanding of the Heisenberg constraint on a weak continuous measurement can be found by considering a sequence of weak measurements with imprecision Δx and backaction Δp [115]. A detector performs a sequence of N displacement measurements separated by a time τ. Each measurement has an imprecision Δx and backaction Δp. I assume that there is no correlation between Δx and Δp or between the measurements at different times. Averaging the sequence of measurements taken over a time $t = N\tau$, the average displacement uncertainty $\Delta x_{avg}(t) = \Delta x\sqrt{\tau/t}$ decreases and the average backaction $\Delta p_{avg}(t) = \Delta p\sqrt{t/\tau}$ increases as in a random walk.

This sequence of measurements becomes a weak continuous measurement in the limit that the time between measurements $\tau \to 0$ and each measurement's uncertainty

$\Delta x \to \infty$. Since each measurement in the sequence is uncorrelated, the imprecision spectral density $S_x = 2(\Delta x)^2\tau$ of the continuous measurement is frequency independent. The factor of two is present because I use single-sided spectral densities which are only defined for positive frequencies. So that the imprecision spectral density is independent of τ, the measurement uncertainty is increased as $\Delta x \propto 1/\sqrt{\tau}$. In this case the average displacement uncertainty $\Delta x_{avg}(t) = \sqrt{S_x/t} = \Delta x\sqrt{\tau/t}$ is also independent of the measurement spacing. Similarly, in the limit of a continuous measurement the detector's backaction $\Delta p \to 0$ and creates a white backaction force with a spectral density $S_F = 2(\Delta p)^2/\tau$. I set the backaction $\Delta \propto \sqrt{\tau}$ so that the spectral density and the average backaction $\Delta p_{avg}(t) = \sqrt{S_F t} = \Delta p\sqrt{t/\tau}$ are independent of the measurement spacing τ.

Using this description of a weak continuous measurement with uncorrelated backaction S_F and imprecision S_x I can find the Heisenberg constraint on the imprecision-backaction product. The imprecision-backaction product is

$$S_x S_F = \left[2(\Delta x)^2\tau\right]\left[\frac{2(\Delta p)^2}{\tau}\right] = (2\Delta x\Delta p)^2 \tag{3.46}$$

From the Heisenberg relationship on a single measurement above, $\Delta x\Delta p \geq \hbar/2$, the constraint on a weak continuous measurement is

$$S_x S_F \geq \hbar^2 \tag{3.47}$$

This formula applies when the imprecision S_x and backaction S_F are uncorrelated and the spectral densities are single-sided. Weak continuous measurements with correlations are considered in detail in references [29, 72, 75, 115].

The total imprecision in the measurement of the position of a harmonic oscillator, such as a mass on a spring, is limited by quantum mechanics. The spectral density of the total displacement noise S_{xtot} is composed of two types of noise. First, there are the apparent fluctuations in the position of the harmonic oscillator due to the measurement

noise S_x which I assume has a white spectral density (as above). Second, the backaction force S_F creates real fluctuations in the position of the harmonic oscillator S_{xBA}. A force F at frequency ω on a mass m with spring constant $m\omega_0^2$ and damping γ will result in displacement $x = H(\omega)F$ where $H(\omega)$ is the harmonic oscillator's response function (see section 3.3)

$$H(\omega) = \frac{1}{m\left[\omega_0^2 - \omega^2 + i\gamma\omega\right]} \tag{3.48}$$

The backaction force S_F creates random motion with a spectral density

$$S_{xBA} = |H(\omega)|^2 S_F = \frac{S_F}{m^2\left[(\omega_0^2 - \omega^2)^2 + \gamma^2\omega^2\right]} \tag{3.49}$$

These two sources of noise, one due to apparent motion and and one due to actual motion, result in a total displacement measurement noise with spectral density

$$S_{xtot} = S_x + S_{xBA} = S_x + \frac{S_F}{m^2\left[(\omega_0^2 - \omega^2)^2 + \gamma^2\omega^2\right]} \tag{3.50}$$

Using the Heisenberg constraint

$$S_{xtot} \geq S_x + \frac{\hbar^2}{S_x m^2\left[(\omega_0^2 - \omega^2)^2 + \gamma^2\omega^2\right]} \tag{3.51}$$

which has a minimum

$$S_{xtot} \geq \frac{2\hbar}{m\sqrt{(\omega_0^2 - \omega^2)^2 + \gamma^2\omega^2}} \tag{3.52}$$

when the contribution to the noise from the apparent motion and actual motion are equal

$$S_x = S_{xSQL} = \frac{\hbar}{m\sqrt{(\omega_0^2 - \omega^2)^2 + \gamma^2\omega^2}} \tag{3.53}$$

$$S_F = S_{FSQL} = \hbar m\sqrt{(\omega_0^2 - \omega^2)^2 + \gamma^2\omega^2} \tag{3.54}$$

This minimum is called the standard quantum limit (SQL). Experimental displacement

detectors are usually compared to the SQL on-resonance $\omega = \omega_0$ where

$$S_{xtot} \geq \frac{2\hbar}{m\gamma\omega_0} \tag{3.55}$$

$$S_{xSQL} = \frac{\hbar}{m\gamma\omega_0} \tag{3.56}$$

$$S_{FSQL} = \hbar m\gamma\omega_0 \tag{3.57}$$

The quantum limits discussed above apply to a continuous, linear position measurement. It is possible to evade these limits by, for example, only measuring a single quadrature of a harmonic oscillator by modulating the strength of the measurement at the harmonic oscillator resonance frequency. This type of measurement is called a back-action evading measurement and is discussed in more detail in references [29, 115]. The displacement measurements in this thesis are continuous, linear position measurements.

3.2.2 APC displacement detection

The physics of an atomic point contact (APC) can be used to create a sensitive detector of the motion of a nanomechanical system. I use the same approach as was proposed in reference [62] and measure the change in APC resistance caused by nanomechanical motion. Conceptually, the APC resistance change is measured by placing the APC in series with a dc voltage source and a high impedance voltage amplifier (figure 3.7). Changes in APC resistance create a voltage signal at the amplifier. In this subsection I assume that the amplifier noise is negligible compared to the shot noise. Experimentally (chapter 6 and 7) this is usually true at large bias voltages $V_{APC} > 10$ mV; the amplifier noise and actual measurement circuit is discussed in detail in chapter 5.

A change in APC resistance will change the voltage measured by the amplifier. From the circuit in figure 3.7, the voltage measured by the amplifier is

$$V_{amp} = V_b \frac{R_{amp}}{R_{amp} + R_{APC}} \tag{3.58}$$

Small changes in the APC resistance $R_{APC} \rightarrow R_{APC} + \delta R(t)$ creates a small change in

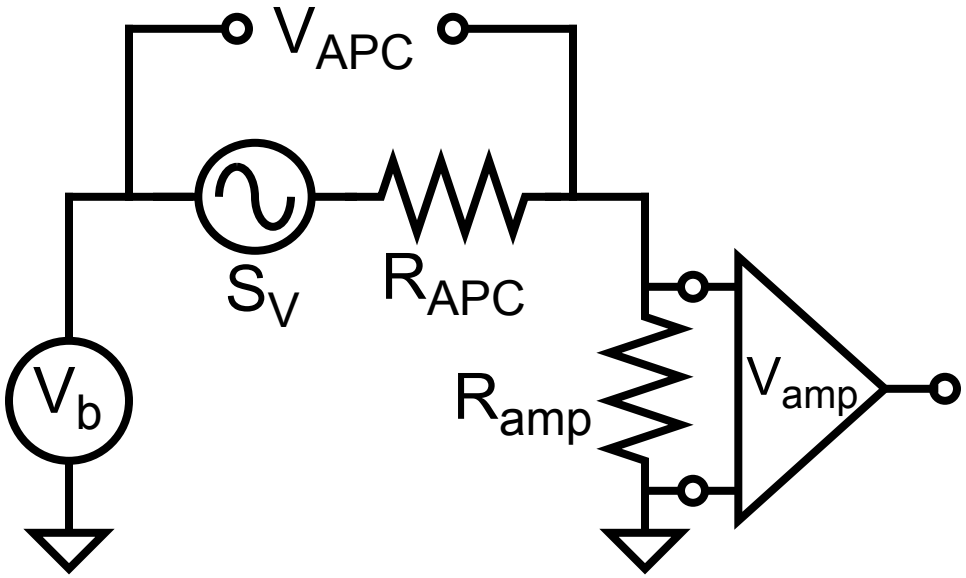

Figure 3.7: Circuit diagram used in a basic APC displacement measurement. An applied voltage V_b creates a voltage V_{APC} across the APC resistance R_{APC} and shot noise in the tunneling current creates a voltage noise source $S_V = 2eR_{APC}V_{APC}$. The APC is in series with a voltage amplifier with input impedance R_{amp}. The applied voltage V_b creates a voltage V_{amp} at the input of the amplifier. Changes in the APC resistance also changes the measured voltage V_{amp} creating a signal δV. The voltage fluctuations S_V limit the precision of the measurement.

the voltage at the amplifier $V_{amp} \rightarrow V_{amp} + \delta V(t)$

$$\delta V(t) = -\delta R(t) \frac{V_b R_{amp}}{(R_{amp} + R_{APC})^2} \tag{3.59}$$

As discussed earlier, changes in the width of the APC tunneling barrier $\delta x(t)$ will change the APC resistance (equation 3.43) $\delta R = \delta x(t)\lambda/2R_{APC}$ where λ is the length scale that controls the probability of electron tunneling. The APC is fabricated as part of a nanomechanical structure. Resonant motion of the structure can be modeled as a mass on a spring system (see section 3.3) with mass m_{eff}, resonance frequency ω_0, and displacement $y(t)$. Nanomechanical displacement will change the width of the gap

$$\delta x(t) = \chi y(t) \tag{3.60}$$

and create a voltage signal

$$\delta V(t) = -y(t)\frac{\chi}{\lambda}\frac{2V_b R_{APC} R_{amp}}{(R_{amp}+R_{APC})^2} \tag{3.61}$$

The shot noise of tunneling electrons will create voltage noise at the amplifier. The shot noise is modeled by a voltage noise source in series with the APC (figure 3.7) with spectral density (from equation 3.21) when the tunneling probability is small $R_{APC} \gg h/2e^2$

$$S_V = 2eR_{APC}|V_{APC}| \tag{3.62}$$

where V_{APC} is the voltage across the APC. This voltage noise creates uncertainty in the displacement measurement. The displacement imprecision spectral density is

$$S_x = S_V \left|\frac{y}{\delta V}\right|^2 = \frac{e}{2|V_{APC}|}\left|\frac{\lambda}{\chi}\right|^2 \frac{R_{APC}(R_{amp}+R_{APC})^2}{R_{amp}^2} \tag{3.63}$$

The minimum imprecision occurs when $R_{amp} \gg R_{APC}$. I also assume a simple mass-on-a-spring structure where $\chi = 1$, so the APC displacement detector can be used to measure impression with a sensitivity

$$S_x = \frac{e|\lambda|^2}{2}\frac{R_{APC}}{|V_{APC}|} \tag{3.64}$$

Using a gold atomic point contact ($\lambda \approx 86$ pm) and an experimentally realizable current $V_{APC}/R_{APC} = 0.1$ μA, it should be possible to achieve a displacement imprecision $\sqrt{S_x} \approx 80$ am/$\sqrt{\text{Hz}}$.

3.2.3 APC backaction and the quantum limit

I follow Bocko, Stephenson, and Koch [58–62] and approximate the APC detector backaction by estimating the momentum kick delivered by each tunneling electron. The experimentally applied APC voltages $V_{APC} \leq 50$ mV are much smaller than both the Fermi energy in gold $E_F = 5.5$ eV and the height of the barrier $\phi = 5.1$ eV above the Fermi energy. Therefore the tunneling electrons have an energy approximately equal

to the Fermi energy and are expected to apply an average momentum kick p_e to the nanostructure equal to the Fermi momentum $p_F \approx 10^{-24}$ N·sec. The shot noise in the tunneling current creates a random backaction force with a spectral density

$$S_{Fcorr} = 2\frac{p_e^2}{e}\frac{|V_{APC}|}{R_{APC}} \tag{3.65}$$

This backaction force is correlated with the shot noise. Technically, the force due to the average momentum of each tunneling electron p_e can be canceled. The shot noise can be detected electronically, and an external force can be applied to the nanostructure with equal magnitude but in the opposite direction.

The uncertainty Δp_e in the magnitude of the momentum of each tunneling electron also creates a random backaction force. This backaction force is not correlated with the shot noise of tunneling electrons and enforces the quantum limits described earlier. Each tunneling electron imparts a random momentum kick Δp_e which creates a random force with spectral density

$$S_{F\Delta} = 2\frac{(\Delta p_e)^2}{e}\frac{|V_{APC}|}{R_{APC}} \tag{3.66}$$

Following Bocko [62], I use the Heisenberg uncertainty principle to estimate the uncertainty Δp_e in the electron momentum. During electron tunneling, the position of the electron is localized with an uncertainty Δx_e that is about equal to the length scale $\lambda/2$ (equation 3.41) that controls the probability of electron tunneling. This effective measurement of the electron's position results in an uncertainty in the electron's momentum

$$\Delta p_e \approx \frac{\hbar}{2\Delta x_e} \approx \frac{\hbar}{\lambda} \tag{3.67}$$

Using this estimate of Δp_e, there is a backaction force

$$S_{F\Delta} = 2\frac{\hbar^2}{e\lambda^2}\frac{V_{APC}}{R_{APC}} \tag{3.68}$$

which is not correlated with the shot noise or the imprecision S_x.

I calculate the imprecision-backaction product from the imprecision S_x (equation 3.64) and the uncorrelated backaction force $S_{F\Delta}$ (equation 3.68). Based on these estimations, the APC displacement detector can achieve the Heisenberg limit

$$S_x S_{F\Delta} \approx \hbar^2 \tag{3.69}$$

More detailed and accurate calculations of the backaction and imprecision also indicate that the APC displacement detector can be quantum-limited [64–77].

In the experiments described in this thesis I do not attempt to cancel the correlated backaction force S_{Fcorr}, so the total backaction has a spectral density

$$S_{Fba} = S_{Fcorr} + S_{F\Delta} = \frac{2}{e}\left(p_e^2 + \frac{\hbar^2}{\lambda^2}\right)\frac{V_{APC}}{R_{APC}} \tag{3.70}$$

In gold the work function and Fermi energy are approximately equal, so $p_e \approx \hbar/\lambda$. Ignoring correlations, the best imprecision-backaction product is expected to be

$$S_x S_{F\Delta} = 2\hbar^2 \tag{3.71}$$

There are also other ways in which measuring displacement with the APC detector can create a backaction force. The fluctuating voltage across the APC, due to shot noise, will create a backaction force

$$S_{FC} = 2eV_{APC}R_{APC}\left(\frac{\partial C}{\partial x}V_{APC}\right)^2 \tag{3.72}$$

because the capacitance C of the APC depends on the size of the APC gap x. The fluctuating voltage can also launch surface acoustic waves onto the surface of the substrate, shaking the nanostructure's supports and creating a backaction

$$S_{FV} = 2eV_{APC}R_{APC}\sigma^2 \tag{3.73}$$

where the proportionality constant σ depends on the substrate material and the coupling between the nanomechanical motion and the motion of the supports. The presence of trapped charge near the nanostructure will also create a backaction force with the same

spectral density (equation 3.73), but in this case σ will depend on the number, location, and sign of the trapped charges. Finally, passing a current I_{APC} through the APC will result in power $I_{APC}^2 R_{APC}$ being dissipated in the contacts. If this dissipated power heats the nanostructure by a temperature ΔT then the measurement creates an additional backaction force

$$S_{FT} = 4 m_{eff} \gamma k_B \Delta T \tag{3.74}$$

where γ is the nanomechanical damping and m_{eff} is the effective mass. The presence of any additional backaction force will keep the APC displacement detector from operating with a Heisenberg limited imprecision-backaction product.

3.3 Simple Harmonic Motion of the Nanostructure and APC

The atomic point contact (APC) is fabricated as part of a nanostructure. Mechanical motion of the nanostructure can be described by adding together a set of normal modes; each mode can be modeled as a simple harmonic oscillator. I calculate the mode shapes and frequencies of a long beam with a small cross-section. Each mode shape is a vector $\vec{U}(x, y, z)$ which describes the normalized displacement, in three dimensions, at every point in the structure. The physical displacement of the nanostructure is equal to the $\vec{U}(x, y, z)$ times a magnitude $u(t)$. The magnitude $u(t)$ is the coordinate of a simple harmonic oscillator with frequency ω_0, an effective mass m_{eff}, and damping constant γ; these three quantities can be different for each mode. I normalize the mode shapes so that the effective mass is equal to the mass of the nanostructure.

The nanostructures used in this thesis would be, in the absence of the APC, either doubly or singly clamped beams. However, the addition of an APC adds a more complicated element. I estimate the effect of the APC on the structure's vibrational modes using a finite element model (FEM).

I calibrate the measured voltage signal in units of displacement using the known

spectral density S_x of the nanostructure's Brownian motion. Determining the measurement sensitivity to displacement at the APC requires knowing the mode shape; the mode shape is difficult to determine because of the presence of the APC. However, the comparison between the APC detector's characteristics and the standard quantum limit is independent of the mode shape.

3.3.1 The modes of a nanomechanical beam

In general, the displacement of a mechanical system can be described by defining a vector $\vec{U}(x, y, z)$ which gives the displacement of a small volume dV of a mechanical system from it's equilibrium position at (x, y, z). The elastic nature of the mechanical structure implies that each displaced volume dV will feel a restoring force. The normal mode shapes and frequencies are the solutions to the equations (and boundary conditions) which describe the relationship between displacement and force. The solutions cannot be found analytically for most cases, but there are analytic solutions for small displacements of simple geometries.

One of these simple cases (covered in numerous text books such as [14, 159, 160]) is that of a thin rectangular beam, that is, a beam whose width and height are much smaller than it's length. Any mechanical system's motion $\vec{X}(x, y, z, t)$ can be described by a sum of normal modes weighted by a time-dependent coordinate $u_n(t)$

$$\vec{X}(x, y, z, t) = \sum_{n=1}^{N} u_n(t)\vec{U}(x, y, z) \tag{3.75}$$

where $N \to \infty$ for a continuous system with an infinite number of degrees of freedom. In the simple case of a beam, the modes split into flexural modes (motion perpendicular to the beam's long direction), rotational modes (rotational motion around the axis defined by the beam's long direction), and compressional modes (motion parallel to the beam's length). The flexural modes are much easier to excite, therefore it is possible to describe the experimentally observed displacement by ignoring the rotational and compressional

modes.

This simplifies the analysis, since small volumes of the beam are only going to be displaced in a direction perpendicular to the beam's length (figure 3.8a). Therefore, I can define a small volume by slicing the beam into small sections with length dx so that each element has a volume $dV = Adx$, where $A = wh$ is the area of the beam, w is the width in the $\hat{y}$ direction, and h is the height in the $\hat{z}$ direction. Each of these elements can be described by it's position along the length of the beam and the displacement of

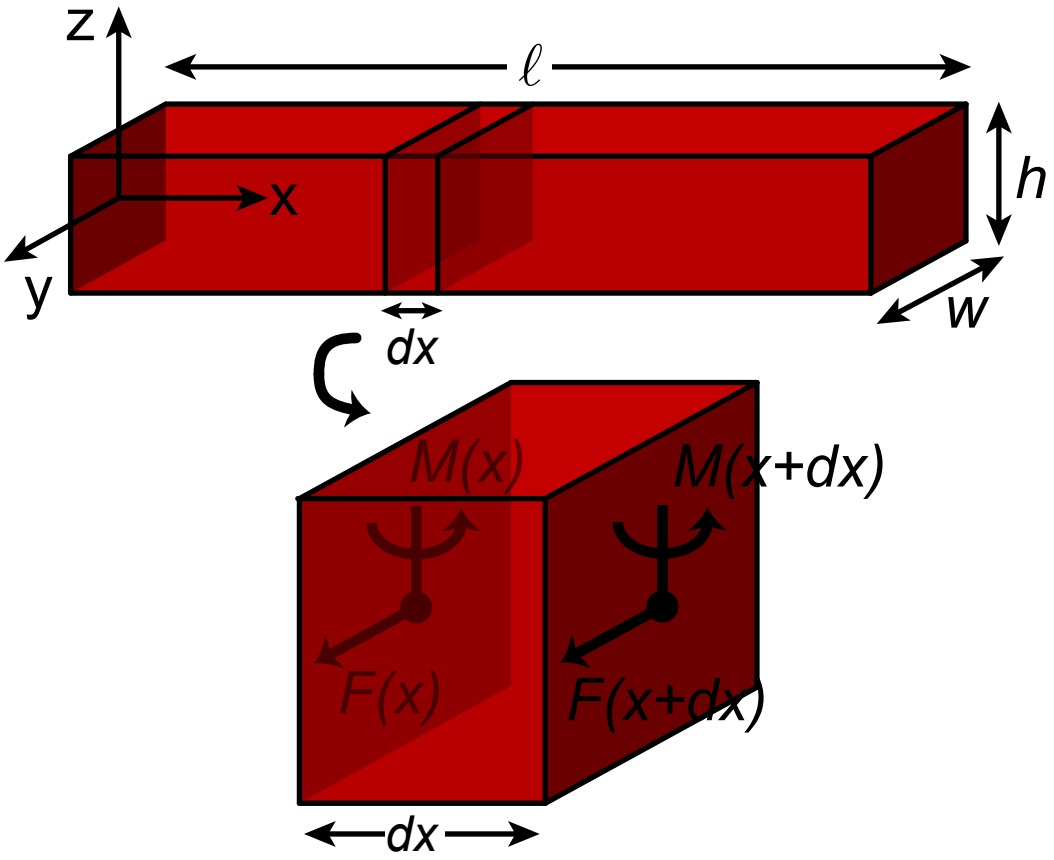

Figure 3.8: (a) Diagram of a thin, narrow nanomechanical beam with length l, height h, and width w where $w, h \ll l$. (b) I calculate the mode shapes in the $\hat{y}$ direction by summing the forces on a small volume element $hwdx$ due to the neighboring elements. For small displacements, rotational inertia and shear forces can be ignored and the relevant forces are the elastic force $F(x)$ in the $\hat{y}$ direction and the torque $M(x)$ around the $\hat{z}$ axis.

each element is $\vec{X}(x,y,z,t) = \vec{X}(z,t)$.

Using rectangular coordinates, the flexural normal modes can be further divided into modes which have displacement in the $\hat{y}$ direction and modes which have displacement in the $\hat{z}$ direction. I am going to analyze motion in the $\hat{y}$ direction (an identical analysis can be applied to motion in the $\hat{z}$ direction). Therefore, the displacement of each element in this analysis is $\vec{X}(x,y,z,t) = \hat{y}X(z,t)$.

I can now balance the forces (all applied along the $\hat{y}$ direction) and torques (all applied around the $\hat{z}$ axis, that is, NOT rotation around the long axis of the beam) on a single element (figure 3.8). The neighboring element on the left will exert a force $-F(x)$ and the neighboring element on the right will exert a force $F(x+dx)$; the resulting acceleration of the element under consideration is

$$-F(x) + F(x+dx) = \rho A dx \frac{\partial^2 X(z,t)}{\partial t^2} \tag{3.76}$$

$$\frac{\partial F}{\partial x} = \rho A \frac{\partial^2 X}{\partial t^2} \tag{3.77}$$

Similarly, I sum the torques exerted on the left side of the element (at position x). the neighboring elements will directly exert a torque $-M(x)$ and $M(x+dx)$. The force $F(x+dx)$ on the right side of the element (at position $x+dx$) also exerts a torque $F(x+dx)dx$. In the case of flexural vibrations there should be no net torque and so these torques must balance:

$$-M(x) + M(x+dx) + F(x+dx)dx = 0 \tag{3.78}$$

$$F = -\frac{\partial M}{\partial x} \tag{3.79}$$

I assume that the beam is made out of a single material with a constant Young's modulus Y and has a moment of inertia about the $\hat{y}$ axis I, therefore

$$M = EI\frac{\partial^2 X}{\partial x^2} \tag{3.80}$$

and so the partial differential equation relating the beam's displacement to the beam's

acceleration is

$$-\frac{\partial^2}{\partial x^2}\left(EI\frac{\partial^2 X}{\partial x^2}\right) = \rho A\frac{\partial^2 X}{\partial t^2} \tag{3.81}$$

$$-EI\frac{\partial^4 X}{\partial x^4} = \rho A\frac{\partial^2 X}{\partial t^2} \tag{3.82}$$

This partial differential equation is similar to that of a mass on a spring, but has a fourth order partial derivative with respect to displacement instead of a second order. The solutions to this equation have the form

$$\begin{aligned} X(x,t) = &[A\cos(\omega_n t) + B\sin(\omega_n t)] \\ &[a_n\cos(k_n x) + b_n\sin(k_n x) + c_n\cosh(k_n x) + d_n\sinh(k_n x)] \end{aligned} \tag{3.83}$$

This solution is usually split into a normalized mode shape

$$U_n(x) = a_n\cos(k_n x) + b_n\sin(k_n x) + c_n\cosh(k_n x) + d_n\sinh(k_n x) \tag{3.84}$$

and a coordinate

$$u_n(t) = A\cos(\omega_n t) + B\sin(\omega_n t) \tag{3.85}$$

whose overall magnitude depends on the normalization of the mode shape. Using this solution in the partial differential equation above, the eigenfrequency ω_n is related to the wave vector k_n

$$\omega_n = \pm\sqrt{\frac{EI}{\rho A}}k_n^2 \tag{3.86}$$

I now have a general solution to the mode shape, but the boundary conditions and normalization must also be specified in order to determine the constants above (a_n, b_n, c_n, d_n, and k_n). I am going to look at two different sets of boundary conditions: a doubly clamped beam and a singly clamped beam. In this section I normalize the magnitude of the mode shapes so that the average of the mode shape squared is equal to one (see section 3.3.2).

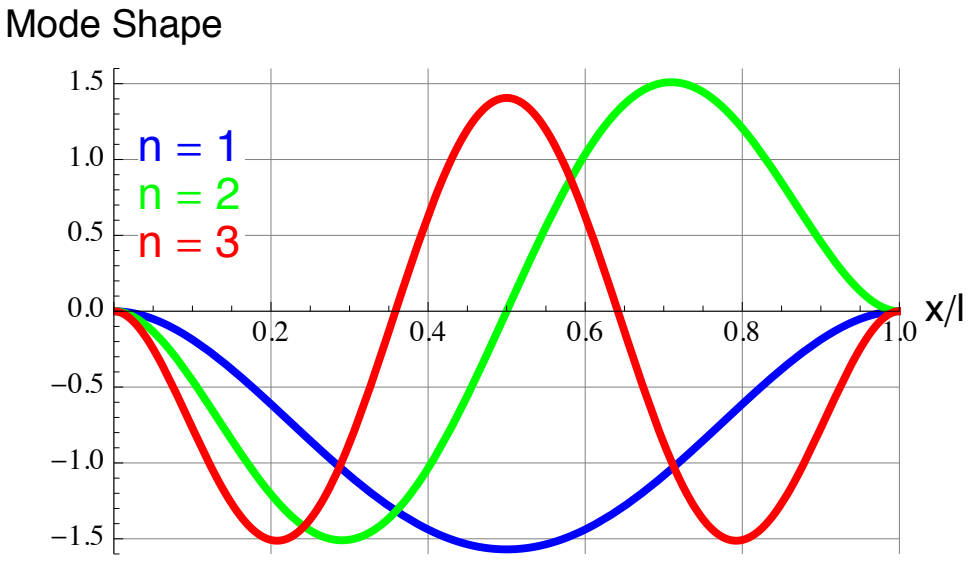

Figure 3.9: The mode shapes $U(x)$ of the fundamental ($n = 1$), second, and third mode of a doubly-clamped nanomechanical beam are plotted as a function of the position x along the beam. Since the beam is clamped at both ends, both the displacement and slope of the beam is zero at both ends.

A doubly clamped beam is constrained so that both ends of the beam do not move and are not sloped (that is, $U(0,t) = U(l,t) = 0$ and $\partial U(x,t)/\partial x|_{x=\{0,l\}} = 0$). Therefore $a_n = -c_n$, $b_n = -d_n$,

$$b_n = -\frac{\cos(k_n l) - \cosh(k_n l)}{\sin(k_n l) - \sinh(k_n l)} a_n \tag{3.87}$$

and

$$\cosh(k_n l)\cos(k_n l) = 1 \tag{3.88}$$

This transcendental equation does not have an analytic solution, but it can be solved numerically and the first few solutions are $k_n l = \{0, 4.73004, 7.8532, 10.9956, 14.1372, \ldots\}$. Therefore, the resonance frequencies of the first few $\hat{y}$ flexural modes of a doubly clamped narrow, thin beam are

$$\omega = \sqrt{\frac{EI}{\rho A l^4}}\{22.3733, 61.6728, 120.903, 199.859, \ldots\} \tag{3.89}$$

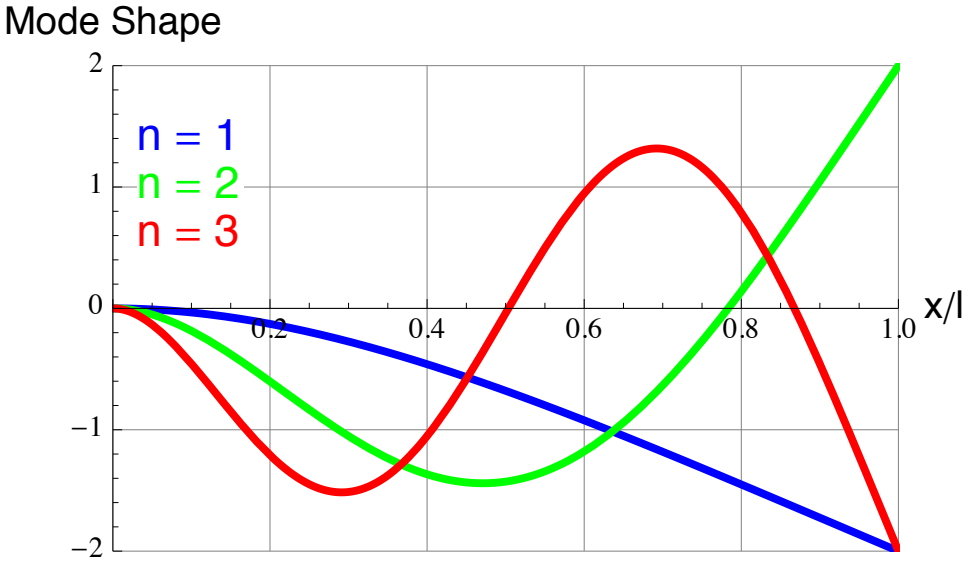

Figure 3.10: The mode shapes $U(x)$ of the fundamental ($n = 1$), second, and third mode of a single-clamped nanomechanical beam are plotted as a function of the position x along the beam. The displacement and slope of the beam is zero at $x = 0$ because the beam is clamped, but the beam's displacement and slope at $x = l$ is unconstrained.

and the mode shapes are given in figure 3.9.

The solution for a singly clamped beam proceeds along a similar path, but only one end is clamped ($U(0,t) = 0$ and $\partial U(x,t)/\partial x|_{x=0} = 0$). The other end is free so $U(l,t)$ and $\partial U(x,t)/\partial x|_{x=l}$ are unconstrained. However, there is also no force or torque on the free end so $\partial^2 U(x,t)/\partial x^2|_{x=l} = 0$ and $\partial^3 U(x,t)/\partial x^3|_{x=l} = 0$. Therefore $a_n = -c_n$, $b_n = -d_n$,

$$b_n = \frac{\cos(k_n l) + \cosh(k_n l)}{\sin(k_n l) + \sinh(k_n l)} a_n \tag{3.90}$$

$$\cosh(k_n l)\cos(k_n l) = -1 \tag{3.91}$$

This transcendental equation must also be solved numerically, and the first few solutions are $k_n l = \{1.8751, 4.69409, 7.85476, 10.9955, 14.1372, \ldots\}$. Therefore, the resonance frequencies of the first few $\hat{y}$ flexural modes of a singly clamped narrow, thin beam are

$$\omega = \sqrt{\frac{EI}{\rho A l^4}}\{3.51602, 22.0345, 61.6972, 120.902, 199.86, \ldots\} \tag{3.92}$$

and the mode shapes are given in figure 3.10.

3.3.2 Mechanical modes modeled as harmonic oscillators

Detectors of nanomechanical displacement such as the APC detector are usually used to measure resonant mechanical motion. The simplest type of mechanical resonance is a single-degree-of-freedom system such as a mass on a spring in one dimension. The use of the word "single" to describe the system can be confusing because there are actually two degrees of freedom: the position and the velocity. Using the example of a mass on a spring, the spring provides a restoring force $F = -kx$ proportional to the displacement x of the mass m. In the absence of any driving force, the free undamped motion $x(t)$ is found by solving the differential equation derived from Newton's laws, $m\ddot{x} = -kx$. The solution has the form $x(t) = ae^{i\omega_0 t} + be^{-i\omega_0 t}$. The displacement occurs at the system's natural resonance frequency $\omega_0 = \sqrt{k/m}$ and with a magnitude that depends on the initial position $x(0)$ and velocity $\dot{x}(0)$

$$x(t) = \frac{x(0)}{2}\left[e^{i\omega_0 t} + e^{-i\omega_0 t}\right] + \frac{\dot{x}(0)}{2i}\left[e^{i\omega_0 t} - e^{-i\omega_0 t}\right] \tag{3.93}$$

I can include a generic viscous damping force $-\gamma\dot{x}$ and calculate the damped displacement $x(t)$ in response to a force $F(t) = F_0 e^{i\omega t}$. The displacement is also found by solving a similar differential equation derived from Newton's laws, $m\ddot{x} = -kx - \gamma\dot{x} + F(t)$. The solution has the form $x(t) = H(\omega)F_0 e^{i\omega t}$ where $H(\omega)$ is the mechanical response function

$$H(\omega) = \frac{1}{m\left[\omega_0^2 - \omega^2 + i\gamma\omega\right]} \tag{3.94}$$

The largest response occurs when the force is applied at the mechanical resonance frequency $\omega = \omega_0$.

As was described earlier for the simple case of the flexural vibrations of a beam, the displacement $\vec{X}(x, y, z, t)$ of a volume dV of the mechanical structure located at

the point (x, y, z) can be decomposed into a sum of orthogonal modes $\vec{U}_n(x, y, z)$ each weighted by a time-dependent coordinate $u_n(t)$

$$\vec{X}(x, y, z, t) = \sum_{n=1}^{N} u_n(t)\vec{U}_n(x, y, z) \tag{3.95}$$

where N is the number mechanical degrees of freedom and $N \to \infty$ for a continuous mechanical structure. I describe the normalization of each mode shape using a coefficient α_n

$$\int \vec{U}_m \cdot \vec{U}_n dV = \delta_{mn}\alpha_n V \tag{3.96}$$

where the integral is over the mechanical structure and $V = \int dV$ is the volume of the mechanical structure. The units and magnitude of α_n determine the units and magnitude of the mode shapes $\vec{U}_n(x, y, z)$. Two common choices of normalization are $\alpha_n = 1$ and $\alpha_n = L^2$ where L is the significant length scale of the mechanical structure. In the first case $\alpha_n = 1$, the coordinate $u_n(t)$ is equal to the root-mean-squared displacement of the mechanical structure along the normal mode and the mode shapes are unit-less. I will use this normalization $\alpha_n = 1$ in the rest of this thesis. In the second case $\alpha_n = L^2$, the mode shapes have units of displacement and the coordinate $u_n(t)$ is unit-less.

The response of the coordinate $u_n(t)$ to an applied force per unit volume $\vec{F}(x, y, z)e^{i\omega t}$ is effectively that of a harmonic oscillator. When the displacement is small compared to the dimensions of the mechanical structure, the differential equation that is used to calculate the response $\vec{X}(x, y, z, t) = \sum_{n=1}^{N} u_n(t)\vec{U}_n(x, y, z)$ to the applied force usually simplifies to

$$-\rho\omega^2 \left(\sum_n u_n(t)\vec{U}_n \right) + \rho \left(\sum_n \omega_{0_n}^2 u_n(t)\vec{U}_n \right) = \vec{F}e^{i\omega t} \tag{3.97}$$

$$\sum_n \rho(\omega_{0_n}^2 - \omega^2)u_n(t)\vec{U}_n = \vec{F}e^{i\omega t} \tag{3.98}$$

Since the modes $\vec{U}_n$ are orthogonal, this response can be separated into N independent equations, each equation describing the response of the time-dependent coordinate $u_n(t)$,

$$\sum_n \rho(\omega_{0_n}^2 - \omega^2)u_n(t) \int \vec{U}_m \cdot \vec{U}_n dV = e^{i\omega t} \int \vec{U}_m \cdot \vec{F} dV \tag{3.99}$$

Including a mode-dependent damping γ_n and assuming that $\gamma_n \ll \omega_{0_n}$, the response of the coordinate $u_n(t)$ is approximately

$$m(\omega_{0_n}^2 - \omega^2 + i\gamma_n\omega)u_n(t) = e^{i\omega t} f_n \tag{3.100}$$

where m is the mass of the mechanical structure (I assume the density ρ is constant) and $f_n = \int \vec{U}_n \cdot \vec{F} dV$ is the mean force driving mode n. This is equivalent to a SHO with frequency ω_{0_n}, mass m_{eff_n}, displacement $u_{eff_n}(t)$, and an applied force f_{eff_n}

$$m_{eff_n}(\omega_{0_n}^2 - \omega^2 + i\gamma_n\omega)u_{eff_n}(t) = e^{i\omega t} f_{eff_n} \tag{3.101}$$

Because only the displacement $u_{eff_n}(t)$ and the coordinate $u_n(t)$ are time-dependent, they are related by a constant $\chi_n u_{eff_n}(t) = u_n(t)$. The values of the effective mass, force, and proportionality constant χ_n are related to the total mass m and mean force f_n by

$$\frac{m_{eff_n}}{m\chi_n} = \frac{f_{eff_n}}{f_n} \tag{3.102}$$

In this thesis and in many other experiments, the measured mechanical motion is dominated by a single mode n and the motion is described by a single effective SHO. Mechanical motion is measured at frequencies ω near the eigenfrequency ω_{0_n} of the mode n. The difference between this eigenfrequency and all other eigenfrequencies is usually large compared to both the measurement bandwidth and the width of the mechanical resonance γ, so $|\omega_{0_k}^2 - \omega^2| \gg \omega\gamma_n$ for all modes $k \neq n$. The measured displacement is also generally due to a force that effectively drives the mode n of interest; that is, the force per unit volume $\vec{F}(x, y, z)e^{i\omega t}$ generates effective forces $f_k = \int \vec{U}_k \cdot \vec{F} dV$ and the force f_n on the mode n of interest is not significantly smaller than the force f_k on other modes. With these restrictions, the contribution of the modes $k \neq n$ to the total motion $\vec{X}(x, y, z, t)$ is going to be attenuated by a large factor $|\omega_{0_k}^2 - \omega^2|$ compared to the contribution from mode n. The total motion (from equations 3.95 and 3.100) is

approximately

$$\vec{X}(x,y,z,t) \approx \frac{f_n}{m\left[\omega_{0_n}^2 - \omega^2 + i\gamma_n\omega\right]}\vec{U}(x,y,z)e^{i\omega t} \tag{3.103}$$

I place additional constraints on the parameters of the effective SHO (equation 3.101) by requiring that the temperature of the effective SHO and the mechanical structure is the same. The effective SHO has two degrees of freedom, position and velocity, so the average total energy of the SHO in thermal equilibrium at temperature T is $\langle E_{eff}\rangle = k_B T$, as described by the equipartition theorem. Thermalization occurs because of a random force on the SHO with a one-sided spectral density S_{Feff}^T. I calculate the magnitude of this force spectral density from the average kinetic energy

$$\frac{1}{2}k_B T = \frac{1}{2}m_{eff}\omega_0^2\langle u_{eff}^2\rangle \tag{3.104}$$

which is in response to S_{Feff}^T

$$\frac{k_B T}{2} = \frac{1}{2}m_{eff}\omega_0^2\int_0^\infty S_{Feff}^T|H(\omega)|^2\frac{d\omega}{2\pi} \tag{3.105}$$

$$S_{Feff}^T \approx 4m_{eff}\gamma k_B T \tag{3.106}$$

where $H(\omega)$ is the SHO response function (equation 3.94) and I assume that $\gamma \ll \omega_0$ and $\hbar\omega_0 \ll k_B T$.

Similarly, the thermalization of a continuous mechanical structure at temperature T occurs because of a random force per unit volume $\vec{F}^T(x,y,z,t)$. The random force at different points in the structure is uncorrelated. The random force $V\vec{F}^T(x,y,z,t)$ can be decomposed into a sum of mode shapes weighted by uncorrelated random forces $f_n^T(t)$

$$\vec{F}^T(x,y,z,t) = \frac{1}{V}\sum_n f_n^T(t)\vec{U}_n(x,y,z) \tag{3.107}$$

where $f_n^T = \int \vec{U}_n \cdot \vec{F}^T dV$. The coordinate $u_n(t)$ is equal to the root-mean-squared motion of the structure and the average kinetic energy of the mode is

$$\frac{1}{2}m\omega_{0_n}^2\langle u_n^2\rangle = \frac{1}{2}k_B T \tag{3.108}$$

As for the single SHO above, the spectral density $S_{F_n}^T$ of f_n^T derived from the average kinetic energy is

$$S_{F_n}^T \approx 4m\gamma_n k_B T \tag{3.109}$$

The requirement that the temperature of the effective SHO and the continuous structure are the same places an additional constraint on the parameters of the SHO in equation 3.102. This constraint can be derived in two different ways. First, the equipartition theorem implies that the thermalized average kinetic energy of the effective SHO and the relevant mode of the continuous structure are the same (equations 3.104 and 3.108). The mean-squared displacement of the effective SHO and the mean-squared displacement of the mechanical mode are related by the proportionality constant $\chi_n^2 = \langle (u_n)^2 \rangle / \langle u_{eff_n}^2 \rangle$. This leads to the constraint

$$m = \frac{m_{eff_n}}{\chi_n^2} \tag{3.110}$$

This same constraint can be found by examining the thermal force on the effective SHO and on a mode of the continuous structure. From equations 3.106 and 3.109, the constant temperature T implies that the ratio of the effective SHO force f_{eff_n} to $f_n = \int \vec{U}_n \cdot \vec{F} dV$ is

$$\frac{f_{eff_n}}{f_n} = \sqrt{\frac{S_{F_effn}^T}{S_{F_n}^T}} = \sqrt{\frac{m_{eff}}{m}} \tag{3.111}$$

Applying this constraint to equation 3.102 shows that this constraint and equation 3.110 are equivalent.

Since there are only two constraints on the three parameters in the effective SHO, there is a single free parameter. A common approach is to treat χ_n, that is, the proportionality constant $\chi_n u_{eff_n} = u_n$, as the free parameter. Given χ_n, the mass m_{eff_n} of the effective SHO is

$$m_{eff_n} = \chi_n^2 m \tag{3.112}$$

and the force f_{eff_n} on the effective SHO is

$$f_{eff_n} = \chi_n f_n = \chi_n \int \vec{U}_n \cdot \vec{F} dV \tag{3.113}$$

The parameter χ_n is often set equal to one or chosen so that the measured displacement at a specific point (x_0, y_0, z_0) in the structure due to mode n, $|\vec{X}(x_0, y_0, z_0)| = u_n(t)|\vec{U}_n(x_0, y_0, z_0)|$, is equal to the displacement of the effective SHO

$$\chi_n = \frac{1}{|\vec{U}_n(x_0, y_0, z_0)|} \tag{3.114}$$

If the displacement is measured at a spot on the structure where the mode's displacement is larger than the root-mean-squared displacement, then $\chi_n < 1$, the effective mass m_{eff_n} will be smaller than the total mass m, and the effective force f_{eff_n} will also smaller than the force f_n.

3.3.3 The influence of the APC on the nanomechanical modes

As discussed above, for very simple mechanical structures it is possible to find an analytic solution for the low frequency modes of the structure. However, the presence of an APC makes finding an analytic solution difficult. The APC introduces a mechanically weak spot in the system, which I often model as a spring, and removes some of the useful symmetries. In addition, a physically accurate model would require a difficult transition from bulk gold to the atomic-scale properties near the APC.

While the presence of the APC creates an intractable analytic problem, I can still attempt to numerically model the structure's bulk mode-shapes and frequencies. These numerical approaches fit under the broad heading of finite element modeling (FEM) and approach the problem by splitting the mechanical system into small elements with analytically understood behavior. These small elements are linked together, creating a matrix which describes the effect of each element on all of the other elements. In the simple of case, this matrix is inverted in order to determine the mechanical system's

normal mode shapes and resonance frequencies. This approach has been used in creating numerous different professional software packages; I have been using the ANSYS software package.

Finite element modeling programs are quite often used to model the resonance frequencies and mode shapes of nanomechanical systems, where the model of the mechanical system is designed using scanning electron microscope (SEM) pictures of the device and knowledge of the materials used in fabrication. In this case, there is also the question of how to model the APC. The FEM software is not designed for use with individual atomic/molecular bonds, and, in any case, I do not know the atomic configuration. However, it is possible to continue with the idea of a finite element model and attempt to model the effect of the APC on the mechanical system by replacing the APC with other elements. I can then modify the parameters of the APC element in order to reproduce the observed mode frequencies using the FEM.

I should mention that, while this is a good way to gain a qualitative understanding of the mechanical modes (especially if it is possible to accurately reproduce the observed mode frequencies), there are problems with progressing towards quantitative predictions. Specifically, this technique will attempt to compensate for any differences between the mechanical model and the physical system by changing the parameters of the APC element. Also, one of the most interesting parts of these models is the strain at the APC (that is, the quantity which is directly measured by the APC displacement measurement), however this is also the quantity which is represented by the least physical part of the model: the finite element that is chosen to represent the physical effect of the APC.

There are two different ways in which I have attempted to include the effect of the APC in a FEM. In both cases, the first step is to create the usual FEM of the nanomechanical system with a gap in place of the APC. In the next step, the coupling created by the APC is modeled by connecting the two sides of the gap using either an

ideal spring or a small piece of material with the same properties as the rest of the nanomechanical system. Finally, I modify either the spring constant (in the case of the ideal spring) or the dimensions of the material (in the case of the small piece of material) until the frequencies of the FEM modes approximately match the observed mechanical resonance frequencies.

I measure the motion of two types of nanomechanical structures in this thesis. The first type of structure is a nanomechanical beam which is touched in the middle by an APC (figure 3.11a). The APC is created using electromigration (see chapter 4) and the nanomechanical displacement measurements are discussed in chapter 6. In this case, I model the effect of the APC on the mechanical mode shapes by replacing the APC with a spring. A spring constant of 180 N/m results in FEM modes with resonance frequencies which approximately match the observed resonance frequencies.

The spring constant of APCs has also been measured in other experiments. The repeated breaking and reformation of the connection between two gold atoms ("training behavior," see chapter 7) has been used to infer APC spring constants ranging from 5 to 32 N/m [9]. However, unlike the APC modeled above, these junctions were formed using mechanical strain and carefully trained so that the effect of the leads connected to the atoms on the spring constant is minimal. The static force needed to displace an APC connected to a tuning fork (as in an AFM) has also been used to determine that the spring constant of contacts composed of a few (< 30) atoms is between 30-130 N/m [8, 161]. These junctions are also unlike the APC modeled above because the APCs are low resistance $R_{APC} \leq 2$ kΩ, thus composed of multiple atoms. Despite the differences between the contacts and the simplicity of the FEM, the spring constant I infer from the FEM model above is within a factor of 5 of the spring constants observed in other experiments.

The presence of the APC significantly effects the shape of the nanostructure's modes (figure 3.11b). The nanostructure is partially clamped by the APC and the

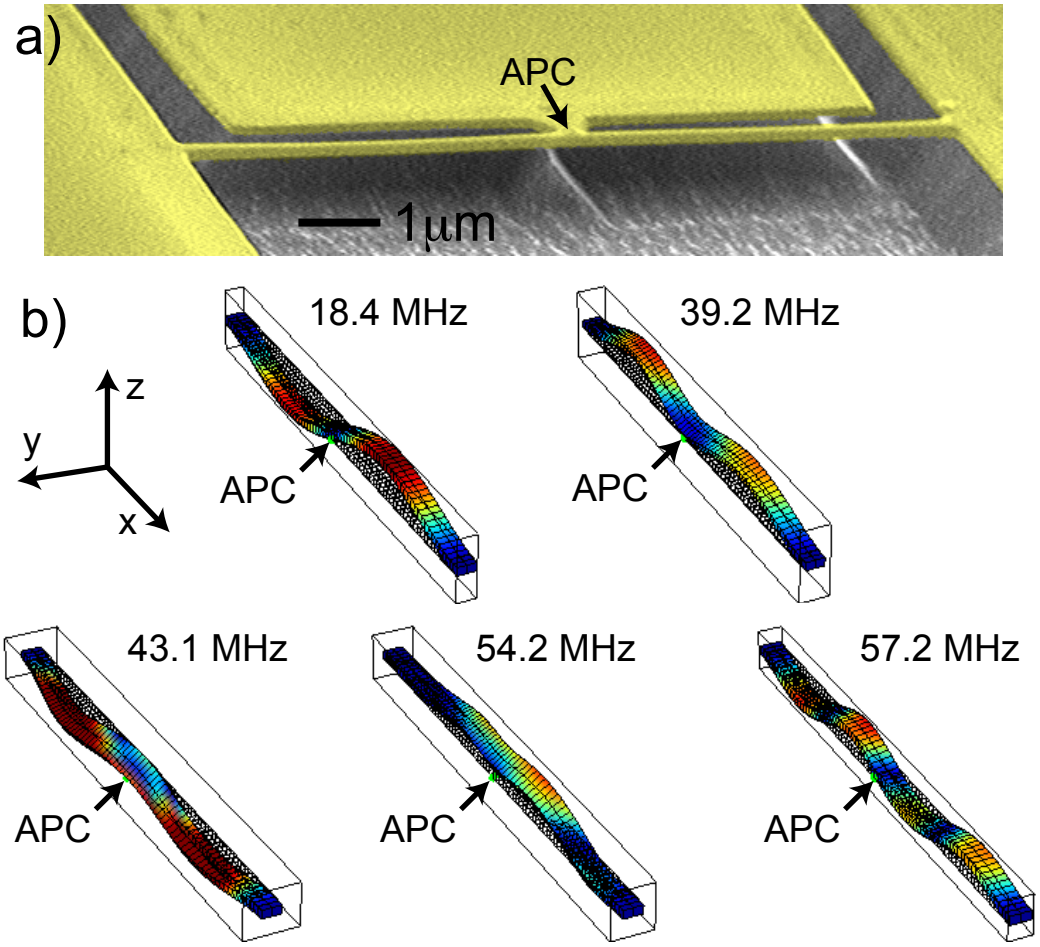

Figure 3.11: (a) Scanning electron micrograph of a gold nanostructure (yellow) containing an APC, prior to the *in situe* creation of the APC. The APC will be created at the constriction between the top electrode and the suspended nanomechanical beam. (b) A simple finite element model is used to estimate the mode shapes associated with the nanostructure in (a). The APC is modeled as a spring which is connected to the bottom of the beam, because the constriction is thinner than the beam, and close to the middle of the beam. The presence of the spring causes the mode shapes to be a combination of the in-plane, out-of-plane, and torsional modes expected from a simple doubly-clamped beam. The sensitivity of the APC displacement detector to a mode can be estimated from the normalized displacement of the point on the nanostructure connected to the spring.

displacement at the APC, that is, the quantity measured by the APC detector, depends on the mode. For the 18 MHz mode, which is similar to the 2nd mode of a doubly-clamped beam, the APC is close to a node of the system. The APC detector should be

relatively insensitive to 18 MHz displacement. On the other hand, the 43 MHz mode has an anti-node near the APC so the APC detector should be more sensitive to 43 MHz displacement. This aspect of the FEM is qualitatively consistent with the experimentally observed sensitivity. The presence of the APC also causes the nanostructure's modes to have in-plane, out-of-plane, and torsional components; a good example of this mixing is the 54 MHz mode.

The second type of structure is a nanomechanical beam which is interrupted in the middle by an APC (figure 3.12a). The APC is created by mechanically straining the beam (see chapter 4) and the nanomechanical displacement measurements are discussed

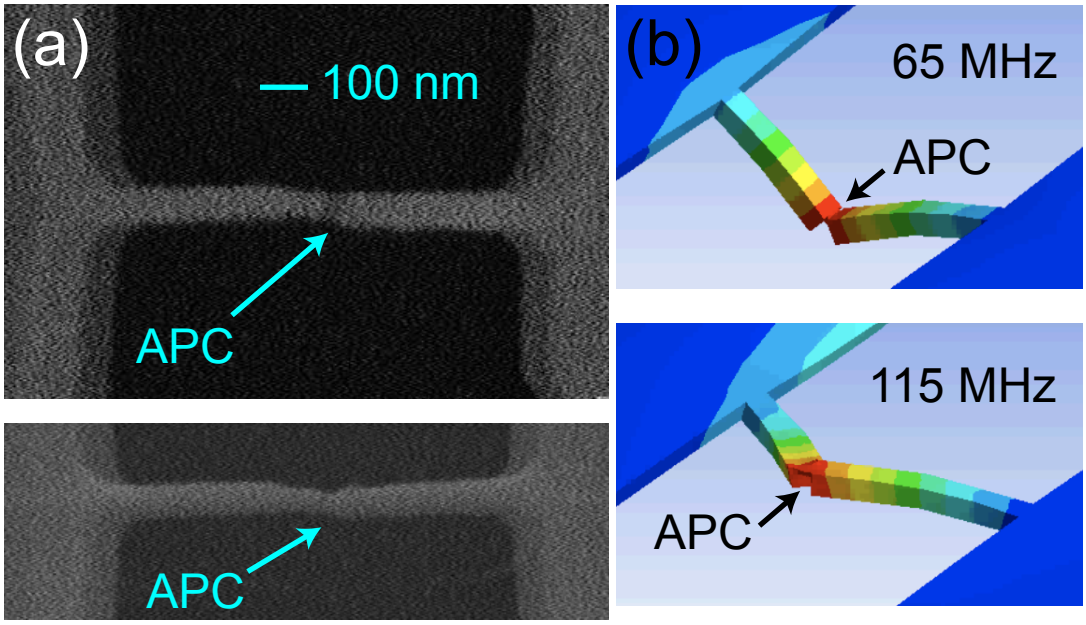

Figure 3.12: (a) Scanning electron micrograph of a gold nanostructure (white/grey) containing an APC, prior to the *in situ* creation of the APC. The top SEM is a top-down view of the beam and the bottom SEM is an angled view. The APC will be created at the constriction in the middle of the suspended nanomechanical beam. (b) A finite element model is used to estimate the mode shapes associated with the nanostructure in (a). The APC is modeled as a thin element connecting the two singly-clamped beams. The presence of the connection causes the mode shapes to be similar to the mode shapes of a doubly-clamped beam. The sensitivity of the APC displacement detector to a mode can be roughly estimated from the strain at the constriction.

in chapter 7. I model the effect of the APC on the mechanical mode shapes of this nanostructure by replacing the APC with a thin, narrow constriction with the same mechanical properties as the rest of the structure. I vary the height, width, and length of the constriction until the FEM mode frequencies approximately match the observed resonance frequencies.

This APC model is less intuitive because bulk material is used instead of a spring, but I used the more realistic FEM to improve the design of the nanostructure. This FEM model was used create a nanostructure with a larger coupling between the fundamental mode of the nanostructure and APC displacement, compared to the type of structure discussed earlier. The more realistic modeling of the structure's boundary conditions was also used avoid interference between flexural modes in the structure's supports and the APC measurement of the fundamental mode of the nanostructure. Low quality factor modes were observed below 500 MHz due to the flexing of the structure's supports. The frequency of these modes made it difficult to measure the fundamental mode with the APC displacement measurement. The FEM model was used to design stiffer supports which pushed the frequency of the low quality factor modes above 500 MHz and successfully removing their effect on the APC measurement.

The observed linear coupling between resistance R_{APC} and nanomechanical displacement can also be understood in the context of the FEM. In the first type of structure (figure 3.11), it is easy to see that small nanomechanical motion will create a linear change in the APC gap. However, the linear coupling observed in the second type of structure (figure 3.12) is less intuitive. If the measured change in R_{APC} was caused by the total change in the length of the beam, then the resistance R_{APC} would be, for small displacements, proportional to the absolute value of the displacement and the dominate voltage signal would be at a frequency equal to twice the frequency of the displacement. However, I observe that a driving force creates a voltage signal at the frequency of the driving force. This linear coupling is due to the resistance's depen-

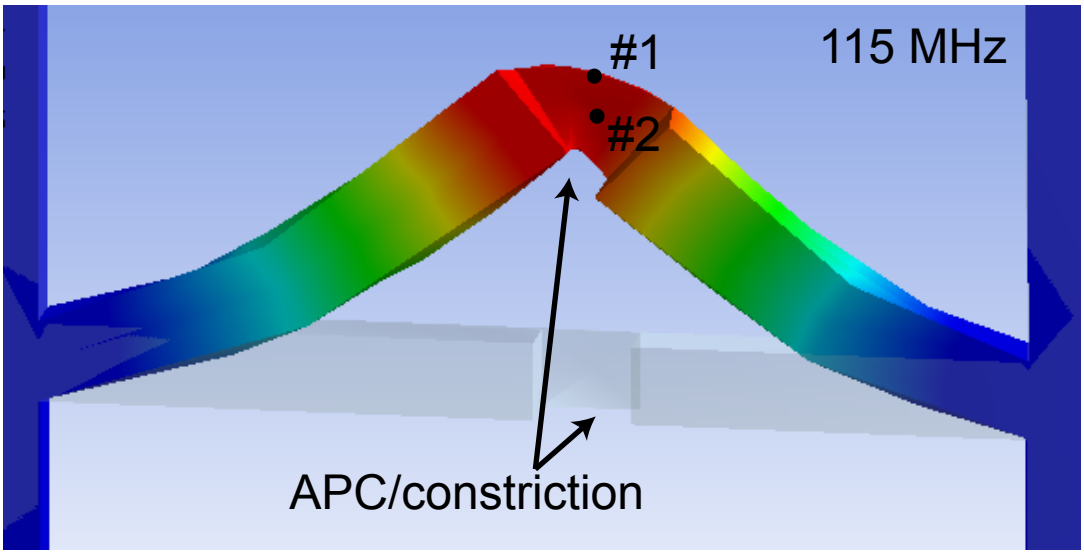

Figure 3.13: A view from the top of the FEM solution (color) to the shape of the 2nd mode of the nanostructure in figure 3.12; the grey shadow shows the relaxed shape of the nanostructure. The APC is located somewhere in the nano-scale constriction. If the APC is located near point #1 then the APC gap is currently expanded and will be compressed a half cycle later, leading to a linear coupling between nanomechanical displacement and the width of the APC gap. It is only if the APC is located near point #2 in the middle of the constriction that the width of the APC gap will depend on the absolute value of the nanomechanical displacement.

dence on the atomic-scale strain. Figure 3.13 contains a close-up view of a section of the nanostructure near the constriction used to model the APC. The length of the top of the constriction is increased, while the length of the bottom of the constriction is decreased. Since the APC resistance depends on this local strain, the APC resistance will be linearly coupled to displacement unless the APC is located in the center of the constriction.

3.3.4 Calibrating nanomechanical motion

I use the known thermal force $S_F^T = 4m_{eff}\gamma k_B T$, discussed in subsection 3.3.2, to calibrate the APC displacement detector. The measured nanomechanical displacement and backaction force need to be calibrated on two similar scales: in real units represent-

ing the displacement of the nanostructure and the force on the nanostructure, and in comparison to the quantum limits.

Earlier in this chapter I calculated the expected sensitivity of an APC displacement detector composed of gold atoms based on the work function of bulk gold. However, the atomic-scale system is complicated and, especially at low resistances $R_{APC} < 100\ \mathrm{k}\Omega$, the actual sensitivity may deviate from the expected sensitivity. The actual sensitivity is determined by measuring the signal in response to a known force. In general, it is difficult to calculate the exact magnitude of an applied force and the complicated mode shapes caused by the presence of the APC increase this difficulty. However, the spectral density of the thermal force $S_F^T = 4m_{eff}\gamma k_B T$ is known so the spectral density of the measured voltage signal $S_V^T(\omega)$ (figure 3.14) at a temperature T is used to calibrate the transduction G between displacement and voltage

$$G^2 = \frac{S_x^T}{S_V^T} = \frac{1}{S_V^T}\frac{4\gamma k_B T}{m_{eff}}\frac{1}{(\omega_0^2-\omega^2)^2+\gamma^2\omega^2} \tag{3.115}$$

In chapters 6 and 7, I discuss a more complicated version of this calibration which I use to analyze the experimental data.

The APC detector's imprecision S_x and backaction S_F^{BA} are determined from the white noise background in the voltage signal S_V^{imp} and the additional voltage signal above the thermal noise S_V^{add}, respectively (figure 3.14), as well as the transduction factor G. On-resonance where $\omega = \omega_0$, the transduction is $G = 4k_BT/S_V^T m_{eff}\gamma\omega_0^2$. The measurement imprecision on-resonance in displacement units S_x is

$$S_x = G^2 S_V^{imp} = \frac{S_V^{imp}}{S_V^T}\frac{4k_BT}{m_{eff}\gamma\omega_0^2} \tag{3.116}$$

The measurement backaction S_F^{BA} is inferred from the additional on-resonance signal S_V^{add}

$$S_F^{BA} = G^2 S_V^{add}\left(m_{eff}^2\omega_0^2\gamma^2\right) = \frac{S_V^{add}}{S_V^T}4\gamma k_B T m_{eff} \tag{3.117}$$

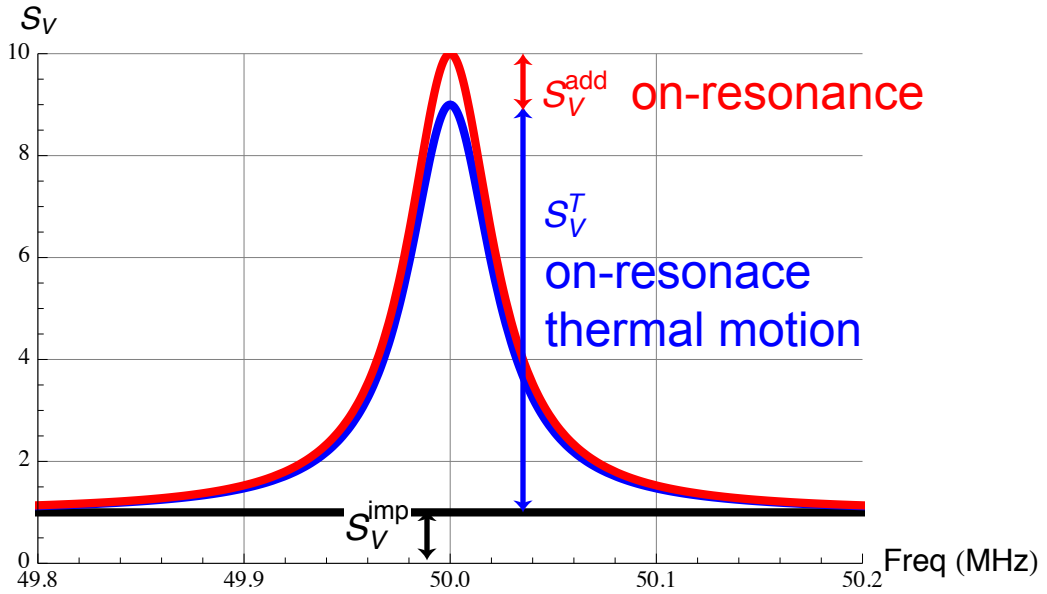

Figure 3.14: An example of a voltage spectral density S_V used to measure the APC imprecision and backaction. The shot noise of tunneling electrons results in a white background S_V^{imp} (black). The Brownian motion of the nanostructure has a Lorentzian line shape (blue, imprecision plus Brownian motion) and is used to calibrate the voltage measurement in units of displacement. The backaction force causes additional random motion of the nanostructure and an additional Lorentzian signal S_V^{add} (red, imprecision plus backaction plus Brownian motion). Both the shot noise (black arrow) and backaction (on-resonance, red arrow) contribute to the total uncertainty in the displacement measurement of, for example, the Brownian motion of the nanostructure (on-resonance, blue arrow).

The values of the displacement imprecision and backaction force in displacement units depend on the effective mass of the SHO. As discussed in subsection 3.3.2, when measuring the root-mean-square displacement of the nanostructure the effective mass of the SHO is equal to the total mass of the nanostructure. In this thesis, I use the total mass of the nanostructure in the calibration and quote the displacement imprecision

in terms of the root-mean-square displacement of the structure. I could attempt to use the mode shapes from the FEM models to find the effective mass associated with displacement at the APC. I do not attempt to use this calibration because it would add a large source of systematic error to the calculation; on the other hand, the total mass of the nanostructure is known with an error of about about 20%.

The choice of an effective mass is also less important because it is irrelevant when comparing the APC displacement detector, calibrated using the thermal force, to the quantum limits. Both the backaction force at the standard quantum limit $S_{FSQL} = \hbar m_{eff}\gamma\omega_0$ (equation 3.55) and the thermal force have the same mass dependence. Using the thermal calibration above, the ratio of the measured backaction force to the backaction force at the standard quantum limit does not depend on the effective mass

$$\frac{S_F^{BA}}{S_{FSQL}} = \frac{S_V^{add}}{S_V^T}\frac{4k_BT}{\hbar\omega_0} \tag{3.118}$$

Similarly, the ratio of the measured imprecision and the imprecision at the standard quantum limit does not depend on the effective mass

$$\frac{S_x}{S_{xSQL}} = \frac{S_V^{imp}}{S_V^T}\frac{4k_BT}{\hbar\omega_0} \tag{3.119}$$

Finally, the product of the imprecision and the backaction, which is equal to $\hbar^2$ if the detector is quantum limited, is also independent of the effective mass

$$S_xS_F^{BA} = \frac{S_V^{imp}}{S_V^T}\frac{S_V^{add}}{S_V^T}\left(\frac{4k_BT}{\omega_0}\right)^2 \geq \hbar^2 \tag{3.120}$$

The mode shape is important when estimating the magnitude of a specific force required to produce the observed backaction force. While this is true for any type of force, I am going to specifically consider the phenomenological description of the backaction force F_I due to tunneling electrons. I assume that the force is applied near the APC at the point $(x_{APC}, y_{APC}, z_{APC})$ and in a direction parallel to the changing

APC gap. The force f_n on mode n due to the backaction force F_I is then

$$f_n = \int \vec{U}_n \cdot \vec{F} dV \approx |F_I||\vec{U}_n(x_{APC}, y_{APC}, z_{APC})| \tag{3.121}$$

The proportionality constant $\chi_n = 1/|\vec{U}_n(x_{APC}, y_{APC}, z_{APC})|$ relates the change in the size of APC gap x_n to the displacement of the mode $u_n = x_n\chi_n$ and can be used to determine an effective mass, as discussed earlier in subsection 3.3.2.

Based on the FEM simulations described in the previous section, I estimate that $\chi \approx 1/2$ for the modes and nanostructures discussed in chapters 6 and 7. However, the FEM models are very rough approximations and assume that the atomic-scale strain is the same as the 10 nm scale strain. Such an estimate is probably accurate to within an order of magnitude, but making a more precise estimate based on mechanical models is beyond the scope of this thesis.

I also independently estimate that $\chi \approx 1$ by comparing the expected sensitivity of the APC detector to the measured sensitivity. At large resistances $R_{APC} > 500$ kΩ (chapter 7) the measured sensitivity, which is parameterized by a length scale λ, is consistent with the theoretical predictions to within a factor of two. This data implies that the root-mean-squared motion of the mode is equal to the change in the size of the APC gap and $\chi \approx 1$ to within a factor of two.

These two estimates are consistent and in chapters 6 and 7 I assume that $\chi = 1$ unless noted otherwise. Specifically, this assumption effects my estimates of the momentum impulse delivered by each tunneling electron. I generally estimate each electron's momentum kick by assuming that the entire backaction force is due to momentum kicks from tunneling electrons and is described by the phenomenological model discussed above. If χ is actually > 1, then the motion at the APC is smaller than the root-mean-squared motion of the structure and I will have underestimated the magnitude of the electron momentum needed to explain the observed backaction force. On the other hand, if χ is actually < 1 then the APC is closer to an anti-node of the mode and the

estimated electron momentum in chapters 6 and 7 is too large. The uncertainty in χ is a major source of systematic error in the estimates of the momentum kick delivered by each tunneling electron.

Chapter 4

Experimental realization of an APC embedded in a nanomechanical oscillator

In this chapter I describe the two different methods that I use to create an atomic point contact (APC) which is coupled to a nanomechanical oscillator. Both of these techniques are commonly used to create APCs (as described in chapter 2), but the previous work concentrated on the static properties of the APC and did not measure the dynamics of nanomechanical motion.

The first method of APC creation is called electromigration and involves passing a large current through a constriction. Atoms in the high current-density region caused by the constriction migrate into the low current-density region until finally the flow of current is due to the connection between only two atoms: an atomic point contact. The main advantage of this technique is the simplicity. The fabrication procedure involves relatively few steps (compared to many nanomechanical devices) and minimal infrastructure is required to pass a current through a constriction. However, it is very difficult to control the resistance of the APC while electromigrating which leads to a number of disadvantages: the procedure is unreliable with more than 50% of the electromigrated devices have an unmeasurably high resistance, the resistance of the APC after electromigration is largely random, and it is usually not possible to reduce the resistance of the APC using electromigration.

The second method of APC creation is to physically stretch a constriction until it

flows and fractures to form an APC. This type of device is commonly called a mechanically controllable break junction (MCBJ), and the resistance of a MCBJ can be tuned from less than 100 Ω to more than 10 GΩ by changing the strain (that is, the amount that the constriction is stretched). In this method, the constriction is fabricated on a flexible substrate, and the strain is applied by bending the substrate. The infrastructure required to controllably bend the substrate makes the second method both more complicated and more controlled than electromigration.

4.1 APC Creation Using Electromigration

4.1.1 Introduction to electromigration

The interest in electromigration, the motion of atoms in a conductor due to the application of an electric field, has gone through three distinct phases. In the first phase prior to the 1960s, most research in electromigration involved basic studies of bulk materials, concentrating on mass transport in metals and the effect of charge carriers on conductors [162]. By the late 1960s electromigration had become a problem for the integrated circuit industry because the metal lines in integrated circuits were, by then, small enough that electromigration could create gaps in the lines over time. In this second phase, the industrial problem led to a great deal of both experimental and theoretical research with the goal of understanding electromigration in thin films and preventing the failure of integrated circuits [162–164]. This type of applied research continues today (for example, [165]), but a third phase began in the late 1990s as electromigration became a tool for creating electrodes with a small (sub-5 nm) gap [41]. This tool is used in ongoing research into the electrical and mechanical characteristics of atomic point contacts (for example, [166]) and single molecules (starting with [40]).

In the context of this thesis, the third phase of research led to the most convenient theoretical description of electromigration. The basic idea of an electromi-

gration force from earlier work [167] is combined with thermal effects [168, 169]. In theoretical explanations of electromigration, the force on an impurity is divided into two parts [162, 167, 168, 170]. The first part, called the "direct force" F_d, is due to the electric field $\vec{E}$ acting directly on an impurity atom

$$\vec{F_d} = Z_d e\vec{E} \tag{4.1}$$

where Z_d is the effective electric charge of the atom. The second part, called the "electron wind force" F_w, is due to the net momentum transfered to the atom by scattered electrons

$$\vec{F_w} = Z_w e\vec{E} \tag{4.2}$$

where $Z_w = K/\rho$, ρ is the total resistivity, and K is a phenomenological constant related to the mobility of the impurity. Therefore the atom behaves as if it had a charge $Z^* = Z_d + Z_w$ though in general $|Z_d| \ll |Z_w|$, [168–170].

From reference [169], the flow of atoms in a constriction can be described using a theory based on the basic description of the force on an atom F_d and an evaluation of the flow of electrons, atoms, and energy using the thermodynamics of irreversible processes. This description assumes electromigration occurs at a constriction which can be treated in the continuum limit. If the constriction is composed of many atoms, the constriction has a resistance $R_{APC}(t) = \rho L/A(t)$ and electromigration does not change the length L or electrical resistivity ρ but does have the effect of decreasing the average cross-sectional area $A(t)$ over time t. (I should also point out that I am going to use the symbol R_{APC} to refer to the constriction resistance even when the constriction resistance $R_{APC} < 100\ \Omega$ and there is no APC, that is, no electron tunneling).

With these assumptions, the expected flux of atoms J_m due to the flow of a large electrical current with density j through a thin, narrow gold wire that is heated by the

flow of current from a temperature T_0 to a temperature T is

$$J_m = \frac{\alpha}{T}\left(|j| - j_{min}\right)\exp\left[-\frac{E_a}{k_B T}\right] \tag{4.3}$$

In this model, the cross-sectional area $A(t)$ of the constriction, and thus R_{APC}, changes slowly or not at all ($dR_{APC}/dt < 100\ \mu\Omega/\text{sec}$) unless the atom flux J_m is greater than some critical value J_m^c which is experimentally determined. In this equation, the activation energy of gold diffusion on a surface is $E_a = 0.12$ eV. The other constants, α and j_{min}, are experimentally determined though it is expected that $\alpha \propto Z^*\rho$ and $j_{min} \propto 1/(Z^*\rho)$. If the inelastic scattering length is smaller than the size of the constriction, then it is possible to express the temperature of the constriction as a function of the current density $T = T_0 + \beta j^2$. This assumption is valid for the relatively large voltage biases (> 15 mV) and bath temperatures ($T_0 \approx 4$ K) used here. Then the equation for the flow of atoms is

$$J_m = \frac{\alpha}{(T_0 + \beta j^2)}\left(j - j_{min}\right)\exp\left[-\frac{E_a}{k_B(T_0 + \beta j^2)}\right] \tag{4.4}$$

where β is also experimentally determined. In the experiment described by reference [169], $\beta \approx 1.7 \times 10^{-15}$ K cm^4/A^2, $j_{min} \approx 10^8$ A/cm^2, and $J_m^c/\alpha \approx 1.5 \times 10^4$ A/K cm^2, though these constants are dependent upon the device geometry and material.

Using equation 4.4, it is possible to gain a better understanding of how the resistance of the constriction R_{APC} changes during electromigration and understand why controlling electromigration requires controlling the voltage across the constriction. Experimentally, the process of electromigration starts by slowly increasing the current I_{APC} that flows through a constriction with a resistance $R_{APC} < 100\ \Omega$. This increasing current has the effect of increasing both the current density j and the temperature $T = T_0 + \beta j^2$ in the constriction. Eventually the combination of a rising temperature and increasing force due to the increasing current density causes the flux of atoms J_m to pass a critical value J_m^c where the constriction cross-section begins to shrink.

As the average cross sectional area $A(t)$ of the constriction shrinks, the APC resistance $R_{APC}(t) = \rho L/A(t))$ also begins to change and controlling the rate of change requires controlling the voltage across the constriction. The simplest way to control the voltage is to voltage bias the constriction (i.e., impose a voltage) so that the voltage V_{APC} across the constriction is independent of the resistance $R_{APC}(t)$. In this case, the current density $j = I_{APC}/A(t) = V_{APC}/\rho L$ will be constant. The atom flux J_m and the rate of gap formation (dR_{APC}/dt) will also be constant and under control. On the other hand, if the constriction is current biased so that the current I_{APC} passing through the constriction, instead of the voltage V_{APC}, is imposed then the current density $j(t) = I_{APC}/A(t) = I_{APC}R_{APC}(t)/\rho L$ and the constriction temperature T increases as the cross-sectional area $A(t)$ of the constriction shrinks. This creates a feedback loop which causes the rate of atom flux away from the constriction J_m and thus the rate at which the area $A(t)$ of the constriction shrinks to increase almost exponentially until the assumptions in the model are violated (usually either the material melts or the way in which electrons pass through the constriction changes from the diffusive regime to the tunneling regime). Since it is very difficult to stop the exponential decrease in area $A(t)$ and increase in R_{APC} by effectively duplicate a voltage bias and quickly lowering the current bias I_{APC}, voltage biasing the constriction is an important step towards controlling the process of electromigration.

To proceed with this description of how the cross-sectional area of the constriction shrinks during electromigration, the area of the constriction eventually reaches the atomic scale where the discrete nature of atoms becomes relevant [8, 169, 171, 172]. At that point, the change in resistance R_{APC} is no longer continuous but proceeds in jumps as the configuration of atoms changes. This rearrangement is uncontrollable. Once the conduction through the constriction is dominated by only a few atoms (that is, the resistance $R_{APC} \geq 1$ kΩ) then the change in conductance is usually equal to the conductance quanta $G_q = 2e^2/h = 1/(12.9\ \text{k}\Omega)$ (see chapter 3 and reference [8] for more

details on conductance quanta).

As these rearrangements continue under the influence of a large current density, the conductance will eventually be dominated by electrons tunneling between two atoms thus forming an atomic point contact (APC). The resistance $R_{APC} \geq 12.9$ kΩ is an exponential function of the gap size (with a length scale of about 1 Å, see chapter 3) therefore atomic rearrangements have a large effect on R_{APC} making it impossible to stop electromigration at a predetermined value. It is possible to continue passing a current with a large density through the APC and hope that a favorable reconfiguration occurs, however in the tunneling regime the reconfigurations almost always result in a higher APC resistance.

4.1.2 Design of devices for electromigration

The desire to control the location and speed of electromigration places a number of constraints on the design of the nanomechanical structure. First, and most importantly, the current density at the desired location of the APC must be as large as possible in comparison to the current density everywhere else. There are two other similar ways of stating this condition: in comparison with the rest of the device, there should be a thin, narrow constriction at the desired location of the APC; and the resistance of the circuit should be dominated by the resistance at the constriction. Otherwise, the location of the APC is poorly defined and it is not possible to voltage bias the constriction.

Second, the constriction (that is, the desired location of the APC) should be located near the point which is most likely to melt when current is flowing through the nanostructure. As described above, the process of electromigration is thermally assisted and a large local temperature can result in gap formation even if there is a larger current density at other, cooler, locations (see equation 4.4). In structures which are fabricated on a substrate and thus cooled through the substrate, the large resistance of the desired site of the APC ensures that this constraint is naturally satisfied. However, with a

suspended nanomechanical structure it is possible to create hot spots because regions close to the supports are cooler than those which are remote (in the middle of the suspended structure), and the structure can either electromigrate or melt at these hot spots instead of at the desired location.

Third and finally, there should not be a large stress on the suspended structure

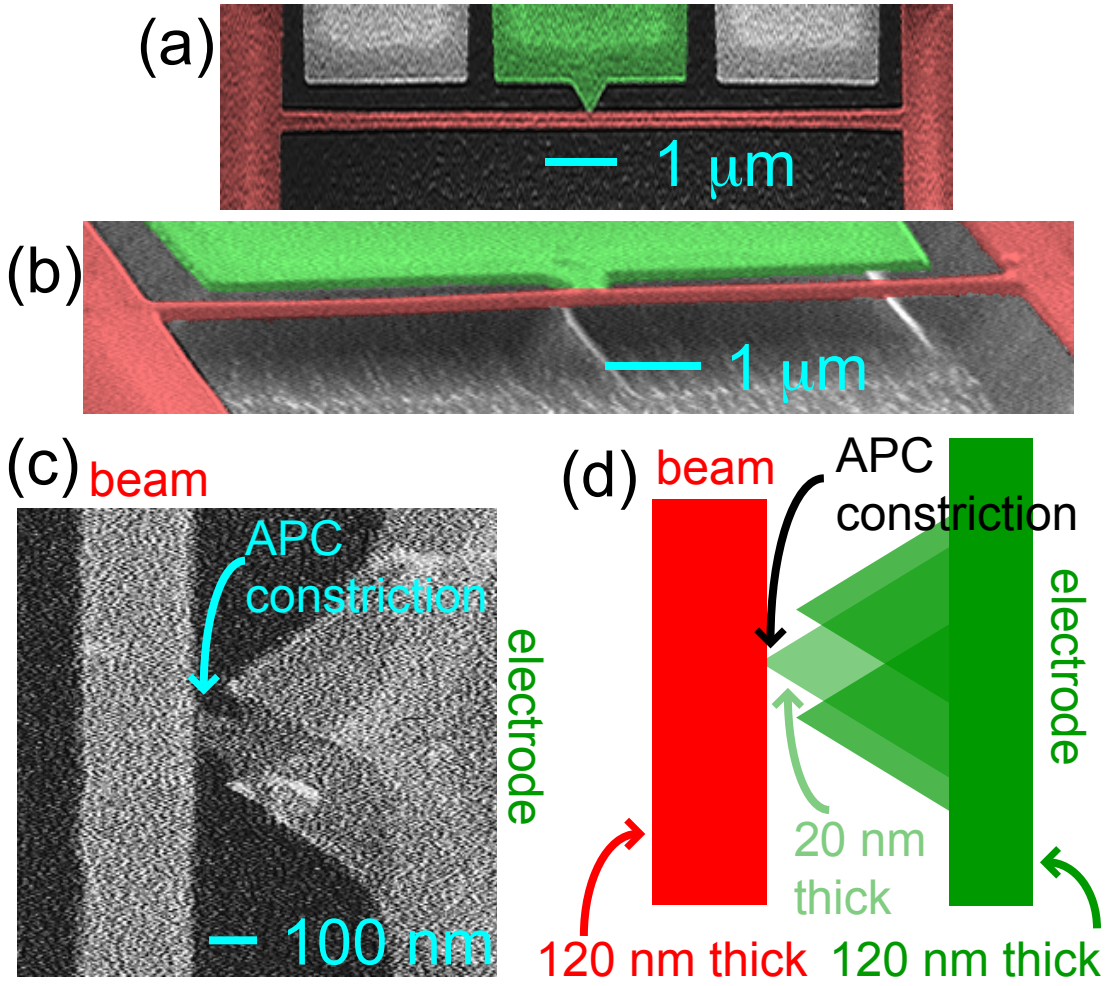

Figure 4.1: Scanning electron micrographs of devices prior to electromigration; the APC will be formed in the thin, narrow constriction between the red nanomechanical beam and green electrode. (a) top down view of device. (b) isometric view of different device. (c) close up view of constriction. (d) schematic representation of an ideal constriction. A triple-angle evaporation is used to make the constriction thin in comparison to the beam and the electrode.

(particularly at the location of the APC). If the stress is too large, the mechanical structure will eventually not be able to withstand the stress as atoms are removed from the desired location of the APC and the constriction will fracture resulting in a large (on the atomic scale) gap. This is a particular problem when a suspended structure is cooled to cryogenic temperatures because the relative thermal contraction of different materials can result in a large stress.

The nanomechanical structure that I use to satisfy these three constraints is shown in figure 4.1. The main structure is composed of a doubly-clamped beam (red, figure 4.1) that is about 10 μm long by 250 nm wide by 120 nm thick and is contacted in the middle by another electrode (green, figure 4.1). The beam and part of the other electrode are suspended above the gallium arsenide (GaAs) substrate (figure 4.1b) and the suspended structure is made entirely out of gold. The APC will be formed using electromigration at the constriction between the center electrode and the beam (labeled "APC constriction" in figure 4.1c, d).

The constriction in figure 4.1c is 20 nm thick by 75 nm wide and therefore satisfies the first constraint required for electromigration (described in detail above); the constriction is thinner and narrower than the rest of the electrode and the beam. In devices that have been successfully electromigrated, the resistance R_{APC} of the constriction is greater than the resistance $R_0 + [R_{beam}/4]$ of the rest of the structure (figure 4.2). Experimentally, for electromigration to succeed the constriction must have a resistance $R_{APC} \geq 30\ \Omega$ while the resistance of the remaining structure is $R_0 + [R_{beam}/4] \approx 15\ \Omega$. The smallest achievable constriction size and therefore the largest achievable constriction resistance ($R_{APC} \leq 60\ \Omega$) is limited by the resolution of the fabrication technique.

In order to satisfy the second constraint and avoid melting the nanomechanical beam instead of electromigrating the constriction, it is necessary to take care when designing the beam's dimensions. When power is dissipated in the beam in figure 4.1a,b the beam is cooled through the three connections to the substrate: the two clamped

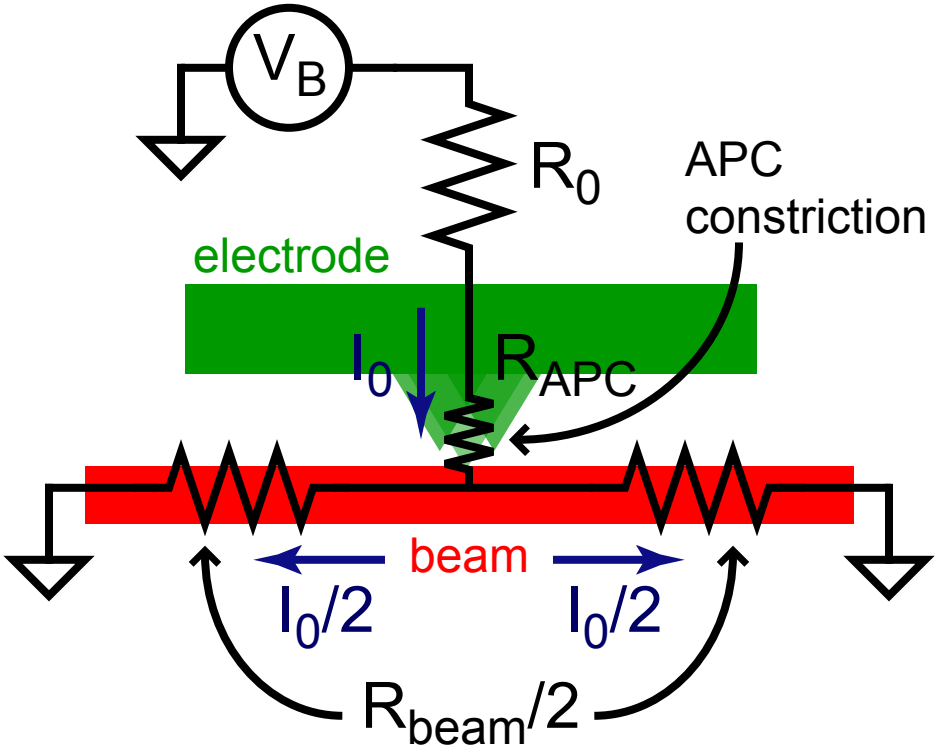

Figure 4.2: A simple electrical diagram of the DC circuit used during electromigration. The resistance R_0 represents the series resistance between the constriction R_{APC} and the voltage bias V_b, including the cryostat wiring and on-chip electrode. The current is split at the beam by grounding both sides of the beam; since the constriction touches the middle of the beam, the resistance of and current through the beam are split into two equal parts. Typical values are $R_0 \approx 5\ \Omega$, $R_{beam} \approx 40\ \Omega$, and $30\ \Omega < R_{APC} < 60\ \Omega$

ends (in red) and the central electrode (in green). The beam will first melt at the points that are furthest from these cold reservoirs, so in this geometry there are two hot spots which are halfway between the central electrode and the ends of the beam. Because these hot spots are cooled through the body of the beam, there is a compromise between designing a more compliant beam, which is longer and narrower, and designing a beam which will not melt during electromigration. The beam design in figure 4.1 can handle a current of about 5 μA; the resulting 10 μA of current through the constriction is sufficient to electromigrate constrictions similar to that in figure 4.1c. The required current is very sensitive to the size of the APC constriction.

The nanomechanical structure in figure 4.1 also satisfies the third and final condition that the strain at the constriction is small by limiting the distance between the beam support and the central electrode support. Most of the strain in the system is due to the different coefficients of thermal contraction of the metal nanostructure and the semiconductor substrate. If a relaxed nanostructure (that is, not under strain) at room temperature is cooled to 4 K, then the gold nanostructure will shrink by about $\Delta l/l = 0.003$ while the GaAs substrate will only shrink by about $\Delta l/l = 0.001$ resulting in a gold nanostructure with a stress consistent with a strain of $\Delta l/l = 0.002$. In other words, at 4 K the relaxed size of the nanostructure is 0.2% smaller than the actual size. The distance between the central electrode support and the beam is only 500 nm. The maximum separation of the APC gap due to the strain is therefore only 1 nm which is the same order of magnitude as the expected size of the APC gap. Some of the tension is also released during electromigration since the large temperature at the constriction effectively anneals the constriction. Experimentally, the total strain is small enough to allow successful electromigration.

4.1.3 Fabrication of devices for electromigration

The device in figure 4.1 is fabricated using the standard tools of nanolithography. A detailed description of the recipe is given in appendix A, however the basic steps are described in chronological order in this subsection (and in figure 4.3). This fabrication process is simpler than most nanomechanical fabrication recipes because the nanomechanical structure is made purely out of metal instead of a semiconductor/metal bilayer. Although I will describe the fabrication process used with a GaAs substrate, later devices were made using a silicon substrate because silicon has a smaller peizoelectric response than GaAs. The main difference in fabrication is just the use of different techniques to etch the GaAs and the silicon.

When using a GaAs substrate, the process starts with a GaAs wafer which

is cleaved into chips that are about 5 mm on a side. An organic polymer bilayer (PMGI/PMMA) is spun on the chip (figure 4.3a). This layer is exposed in the desired two dimensional pattern using the electron beam from a scanning electron micoscope (SEM). The exposed organic polymer is developed and removed. There is now a three dimensional pattern in the organic polymer determined by a combination of the pattern written by the electron beam and the chemistry of the organic polymer (figure 4.3b).

Gold is evaporated onto the entire chip at three different angles in order to create a thick beam and thick electrodes as well as a thin region at the desired APC location (figure 4.3c). The organic polymer and all of the gold that is not touching the substrate is removed using a chemical wash (figure 4.3d). Finally, the nanomechanical structure is suspended using a citric acid/hydrogen peroxide wet etch (figure 4.3e). An SEM picture of the final device is shown in figure 4.3f. As described in the previous subsection (and figure 4.1), the APC will be created at the constriction where the triangular central electrode touches the doubly-clamped nanomechanical beam.

One major difference between the nanomechanical structure used in this experiment and most other nanomechanical devices is the use of an all-metal (gold) structure; the semiconductor material is only used as a sacrificial layer (that is, the semiconductor is removed by etching). Most nanomechanical devices are made of a single-crystal semiconductor material in order to maximize the nanomechanical quality factor. However, in this experiment the quality factor is limited by the presence of the APC. The use of an amorphous metal structure instead of a single-crystal is not expected to significantly reduce the quality factor and does make the fabrication simpler by avoiding the need to pattern and etch the single-crystal structural layer. (Reference [14, 15] or any textbook on nanomechanics will contain a more detailed description of the fabrication steps involved in creating a nanomechanical structure out of single-crystal semiconductor material).

After the initial measurements of devices on top of GaAs substrates, I realized

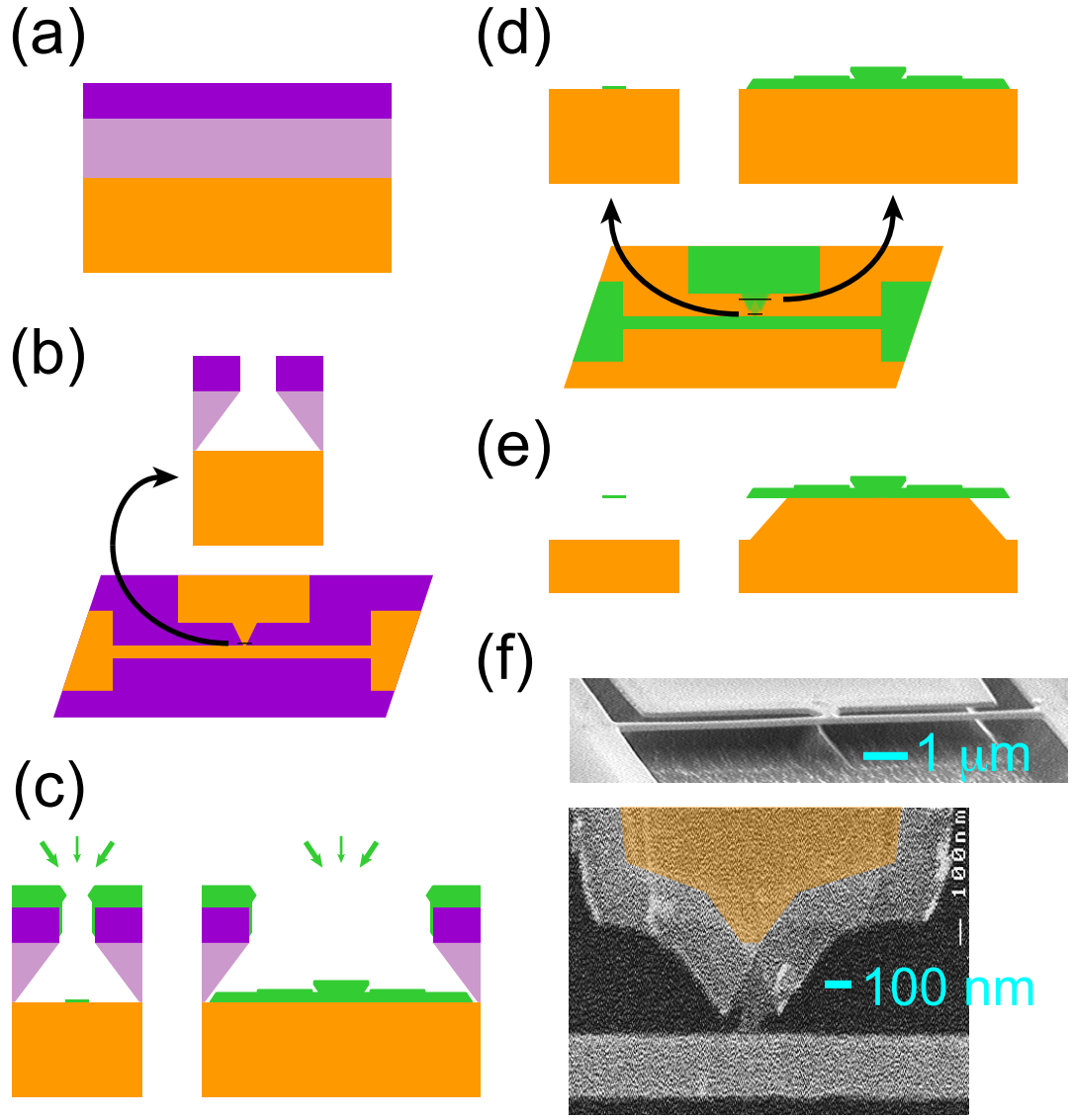

Figure 4.3: Fabrication steps on a GaAs substrate; for more detail, see A. (a) spin a layer of PMGI (light purple) and then PMMA (dark purple) resist on the GaAs surface (orange), shown in cross-section. (b) after exposing a two-dimensional pattern using the electron beam of an SEM, the PMGI/PMMA bilayer is developed removing the exposed resist. The top view shows a cross-section at the APC constriction; the cross-section is taken at the black line in the top-down view. (c) Gold is evaporated at three angles, shown by the green arrows. When the gap in the resist is narrow, then the angled evaporations do not deposit gold on the GaAs surface, but when the gap is large then a thick layer of gold is deposited. (d) The resist is removed by rinsing in acetone, leaving behind the gold which was deposited directly on the GaAs substrate. (e) The GaAs is etched using an isotropic wet etch of citric acid/hydrogen peroxide, suspending the naomechanical beam and undercutting the larger electrodes. (f) Scanning electron micrographs of the finished structure; in the lower figure, the area where the gold contacts the GaAs is shown in orange. The grey area of the gold is suspended.

that the peizoelectric property of GaAs was complicating my measurements of forces applied to the nanomechanical structure. I therefore switched to using silicon substrates. An electrostatic force can be applied to the nanomechanical structure by voltage biasing a gate electrode that is capacitively coupled to the structure. However, the peizoelectric nature of GaAs implies that this voltage also launches surface acoustic waves onto the chip. These surface acoustic waves shake the supports of the nanomechanical structures, creating a force on the nanomechanical structure. The etched surface of the chip is a complicated boundary condition and therefore the magnitude of the force on the structure has a complicated frequency dependence due to the constructive and destructive interference of surface acoustic waves rebounding from the boundaries. When using GaAs substrates, the magnitude of the surface acoustic waves and the frequency dependence interferes with measurements of the electrostatic force. Therefore later devices were made on a silicon substrate where the peizoelectric response is small enough to be ignored. This change required small modifications to the fabrication procedure (the recipe is in appendix B) including a different recipe to etch silicon.

4.1.4 Electromigration procedure

Once a device with a constriction attached to a nanomechanical beam has been fabricated, the device is placed in the ultrahigh vacuum environment of a 4 K cryogenic system and the constriction is electromigrated to form an atomic point contact (APC) by passing a current through the constriction. The magnitude of the current must be carefully controlled to create an atomic point contact with a small gap instead of a larger gap with a vanishing probablity of electron tunneling. This control takes two forms: the constriction should be voltage biased (as explained in section 4.1.1) and a feedback loop is needed to slow the rate of resistance change to a more controllable pace by lowering the voltage. Even with feedback, the electromigration procedure becomes uncontrollable at resistances greater than 1 kΩ where only a few atoms are involved and

it is not possible to control the final resistance.

In order to simultaneously measure the resistance of the constriction R_{APC} and apply a stiff voltage bias, I use the circuit in figure 4.4. In this figure, the area in the

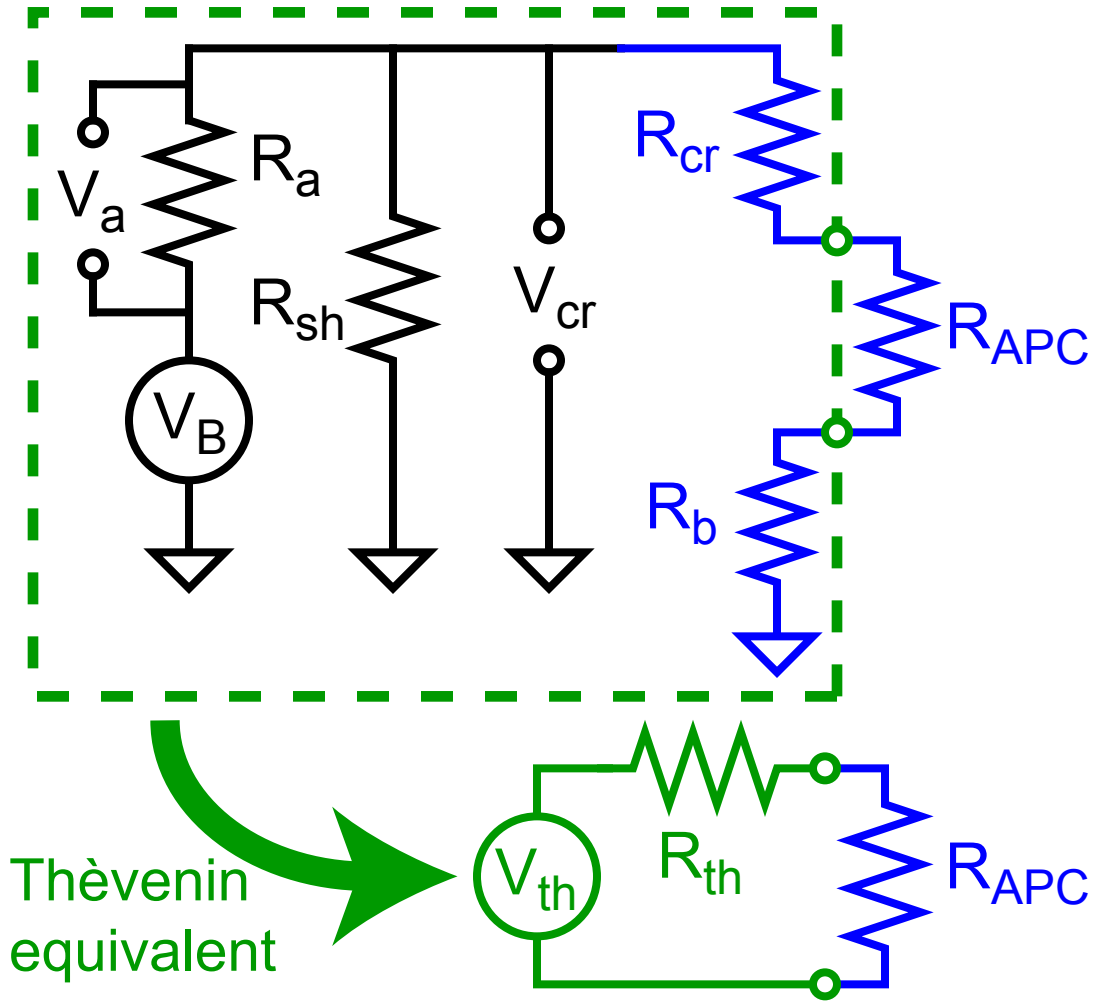

Figure 4.4: DC electromigration circuit. The black portion of the circuit diagram is at room temperature, and the resistors R_a and R_{sh} are usually chosen to be small and equal in comparison to the sum of the resistance in the cryostat, shown in blue. R_{cr} is the resistance of the cryostat wiring and on-chip electrodes, R_{APC} is the resistance of the constriction, and R_b is the resistance between the constriction and ground due to the nanomechanical beam. The area in the green dashed-box is a one-port network biasing the constriction R_{APC} and, according to Thévenin's theorem, is equivalent to a voltage source V_{th} in series with a resistor R_{th}.

blue-dashed box represents the resistance in the cryostat which can be divided into three parts: the resistance of the wires in the cryostat and on-chip leads R_{cr}, the resistance of the beam R_b ($R_b = R_{beam}/4$, see figure 4.2), and the resistance of the constriction R_{APC}. This circuit diagram also includes two resistors whose values I can change during electromigration: a resistor R_a with a known resistance which is used to measure the current flowing through the circuit and a shunt resistor R_{sh}.

Successful electromigration requires a clear hierarchy in the values of the resistors in figure 4.4, $R_a \approx R_{sh} \ll (R_{APC} + R_{cr} + R_b)$ and $R_{APC} \gg R_{cr} + R_b$. This relationship will be described in more detail below, but, as a brief outline, the measured resistance of the APC is more precise if $R_a \approx R_{sh}$, voltage biasing the restriction requires $R_{sh} \ll R_{APC}$, and $R_{APC} \gg R_{cr} + R_b$ in order to both voltage bias the constriction and satisfy the conditions for electromigration described in section 4.1.2. In this experiment, $R_b \approx 10\ \Omega$, $R_{cr} \approx 5\ \Omega$, and the initial resistance of the constriction before electromigration is $60\ \Omega \geq R_{APC} \geq 30\ \Omega$, thus the third and last condition is satisfied.

I will describe the DC resistance measurement in more detail in chapter 5, however the basic technique is to measure the voltage V_a across the known resistor R_a and the voltage drop across the cryostat V_{cr} (see figure 4.4). These quantities are a direct measurement of the resistance R_{tot}, the parallel combination of the resistance in the cryostat $R_{APC} + R_{cr} + R_b$ and the shunt resistor R_{sh},

$$V_{cr}\frac{R_a}{V_a} = R_{tot} = \frac{R_{sh}(R_{APC} + R_{cr} + R_b)}{R_{sh} + R_{APC} + R_{cr} + R_b} \tag{4.5}$$

and since the resistances R_{sh} and R_a are known it is easy to calculate the resistance in the cryostat $R_{APC} + R_{cr} + R_b$

$$R_{APC} + R_{cr} + R_b = \frac{R_{tot}R_{sh}}{R_{sh} - R_{tot}} = \frac{V_{cr}R_aR_{sh}}{V_aR_{sh} - V_{cr}R_a} \tag{4.6}$$

In order to most accurately measure R_{tot} the two voltages V_{cr} and V_a should be approximately equal, and since $(R_{cr} + R_b + R_{APC}) \gg R_{sh}$ the resistance $R_{tot} \approx R_{sh}$.

Therefore, the resistor R_a should be chosen so that $R_a \approx R_{sh}$ as suggested in the previous paragraph.

In section 4.1.1, I described how a voltage bias limits the current density in the constriction. The same behavior that limits the current density also limits the power dissipated in the constriction. Because the electromigration is thermally assisted, limiting the dissipated power helps slow the rate of electromigration and allows the final resistance to be somewhat controlled.

The simplest way to properly choose the value of R_a and R_{sh} so that the power at the constriction P_{APC} decreases during electromigration is to employ a Thévenin equivalent circuit to describe the circuit which biases the constriction R_{APC} (figure 4.4). As discussed earlier, I am going to set $R_{sh} = R_a$. Thévenin's theorem states that a one-port network of voltage sources, current sources, and resistors can be described using a single voltage source V_{th} in series with a single resistor R_{th} [173]. For the circuit in figure 4.4, the Thévenin equivalent is

$$V_{th} = V_b \frac{R_{sh}}{R_a + R + sh} \tag{4.7}$$

$$R_{th} = \frac{R_{sh}\left(R_b + R_{cr}\right) + R_a\left(R_b + R_{cr} + R_{sh}\right)}{R_a + R_{sh}} \tag{4.8}$$

$$R_{th}\big|_{R_a = R_{sh}} = \frac{R_{sh}}{2} + R_b + R_{cr} \tag{4.9}$$

and the power dissipated in the constriction P_{APC} is

$$P_{APC} = \left(V_{th} \frac{R_{APC}}{R_{APC} + R_{th}}\right)^2 \frac{1}{R_{APC}} \tag{4.10}$$

The power P_{APC} is plotted in figure 4.5a versus the constriction resistance R_{APC}. Electromigration will be controllable when the power dissipated in the constriction P_{APC} decreases as the constriction resistance R_{APC} increases, that is, when $R_{APC} > R_{th}$ given a constant V_{th} and R_{th}.

Achieving the goal of $R_{APC} > R_{th}$ at all constriction resistances requires careful fabrication of the initial constriction so that the constriction resistance R_{APC} prior

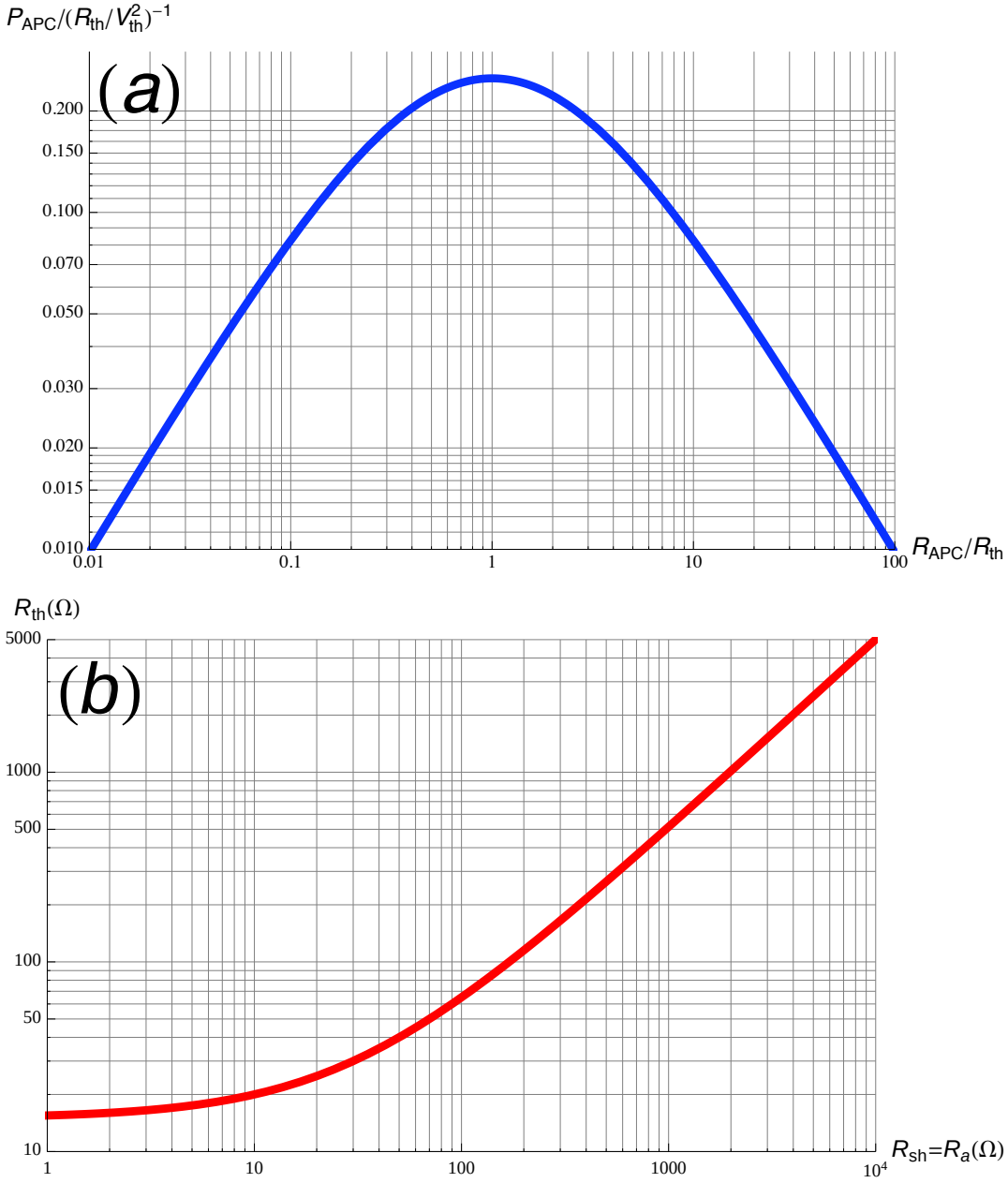

Figure 4.5: Analysis of Thévenin equivalent circuit. (a) power dissipated in the constriction P_{APC} versus the constriction resistance R_{APC}, where both values are normalized based on the Thévenin equivalent circuit. For constant bias conditions, the power at the constriction will decrease as the constriction resistance increases if $R_{APC} > R_{th}$. (b) The Thévenin resistance R_{th} as a function of the shunt resistor R_{sh}, where $R_a = R_{sh}$ and $R_b + R_{cr} = 15\ \Omega$. The device fabrication should ensure that before electromigration $R_b + R_{cr} < R_{APC}$ and then the shunt resistor R_{sh} can be chosen so that $R_{th} < R_{APC}$.

to electromigration is larger than the typical impedance in the cryostat $R_b + R_{cr} = 15\ \Omega$. The Thévenin resistance R_{th} is plotted in figure 4.5b as a function of R_{sh}, where $R_a = R_{sh}$ and $R_b + R_{cr} = 15\ \Omega$. At large constriction resistances $R_{APC} > 100\ \Omega$, it is possible to choose a shunt resistor $R_{sh} > 2R_{APC}$ so that $R_{APC} > R_{th}$ as desired. At small constriction resistances R_{th} is dominated by $R_{cr} + R_b$. To ensure that the power at the constriction decrease with increasing R_{APC} it is necessary that the initial fabrication of the constriction results in a constriction resistance $R_{APC} > R_{cr} + R_b$. While having $R_{th} > R_{APC}$ is sufficient to ensure that the power at the APC does not increase during electromigration (figure 4.5a), electromigration is more often successful when $R_{th} > 2R_{APC}$ and the power at the APC decreases significantly with increasing R_{APC}.

Although in some nanoscale structures an APC (with $R_{APC} < 1\ \mathrm{M}\Omega$) can be created just by ramping a stiff voltage bias [41, 169, 174], I have found that it is also necessary to implement a feedback loop (as in references [171,172,175–177]) that lowers the applied voltage bias in order to slow the rate of resistance change. Because there are multiple detailed descriptions of this type of feedback control in the literature, I am only going to describe the basic procedure.

Electromigration is initiated by slowly increasing the voltage bias V_b while continuously monitoring the resistance of the APC. Increasing the voltage bias heats the system which initially causes the measured resistance to change in a reversible way because the resistivity of the constriction material is temperature dependent. Eventually the measured resistance will begin to change irreversibly while the voltage bias is held constant; this usually occurs when a few microamps of current flow through the APC. At this point, a feedback loop modifies the voltage bias to keep the rate of fractional resistance change $dR_{APC}/R_{APC}dt$ constant. This procedure works well up to a constriction resistance $R_{APC} \approx 1\ \mathrm{k}\Omega$.

When $R_{APC} \approx 1\ \mathrm{k}\Omega$, the constriction resistance begins to change in discrete,

uncontrolled steps (see section 4.1.1, references [8,169,171,172]). This is not a surprise; the constriction has gone from the continuum limit where the resistance is due to many atoms to the atomic scale where there are only a couple of atoms contributing to the resistance. The rearrangment of these atoms then leads to discrete changes in the resistance. In a successfully electromigrated junction, the resistance jumps from the kΩ regime to a resistance less than 1 MΩ, but in an unsuccessful electromigration the resistance jumps to completely open (> 10 GΩ). An example of the resistance evolution during a successful electromigration procedure is given in figure 4.6.

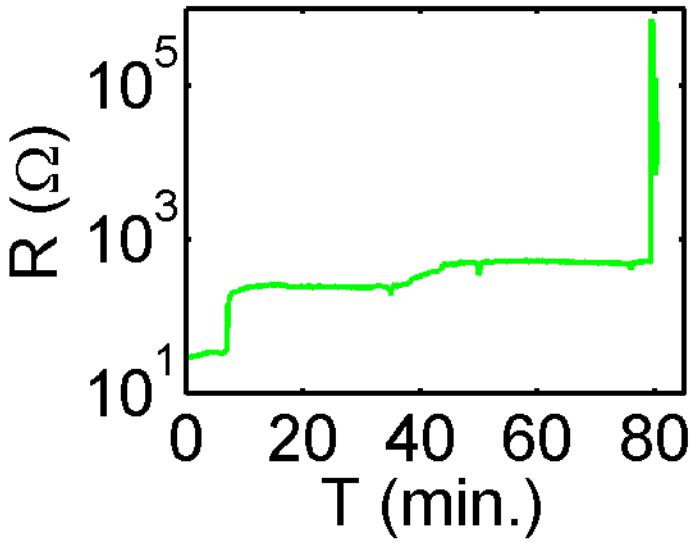

Figure 4.6: Resistance as a function of time during a successful electromigration. The change in resistance at about 5 min is successfully controlled using a feedback loop, after which the contact is composed of less than 100 atoms. After this point, the resistance changes in steps due to atomic rearrangement until an uncontrolled adjustment results in an atomic point contact with 23 kΩ $< R_{APC} <$ 100 kΩ.

4.1.5 Electromigration failures and frustrations

Electromigration has multiple failure modes, the most spectacular of which is when the nanomechanical beam melts (figure 4.7). As mentioned earlier, this usually

occurs when the resistance of the APC is not large enough compared to the resistance of the beam. The points of the nanomechanical beam farthest from the cold reservoir provided by the supports (labeled A and B in figure 4.7) will melt if a large enough current is passed through the beam. This occurs when the constriction at the desired APC location (labeled C in figure 4.7) is not weak enough and the beam melts (or gets hot enough to electromigrate) before the APC location begins to undergo electromigration. This problem has a simple solution: better fabrication resulting in a smaller constriction at the desired APC location.

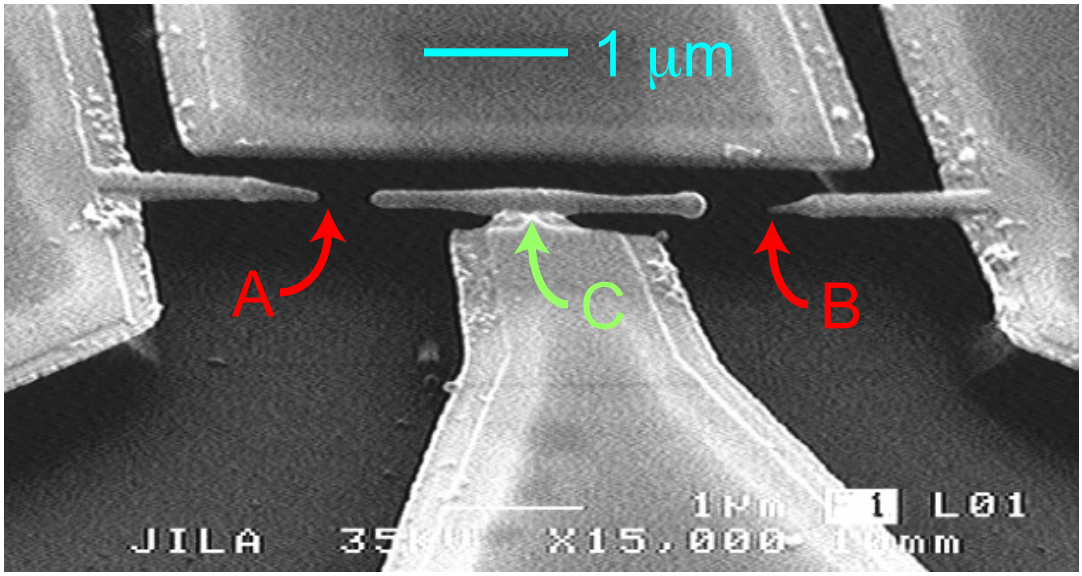

Figure 4.7: Scanning electron micrograph of device after failed electromigration. In this case, the current through the beam was enough to melt the beam at points A and B before the current was large enough to electromigrate the constriction at point C.

Another failure mode is when electromigration begins at the appropriate location, but as the electromigration progresses the resistance jumps from a resistance less than 1 kΩ to completely open (> 10 GΩ). In some of these cases there is a gap at the desired location of the APC which is noticeable in the SEM (figure 4.8), but in general it is difficult to determine the reason for electromigration failure. One possible explanation

is that the third constraint in section 4.1.2 is not satisfied. The nanomechanical beam could separate from the APC electrode in order to relieve stress which could result in a large gap. Another possible explanation is that the temperature near the constriction becomes larger than the melting point of gold, resulting in a large scale motion of atoms and a large gap. This would usually happen either because the APC location is not sufficiently in the limit of a voltage bias resulting in increasing power dissipation as the APC resistance increases or because the power dissipated at the constriction melted the thin, suspended gold at a lower current density than would have been needed to start electromigration.

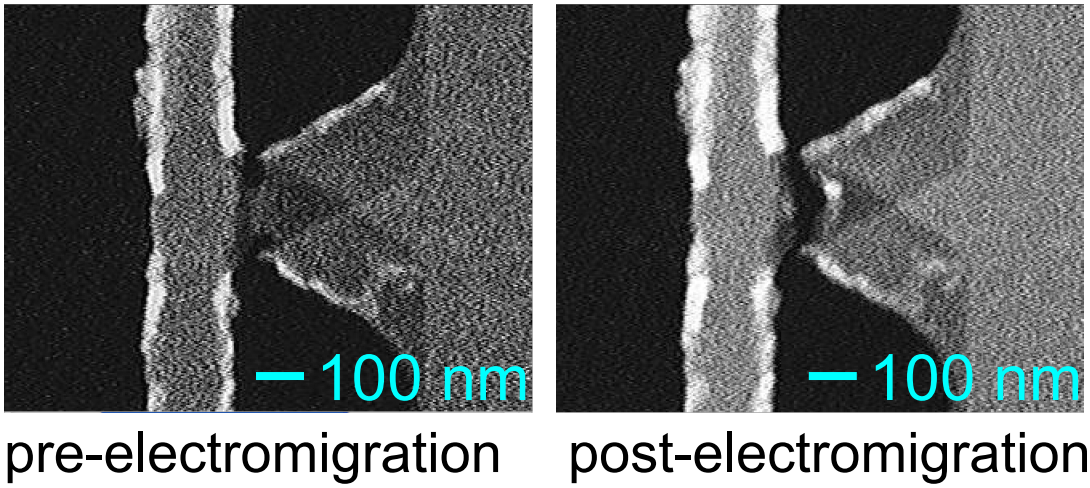

Figure 4.8: Unsuccessful electromigration. (a) Scanning electron micrograph of the constriction prior to electromigration. (b) Scanning electron micrograph of the constriction after electromigration. While the initial device appears promising, the gap created by electromigration is greater than 20 nm and therefore the device is useless.

At the end of the previous subsection I mentioned the final way in which electromigration fails: electromigration proceeds in a promising fashion up to about 1 kΩ, but then jumps to completely open. One possible explanations for this failure is that the final adjustment of the position of the final couple of atoms could randomly results in a very large gap. A second explanation is that, as described in the previous para-

graph and section 4.1.2, there could still be a small residual stress at the APC when the constriction cools down (due to the lower power dissipated at higher resistances) which results in a large final gap. In general, I do not have a method for imaging the final atom configuration and therefore it is not possible to confirm any of these hypothesis. Unfortunately this failure of electromigration is irreversible; once there is a large gap resulting in a > 10 GΩ APC resistance, the device is useless.

A final frustration with electromigration is the possibility of contaminants becoming integrated into the atomic point contact. This contamination will change the barrier through which electrons tunnel when crossing the APC and can also effect the APC's mechanical properties [8, 178–181]. While the contaminants can have a positive effect on the mechanical stability of the APC, the changes in the barrier often result in a decrease in the barrier height [178,179,182] and thus decrease the sensitivity of the APC to nanomechanical motion (see chapter 3). Since the actual electromigration occurs in the ultrahigh vacuum provided by a vacuum space surrounded by 4 K liquid helium, there are two main sources of contaminants: residual contamination from fabrication and contamination by the helium exchange gas (used to cool the cryogenic system to 4 K) which has condensed on the entire surface of the chip. While it is hoped that the temperature during electromigration will cause contaminates to evaporate, a better way of dealing with possible contaminates would be to use the STM tip-cleaning procedure of pressing together the two sides of the APC and then retracting multiple times to remove contaminants and form a clean APC.

This list of frustrations and failures leads to the main problem with electromigration: it is not possible to reliably control the size of the gap. The initial atomic point contact creation requires careful device design and fabrication; even then it is unreliable. After the initial creation it is not possible to control the APC resistance. At best, an uncontrollable change to an almost always larger resistance can be achieved by applying a large voltage across the atomic point contact. Unfortunately, this procedure

often results in a completely open APC. It is also impossible to recreate the APC. In scanning tunneling microscopes a common method of cleaning the tip is to press the tip into the substrate, creating a low resistance contact, and then pulling away from the surface resulting in a tip composed of a new set of atoms. This control of the atomic separation is not possible when the APC is created using electromigration. Therefore the technique of electromigration allows the study of a single atomic point contact with a unique resistance and configuration coupled to a unique nanomechanical system (assuming that electromigration is successful). Being able to change the resistance and configuration of the APC, as well as to measure the motion a single nanomechanical system with multiple different APCs, would facilitate the study of the effect of the APC on the nanomechanical system and make it possible to optimize the APC displacement measurement.

4.2 APC Creation Using a Mechanically Controllable Break Junction

4.2.1 Mechanically controllable break junctions

In fact, there is a widely used technique for creating an atomic point contact with an adjustable gap size: the mechanically controllable break junction (MCBJ) [8, 44, 47, 48, 183, 184]. MCBJs have been used to study both how a metal constrictions transitions from containing many atoms, where the discreteness of atoms can be ignored, to containing only a small number of atoms and the electrical and mechanical properties of these junctions (reference [8] summarizes these studies). MCBJs composed of two atoms have also been used to electrically contact single molecules (for example, [51, 53, 57]).

A constriction in a section of material goes through three distinct phases under strain. First, the constriction stretches until it fractures creating a MCBJ; usually a

5% strain is sufficient to fracture a metal constriction. Second, this MCBJ stretches until eventually the narrowest part of the MCBJ is composed of only a small number of atoms. Finally, under additional strain the atoms in the MCBJ will rearrange creating an atomic point contact (APC) where the electrical contact through the constriction is due to tunneling between two atoms. In this way, a MCBJ can be used to create an APC and the width of the tunneling gap can be controlled by changing the strain on the constriction.

Using a two-stage design, it is possible to both apply a large enough strain to fracture a metal constriction and minimize the effect of mechanical vibrations or noise on the MCBJ. In the first stage, a strain is applied to the top surface of a chip by pushing on the back surface of the chip with a plunger (figure 4.9a). Mechanical noise couples to the MCBJ by vibrating the plunger, but the displacement at the MCBJ is less than 10^{-3} times the motion of the plunger. Thus the MCBJ is partially protected from mechanical noise. In the second stage, the strain from the first stage is concentrated at a constriction suspended above the top surface of the chip (figure 4.9b). This concentration has two effects: it determines the location of the MCBJ (if the strain was constant, then the metal would fracture at an unknown location) and more importantly makes it possible to fracture metal using a chip that is compatible with nano-lithography.

Given this basic description of a two-stage MCBJ apparatus, it is possible to make a more quantitative description of the strain applied by the first stage based on the typical bending structure in figure 4.9a. A chip with some thickness t is supported on two sides (brown supports in figure 4.9a) and then the chip is bent using a moveable plunger (in green in figure 4.9). The movement of the plunger displaces the middle of the chip by an amount u. If the two supports are separated by a distance L, then the strain $\delta D/D$ (that is, a length D is stretched to a length $D + \delta D$) on the top surface of

the chip (the surface not touched by the plunger) is

$$\frac{\delta D}{D} = \frac{3ut}{L^2} \tag{4.11}$$

assuming the ideal case of homogenous strain [8, 46, 183].

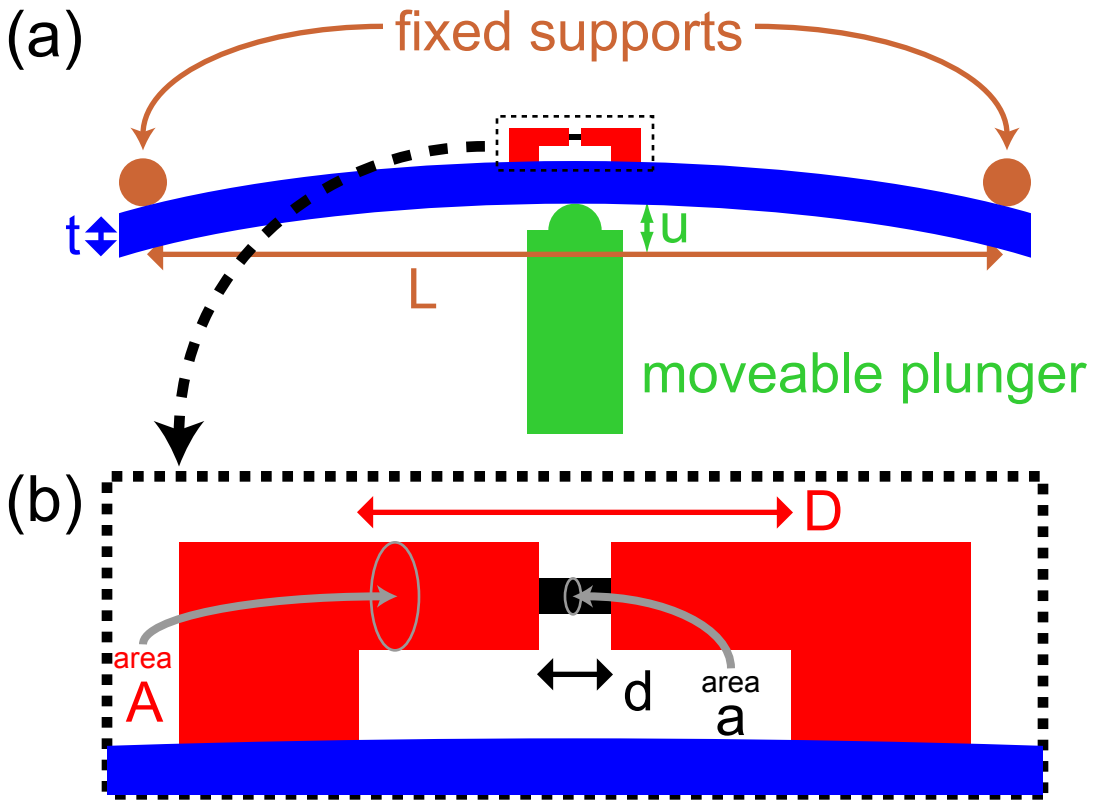

Figure 4.9: Basic setup used to create a mechanically controllable break junction. (a) The chip, in blue with a thickness t, rests on two fixed supports (brown) which are separated by L. A moveable plunger displaces the center of the chip by an amount u, straining the top surface of the chip. (b) A device is fabricated on the top surface of the chip which concentrates the strain at a constriction. The constriction has a length d and cross-sectional area a. It is suspended above the top surface of the chip by a structure with cross-sectional area A; the suspended structure has a total length D along the strained direction.

The concentration of strain due to the second stage of a MCBJ apparatus and thus the total strain at the constriction can be calculated from the typical structure in figure 4.9b. A constriction of length d and cross-sectional area a is suspended above the substrate by a larger structure of total length D and cross-sectional area A. When

the substrate is strained, then the supports will separate by an amount δl, as described by equation 4.11, however the strain will not be constant throughout the suspended structure. Instead, the mechanically weak constriction will experience a strain that is larger by a factor ϵ [44].

The simplest way to calculate ϵ is to treat the system as two springs in series, where the constriction is the softer spring with relaxed length d and spring constant $k = Ea/d$ (E is the elastic constant of the material) and the constriction's support structure is the stiffer spring with a relaxed length $D - d$ and spring constant $K = EA/(D - d)$. Stretching the two springs by a total amount δD will stretch the constriction spring by an amount δd

$$\delta d = \delta D \frac{K}{k + K} \tag{4.12}$$

and therefore the strain in the constriction is

$$\frac{\delta d}{d} = \frac{\delta D}{d + (D - d)(a/A)} = \frac{3ut}{L^2} \frac{D}{d + (D - d)(a/A)} \tag{4.13}$$

and the strain concentration $\epsilon = (\delta d/d)/(\delta D/D)$ is therefore

$$\epsilon = \frac{D}{d + (D - d)(a/A)} \tag{4.14}$$

The design of the MCBJ bending structure and on-chip device is determined by equation 4.13 and the main requirement of applying a strain $\delta d/d > 0.05$ plus the secondary desire to isolate the MCBJ from mechanical noise and vibrations. In general, the maximum amount of deflection $u = u_{max}$ that can be applied is limited either for semiconductor substrates by the substrate shattering or for metallic substrates by bending the substrate past the point where the strain is homogenous. While this limit on metallic substrates is actually a limit on the applicability of equation 4.11 and 4.13, it is preferable to stay close to this limit because otherwise the strain becomes very dependent upon the way in which the chip is supported and the location of the device on the chip. This dependence makes $\delta d/d$ both difficult to calculate and a nonlinear

function of u. Mechanical noise will couple to the MCBJ by vibrating the plunger and making u a noisy variable. In order to minimize the effect of noisy plunger vibrations on the MCBJ strain, the dependence of $\delta d/d$ on u should be minimized by making $\alpha = (3t/L^2)D/(d+(D-D)(a/A))$ as small as possible. This is a secondary goal, but it implies that α should be designed so that the constriction will fracture at the maximum plunger displacement $u_{max}\alpha \approx 0.05$ which minimizes the effect of noise on the MCBJ. In most MCBJ setups $\alpha < 10^{-3}$ [8, 44].

As the constriction is transformed into an APC using strain, equation 4.13 becomes irrelevant (and inaccurate) and instead the change in the size of the APC gap due to strain becomes important. Equation 4.13 relies on the assumption that the constriction is a continuous cylinder of material; however, this model becomes incorrect as the constriction stretches and fractures under strain. In fact, once the MCBJ is composed of only a small number of atoms then calculating the strain and the effect on the atomic configuration becomes a very complicated problem [8, 185–187]. However, once the junction in the MCBJ is an APC composed of only two atoms with a gap w then the problem becomes much simpler. The two atoms are in a potential well with an effective spring constant that is much weaker than all of the other effective spring constants in the problem, so any additional strain due to the motion of the plunger δu will result in a change in the size of the gap δw with

$$\delta w = \delta D = \frac{3tD}{L^2}\delta u \tag{4.15}$$

This equation for δw can be used in two ways: first to calculate the effect of mechanical noise, and second for calibration purposes. First, as described earlier, most mechanical vibrations effectively couple to the MCBJ through the plunger u. Therefore, when the APC has formed, the mechanical noise will be attenuated by a factor $\alpha' = 3tD/L^2$. Second, equation 4.15 can be used to compare the expected change in resistance due to the change in the tunneling gap $R_{APC}(\delta w) = R_0 \exp[2\delta w/\lambda]$ (see chapter 3) with

the experimentally observed resistance change, either to calibrate α if λ (which is related to the height of the barrier, see chapter 3) is known or to calibrate λ if α is known. While I can measure the dimensions of the bending apparatus, chip, and on-chip structure in order to calculate α and I am interested in measuring λ, the chip is often bent past the point of where the substrate is homogeneously strained and therefore I have not been able to use equation 4.15 to accurately measure λ.

4.2.2 MCBJ bending apparatus in a ^{3}He cryostat

Having given a general description of a MCBJ, I now describe the MCBJ bending apparatus I use to implement the conceptual diagram in figure 4.9a and strain the top of the chip. The main constraint on my experimental realization of figure 4.9a is my desire to create an APC using a MCBJ in the ultralow pressure cryogenic environment provided by a ^{3}He cryostat. The APC's stability and purity both benefit from this low pressure environment. Low temperatures are also needed to detect small forces on the nanomechanical system. The bending apparatus must therefore both be compatible with the physical structure of the cryostat and also must not disrupt the carefully designed thermal isolation in the cryostat.

The need for the bending apparatus to be physically compatible with the cryostat creates three main design constraints. First, and simplest, the chip must fit in the cryostat and therefore the maximum separation L of the supports (figure 4.9a) is determined by the size of the cryostat. I successfully strain a constriction using chips with supports that are about $L = 5$ mm apart and a cryostat with a diameter greater than 5 cm, so the chip fits easily into the cryostat. Second, there should not be any risk of bending or twisting the cryostat while bending the chip. This constraint will be discussed in more detail below, but basically implies that the bending structure should be largely self-contained and not exert a force on any of the physically delicate parts of the cryostat. Finally, the entire bending apparatus must be carefully designed to fit

into the cryostat. Tracy Keep from the JILA shop designed the the MCBJ bending apparatus and machined the parts. He also created the nice 3D CAD drawings used in this thesis.

In order to understand the thermal constraints on the MCBJ bending apparatus it is first necessary to understand the basic operation of the ^{3}He cryostat, shown in figure 4.10. Starting with the coldest part of the cryostat, the base temperature stage (blue stage in figure 4.10) is cooled to about 300 mK by pumping on liquid ^{3}He. However the cooling power of this process is not very large, so the base stage must be thermally isolated from the other temperatures in the system.

The initial step in this thermal isolation is placing the base stage in a vacuum space surrounded by liquid helium (see figure 4.10) which helps thermally isolate the base stage in three different ways. First, it cools the walls of the vacuum can so that any remaining gas in the vacuum space freezes on the 4 K walls creating an ultra-low pressure environment and removing any thermal connection through gas. Second, the cold walls and the use of baffles in the line-of-sight port minimizes the amount of thermal radiation. Finally, the liquid helium bath provides a 4 K heat sink (red stage in figure 4.10) which can be used to cool everything in the vacuum space to 4 K.

The final step is therefore to isolate the base stage from the 4 K liquid helium bath. This is accomplished by attaching the base stage to 4 K using thin-walled stainless steel (black connections in figure 4.10) which has a low thermal conductivity. The total heat load on the base stage is also decreased by interrupting the heat load at an intermediate stage (green stage in figure 4.10) which is cooled to 1 K by pumping on liquid helium.

In order to avoid creating a large heat load on the base stage, the thermal design of the MCBJ bending apparatus should be similar to the thermal design of the entire ^{3}He cryostat. Any radiation from 300 K room temperature should be blocked, and the thermal load from room temperature should be small and should be heat sunk to the 4 K liquid helium bath. As in the basic ^{3}He cryostat, low thermal conductivity

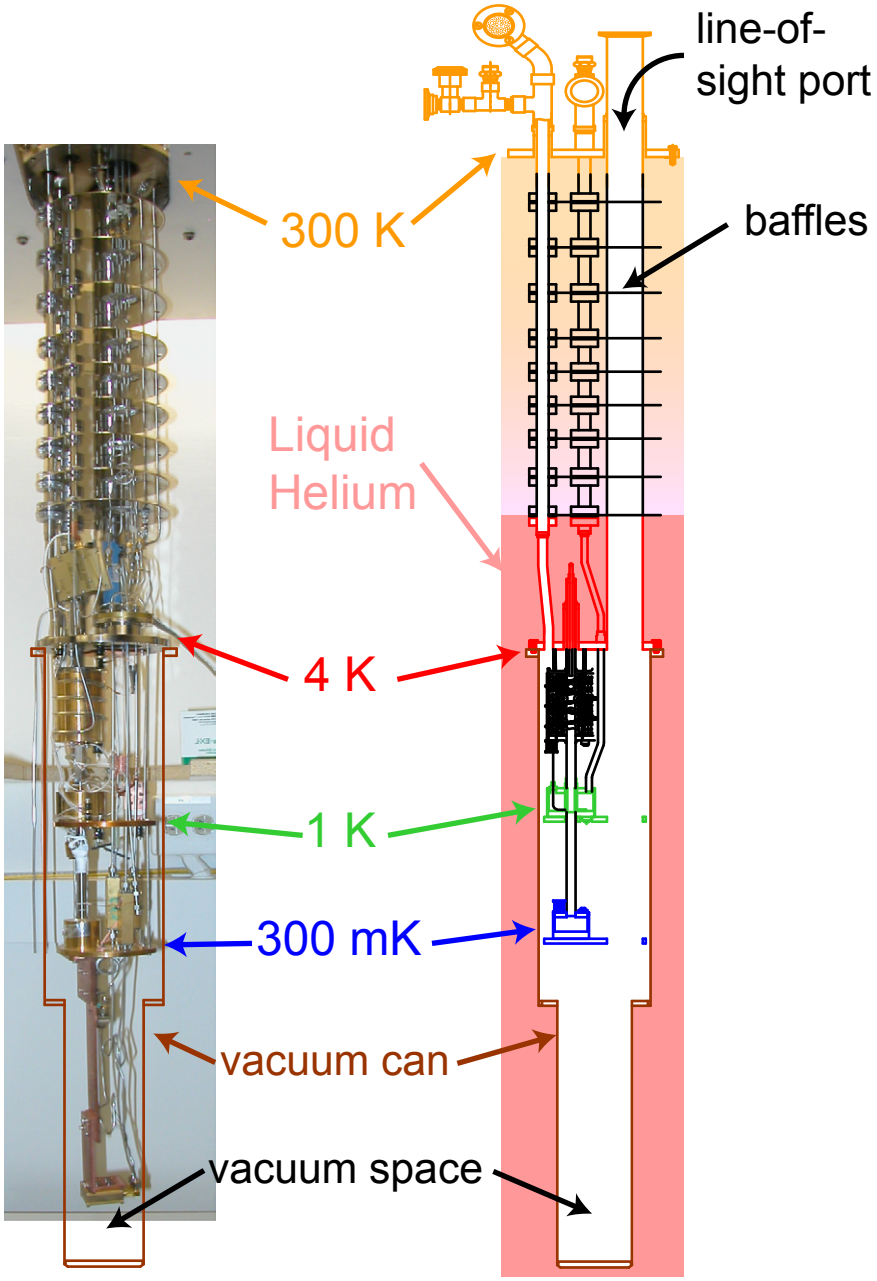

Figure 4.10: ^{3}He cryostat; the actual cryostat is on the left and a diagram is on the right. When the cryostat is in use, the brown vacuum can is surrounded by liquid helium (pink in the diagram) and the inside of the vacuum can is under vacuum (the white area in the diagram). The top of the cryostat (orange) is at room temperature, and the 4 K stage (red) is directly cooled by liquid helium and protected from 300 K radiation through the line of sight port by a set of baffles. Thin-walled stainless steel (black) is used to connect the 4 K stage to the 1 K stage (green) and then the 1 K stage to the 300 mK stage (blue).

structures should then be used to connect the 4 K part of the MCBJ bending apparatus first to a heat sink at 1 K and then from 1 K stage to the base temperature stage thus minimizing the heat load on the base temperature stage.

The MCBJ bending apparatus used in this experiment, which satisfies both the thermal and mechanical constraints described above, is shown in figure 4.11. The basic idea of the bending apparatus is to use a straight rod from the top of the cryostat to turn a screw. The rotation of the screw then coarsely determines the position of a plunger which is used to bend a chip. Fine positioning of the plunger is accomplished using a piezo crystal (see figure 4.12b,c for details).

In order to reduce the thermal conductivity of the straight rod, it is split into three different pieces. The piece between 300 K and 4 K is made out of a low thermal conductivity ceramic rod and is passed through baffles which reduce thermal radiation (figure 4.11). At 4 K, the ceramic rod turns a screw with 100 threads/inch which is attached to the second piece of the straight rod, a thin-wall stainless steel tube (figure 4.12a). The screw passes through a brass piece (figure 4.11 and 4.12a, shown in red) which is anchored to 4 K, thus blocking any remaining thermal radiation and heat sinking the top of the stainless steel tube to 4 K. The stainless steel rod turns the top half of a fork-coupling and the bottom half of the fork coupling is attached to a screw (also 100 threads/inch) which moves the plunger (figure 4.12b, the screw is red). Thermal isolation is provided both by the thin-wall stainless steel tube and by the fork coupling. The fork coupling can be disengaged, thus breaking the thermal connection to 4 K, when the position of the plunger does not need to be coarsely adjusted.

While this long, multi-stage rod does provide thermal isolation, it also results in two types of imperfections in the conversion of rotation at the top of the cryostat into plunger motion at the bottom of the cryostat. The first type of imperfection is backlash, that is, in order to reverse the direction of plunger motion it is first necessary to rotate the knob at the top of the cryostat by about 110° in the reverse direction.

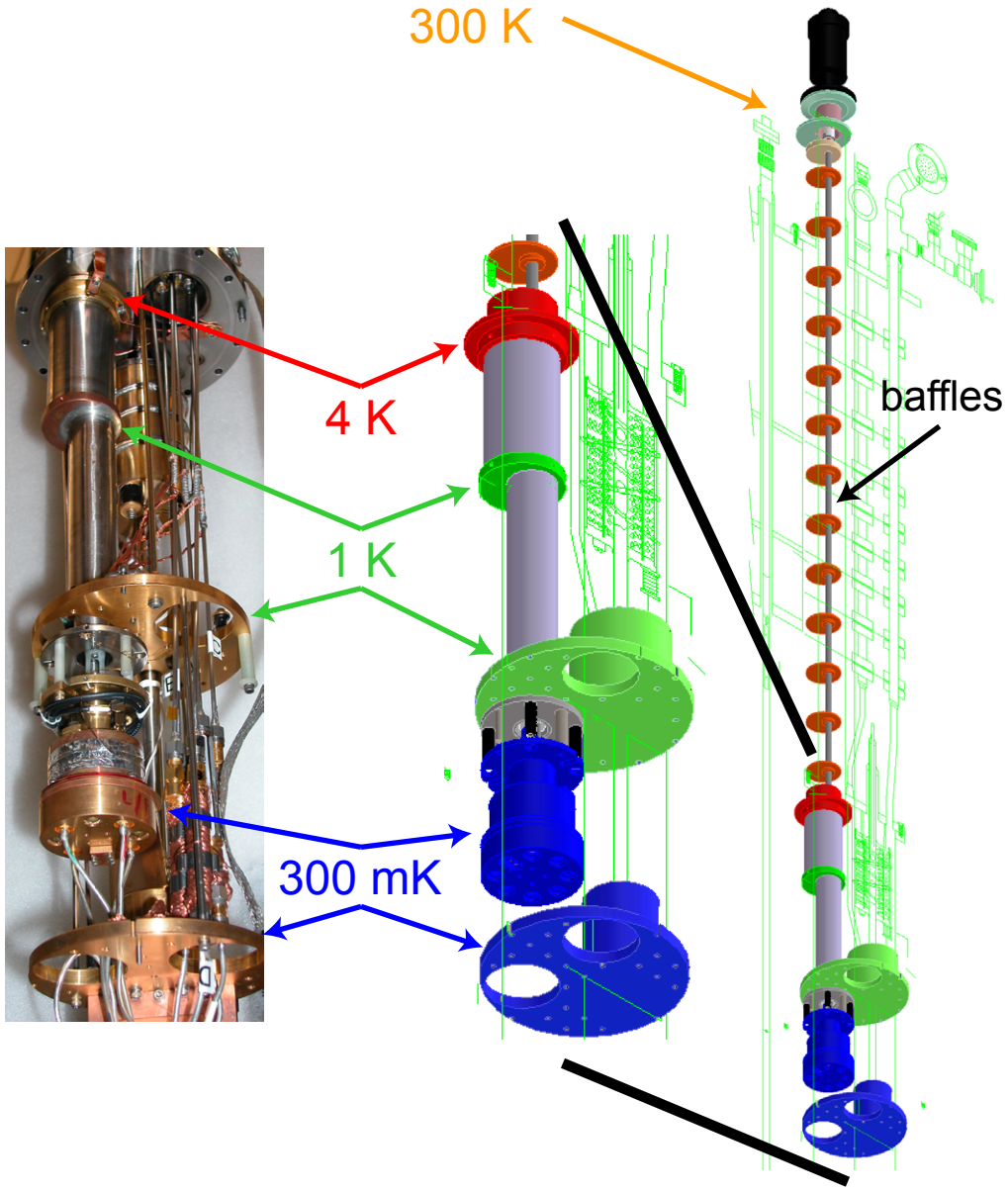

Figure 4.11: ^{3}He cryostat with MCBJ bending apparatus. The diagram on the far right shows the entire apparatus, starting with a vacuum feedthrough at 300 K which connects to a rod that passes through the baffles in the line-of-sight port. The middle diagram and left picture show a close-up of the outside of the MCBJ bending apparatus. Thin stainless steel tubing, in grey, is used to rigidly connect the 4 K brass piece, 1 K copper piece (upper green piece), and the sample holder at 300 mK (blue). The final connection between the stainless steel tubing and the sample holder is made using four thin fiberglass tubes. The 4 K brass piece, 1 K copper piece, and 300 mK sample holder are heat sunk to the appropriate ^{3}He cryostat stages using flexible oxygen-free copper straps, though the 4 K brass piece is also rigidly connected to the ^{3}He cryostat.

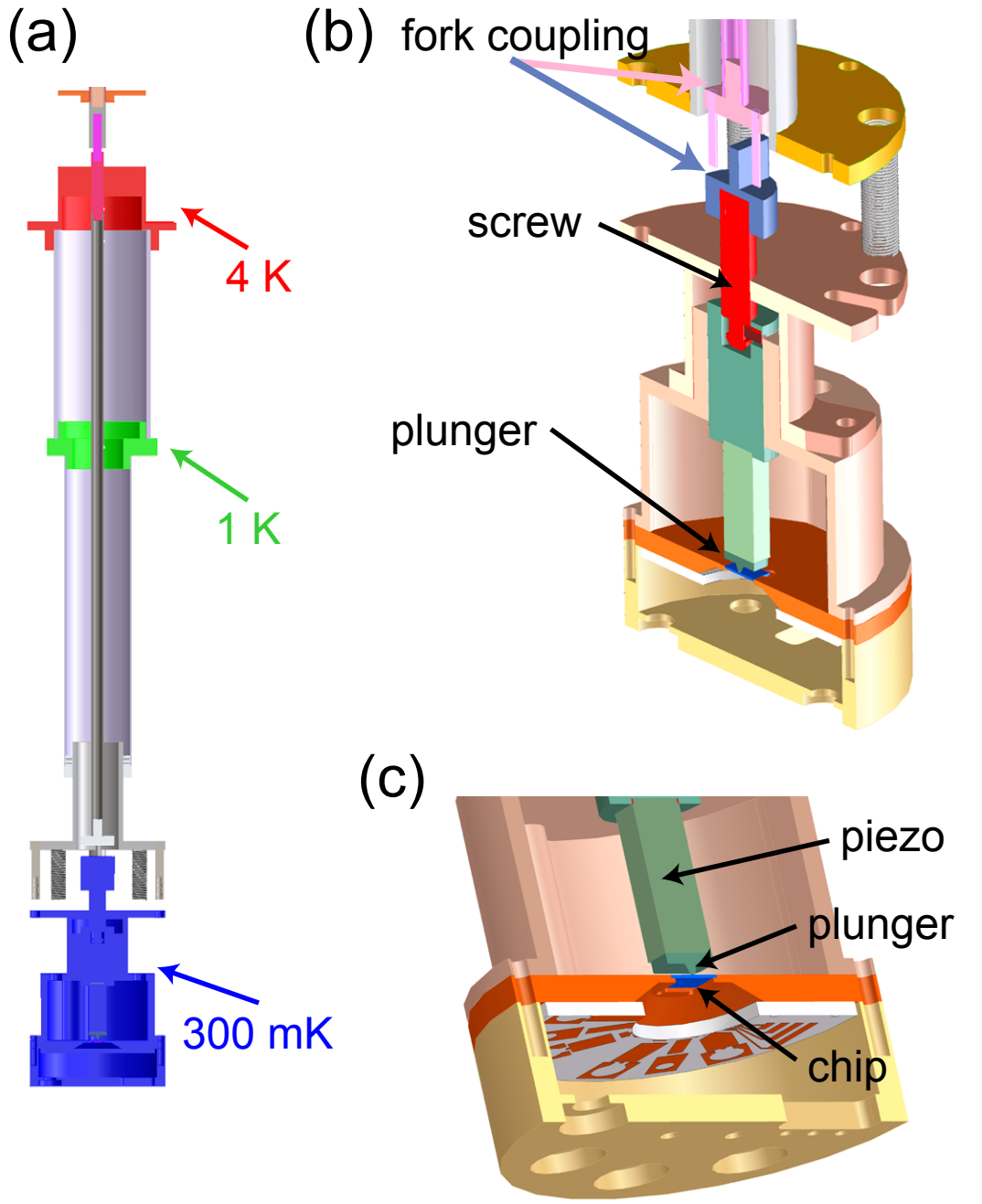

Figure 4.12: Details of MCBJ bending apparatus. (a) cut-away diagram of apparatus from 4 K to base temperature. The heat sunk pieces (4 K in red, 1 K in green, and 300 mK in blue) are connected by thin-wall stainless steel tubing (light grey), while a thin stainless steel rod (dark grey) passes through the center of the support structure and turns the fork coupling. (b) cutaway view of fork coupling (pink and blue) and sample holder. The fork coupling is used to turn a screw (red) and thus coarsely control the plunger (green) position. (c) cut-away view of chip holder (orange) and plunger (green). The piezo crystal is used to finely control the plunger position.

Most of this hysteresis is due to the fork coupling, but some is also due to the torsional spring constant of the other pieces of the multi-stage rod. Since this type of backlash is repeatable, it can be accounted for during operation and does not affect the resolution of plunger motion. However, the static friction in the screws and the torsional compliance of the long multi-stage rod causes the rotation to occur through a stick-slip process which does limit the resolution of plunger motion. In this stick-slip process, rotation at the top of the cryostat does not immediately cause the screw at the bottom of the cryostat to rotate, but instead causes force to build in the system (i.e, the system sticks). When the force is large enough to overcome the static friction, then the screw at the bottom of the cryostat finally rotates (i.e, slips) and this rotation has a minimum step-size. In this system, that minimum step size is about 0.5° or, in terms of plunger motion, $\delta u = 0.1$ mm.

The MCBJ bending structure must be supported in space so that no torque is transfered by the rod to the fragile base stage of the cryostat. The sample is supported by a structure with low thermal conductivity that is rigidly connected to the stiff 4 K stage in the cryostat (red, figure 4.10). At the 4 K stage, a thin-wall stainless steel tube is soldered to the brass piece discussed in the previous paragraph (figure 4.11 and 4.12a). The other end of this stainless steel tube is soldered to a copper block (figure 4.12a, green) which is heat sunk to 1 K . Another thin-wall stainless steel tube is soldered to the other side of the copper block. Finally, the sample holder and the threads for the final screw that is used to adjust the plunger position are attached to this stainless steel tube using two thin fiberglass tubes. The sample holder is then thermally connected to the base stage (blue, figure 4.10) using a flexible, gold-plated, oxygen-free copper plate.

4.2.3 MCBJ device fabrication

I now describe the design and fabrication of the on-chip nanomechanical structure I use to concentrate strain on a constriction (the experimental realization of figure 4.9b)

thus creating a MCBJ coupled to nanomechanical motion. This design can be split into two pieces. First, designing a nanostructure where the strain $\delta d/d$ at a constriction (see equation 4.13) is enough to fracture the constriction $\delta d/d > 0.05$, creating a MCBJ before the plunger displacement u reaches it's maximum displacement u_{max}. Second, designing a nanostructure so that nanomechanical motion will create a large strain at the MCBJ. Coupling nanomechanical motion and strain at the MCBJ is an important step towards creating a sensitive detector of nanomechanical motion (see chapter 3).

Achieving the first goal of fracturing a constriction to create a MCBJ is dependent upon both the chip material and the nanomechanical structure on the chip's surface. I follow the work of van Ruitenbeek, et. al. [44] and use a chip made out of phosphor bronze with an insulating layer of polyimide spun on the top surface. More specifically, my chips are 5 mm squares of 0.35 mm thick polished phosphor bronze shim stock. Experimentally, these chips can be bent by an amount $u_{max} \approx 0.2$ mm before the strain is no longer homogenous and plastic deformation begins. It is possible to apply a greater strain $u > u_{max}$ without catastrophic consequences because the chip is made of metal; however, as described earlier, the amount of strain varies greatly over the surface of the chip and is no longer described by equation 4.13.

Given the characteristics of the phosphor bronze chip from the previous paragraph and the MCBJ bending apparatus described in the previous subsection, the maximum strain $(\delta D/D)_{max}$ that can be applied to the top surface of the chip is given by equation 4.13. The maximum strain occurs when the plunger has displaced the center of the chip by an amount $u = u_{max} = 0.2$ mm, therefore

$$\left(\frac{\delta D}{D}\right)_{max} = \frac{3u_{max}t}{L^2} = \frac{3(0.2 \text{ mm})(0.35 \text{ mm})}{(5 \text{ mm})^2} = 0.0084 \tag{4.16}$$

and so the maximum strain $(\delta D/D)_{max} = 0.8\%$ on the surface of the chip is less then the 5% strain usually needed to fracture metal.

To fracture a metal trace and create a MCBJ it is necessary to concentrate the

strain on the constriction using a suspended nanostructure as described in subsection 4.2.1 and in figure 4.9b. The actual nanomechanical structure that I use in this experiment is a doubly-clamped nanomechanical beam with a constriction in the middle of the beam (figure 4.13). The structure is made entirely out of gold, the beam is 1 μm long by 100 nm thick by 150 nm wide, and the constriction located in the middle of the beam is about 50 nm long by 20 nm thick by 100 nm wide. These dimensions are used to calculate the factor ϵ by which the strain is concentrated at the constriction using equation 4.14

$$\epsilon = \frac{D}{d + (D - d)(a/A)} = \frac{1\ \mu\text{m}}{50\ \text{nm} + (950\ \text{nm})(7.5)} = 5.7 \tag{4.17}$$

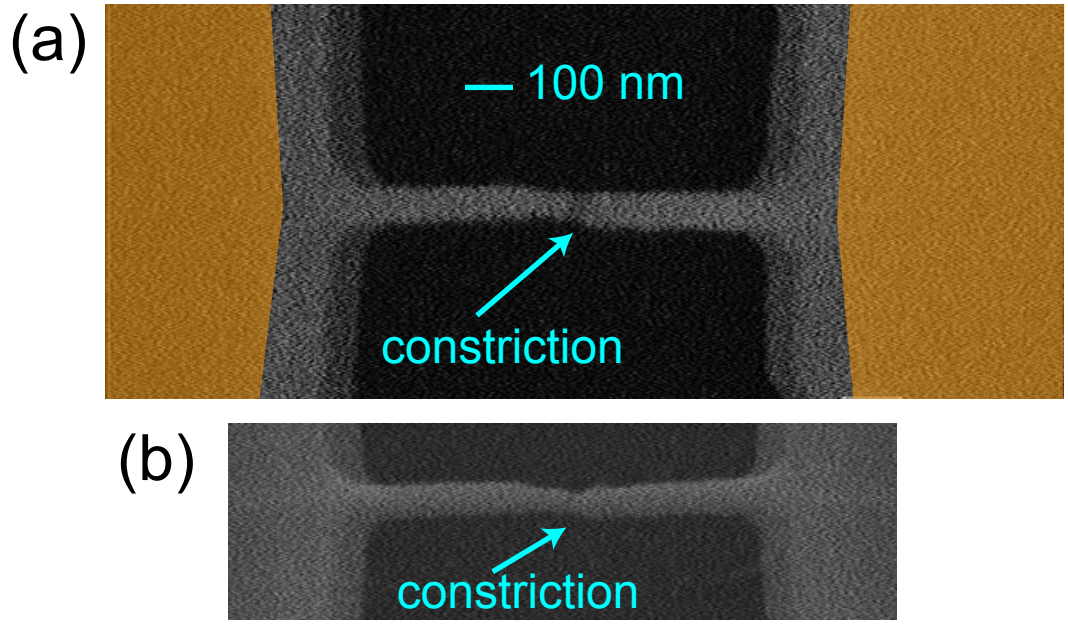

Figure 4.13: Scanning electron micrographs of nanomechanical structure with constriction prior to stretching. In general, the scanning electron beam caused electrical charge to be trapped in the insulating polyimide and made it difficult to image devices. (a) top-down view, the gold which is supported by polyimide is colored orange and the gold structure in white is suspended. The contrast difference between the constriction and the supporting structure is due to the difference in the thickness of the gold. (b) isometric view of the same device, where it is possible to more directly observe the thin constriction.

The constriction in this nanostructure should fracture when the chip is bent by an amount close to, or a little more than, u_{max}.

While the dimensions of the beam and constriction are constrained by the need to fracture the constriction, the location of the constriction can be chosen to maximize the strain created at the MCBJ by nanomechanical motion. I choose to concentrate on the fundamental, lowest frequency, mode of the nanomechanical system which is usually more sensitive to forces than the higher frequency modes. In a simple doubly-clamped beam without a constriction, the strain caused by motion of the fundamental mode is largest at the midpoint of the beam. While the presence of a MCBJ changes the mode shape (see the finite element analysis in chapter 3) and complicates the analysis of the strain, placing the constriction in the middle of the beam is still a good choice.

The fabrication recipe used to create this nanomechanical structure is very similar to the fabrication recipe used to create the nanomechanical structure on GaAs for electromigration, described in subsection 4.1.3 and figure 4.3. The differences in the recipe are due to the chip material; instead of a semiconductor, the MCBJ nanostructure is fabricated on top of an insulating sacrificial layer which is spun on top of the polished phosphor bronze substrate. This sacrificial layer is composed of a 15 μm thick layer of PI-2611 polymide from HD MicroSystems. The polyimide also creates a smooth top surface for nano-fabrication and electrically isolates the nanostructure from the phosphor bronze which is electrically grounded to the cryostat. After the metal nanostructure has been created on the surface of the polyimide using the same basic process as for GaAs electromigration devices, the nanostructure is suspended by etching the polyimide using a simple SF_6 reactive ion etch (for a detailed recipe, see appendix C).

Using a polyimide sacrificial layer does have one negative effect on the fabrication procedure; imaging the devices in the scanning electron microscope (SEM) after processing is difficult and can destroy the device. When imaging the structure on top of the insulating polyimide with a SEM, some of the imaging electrons do not flow to

ground through the insulating polyimide but instead collect on the nanostructure and in the polyimide. The build-up of charge results in poor image quality and can pull the suspended conducting nanostructure to the surface of the chip, breaking the nanostructure at the weak constriction. This problem is reduced by connecting the metal nanostructure to ground during imaging.

In comparison to the work of van Ruitenbeek *et. al.* [44], I make fast measurements of the MCBJ resistance and therefore need to minimize the capacitance between the nanomechanical device and ground (chapter 5 explains why it is important to minimize the capacitance in parallel with the APC). This total capacitance is decreased by minimizing the capacitance between the grounded phosphor bond substrate and the bond pads which are used to electrically contact the MCBJ. The Leiden group of van Ruitenbeek uses a 3 μm thick layer of polyimide to insulate the bondpads and nanomechanical structure from the phosphor bronze substrate. They also electrically connect to the device by using tweezers to press a wire into a macroscopic pellet of indium that was placed on a large, 1 mm by 1 mm bond pad [44]. The combination of large bond pads and a thin insulating layer results in a large stray capacitance $C_s = 3$ pF, which limits the resistance measurement bandwidth (see chapter 5).

In contrast, I use a 15 μm thick layer of polyimide and wirebond to smaller 100 μm by 100 μm bondpads, resulting in a stray capacitance $C_s = 10$ fF which is negligible compared to other sources of stray capacitance. Pressed indium bonds were used by van Ruitenbeek instead of wirebonds because he found the wirebonding process to be very delicate and unreliable [44]. I also found this to be true, however wirebonding was possible by carefully adjusting the wirebonder settings and, more importantly, by using a very thick titanium/gold layer for the bondpads. It is still only possible to make one or two wirebonding attempts before the bondpads separated from the polyimide surface.

4.2.4 Creating an APC using a MCBJ

Using the nanomechanical structure in figure 4.13 and the MCBJ bending apparatus in figure 4.12, I fracture a metal constriction and create a MCBJ. After applying strain and fracturing the metal constriction, it is possible to remove the strain, forcing the two sides of the fracture together and healing the fracture. An example of the hysteretic loop formed by this breaking and then healing cycle is shown in figure 4.14, where the plunger position is manipulated using the piezo (figure 4.12) in the ultra-high vacuum provided by the 4 K cryogenic environment.

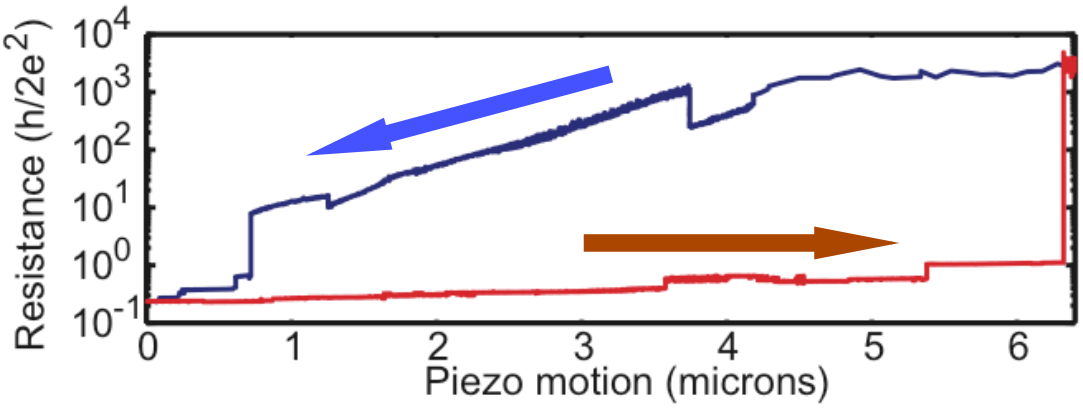

Figure 4.14: MCBJ plunger resistance versus plunger position, where the plunger's position is finely controlled using the piezo crystal. The rearrangement of atoms around the MCBJ causes a hysteretic loop as the strain is applied (red) and then removed (blue).

Looking in more detail at the hysterisis loop, the constriction is initially composed of many atoms and then stretches under strain to a single atom contact, that is, an APC. The constriction stretches under applied strain, the number of atoms at the fracture point decreases, and the resistance increases in a roughly continuous manner. Eventually the discreteness of atoms becomes important and larger jumps are observed as the rearrangement of single atoms causes large fractional changes in the resistance. As this rearrangement continues due to increasing strain, gold atoms have a tendency

to form a chain composed of single atom links [8,151,186,187], which causes the plateau at about 13 kΩ in figure 4.14. The large jump from 13 kΩ then occurs when the chain breaks under increasing strain. At this large resistance ($R \gg 13$ kΩ) the MCBJ is an APC, since electrons flow through the MCBJ by tunneling through the vacuum gap between two atoms. While it is possible to apply additional strain thus increasing the APC gap and increasing the resistance of the APC, in figure 4.14 I begin to remove the strain after breaking the chain of gold atoms. Since the atoms that had been part of the chain have been reincorporated into the sides of the MCBJ [151], the resistance decreases in a hysteric manner as strain is removed until the fracture in the constriction has effectively been healed and the resistance is approximately equal to the original constriction resistance. In general, it is possible to sweep out a hysteretic loop from < 100 Ω to greater than 10 GΩ and back to < 100 Ω. This type of hysteretic loop will be discussed in more detail in chapter 7.

Chapter 5

Electrical measurement of APC Resistance

In this chapter I describe the electrical measurement of the atomic point contact (APC) resistance. The main goal of this measurement is to enable the detection of nanomechanical motion with an imprecision that is limited by the fundamental source of noise in the measurement, the shot noise of tunneling electrons (see chapter 3). This is important, because it is a prerequisite for making a quantum limited measurement of position. I accomplish this goal by using the same microwave matching technique that was used to create the radio-frequency single electron transistor (RF SET, [128]) to make a fast, large bandwidth, measurement of small changes in the APC resistance.

I start by explaining, in general terms, how the precise measurement of a small resistance change is limited by amplifier noise and shot noise. By comparing the effect of the amplifier noise and shot noise, I calculate the voltage V_{APC} across the APC that is required for the shot noise contribution to the measurement noise to be greater than or equal to the contribution from the amplifier noise. Because the APC is only stable at $V_{APC} < V_{APC}^{max} \approx 50$ mV, realistic measurement circuits are, at best, only shot noise limited over a finite bandwidth determined by the frequency dependent noise added by the measurement circuit.

The noise and bandwidth of the resistance measurement can be used to calculate the expected imprecision in the measurement of nanomechanical motion. I consider three similar types of resistance measurements. First, I can make a baseband mea-

surement: I apply a dc voltage across the APC and changes in the resistance R_{APC} at frequency ω creates a voltage signal at frequency ω. Ideally, the noise in a baseband measurement would be dominated by shot noise at the mechanical resonance frequency over a bandwidth that is about an order of magnitude greater than the < 1 MHz width of the mechanical resonance. Second, I can make a double sideband measurement by applying a microwave voltage at frequency ω_b across the APC instead of a dc voltage. Changes in the resistance R_{APC} at frequency ω creates a voltage signal at frequencies $\omega_b \pm \omega$, assuming $\omega_b \gg \omega$. To make a shot-noise limited measurement of both sidebands, the noise in the double sideband measurement would have to be dominated by shot noise at the microwave voltage frequency ω_b over a bandwidth slightly greater than twice the mechanical resonance frequency. Finally, I consider a single sideband measurement which uses the same microwave voltage as the double sideband measurement but only measures the voltage signal of a single sideband at $\omega_b + \omega$ *or* $\omega_b - \omega$. This technique has the advantage that it only requires a shot-noise limited bandwidth that is about an order of magnitude greater than the < 1 MHz width of the mechanical resonance at $\omega_b + \omega$ or $\omega_b - \omega$ and can be used to measure nanomechanical motion at an arbitrary frequency, but has the disadvantage that the displacement imprecision spectral density is twice that of the double sideband measurement. The imprecision of the double sideband measurement is about the same as the imprecision of the baseband measurement.

I then analyze whether two specific amplifier configurations have a large enough bandwidth to detect nanomechanical motion. The first amplifier configuration uses a low-noise high-impedance amplifier. The cable capacitance shorts the amplifier input at high frequencies; thus the measurement noise is only limited by shot noise at frequencies less than 100 kHz. This 100 kHz bandwidth is less than or about equal to the width of a nanomechanical resonance, and therefore is not sufficient for sensitively detecting nanomechanical motion. However, this configuration is useful for measuring the DC

resistance of the APC and performing IV spectroscopy.

The second configuration uses a 500 MHz resonant circuit and a low-noise 50 Ω amplifier, as in the RF SET [128], in order to make a shot-noise limited measurement over a large bandwidth. I also analyze this circuit from a microwave measurement perspective, where the change in APC resistance results in a change in the fraction of the incident microwave voltage bias that is reflected from or transmitted through the resonant circuit. By using a single sideband measurement and appropriately choosing the frequency of either a reflected or transmitted microwave voltage bias, resistances changes at frequencies between dc and greater than 300 MHz can be observed with shot-noise limited precision.

I also show that it is possible to add to the measurement circuit an additional electrical resonance at the < 200 MHz nanomechanical resonance frequency and a corresponding low frequency amplifier. This resonant circuit is used to measure the shot noise at the nanomechanical resonance frequency, which is important for studying the backaction of the APC detector (see chapter 3). However, the relatively large noise of amplifiers available at the nanomechanical resonance frequencies limited the utility of this technique.

The shot noise of the atomic point contact is used to calibrate the microwave measurement circuit. The dependence of the shot noise due to electrons tunneling across the APC on the dc voltage across the APC and device temperature, as described in chapter 3, is used to calibrate the noise temperature and the gain of the microwave electrical measurement. In addition, the shot noise due to a known dc voltage can be compared to the shot noise due to an uncalibrated microwave voltage in order to calibrate the magnitude of the microwave voltage bias across the APC.

5.1 Shot Noise Limit in Idealized APC Displacement Measurement

5.1.1 Noise in an APC resistance measurement

I now describe the basic measurement of small changes in the APC resistance and then calculate the effect of shot noise and amplifier noise on the measurement. The basic measurement circuit is composed of an APC with resistance R_{APC} and amplifier with input impedance R_a; a voltage bias V_b is applied to this series combination (figure 5.1). The voltage at the input of the amplifier V_a and the voltage across the APC resistor V_{APC} are therefore

$$V_{APC} = V_b \frac{R_{APC}}{R_{APC} + R_a} \tag{5.1}$$

$$V_a = V_b \frac{R_a}{R_{APC} + R_a} \tag{5.2}$$

Small changes δR in the resistance of the APC can be detected by measuring

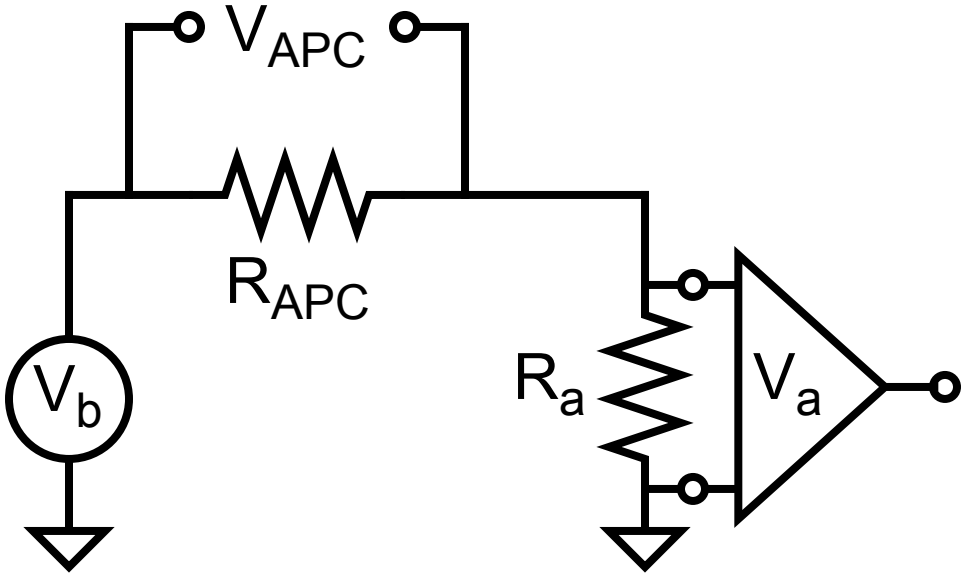

Figure 5.1: Diagram of a simple measurement circuit. V_{APC} is the voltage across R_{APC} due to the voltage bias V_b. $V_a = V_b - V_{APC}$ is the voltage across the amplifier input impedance R_a which will be amplified and measured in order to detect changes in the resistance R_{APC} of the APC.

small changes in the voltage across the amplifier δV_a. Expanding V_a above to first order in δR implies that the signal at the amplifier due to a small change in APC resistance is

$$\delta V_a = -V_b \frac{R_a}{(R_{APC} + R_a)^2} \delta R \tag{5.3}$$

The total measurement noise, that is, the effective noise at the input of the amplifier, is due to both the shot noise of tunneling electrons and the noise of the amplifier. The shot noise is modeled by a voltage noise source in series with the APC (figure 5.2) which has a voltage noise spectral density S_{Vsn}. For relevant APC resistances $R_{APC} > h/2e^2 = 12.9$ kΩ the conduction of electrons through the APC is usually dominated by a single (spin degenerate) conducting channel (see chapter 3) with electron tunneling probability D yielding a resistance $R_{APC} = h/2e^2 D$. In this case, and for low

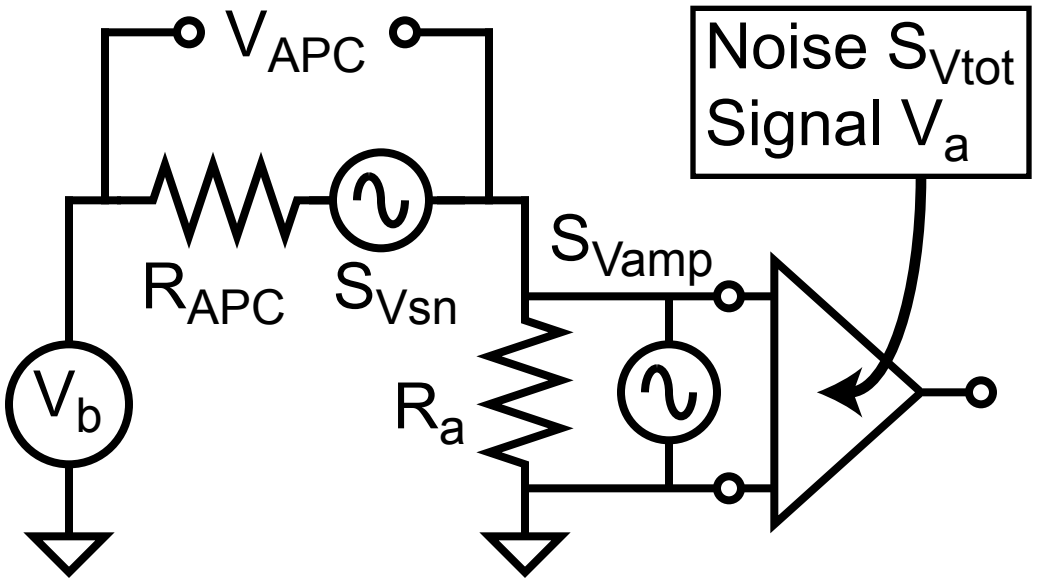

Figure 5.2: Diagram of a simple measurement circuit including the major sources of noise. S_{Vsn} is a noise source due to the shot noise of tunneling electrons. S_{Vamp} is the amplifier noise, which includes the noise of the entire amplifier chain referred back to the input of the amplifier.

temperatures $k_B T \ll eV_{APC}$,

$$S_{Vsn} = 2e|V_{APC}|R_{APC}\zeta\Xi = 2e\zeta\Xi|V_b|\frac{R_{APC}^2}{R_{APC}+R_a} \tag{5.4}$$

where $\Xi = 1 - D$ and $\Xi \to 1$ as $R_{APC} \to \infty$. The constant ζ is unit-less and accounts for the difference between the shot noise created by a dc voltage V_{APC} and the average shot noise created by a peak-to-peak voltage V_{APC} at microwave frequencies. For a dc bias V_b

$$\zeta = \zeta_{dc} = 1 \tag{5.5}$$

and for an ac bias $V_b \cos(\omega_b t)$

$$\zeta = \zeta_{ac} = \frac{\omega_b}{2\pi}\int_0^{2\pi/\omega_b} |\cos(\omega_b t)|\, dt = \frac{2}{\pi} \tag{5.6}$$

These equations for the shot noise are only valid at the experimentally relevant frequencies $\omega \ll k_B T_{cryo}/\hbar$ and $\omega \ll eV_{APC}/\hbar$.

The other major source of noise is the voltage amplifier. The noise added by the amplifier can be modeled by a voltage noise source with spectral density S_{Vamp} in parallel with the input impedance of the amplifier (figure 5.2); the magnitude and frequency dependence of S_{Vamp} is a characteristic of the amplifier. The total noise at the input of the amplifier has a voltage spectral density S_{Vtot}

$$S_{Vtot} = S_{Vsn}\left(\frac{R_a}{R_{APC}+R_a}\right)^2 + S_{Vamp} \tag{5.7}$$

$$S_{Vtot} = 2e\zeta\Xi|V_{APC}|R_{APC}\left(\frac{R_a}{R_{APC}+R_a}\right)^2 + S_{Vamp} \tag{5.8}$$

The final measurement of nanomechanical position, derived from the signal δV_a, is only quantum limited if the noise in the measurement of S_{Vtot} is dominated by the fundamental shot noise due to electrons tunneling through the vacuum gap in the APC instead of the amplifier noise. From equation 5.8, the shot noise contribution dominates

the total noise when

$$2e\zeta\Xi|V_{APC}|R_{APC}\left(\frac{R_a}{R_{APC}+R_a}\right)^2 \geq S_{Vamp} \tag{5.9}$$

$$|V_{APC}| \geq \frac{S_{Vamp}}{2e\zeta\Xi R_{APC}}\left(1+\frac{R_{APC}}{R_a}\right)^2 \tag{5.10}$$

The voltage V_{APC} across the APC required for the shot noise to dominate the measurement noise is minimized by making the amplifier impedance R_a large as possible and the APC resistance R_{APC} equal to the amplifier impedance. This second condition is an impedance matching condition. It ensures that the shot noise power is efficiently coupled into the amplifier.

This analysis of a simple measurement circuit can also be applied to more realistic measurement circuits (figure 5.3). The entire circuit connected to the APC is an effective amplifier with a complex, frequency dependent input impedance $R_a = Z_a(\omega)$ and frequency dependent amplifier noise $S_{Vamp}(\omega)$. This measurement circuit contains a voltage amplifier with an input impedance R'_a and noise S'_{Vamp}. The input impedance $Z_a(\omega)$ is just the impedance of the entire circuit connected to the APC resistance R_{APC} (figure 5.3). If there is a voltage V_a across the effective amplifier input $Z_a(\omega)$, then it is possible to calculate the voltage V'_a across the amplifier in the complex measurement circuit with input impedance R'_a. The effective amplifier noise is then

$$S_{Vamp}(\omega) = S'_{Vamp}\left(\frac{V_a}{V'_a}\right)^2 \tag{5.11}$$

In other words, $S_{Vamp}(\omega)$ is given by the voltage noise of the amplifier S'_{Vamp} referred to the input of the effective amplifier.

Since an APC is only stable when $V_{APC} < V_{APC}^{max} = 50$ mV, equation 5.10 can be used to find the maximum bandwidth of a the amplifier. Rewriting equation 5.10 using the frequency dependent amplifier noise and input impedance,

$$|V_{APC}| \geq \frac{S_{Vamp}(\omega)}{2e\zeta\Xi R_{APC}}\left|1+\frac{R_{APC}}{Z_a(\omega)}\right|^2 \tag{5.12}$$

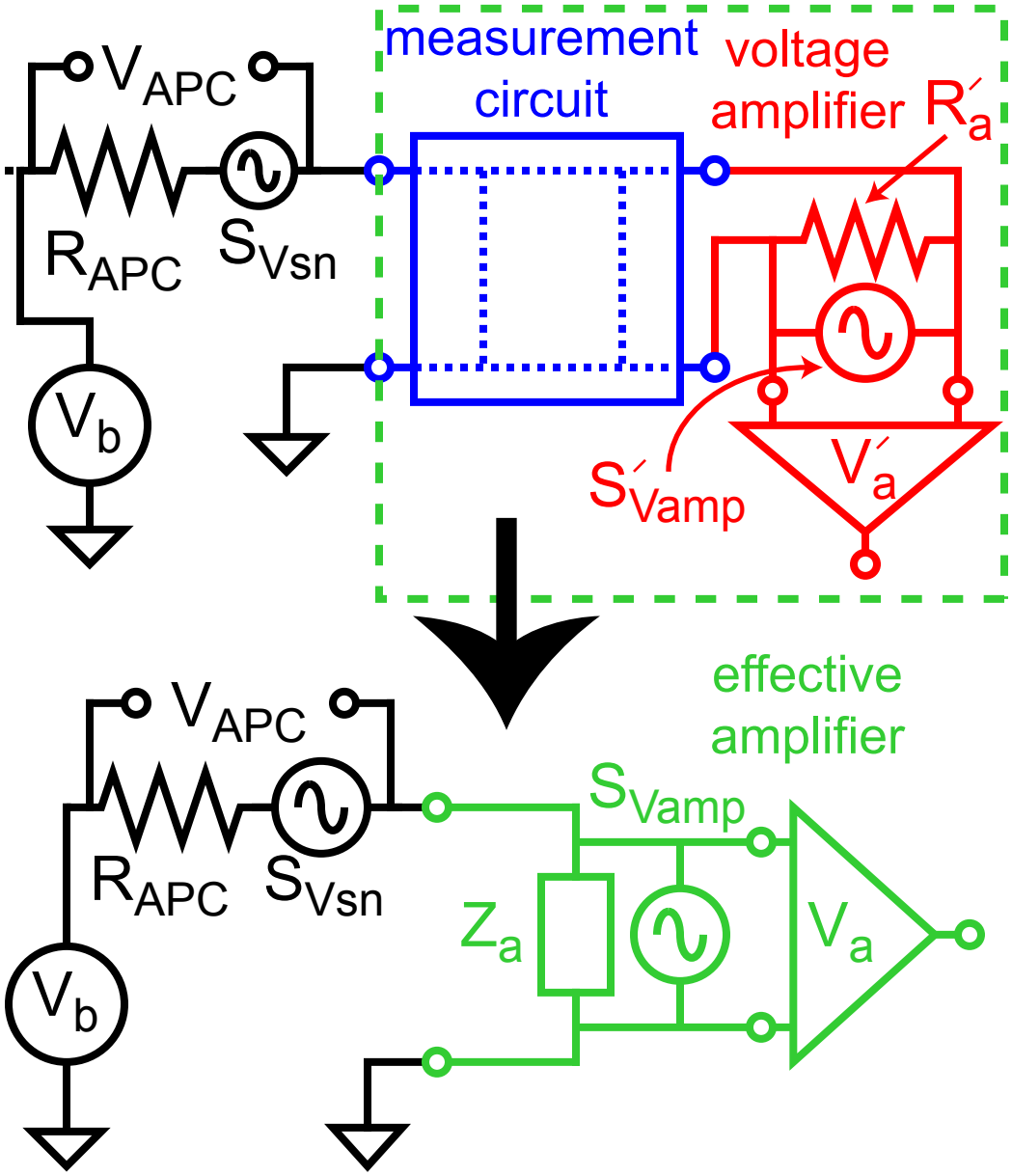

Figure 5.3: For the purpose of determining the noise in a measurement of small resistance changes, a complicated measurement circuit (top, green box) can be treated as a simple effective measurement circuit (bottom, green). A voltage amplifier (red, top) combined with a complex measurement circuit (blue, top) is effectively an amplifier with a different amplifier noise $S_{Vamp}(\omega)$ and a complex input impedance $Z_a(\omega)$ equal to the impedance of the entire complex measurement circuit and amplifier (top, green box).

When this inequality is satisfied, the measurement is in the desired regime where the shot noise dominates the measurement noise. Given a specific measurement configuration with R_{APC}, $S_{Vamp}(\omega)$, and $Z_a(\omega)$, the frequencies at which this inequality is satisfied define a bandwidth and that bandwidth is going to be as large as possible when $V_{APC} = V_{APC}^{max}$. It is also possible that this inequality is never satisfied for a voltage $V_{APC} \leq V_{APC}^{max}$, in which case the measurement noise is always dominated by the noise of the amplifier.

5.1.2 Noise in an APC displacement measurement

Using the relationship between resistance and displacement from chapter 3 and the signal analysis in the previous subsection, it is possible to calculate the expected magnitude and frequency of the voltage signal due to nanomechanical motion and the displacement imprecision due to noise in the voltage measurement. I take the voltage measurement to be dominated by shot noise over a bandwidth γ_{meas} centered at a frequency ω_{meas}. There are three main ways in which I use this voltage measurement to detect nanomechanical motion at frequencies near a nanomechanical resonance frequency ω_m. These three measurement techniques are summarized in table 5.1 and figure 5.4. The first technique is a baseband measurement, where a DC voltage bias V_{APC} is applied across the APC and nanomechanical motion at a frequency ω creates a voltage signal at ω (see figure 5.4a). Using this technique, it is desirable for the nanomechanical resonance to be centered in the measurement band, $\omega_{meas} = \omega_m$. When $\omega_{meas} = \omega_m$, the required measurement bandwidth γ_{meas} is controlled by the width γ_m of the nanomechanical resonance (usually $\gamma_{meas} \geq 10\gamma_m$).

The second type of measurement uses a double sideband technique, where a microwave voltage $V_{APC}\cos(\omega_b t)$ is applied across the APC and nanomechanical motion creates a voltage signal composed of equal sidebands at frequencies $\omega_b \pm \omega_m$ (figure 5.4b). Measuring both sidebands requires a large measurement bandwidth $\gamma_{meas} \approx 2\omega_m$

measurement type	desired measurement bandwidth	measurement frequency
Baseband	$10\gamma_m$, usually 2 MHz	ω_m
Double-Sideband	$2\omega_m$, desire $>$ 100 MHz	ω_b
Single-Sideband larger ($\times\sqrt{2}$) imprecision	$10\gamma_m$, usually 2 MHz	$\omega_b \pm \omega_m$

Table 5.1: Describes the required shot-noise limited bandwidth and measurement frequency for different measurement types. γ_m is the width of the nanomechanical resonance, ω_m is the nanomechanical resonance frequency, and ω_b is the frequency of the applied voltage bias. Since ω_b can be easily varied, the measurement frequency of the double and single sideband measurements can be tuned.

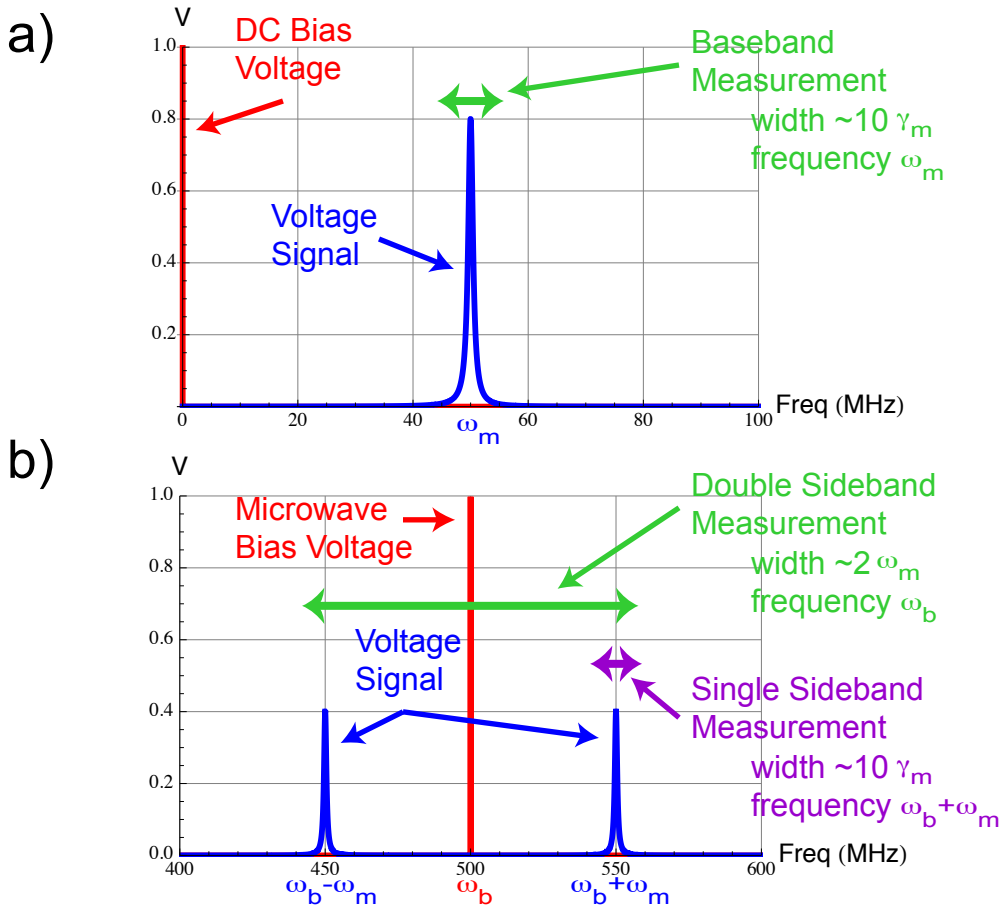

Figure 5.4: (a) baseband measurement (b) double and single sideband measurements

(assuming $\omega_m \gg \gamma_m$) and the bandwidth should be centered at the frequency of the microwave voltage bias $\omega_{meas} = \omega_b$. Since ω_b is easily tuned *in situ*, the frequency of the sidebands can be matched to the frequency of a measurement bandwidth. This is in contrast to the baseband measurement, where the frequency of the measurement bandwidth ω_{meas}, which cannot be tuned *in situ*, must be matched to the frequency of nanomechanical motion ω_m. While it is possible to make a double sideband measurement using a smaller bandwidth when $\omega_{meas} \approx \omega_b < \omega_m$, I am going to analyze and concentrate on the experimentally relevant case where $\omega_{meas} \approx \omega_b \gg \omega_m$.

The third method is a single sideband measurement which is very similar to the double sideband measurement. The same microwave voltage $V_{APC}\cos(\omega_b t)$ is applied across the APC and nanomechanical motion creates voltage sidebands at frequencies $\omega_b \pm \omega_m$. However, in the single sideband measurement, as the name suggests, only a single sideband is measured (figure 5.4b). This technique has the advantage that, in comparison to the double sideband measurement, the needed bandwidth is much smaller $\gamma_{meas} \approx 10\gamma_m$ which is the same as the baseband measurement. The frequency of the measured sideband (either $\omega_b + \omega_m$ or $\omega_b + \omega_m$) can also be tuned to the center frequency of the measurement bandwidth $\omega_{meas} = \omega_b \pm \omega_m$ by changing the frequency of the measurement bias ω_b. This method can therefore be used to detect high frequency nanomechanical motion, limited just by the technical problem of applying a measurement bias at $\omega_b = \omega_{meas} \pm \omega_m$. The disadvantage of of the single sideband measurement is that, since half of the voltage signal is ignored, the displacement imprecision spectral density is twice that of the double sideband measurement.

Having summarized the three different types of measurements (table 5.1), I calculate and compare the voltage signal, noise, and displacement imprecision of the different measurements. The voltage signal due to nanomechanical displacement can be found using the results from chapter 3. A small change δx in the position of the nanomechanical

structure will result in a small change in resistance δR

$$\delta R = \frac{2R_{APC}}{\lambda}\chi\delta x \tag{5.13}$$

where λ is the length scale that controls the probability of electrons tunneling through the APC and χ relates changes in nanomechanical position to changes in the width of the APC gap (see chapter 3). From equation 5.3, the signal at the amplifier is therefore

$$\delta V_a = -\frac{\chi V_b}{\lambda}\frac{2R_{APC}R_a}{(R_{APC}+R_a)^2}\delta x = -\frac{\chi V_{APC}}{\lambda}\frac{2R_a}{R_{APC}+R_a}\delta x \tag{5.14}$$

Both δx and V_{APC} can have a time dependence. Harmonic motion of the nanomechanical oscillator at frequency ω is described as the sum of two quadrature components, $\delta_x(t) = x_1\cos(\omega t) + x_2\sin(\omega t)$.

The baseband measurement uses a dc bias $V_{APC}(t) = V_{dc}$ which does not have a time dependence. The signal at the amplifier using a baseband measurement is therefore

$$\delta V_a^{bb}(t) = V_1^{bb}\cos(\omega t) + V_2^{bb}\sin(\omega t) \tag{5.15}$$

where for $j = \{1, 2\}$

$$V_j^{bb} = -\frac{\chi V_{dc}}{\lambda}\frac{2R_a}{R_{APC}+R_a}x_j \tag{5.16}$$

That is, the nanomechanical motion at frequency ω is going to create a voltage signal at ω.

The double sideband measurement uses a microwave bias $V_{APC}(t) = V_{ac}\cos(\omega_b t)$ and the nanomechanical motion at frequency ω creates a voltage signal at the amplifier at frequencies $\omega_b \pm \omega$

$$\begin{aligned}\delta V_a^{ds}(t) = V_1^{ds}\cos(\omega t + \omega_b t) + V_2^{ds}\sin(\omega t + \omega_b t) + \\ V_1^{ds}\cos(\omega t - \omega_b t) + V_2^{ds}\sin(\omega t - \omega_b t)\end{aligned} \tag{5.17}$$

where for $j = \{1, 2\}$

$$V_j^{ds} = -\frac{\chi V_{ac}}{2\lambda}\frac{2R_a}{R_{APC}+R_a}x_j \tag{5.18}$$

The single side band measurement uses the same microwave bias as the double sideband measurement, but ignores one of the sidebands in equation 5.17. In this case I choose to analyze the measurement of the upper sideband at frequency $\omega_b + \omega$; the analysis of the measurement of the lower sideband is identical. Having chosen the upper sideband, in the single sideband measurement nanomechanical motion at a frequency ω creates a signal at the amplifier at frequency $\omega_b + \omega$

$$\delta V_a^{ss}(t) = V_1^{ss}\cos(\omega t + \omega_b t) + V_2^{ss}\sin(\omega t + \omega_b t) \tag{5.19}$$

where for $j = \{1, 2\}$

$$V_j^{ss} = -\frac{\chi V_{ac}}{2\lambda}\frac{2R_a}{R_{APC} + R_a}x_j \tag{5.20}$$

Even if the mechanical oscillator is stationary, the measured voltage is will fluctuate. This voltage noise will cause a purely apparent fluctuation in the inferred position of the beam, described by a spectral density S_x. As described in subsection 5.1.1, the random voltage noise in the measurement has a spectral density S_{Vtot} due to the shot noise of tunneling electrons and amplifier noise. The noise in a small band $\Delta f \ll \gamma_m/2\pi$ around a voltage signal at frequency ω_V creates uncertainty in the measurement of the voltage signal's quadrature amplitudes V_1 and V_2 with variance (for $j = \{1, 2\}$)

$$\sigma_{V_j}^2 = S_{Vtot}(V_b, \omega_V)\frac{\Delta f}{2} \tag{5.21}$$

where S_{Vtot} is a function of both the voltage bias V_b and frequency of the voltage signal ω_V. The noise in different quadratures and at different frequencies is uncorrelated (see, for example, reference [188]).

For each measurement type, this variance can be used to calculate the variance of the displacement measurement and thus the displacement imprecision spectral density. In the baseband measurement, displacement x_j is related to the voltage V_j^{bb} at frequency ω by equation 5.16, therefore

$$(\sigma_{x_j}^{bb})^2 = \left|\frac{\lambda}{V_{dc}}\frac{R_{APC} + R_a}{2R_a}\right|^2 \sigma_{V_j}^2 = \left|\frac{\lambda}{V_{dc}}\frac{R_{APC} + R_a}{2R_a}\right|^2 S_{Vtot}(V_{dc}, \omega)\frac{\Delta f}{2} \tag{5.22}$$

and the imprecision spectral density S_x^{bb} of the baseband measurement is

$$S_x^{bb}(\omega) = \left| \frac{\lambda}{V_{dc}} \frac{R_{APC} + R_a}{2R_a} \right|^2 S_{Vtot}(V_{dc}, \omega) \tag{5.23}$$

Similarly, in the single sideband measurement the displacement x_j at frequency ω is related to the voltage V_j^{ss} at frequency $\omega_b + \omega$ by equation 5.20, therefore

$$(\sigma_{x_j}^{ss})^2 = \left| \frac{2\lambda}{V_{ac}} \frac{R_{APC} + R_a}{2R_a} \right|^2 \sigma_{V_j}^2 = \left| \frac{2\lambda}{V_{ac}} \frac{R_{APC} + R_a}{2R_a} \right|^2 S_{Vtot}(V_{ac}, \omega_b + \omega) \frac{\Delta f}{2} \tag{5.24}$$

and the imprecision spectral density S_x^{ss} of the measurement of nanomechanical motion at frequency ω using the single sideband technique is

$$S_x^{ss}(\omega) = 4 \left| \frac{\lambda}{V_{ac}} \frac{R_{APC} + R_a}{2R_a} \right|^2 S_{Vtot}(V_{ac}, \omega_b + \omega) \tag{5.25}$$

The double sideband measurement is equivalent to simultaneously making two single-sideband measurements at frequencies $\omega_b + \omega$ and $\omega_b - \omega$ with uncorrelated noise. The variance of this displacement measurement is

$$(\sigma_{x_j}^{ds})^2 = \left| \frac{2\lambda}{V_{ac}} \frac{R_{APC} + R_a}{2R_a} \right|^2 \frac{[S_{Vtot}(V_{ac}, \omega_b - \omega) + S_{Vtot}(V_{ac}, \omega_b + \omega)]}{4} \frac{\Delta f}{2} \tag{5.26}$$

and the imprecision spectral density S_x^{ds} of the double sideband measurement is

$$S_x^{ds}(\omega) = \left| \frac{\lambda}{V_{ac}} \frac{R_{APC} + R_a}{2R_a} \right|^2 [S_{Vtot}(V_{ac}, \omega_b - \omega) + S_{Vtot}(V_{ac}, \omega_b + \omega)] \tag{5.27}$$

While the displacement imprecisions derived above apply to an arbitrary voltage noise spectral density S_{Vtot}, I most interested in the case where the amplifier noise is negligible ($S_{Vamp} \to 0$) and S_{Vtot} is dominated by the fundamental source of noise in the problem, the shot noise of tunneling electrons. In the baseband measurement with $V_{APC}(t) = V_{dc}$, the shot noise creates a fluctuating voltage with a spectral density (see subsection 5.1.1)

$$S_{Vsn}^{bb}(V_{dc}, \omega) = 2e\Xi\zeta_{dc}|V_{dc}|R_{APC} \left(\frac{R_a}{R_{APC} + R_a} \right)^2 \tag{5.28}$$

therefore the shot-noise limited displacement imprecision of the baseband measurement is

$$S_x^{bb}(\omega) = \frac{e\Xi\zeta_{dc}\lambda^2 R_{APC}}{2|V_{dc}|} \tag{5.29}$$

In the sideband measurements with $V_{APC}(t) = V_{ac}\cos(\omega_b t)$, the shot noise creates a fluctuating voltage with a spectral density (see subsection 5.1.1 and chapter 3)

$$S_{Vsn}^{ss}(V_{ac},\omega) = S_{Vsn}^{ds}(V_{ac},\omega) = 2e\Xi\zeta_{ac}|V_{ac}|R_{APC}\left(\frac{R_a}{R_{APC}+R_a}\right)^2 \tag{5.30}$$

Using this voltage noise spectral density, the displacement imprecision spectral density of the double sideband measurement is

$$S_x^{ds}(\omega) = \frac{e\Xi\zeta_{ac}\lambda^2 R_{APC}}{|V_{ac}|} \tag{5.31}$$

and the displacement imprecision spectral density of the single sideband measurement is

$$S_x^{ss}(\omega) = \frac{2e\Xi\zeta_{ac}\lambda^2 R_{APC}}{|V_{ac}|} \tag{5.32}$$

which is twice the imprecision of the double sideband measurement $S_x^{ss} = 2S_x^{ds}$.

The comparison of the baseband imprecision S_x^{bb} and double sideband imprecision S_x^{ds} is complicated by the difference between a dc voltage V_{dc} and microwave voltage $V_{ac}\cos(\omega_b t)$. When comparing noise, the signal and noise from dc voltage V_{dc} is often equated with a microwave voltage that dissipates the same amount of power, that is, $V_{ac} = \sqrt{2}V_{dc}$. This is most applicable if the voltage noise S_V is independent of bias voltage; in this case (not calculated above), S_x^{bb} and S_x^{ds} would be equal when $V_{ac} = \sqrt{2}V_{dc}$. Shot noise S_{Vsn} does depend on the bias voltage; in the shot noise dominated limit S_x^{bb} and S_x^{ds} are equal when $V_{ac} = (\zeta_{dc}/\zeta_{ac})V_{dc} = (\pi/2)V_{dc}$. Therefore if the bias magnitude is limited by a maximum power that can be dissipated in the APC then the smallest imprecision can be achieved using a double sideband measurement. However, if the bias magnitude is limited by a maximum voltage that can be sustained across the

APC then the smallest imprecision can be achieved using the baseband measurement. Experimentally, the maximum voltage or power that can be handled by the APC is not stable enough for the difference in the best imprecision of these two techniques to be relevant.

5.2 Conventional APC Resistance Measurement

I now show that a simple low frequency measurement with a high impedance amplifier has an unacceptably small bandwidth of about 100 kHz starting at 0 Hz. This low frequency measurement can still be used to measure the average and differential resistance R_{APC} of the APC even though the measurement is not fast enough to resolve nanomechanical motion.

5.2.1 Limited bandwidth of a conventional measurement

The simplest way to implement the basic measurement circuit in figure 5.1 is to use a high-impedance amplifier, however the stray capacitance in the physical circuit must also be included (figure 5.5). As desired, The impedance of the amplifier itself R'_a is much larger than the APC resistance, however making the effective amplifier impedance Z_a large over a large range in frequency is actually rather difficult because of the capacitance shunting the amplifier input. Any capacitance between the physical line connecting the APC to the amplifier and the circuit's ground (C_s and C_c in figure 5.5) will shunt the amplifier input. In a cryogenic system this capacitance can be large because the cable between the amplifier and the device results in a capacitance to ground of about 100 pF per meter of cable. Figure 5.5 contains a more realistic circuit diagram including the shunting capacitance to ground on and near the chip C_s and the capacitance to ground of the cable C_c as well as the internal impedance of the voltage amplifier R'_a. The effect of the cable inductance can be ignored because that impedance is much smaller than the internal impedance R'_a of the amplifier. From the circuit in

figure 5.5, the effective amplifier impedance Z_a as a function of frequency is

$$Z_a(\omega) = \frac{R'_a}{1 + i\omega(C_s + C_c)R'_a} \tag{5.33}$$

and taking the ideal case where $R'_a \to \infty$ then

$$Z_a(\omega) = \frac{1}{i\omega(C_s + C_c)} \tag{5.34}$$

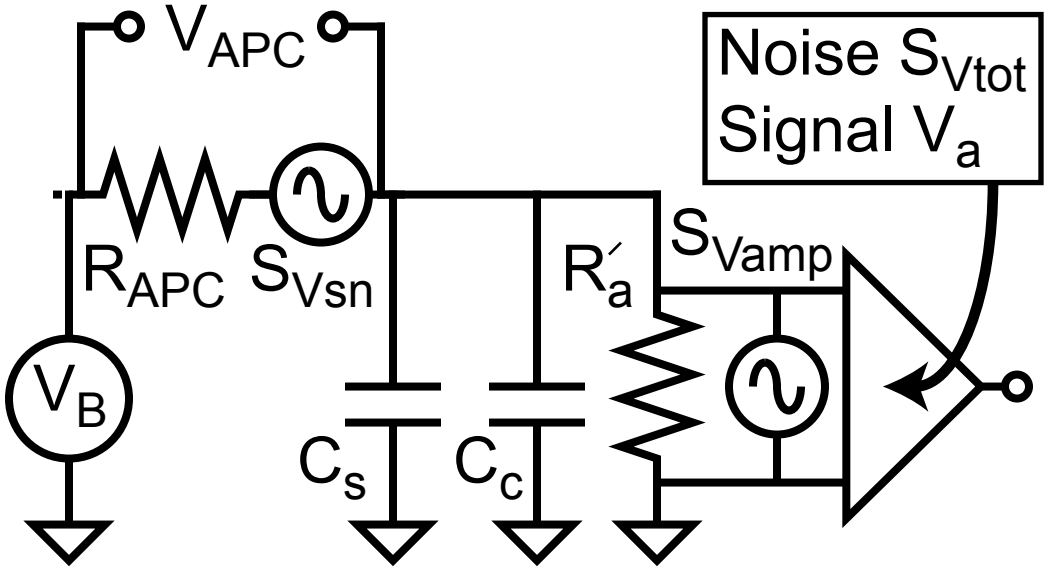

Figure 5.5: Diagram of the measurement circuit using a high-impedance amplifier, including the capacitance to ground C_s from connections near and on the chip and the capacitance to ground C_c due to the cable between the chip and the amplifier at the top of the cryostat .

With this frequency-dependent amplifier input impedance $Z_a(\omega)$, equation 5.12 can be used to calculate the bandwidth over which the noise in this measurement circuit is dominated by shot noise given actual values for the noise $S_{Vamp} = S'_{Vamp}$ of the high-impedance amplifier, the total capacitance $C_s + C_c$, and the APC resistance R_{APC}. From equation 5.12, the measurement noise is dominated by shot noise when

$$|V_{APC}| \geq \frac{S_{Vamp}}{2e\Xi\zeta_{dc}R_{APC}} |1 + i\omega(C_s + C_c)R_{APC}|^2 \tag{5.35}$$

$$\omega \leq \frac{1}{R_{APC}(C_s + C_c)} \sqrt{2e\Xi\zeta_{dc}\frac{R_{APC}|V_{APC}|}{S_{Vamp}} - 1} \tag{5.36}$$

Commercially available high-impedance amplifiers typically have voltage noise spectral densities of about $S_{Vamp} = 10^{-17}$ V^2/Hz, and using conservative assumptions the total capacitance in the system is $C_s + C_c = 200$ pF. Using these values, for voltages such that $|V_{APC}|\Xi R_{APC} > 31$ VΩ there will be a bandwidth where the measurement noise is limited by shot noise. This bandwidth starts at $\omega = 0$ and extends to a maximum frequency given by the equality in equation 5.36. This maximum frequency, which is also the measurement bandwidth, is plotted in figure 5.6 as a function of APC resistance R_{APC} for different APC voltages ranging between $V_{APC} = V_{APC}^{max} = 50$ mV and $V_{APC} = 0.4$ mV.

The bandwidth of this low frequency measurement with a high-impedance amplifier is not large enough to implement a shot-noise limited measurement of nanome-

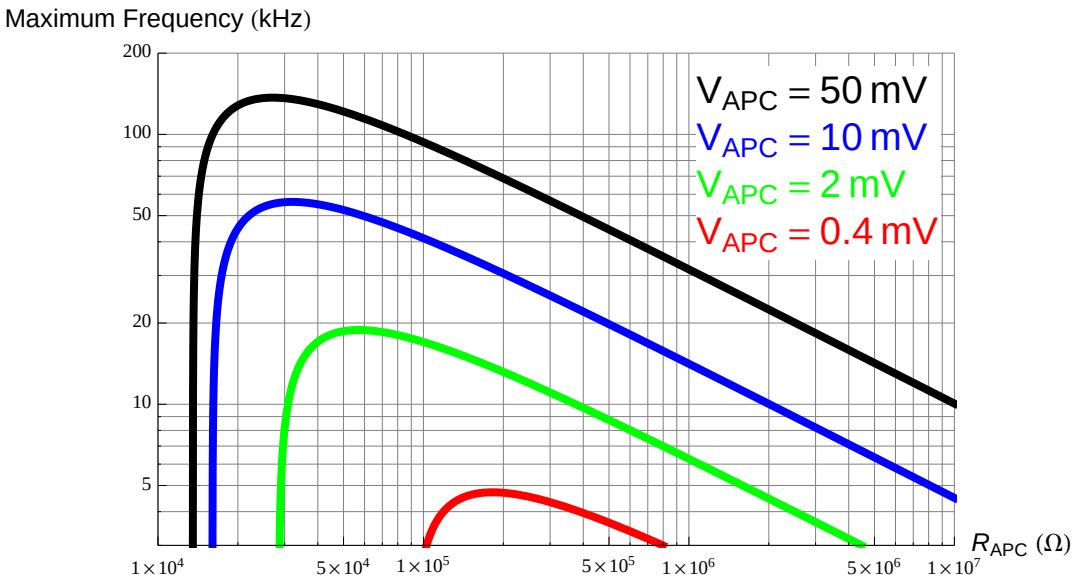

Figure 5.6: In this figure the maximum frequency at which the measurement noise of a low frequency measurement with a high impedance amplifier is dominated by shot noise is plotted as a function of APC resistance R_{APC} for various different APC voltages V_{APC}. I use reasonable values for $S_{Vamp} = 10^{-17}$ V^2/Hz and $C_s + C_c = 200$ pF. The maximum stable APC voltage $V_{APC}^{max} = 50$ mV. The bandwidth of this measurement is between 0 Hz and the maximum frequency plotted in this figure.

chanical motion. All of the measurement schemes in table 5.1 require a bandwidth that is greater than 1 MHz, however the largest bandwidth achieved with this low frequency measurement is less than 150 kHz at an APC resistance $R_{APC} = 25$ kΩ and the largest stable APC voltage $V_{APC}^{max} = 50$ mV (see figure 5.6); at higher frequencies the cable capacitance short circuits the voltage amplifier. A microwave technique must be used to detect nanomechanical motion as described in section 5.3.

5.2.2 Description of low frequency resistance measurement

A low frequency measurement using a high impedance amplifier may not be able to sensitively detect nanomechanical motion, but it can still measure four important quantities: the dc voltage V_{APC} across the APC, the dc current I_{APC} flowing through the APC, the average resistance of the APC $R_{APC}^{avg} = V_{APC}/I_{APC}$, and the differential resistance of the APC $R_{APC} = \partial V_{APC}/\partial I_{APC}$. This measurement uses a circuit (figure 5.7) that has some small differences from the circuit described in the previous section. The biggest difference is the use of a second high impedance amplifier. One amplifier measures the voltage drop V_{APC} across the APC due to a voltage bias V_{LF}; the other amplifier measures the current $I_{APC} = V_R/R_b$ flowing through the APC by measuring the voltage drop V_R across a known resistor R_b. By simultaneously measuring V_{APC} and I_{APC} as a function of bias V_{LF}, I determine the APC current I_{APC}, average resistance R_{APC}^{avg}, and differential resistance R_{APC} as a function of the voltage V_{APC} across the APC. In mesoscopic systems, these electrical characteristics are often summarized by plotting the APC current I_{APC} versus APC voltage V_{APC}; this plot is generally called an I-V curve.

For an ideal resistor the average resistance R_{APC}^{avg} and differential resistance R_{APC} are independent of the voltage bias and $R_{APC}^{avg} = R_{APC}$, however the APC is not an ideal resistor. In particular, the shape of the tunnel barrier under large voltage bias, as described in chapter 3, results in a decrease in resistance at large bias voltages and

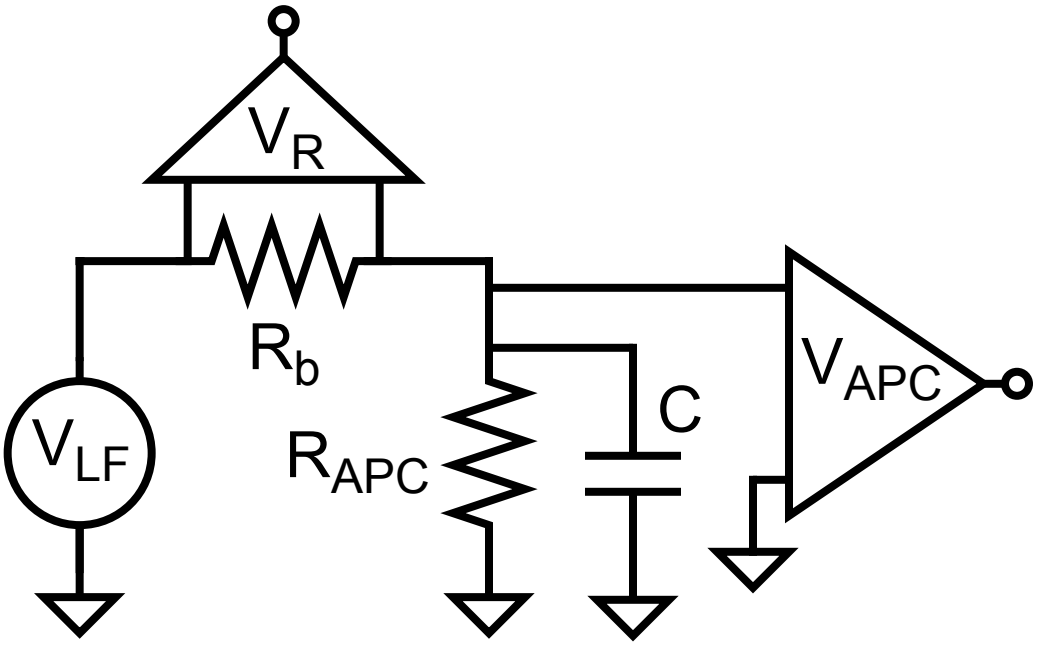

Figure 5.7: Circuit diagram of the low frequency measurement circuit with two high impedance amplifiers that are used to measure the voltage V_{APC} across the APC R_{APC} and the voltage V_R across a known resistor R_b. C is the capacitance to ground in the cryostat, including the cable to the device.

therefore a nonlinear I-V curve. Other mesoscopic effects also create nonlinearities in I-V curve of an APC. The use of an I-V curve and the differential resistance R_{APC} as a function of V_{APC} (or I_{APC}) to understand the characteristics of the APC is called IV or tunneling spectroscopy (see chapter 2, 3, and 7 for more details).

In order to measure the average resistance R_{APC}^{avg} and differential resistance R_{APC}, I apply a small square wave voltage bias V_{LF} with a mean value V_0 and a peak-to-peak voltage V_1 at a frequency between 5 Hz and 100 Hz. I usually choose the frequency so that the the shunting capacitance (C, figure 5.7), which smoothes the square wave transition, can be ignored. I use the amplifiers (figure 5.7) to measure the average voltages at the top of the square wave $\langle V_{APC}^T \rangle$ and $\langle V_R^T \rangle$ as well as the average voltages at the bottom of the square wave $\langle V_{APC}^B \rangle$ and $\langle V_R^B \rangle$ (see figure 5.8). Using these measured

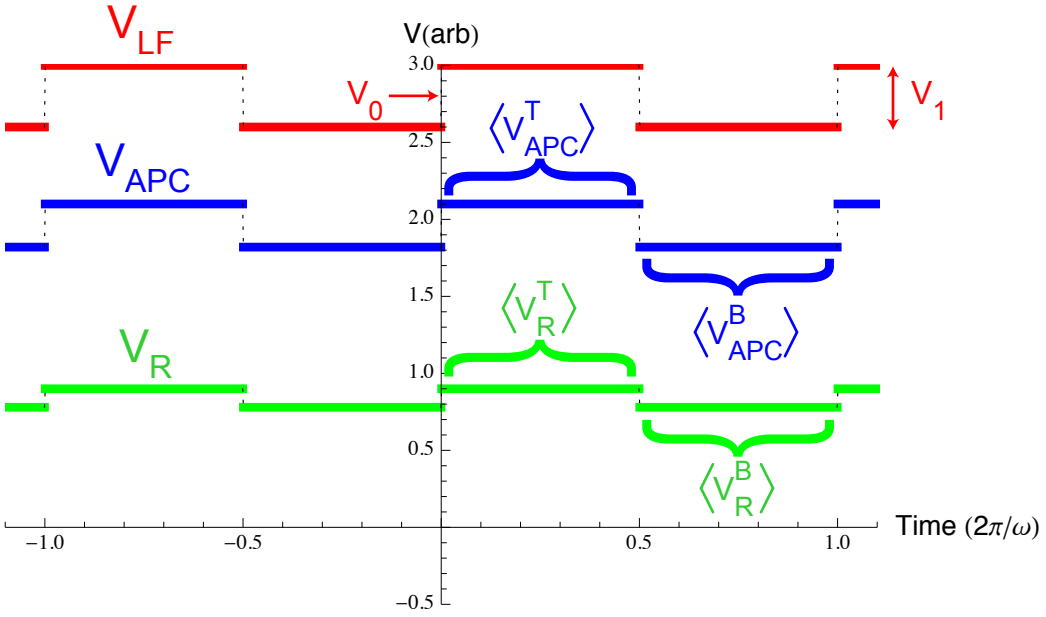

Figure 5.8: In this figure I plot the voltages V_{LF} (red), V_{APC} (blue), and V_R (green) used in the DC measurement as a function of time, using as an example $R_{APC} = 2.3R_b$. The low frequency bias voltage V_{LF} is a square wave at frequency ω with an offset V_0 and peak-to-peak V_1. Two amplifiers are used to measure both the resulting voltage V_{APC} across the APC and the resulting voltage V_R across the known bias resistor R_b. The APC resistance is calculated from the average measured voltages at the top of the square wave $\langle V^T_{APC}\rangle$ and $\langle V^T_R\rangle$ and the bottom of the square wave $\langle V^B_{APC}\rangle$ and $\langle V^B_R\rangle$.

voltages, the average resistance is approximately

$$R^{avg}_{APC} = \frac{V_{APC}}{I_{APC}} \approx \frac{\langle V^T_{APC}\rangle + \langle V^B_{APC}\rangle}{\langle V^T_R\rangle + \langle V^B_R\rangle} R_b \tag{5.37}$$

and the differential resistance is approximately

$$R_{APC} = \frac{\partial V_{APC}}{\partial I_{APC}} \approx \frac{\langle V^T_{APC}\rangle - \langle V^B_{APC}\rangle}{\langle V^T_R\rangle - \langle V^B_R\rangle} R_b \tag{5.38}$$

Ignoring noise in the problem, the approximations become equalities when the peak-to-peak magnitude of the square wave goes to zero, $V_1 \to 0$. IV spectroscopy is accomplished by varying the mean value V_0 of the square wave and measuring R^{avg}_{APC} and R_{APC}. V_1 determines the resolution of the measurement; that is, the spectroscopy can resolve structure in the IV curve on the scale of V_1. The addition of a microwave voltage bias across the APC will also limit the resolution of the spectroscopic measurement.

5.3 Microwave APC Resistance Measurement

Using a 50 Ω amplifier embedded in a 500 MHz resonant circuit (as in the RF-SET [128]), I can make a measurement of nanomechanical motion whose measurement noise is dominated by the shot noise of tunneling electrons over a bandwidth greater than 30 MHz. Using a double sideband measurement this enables shot-noise limited detection of nanomechanical motion at frequencies up to 15 MHz. Using a single sideband measurement, nanomechanical motion at frequencies between 0 Hz and $>$ 300 MHz can be detected with an imprecision that, while still shot noise limited, is twice the imprecision of the double sideband measurement (see section 5.1.2 and table 5.1). This technique employs a microwave voltage bias which is applied using either a transmission or reflection circuit; in a microwave circuit analysis, changes in APC resistance are detected by measuring changes in the resonant circuit's reflection or transmission coefficients. The signal to shot-noise ratio of these two measurements is identical, but there are advantages to using a reflection circuit when making a double sideband measurement (table 5.1) and advantages to using a transmission circuit when making a single sideband measurement (table 5.1).

5.3.1 Improved bandwidth using microwave measurement

I use a microwave circuit composed of a low-noise 50 Ω amplifier embedded in a resonant circuit (figure 5.9, top) in order to make a large bandwidth measurement of changes in the APC resistance. Using a low impedance amplifier avoids the problem created by the cable capacitance to ground; this problem was demonstrated in the previous section. The $R_a' = 50\ \Omega$ amplifier input impedance is matched to the impedance of the cable, therefore the cable capacitance is effectively canceled by the cable inductance and the cable can be ignored in the circuit analysis. The cable will just shift the phase of the voltage signal by an amount determined by the length of the cable.

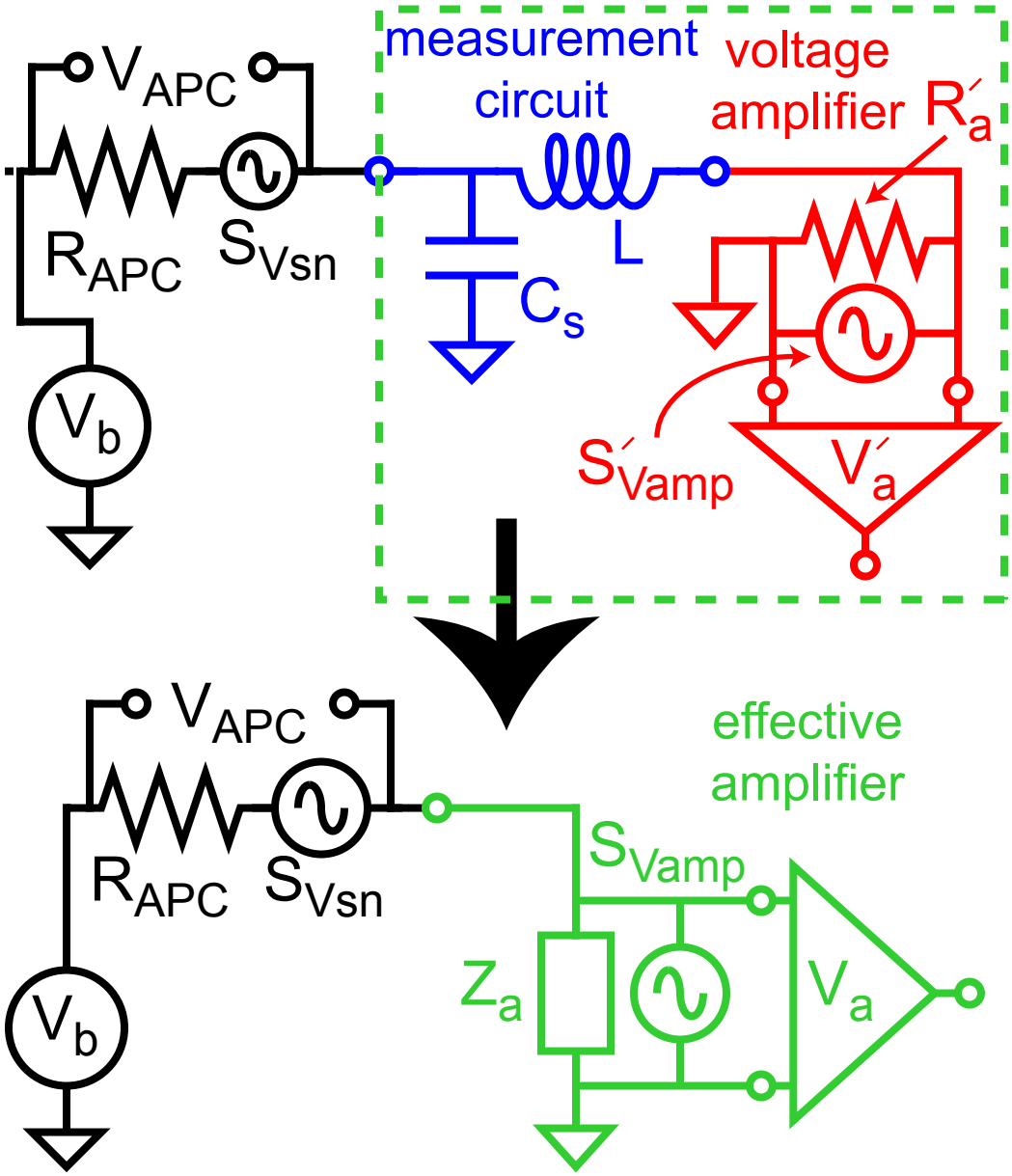

Figure 5.9: (top) Circuit diagram of the microwave measurement circuit. A bias voltage V_b creates a voltage V_{APC} across the APC, also creating shot noise with a spectral density S_{Vsn}. The microwave measurement circuit includes a stray capacitance C_s to ground and an inductor L. The bias also creates a voltage V_a' across an amplifier which has amplifier noise S'_{Vamp} and input impedance $R'_a = 50\ \Omega$. This input impedance is matched to the characteristic impedance of the cable connected the amplifier and the inductor, thus the cable only contributes an overall phase shift which will be ignored. (bottom) As described in subsection 5.1.1, the measurement circuit and amplifier (top, green box) can be described as an effective amplifier (bottom, green circuit) with a complex frequency dependent impedance Z_a, amplifier noise S_{Vamp}, and amplified (that is, measured) voltage V_a.

Simply using a $R'_a = 50\ \Omega$ amplifier will not result in a shot-noise limited measurement noise. Low-noise cryogenic amplifiers at 500 MHz can have a voltage noise spectral density as low as $S_{Vamp} \approx 3{\times}10^{-21}\ \mathrm{V}^2/\mathrm{Hz}$. However, this voltage noise and a $Z_a = 50\ \Omega$ amplifier input impedance implies that an APC bias voltage $|V_{APC}| > 200$ mV would be required to make a measurement whose noise is dominated by shot noise (equation 5.12). Since the APC is generally unstable for an APC bias voltage $|V_{APC}| > 50$ mV, it is necessary to modify the measurement circuit so that the effective impedance of the amplifier is larger than 50 Ω.

I therefore use a microwave resonant circuit (figure 5.9, top) to create an effective amplifier with a large input impedance near the electrical resonance frequency. The electrical resonance is created by adding an inductor L to the stray capacitance C_s to ground present on and around the chip (figure 5.9, top). This type of circuit is also called a matching circuit, since it is used to match the impedances of the high impedance APC and the low impedance amplifier. It's use in mesoscopic physics was pioneered by Schoelkopf *et al* [128] to create the radio-frequency single electron transistor (RF-SET). As described in section 5.1.1 and shown in figure 5.9, the entire measurement circuit is effectively an amplifier with a frequency-dependent input impedance

$$Z_a = \frac{R'_a + i\omega(L - \omega^2 L^2 C_s - C_s R'^2_a)}{(1 - \omega^2 L C_s)^2 + (\omega C_s R'_a)^2} \tag{5.39}$$

and an frequency-dependent effective amplifier noise (from equation 5.11)

$$S_{Vamp}(\omega) = S'_{Vamp}\left|\frac{V_a}{V'_a}\right|^2 = S'_{Vamp}\frac{R'^2_a + \omega^2 L^2}{R'^2_a} \tag{5.40}$$

This effective amplifier description of the measurement circuit can be used to calculate the measurement bandwidth γ_{meas}. The measurement noise will be dominated by shot noise when equation 5.12

$$|V_{APC}| \geq \frac{S_{Vamp}(\omega)}{2e\Xi\zeta_{ac}R_{APC}}\left|1 + \frac{R_{APC}}{Z_a(\omega)}\right|^2$$

is satisfied where S_{Vamp} is the effective amplifier noise given by equation 5.40 and Z_a is the impedance of the measurement circuit given by equation 5.39. The frequencies ω at which this inequality is satisfied defines a bandwidth γ_{meas} centered at ω_{meas} within which the measurement noise is dominated by shot noise.

In order to maximize the measurement bandwidth γ_{meas}, it is simpler to determine the optimal electrical resonance quality factor Q and frequency ω_0 instead of optimizing the inductance L and capacitance C_s. In this change of variables, the quality factor $Q = \sqrt{L/(R_a'^2 C_s)}$ and the undamped (that is, $R_a' \to 0$) resonance frequency is $\omega_0 = 1/\sqrt{LC_s}$. Using these variables and solving equation 5.12,

$$\omega_{meas} = \Re\left[\frac{\omega_0}{2}\left(\sqrt{\alpha+\beta}+\sqrt{\alpha-\beta}\right)\right] \tag{5.41}$$

$$\gamma_{meas} = \Re\left[\omega_0\left(\sqrt{\alpha+\beta}-\sqrt{\alpha-\beta}\right)\right] \tag{5.42}$$

where

$$\alpha = 1 - \frac{1}{2Q^2} - \frac{Q^2 R_a'^2}{2R_{APC}^2} \tag{5.43}$$

and

$$\beta^2 = \frac{1}{4Q^2}\left(\frac{Q^2 R_a'}{R_{APC}}+1\right)^2\left(\frac{Q^2 R_a'^2}{R_{APC}^2}+\frac{1}{Q^2}-\frac{2R_a'}{R_{APC}}-4\right)+\frac{2e\zeta_{ac}\Xi R_a'^2|V_{APC}|}{R_{APC}S'_{Vamp}} \tag{5.44}$$

When β is imaginary then there is no frequency at which the measurement noise is dominated by shot noise and $\gamma_{meas} = 0$. While this equation for the measurement bandwidth γ_{meas} is a complicated function of the quality factor Q, the optimal quality factor Q_{opt} that maximizes γ_{meas} is simple

$$Q_{opt} = \sqrt{\frac{R_{APC}}{R_a'}} \tag{5.45}$$

Qualitatively, this optimal quality factor Q_{opt} can be understood in terms of the impedance Z_a of the measurement circuit. On resonance ($\omega = \omega_0$) the measurement circuit's impedance is

$$Z_a(\omega_0) = R_a Q(Q-i) \tag{5.46}$$

Since $Q_{opt} \gg 1$, when $Q = Q_{opt}$ then the measurement circuit will have an impedance that is matched to the APC impedance $Z_a(\omega_0) = R_{APC}$. Since the maximum shot noise power is coupled into the measurement circuit when the impedance of the APC and the measurement circuit are matched, it is not surprising that the optimal quality factor enforces this condition.

For a given R_{APC} and V_{APC}, the measurement bandwidth γ_{meas} is not only dependent upon the quality factor of the electrical resonance but also on the electrical resonance frequency ω_0 and the amplifier noise S'_{Vamp}. Since $\gamma_{meas} \propto \omega_0$, theoretically the bandwidth can be made infinite by taking electrical resonance frequency $\omega_0 \to \infty$. Since a large Q is still optimal, this is equivalent to taking $C_s \to 0$.

The desire for a small capacitance C_s can also be understood in terms of the Bode-Fano limit. The Bode-Fano limit is a limit on the bandwidth over which it is possible to make a good match to a complex impedance [189]. In this case the complex impedance is the resistance R_{APC} of the APC shunted by the capacitance C_s, and the limit on the bandwidth is proportional to $1/(R_{APC}C_s)$. Therefore taking $C_s \to 0$ is equivalent to taking the Bode-Fano limit on the bandwidth to infinity.

Experimentally, maximizing γ_{meas} by minimizing C_s involves carefully designing the physical connections between the APC and the inductor, including the on-chip electrodes, wirebond, and inductor solder-pad. The bond-pads are designed to have a small area and a large separation from ground (see chapter 4). I also use a short wire between the bondpad and the inductor and use a small surface-mount inductor. In addition, the stray capacitance to ground is further decreased by flipping the inductor and directly wire-bonding to the inductor's soldering pad (see figure 5.10). However, even after using these techniques to limit the stray capacitance there is still $C_s \approx 200$ fF.

The desire to use a surface mount inductor in this experiment instead of an on-chip resonant circuit limits the electrical resonance frequency ω_0 to frequencies less than about 500 MHz. Using surface mount inductors simplifies device fabrication, however

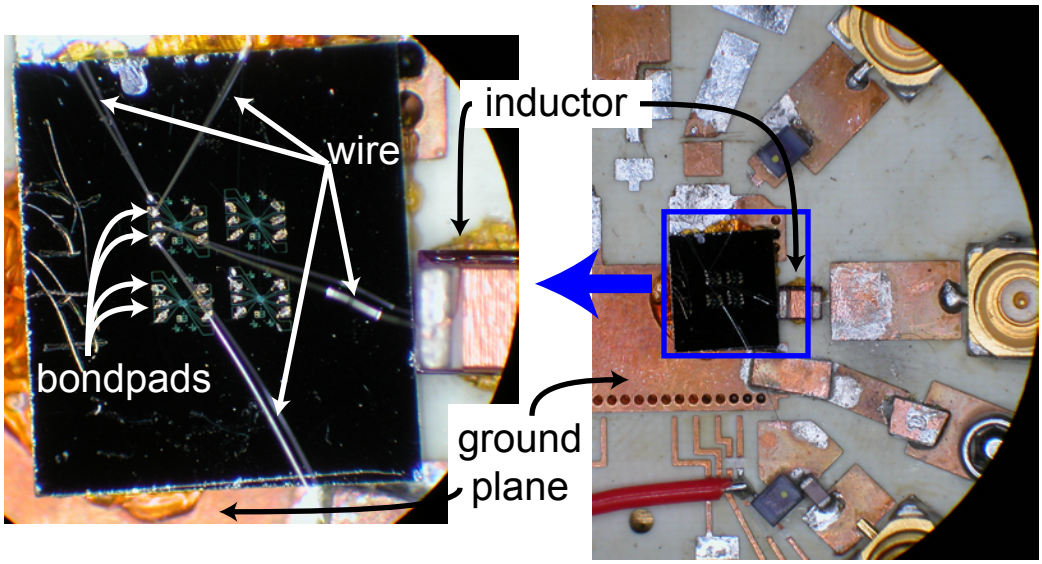

Figure 5.10: Pictures of chip and circuit board used to minimize stray capacitance on the right, higher magnification picture of chip and inductor on the left. The capacitance between the APC and the inductor is minimized by using small bond-pads and directly wirebonding to the solder pad of a surface-mount inductor which is turned over and glued to the circuit board.

it is generally difficult to find inductors that, at frequencies above about 500 MHz, have a large inductance and a large quality factor. I use Coilcraft surface mount inductors from the 0805CS series. These inductors have a large internal quality factor at 4 K (> 50 at 500 MHz) due to the use of high purity copper and therefore the loss in the inductor has little effect on the quality factor Q of the electrical resonance; most of the loss in the circuit is due to the amplifier impedance R'_a as desired. In general, inductors are shunted by a geometrical capacitance which limits the frequency range over which the inductor has a large inductance; that is, an impedance which increases with frequency. This frequency, where the contribution to the inductor's admittance from the inductance and geometrical capacitance is equal in magnitude but opposite in sign, is called the self resonance frequency. The Coilcraft 0805CS inductors have a small shunting capacitance and a large self resonance frequency of about 500 MHz. This limits the desired electrical resonance frequency to frequencies less than about 500 MHz.

While the Bode-Fano limit is important, it does not directly limit the bandwidth γ_{meas} where the noise in the measurement is dominated by shot noise because γ_{meas} can always be increased by making the amplifier noise S'_{Vamp} smaller.

Since the use of a surface mount inductor limits the measurement frequency to less than about 500 MHz, the measurement bandwidth γ_{meas} is maximized by using a $R'_a = 50\ \Omega$ amplifier with a measurement bandwidth centered at 500 MHz. I use a low-noise Berkshire U-500-2 amplifier which has a noise temperature less than 2 K over a bandwidth of about 100 MHz centered around 500 MHz. This is a cryogenic amplifier and to achieve the quoted noise temperature it is placed in the 4 K LHe bath. (The transistors in the amplifier are encapsulated, hence they can withstand the frost that deposits when the cryostat is extracted from LHe bath). Specifying an amplifier noise temperature T_{amp} and input resistance R'_a is equivalent to specifying the voltage noise spectral density

$$S'_{Vamp} = 4k_B T_{amp} R'_a = 5 \times 10^{-21}\ \mathrm{V^2/Hz} \tag{5.47}$$

This choice of $\omega_0 = 2\pi \times 500$ MHz and the minimum stray capacitance $C_s \approx 200$ fF implies a desired inductance of about $L \approx 500$ nF. In general there are small variations in the stray capacitance depending on the details of the configuration of the device, chip, and inductor; I select an inductor value that yields an electrical resonance frequency close to 500 MHz.

The stray capacitance $C_s = 200$ fF, inductance $L = 500$ nH, and amplifier noise $S'_{Vamp} = 5 \times 10^{-21}\ \mathrm{V^2/Hz}$ used in this experiment determine the measurement bandwidth γ_{meas} as a function of the APC resistance R_{APC} and bias voltage V_{APC}. In figure 5.11 I plot the bandwidth as a function of the APC resistance R_{APC} at four different APC bias voltages V_{APC}. For the largest stable APC bias voltage $V_{APC} = V_{APC}^{max} \approx 50$ mV, the bandwidth of the measurement is limited by the bandwidth of the cryogenic amplifier at low APC resistances ($R_{APC} < 200\ \mathrm{k\Omega}$) to approximately 100 MHz. The

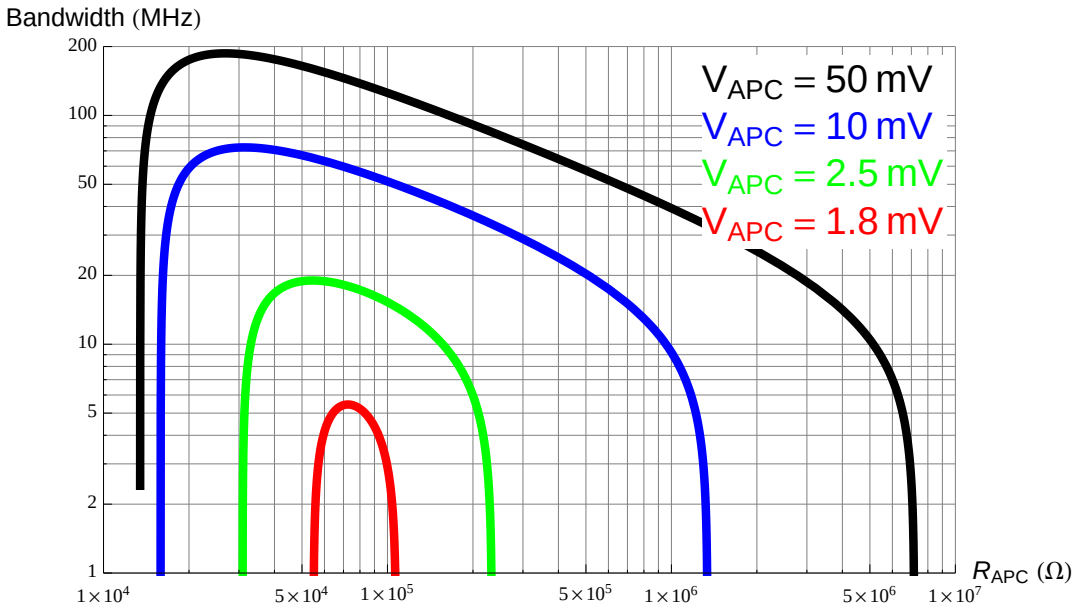

Figure 5.11: The bandwidth of the microwave measurement is plotted as a function of the APC resistance at four different APC voltages, using typical circuit parameters $C_s \approx 200$ fF and $L \approx 500$ nF. This bandwidth is centered at around 500 MHz. While this plot assumes a constant amplifier noise temperature $T_{amp} = 2\ K$, the actual amplifier is in fact as good as $T_{amp} \approx 1\ K$ at 530 MHz but becomes $T_{amp} > 2\ K$ below 450 MHz or above 580 MHz. Therefore, the actual bandwidth is limited to < 100 MHz.

bandwidth is also greater than about 2 MHz both using the largest stable APC bias voltage at $R_{APC} < 5$ MΩ and using a small APC bias voltage $V_{APC} \approx 2$ mV at an APC resistance $R_{APC} \approx 100$ kΩ.

I use this large bandwidth to measure nanomechanical motion. With 100 MHz of bandwidth, it is possible to implement the double sideband measurement described in table 5.1 and make a shot-noise limited measurement of nanomechanical motion at frequencies ≤ 50 MHz. Using a single sideband measurement (table 5.1), it is possible to make a shot-noise limited measurement of nanomechanical motion at a wide range of nanomechanical frequencies (< 300 MHz) using a small bandwidth (≈ 2 MHz) measurement. Because the microwave measurement has a shot-noise limited bandwidth > 2 MHz at a wide range of APC voltage biases and APC resistances, the single side-

band technique can be be used to make a sensitive measurement of nanomechanical motion at a wide range of nanomechanical resonance frequencies, APC voltage biases, and APC resistances. However, the single sideband measurement has the disadvantage that it's shot-noise limited displacement imprecision spectral density is twice as large as that of the double sideband measurement because the single sideband technique ignores half of the voltage signal created by nanomechanical motion (subsection 5.1.2).

5.3.2 Network analysis of microwave measurement

In this subsection I describe the APC and resonant circuit as a two-port network in order to decide whether the microwave voltage bias should be applied in transmission, as was analyzed in the previous section, or in reflection. As I will show, the type of voltage bias does not effect the signal due to small changes in the APC resistance or the measurement noise when they are parameterized as functions of the voltage V_{APC} across the APC. Therefore the measurement bandwidth calculated in the previous subsection and the displacement imprecision will be the same for the two types of voltage biases. However, there is also a tone at the frequency of the voltage bias, which can be used to infer the average resistance of the APC. This signal may be so large that it saturates the low-noise amplifier. By carefully choosing the frequency of the microwave bias and whether it is applied in transmission or reflection, this saturation can often be avoided.

From a microwave engineering perspective, the APC and resonant circuit is a two-port network, a type of network which is analyzed in detail in many microwave textbooks (for example, [189]). The basic circuit diagram is shown in figure 5.12, where the circuit elements form a simple T-network and there is a voltage wave incident on V_1^+ and emerging from V_1^- port 1 and similarly voltage waves V_2^+ and V_2^- incident on and emerging from port 2. These voltages are related using a scattering matrix, or

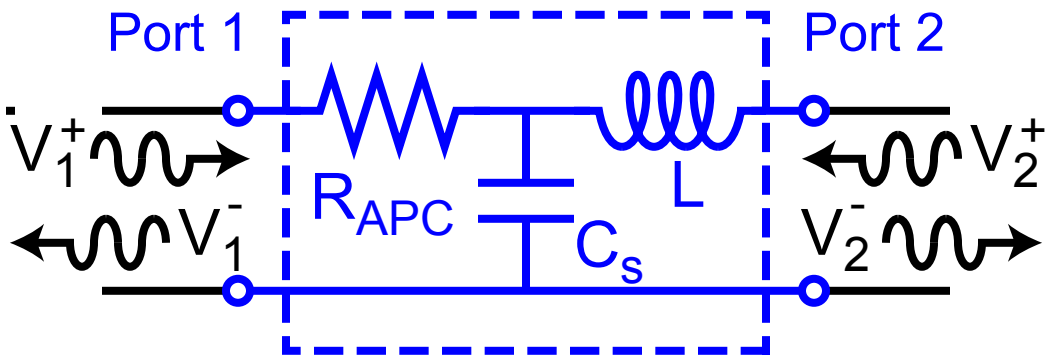

Figure 5.12: Circuit diagram of the microwave measurement circuit as a two-port network. The R_{APC}, C_s, and L are contained within a network (blue box) with two-ports, labeled "Port 1" and "Port 2." These ports are connected to the outside world by cables with a characteristic impedance $Z_0 = 50\ \Omega$. Voltage waves can travel along these cables: a wave V_1^+ (V_1^-) travels towards (away from) port 1 and similarly a wave V_2^+ (V_2^-) travels towards (away from) port 2.

S-matrix,

$$\begin{pmatrix} V_1^- \\ V_2^- \end{pmatrix} = \begin{pmatrix} S_{11} & S_{12} \\ S_{21} & S_{22} \end{pmatrix} \begin{pmatrix} V_1^+ \\ V_2^+ \end{pmatrix} \tag{5.48}$$

The approaching and departing waves are carried on a cable with a characteristic impedance $Z_0 = 50\ \Omega$, and I make the simplifying assumption that these cables are terminated in a 50 Ω load, in the form of an amplifier input impedance, signal generator source impedance, or other circuit element that can be treated as a 50 Ω load termination. Therefore, there will not be any further reflections of V_1^- or V_2^-.

In this picture, changes in the resistance of the APC are detected by measuring changes in the S-matrix coefficients. Section 5.1.1 and the previous subsection analyzed the relationship between the voltage bias V_1^+ and the voltage at the amplifier V_2^- using an analysis of the voltage and current through different circuit elements. However, this is equivalent to measuring changes in the transmission coefficient S_{21} due to changes in the APC resistance. Similarly, if an incident voltage wave V_2^+ is used then the same

amplifier can be used to measure changes in the reflection coefficient S_{22} due to changes in the APC resistance. In fact, this defines the two different types of biases used in the experiment: V_1^+ is a microwave voltage bias applied in transmission and V_2^+ is a microwave voltage bias applied in reflection (figure 5.13).

Calculating the scattering matrix coefficients S_{21} and S_{22} for the network in figure 5.12 can be done rather simply using the conventions and information in a microwave engineering textbook (for example, [189]). The voltages and currents at the two ports

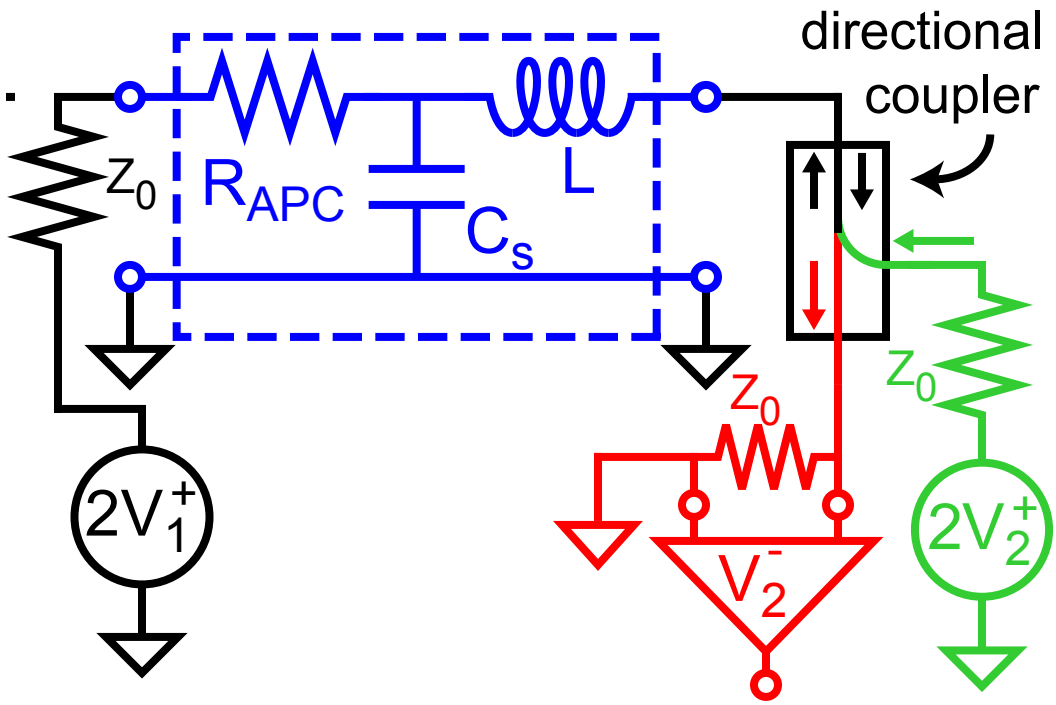

Figure 5.13: Circuit diagram describing the microwave transmission measurement. In reflection, a microwave voltage bias $2V_1^+$ with a source impedance $Z_0 = 50\ \Omega$ is applied to the right side of the two-port network (blue) and the transmitted voltage V_2^- is measured with an amplifier that has an input impedance $Z_0 = 50\ \Omega$. In transmission, a microwave voltage bias $2V_2^+$ with a source impedance $Z_0 = 50\ \Omega$ is applied to the left side of the two-port network (blue) and, as in reflection, the transmitted voltage V_2^- is measured with an amplifier that has an input impedance $Z_0 = 50\ \Omega$. The directional coupler at port 2 separates incoming (green, V_2^+) and outgoing (red, V_2^-) waves.

are related by an ABCD matrix

$$\begin{pmatrix} V_1 \\ I_1 \end{pmatrix} = \begin{pmatrix} 1 + i\omega C_s R_{APC} & R_{APC} + i\omega L + \omega^2 C_s L R_{APC} \\ i\omega C_s & 1 - \omega^2 C_s L \end{pmatrix} \begin{pmatrix} V_2 \\ I_2 \end{pmatrix} \tag{5.49}$$

Using a general transformation which converts this ABCD matrix into a scattering matrix, the reflection coefficient S_{21} and transmission coefficient S_{22} are

$$S_{21} = \frac{2Z_0}{R_{APC}(1 - \omega^2 C_s L) + i\omega(L + C_s Z_0 R_{APC})} \tag{5.50}$$

$$S_{22} = \frac{R_{APC}(1 - \omega^2 C_s L) + i\omega(L - C_s Z_0 R_{APC})}{R_{APC}(1 - \omega^2 C_s L) + i\omega(L + C_s Z_0 R_{APC})} \tag{5.51}$$

where $Z_0 = 50\ \Omega \ll R_{APC}$ is the impedance of the cables, amplifier, and voltage source.

The signal at the amplifier created by small changes in the APC resistance can be calculated from the scattering coefficients:

$$\frac{\partial S_{21}}{\partial R_{APC}} = \frac{-2Z_0(1 - \omega^2 C_s L + i\omega C_s Z_0)}{\left[R_{APC}(1 - \omega^2 C_s L) - i\omega(L + C_s Z_0 R_{APC})\right]^2} \tag{5.52}$$

$$\frac{\partial S_{22}}{\partial R_{APC}} = \frac{2Z_0}{\left[R_{APC}(1 - \omega^2 C_s L) - i\omega(L + C_s Z_0 R_{APC})\right]^2} \tag{5.53}$$

The signal at the amplifier δV_{2T}^- when a voltage bias is applied in transmission due to a small change in APC resistance δR is therefore transmission

$$\delta V_{2T}^- = \left(\frac{\partial S_{21}}{\partial R_{APC}}\delta R\right) V_1^+ = \frac{-2Z_0(1 - \omega^2 C_s L + i\omega C_s Z_0)\delta R}{\left[R_{APC}(1 - \omega^2 C_s L) - i\omega(L + C_s Z_0 R_{APC})\right]^2} V_1^+ \tag{5.54}$$

and the signal at the amplifier δV_{2R}^- when the voltage bias is applied in reflection is

$$\delta V_{2R}^- = \left(\frac{\partial S_{22}}{\partial R_{APC}}\delta R\right) V_2^+ = \frac{2Z_0\delta R}{\left[R_{APC}(1 - \omega^2 C_s L) - i\omega(L + C_s Z_0 R_{APC})\right]^2} V_2^+ \tag{5.55}$$

While these signals δV_{2R}^- and δV_{2T}^- are of different magnitude for the same magnitude incident voltage (V_1^+ and V_2^+ respectively), the resulting displacement measurements have the same imprecision and bandwidth. The voltage signals will be examined in more detail below, with the conclusion that they are the same magnitude for the same voltage V_{APC} across the APC. The voltage V_{APC} across the APC is the relevant quantity because the physics of the APC itself constrains V_{APC} and the noise at the

amplifier S_{Vtot} is due to shot noise which is controlled by V_{APC} and amplifier noise which is independent of bias. Therefore the bandwidth of the measurement, described in the previous subsection, and the displacement imprecision are only dependent upon the voltage V_{APC} across the APC and not dependent on whether V_{APC} is due to a voltage bias applied in transmission V_1^+ or reflection V_2^+.

To demonstrate that the voltage signals δV_{2R}^- and δV_{2T}^- are identical functions of the voltage V_{APC} across the APC, I start by calculating the voltage V_{APC} across the APC due to a bias $2V_1^+$ or $2V_2^+$ and then substitute V_{APC} for V_1^+ or V_2^+ in equations 5.54 and 5.55. From the circuit in figure 5.13, the voltage V_{APC}^T due to a voltage bias applied in transmission V_1^+ is

$$V_{APC}^T = 2V_1^+ \frac{R_{APC}(1-\omega^2 C_s L + i\omega C_s Z_0)}{R_{APC} - \omega^2 L C_s R_{APC} + i\omega(L + C_s R_{APC} Z_0)} \tag{5.56}$$

assuming that $Z_0 \ll R_{APC}$. Similarly, from the circuit in figure 5.13, the voltage V_{APC}^R due to a voltage bias applied in reflection V_2^+ is

$$V_{APC}^R = 2V_2^+ \frac{R_{APC}}{R_{APC} - \omega^2 L C_s R_{APC} + i\omega(L + C_s R_{APC} Z_0)} \tag{5.57}$$

assuming that $Z_0 \ll R_{APC}$.

These relationships between the voltage V_{APC} across the APC and the applied voltage biases can be substituted into equations 5.54 and 5.55 to demonstrate that the voltage signal due to a voltage bias in transmission or reflection is the same function of V_{APC}. When the voltage bias is applied in transmission then signal at the amplifier as a function of the voltage across the APC is

$$\delta V_{2T}^- = -\frac{\delta R}{R_{APC}} \frac{2Z_0 e^{i\theta}}{R_{APC}(1-\omega^2 C_s L) - i\omega(L + C_s Z_0 R_{APC})} \frac{V_{APC}^T}{2} \tag{5.58}$$

and similarly when the voltage bias is applied in reflection then signal at the amplifier as a function of the voltage across the APC is

$$\delta V_{2R}^- = \frac{\delta R}{R_{APC}} \frac{2Z_0 e^{i\theta}}{R_{APC}(1-\omega^2 C_s L) - i\omega(L + C_s Z_0 R_{APC})} \frac{V_{APC}^R}{2} \tag{5.59}$$

where in both cases

$$\theta = 2\tan^{-1}\left[\frac{\omega(L + C_s R_{APC} Z_0)}{R_{APC}(1 - \omega^2 C_s L)}\right] \tag{5.60}$$

Comparing equation 5.58 and 5.59, the magnitude of the signal due to small changes δR in the resistance of the APC is the same function of the voltage V_{APC} across the APC for a voltage bias applied in transmission and reflection.

Although the bandwidth and sensitivity of the displacement measurement are independent of whether the voltage bias is applied in reflection or transmission, the total voltage at the input of the amplifier depends strongly on the type of bias. To avoid saturating the amplifier, it is important to choose the type of bias that minimizes the voltage at the amplifier for a given voltage V_{APC} across the APC, that is, for a given measurement sensitivity.

Qualitatively, the appropriate type of bias can be understood by examining the characteristics of the resonant circuit. As was discussed in the previous section, the resonant circuit is used to create an effective amplifier with a large input impedance. This input impedance is large over approximately the bandwidth of the electrical resonance $\omega_e/Q \approx 20$ MHz and the maximum input impedance is at the electrical resonance frequency where $Z_a \approx 50$ kΩ (using the circuit values above). Then if the circuit is biased in reflection, there will be little reflection when the effective amplifier impedance and the APC impedance are similar and no reflectance if they are the same. On the other hand, if the circuit is biased in transmission then the ratio of the voltage across the APC to the voltage across the amplifier is going to be proportional to the input impedance of the effective amplifier. Based on this qualitative understanding, it is best to bias in reflectance when the APC resistance is not much bigger than the effective amplifier impedance. This occurs approximately when the frequency of the bias is within the bandwidth of the electrical resonance up to some maximum APC resistance. Beyond this maximum APC resistance or at bias frequencies outside the bandwidth of the

electrical resonance, it is better to bias in transmission.

More quantitatively, the appropriate type of voltage bias, V_1^+ in transmission or V_2^+ in reflection, is the one that has the smaller ratio of the voltage at the amplifier V_2^- to the voltage V_{APC} across the APC. When a voltage V_1^+ is applied in transmission and using the previous results for the scattering matrix

$$V_{2T}^- = S_{21}V_1^+ = \frac{2Z_0}{R_{APC}(1-\omega^2 C_s L) + i\omega(L + C_s Z_0 R_{APC})}V_1^+ \tag{5.61}$$

When a voltage V_2^+ is applied in reflection, then

$$V_{2R}^- = S_{22}V_2^+ = \frac{R_{APC}(1-\omega^2 C_s L) + i\omega(L - C_s Z_0 R_{APC})}{R_{APC}(1-\omega^2 C_s L) + i\omega(L + C_s Z_0 R_{APC})}V_2^+ \tag{5.62}$$

Therefore, when the voltage bias is applied in transmission the ratio of V_{APC} (equation 5.56) to the voltage at the amplifier V_{2T}^- is

$$\frac{V_{2T}^-}{V_{APC}^T} = \frac{Z_0}{R_{APC}(1-\omega^2 C_s L + i\omega C_s Z_0)} \tag{5.63}$$

and when the voltage bias is applied in reflection then the ratio of V_{APC} (equation 5.57) to the voltage at the amplifier V_{2R}^- is

$$\frac{V_{2R}^-}{V_{APC}^R} = \frac{R_{APC}(1-\omega^2 C_s L) + i\omega(L - C_s Z_0 R_{APC})}{2R_{APC}} \tag{5.64}$$

These two ratios, V_{2T}^-/V_{APC}^T and V_{2R}^-/V_{APC}^R, are plotted in figure 5.14 versus the frequency ω of the bias voltage for the circuit values $C_s = 200$ fF, $L = 500$ nH, and $Z_0 = 50\ \Omega$ near the center of the measurement bandwidth at 500 MHz.

Examining figure 5.14, the voltage at the input of the amplifier is minimized by applying the voltage bias in transmission when the APC resistance is large $R_{APC} > 150\text{k}\Omega$ or when the frequency of the bias is off resonance. However, when the APC resistance is small $R_{APC} < 150\text{k}\Omega$ and the frequency of the bias is close to the electrical resonance frequency then the amplifier can be protected by applying the voltage bias in reflection. Figure 5.14 also highlights the importance of protecting the amplifier. For example, if a large enough voltage was applied in reflectance to create $V_{APC} = 50$ mV

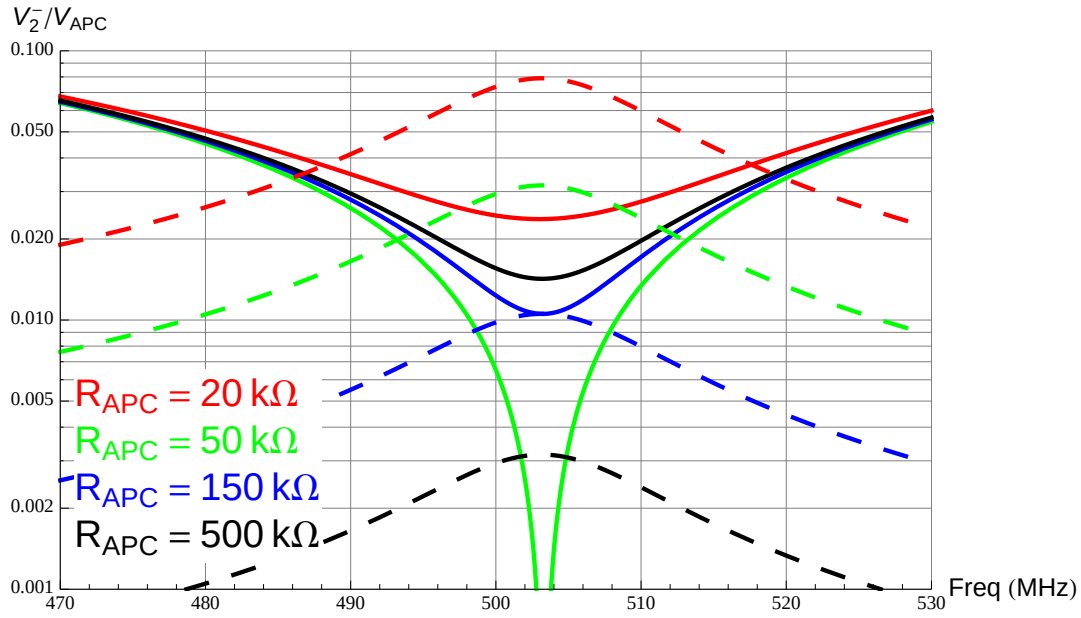

Figure 5.14: The ratio V_2^-/V_{APC} of the voltage at the amplifier to the voltage across the APC versus the frequency of the applied bias for various APC resistances; the bias voltage is applied in reflection (solid lines) or transmission (dashed lines). This calculation uses typical circuit values $C_s = 200$ fF, $L = 500$ nH, and $Z_0 = 50\ \Omega$ which implies that the measurement bandwidth, calculated in the previous section, is centered approximately around 500 MHz. The low-noise cryogenic amplifier can be overwhelmed by large voltages, such as the worst case scenario on this graph of $V_2^- = (0.08) \times V_{APC}^{max} \approx 4$ mV. Therefore the type of bias should be chosen to minimize V_2^-/V_{APC} based on the APC resistance and the frequency of the voltage bias.

at a frequency far from the electrical resonance, then the amplifier would experience a voltage $V_2^- > 1$ mV at the input. This voltage is sufficient to saturate the low-noise cryogenic amplifier. Finally, while I am not going to discuss the procedure in detail, it is also possible to create a large V_{APC} and a negligible voltage V_2^- at the amplifier by simultaneously applying voltages in transmission V_1^+ and reflection V_2^+ with the correct phase and magnitude.

I have now described the dc measurement of APC resistance (subsection 5.2.2) and the fast microwave measurement of changes in the APC resistance (subsection 5.3.1) which can be accomplished using a voltage bias applied in reflection or trans-

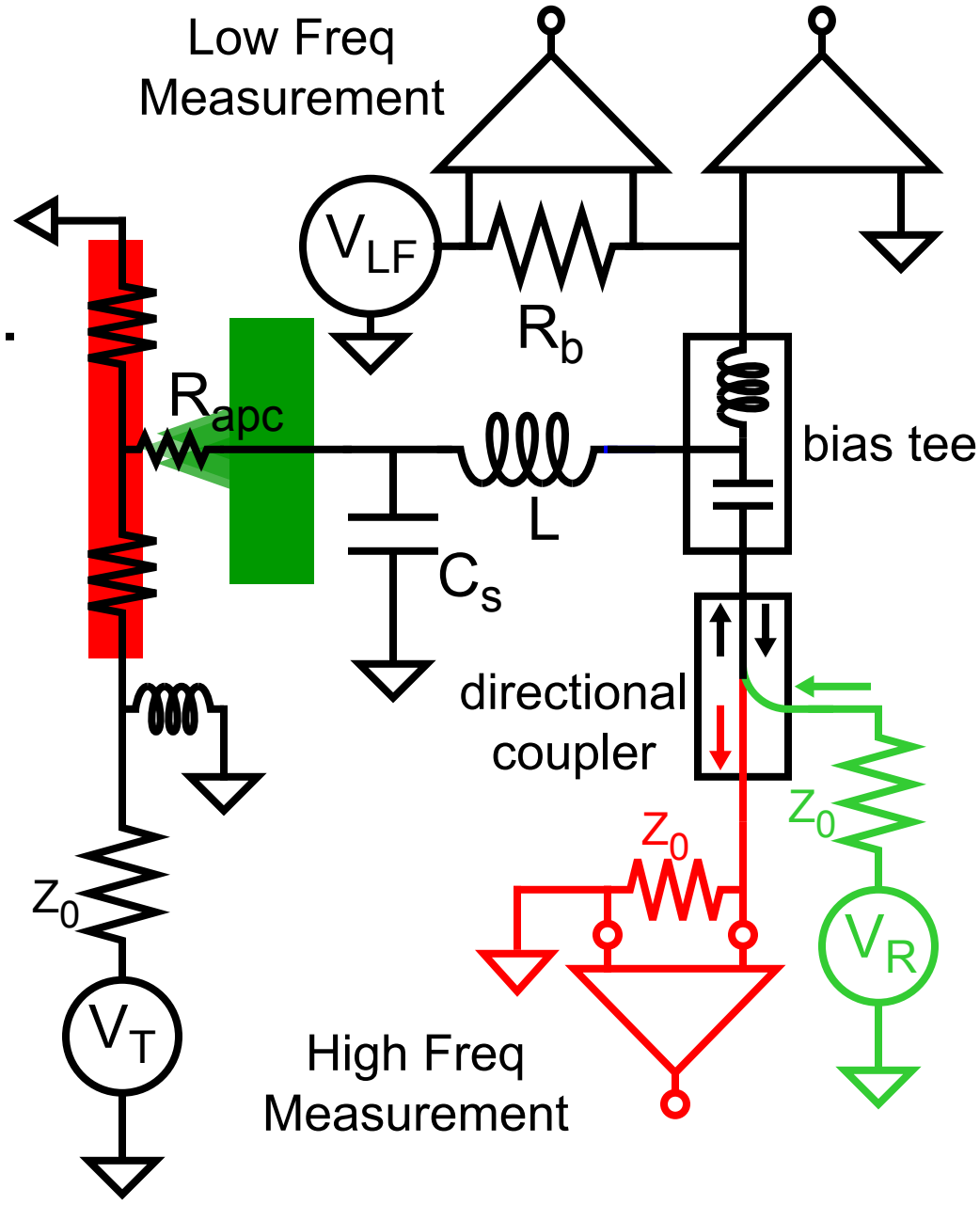

Figure 5.15: Diagram of measurement circuit, including both the low frequency measurement and high frequency measurement. The low frequency and microwave portions of the circuit are separated using a bias tee; the inductor is open at high frequencies, while the capacitor is open at low frequencies. Similarly, both sides of the beam (red) are shorted at low frequencies using an inductor, but the R_{APC} (between the red beam and green electrode) can be biased at high frequencies in transmission using V_T. It is also possible to bias the circuit at high frequencies in reflection using V_R. For more details on the low frequency measurement see figure 5.7 and subsection 5.2.2, as well as figure 4.2 for details around the APC. The high frequency transmission and reflection measurements are described in more detail in figure 5.13.

mission (subsection 5.3.2). In the actual experiment, all of these measurements can be performed simultaneously. While the details of the measurement circuit have evolved over time, figure 5.15 contains a representative circuit diagram showing the combined measurements.

5.4 Measurement of APC resistance at the Mechanical Resonance Frequency

While the 500 MHz voltage measurement described in the previous section can be used as a shot-noise limited displacement measurement, I would also like to make a shot-noise limited measurement of voltage signals around the nanomechanical resonance frequency. Such a voltage measurement can be used with a dc voltage to detect nanomechanical motion (baseband measurement, subsection 5.1.2) and, as described in chapter 3, can be used to detect correlations between nanomechanical motion and shot-noise due to tunneling electrons at the nanomechanical resonance frequency. This correlation is important because may be created by the momentum kicks of tunneling electrons, the fundamental source of measurement backaction in the APC displacement detector (chapter 3).

There are two obstacles to making the noise in a voltage measurement around the nanomechanical resonance frequency dominated by shot-noise. First, it requires a knowledge of the mechanical resonance frequency prior to the creation of the APC at cryogenic temperatures. Second, it requires a low-noise amplifier at the mechanical resonance frequency. In this thesis, the relatively large noise of the available amplifier and the design of the measurement circuit prevent a shot-noise limited measurement and make measuring correlations difficult.

The first obstacle, correctly choosing the electrical resonance frequency, can be avoided using two strategies. First, the mechanical resonance frequencies can be predicted by using a combination of finite element modeling and knowledge of the mechan-

ical resonance frequencies of similar devices. The second more effective and complicated strategy is to use a mechanically controllable break junction (MCBJ, see chapter 4) to measure the mechanical resonance frequency before choosing the electrical resonance frequency. Using a MCBJ, a constriction can be cooled to cryogenic temperatures, stretched into an APC, used to measure nanomechanical motion, returned to almost it's original state, and then returned to room temperature. At room temperature, the electrical resonance frequency can be adjusted to match the measured frequency of nanomechanical motion. Then when the device is again cooled to cryogenic temperatures and a new APC is created using the MCBJ, the resulting mechanical resonance frequency will match the electrical resonance frequency. This procedure can be repeated multiple times, though there is always the worry that contaminates are incorporated into the constriction and APC.

In this project I was unable to overcome the second obstacle, of finding a low-noise amplifier at the mechanical resonance frequency, and the ability to measure correlations was severely limited by the relatively large noise of the amplifier. In general, the nanomechanical resonances which were most strongly coupled to the APC had resonant frequencies below 100 MHz. Therefore a low-noise cryogenic HEMT (high electron mobility transistor) amplifier, like the amplifier used in the previous section at 500 MHz, cannot be used. HEMT amplifiers have 1/f noise which is small at 500 MHz but becomes unacceptably large at frequencies less than 100 MHz. Instead, I used a room temperature amplifier with a 70 K noise temperature, implying a voltage noise with a spectral density of 2×10^{-19} V^2/Hz. This amplifier noise is about 30 times worse than the 500 MHz cryogenic amplifier and makes it difficult to measure both shot noise at the mechanical resonance frequency and correlations between the shot noise and mechanical displacement.

I use the circuit in figure 5.16 to simultaneously measure voltage fluctuations at a 70 MHz nanomechanical resonance using a relatively noisy amplifier and voltage

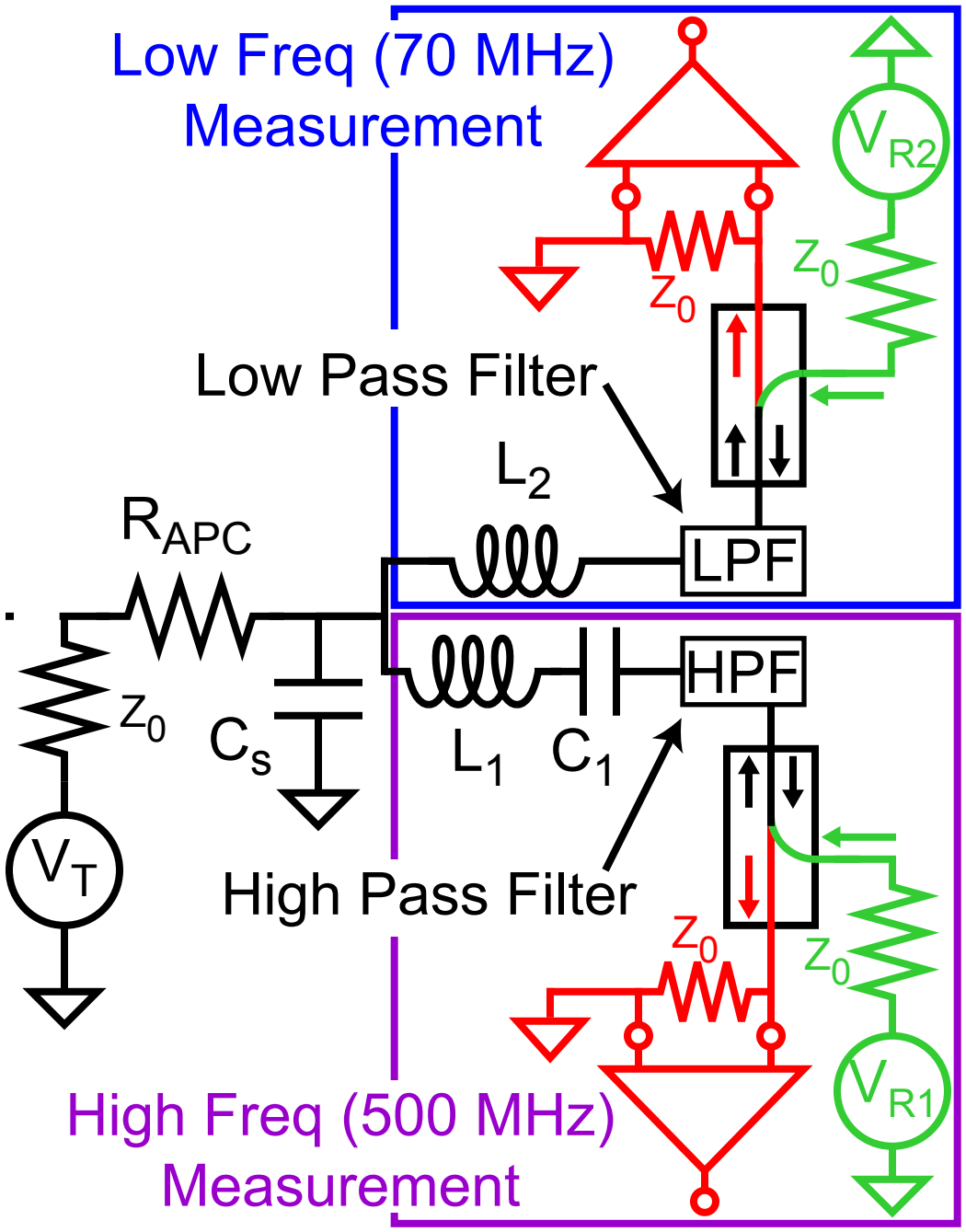

Figure 5.16: Circuit diagram including both a low frequency (70MHz) measurement (blue box) and a high frequency (500 MHz) measurement (purple box). The two measurements are electrically separated using filters (LPF and HPF) and an additional capacitance C_1: the purple box is an open circuit around 70 MHz and the blue box is an open circuit around 500 MHz.

fluctuations at 500 MHz using a low-noise cryogenic amplifier. The two signals are separated by including a low pass filter on the 70 MHz measurement line and a high pass filter on the 500 MHz measurement line. The low pass filter turns the 70 MHz measurement circuit (blue box, figure 5.16) into an open circuit at frequencies above 400 MHz, and therefore the 70 MHz measurement circuit can be ignored when analyzing the 500 MHz measurement (purple box, 5.16). Similarly, the high pass filter (and capacitor C_1) allows the 500 MHz measurement circuit to be ignored when analyzing the 70 MHz measurement.

The values of the circuit elements used in the measurement circuit (figure 5.16) were chosen based on the desired electrical resonance frequencies and wide (approximately 5 MHz) electrical resonance at 70 MHz. The wide electrical resonance is required because the frequency of the nanomechanical resonance often varies by up to 10% and, in this case, is achieved by adding an additional capacitance to ground so that $C_s = 2.5$ pF. As described in the previous section, this large capacitance will have the undesired effect of decreasing the measurement bandwidth; a better solution, which could be used in future experiments, would use a more complicated measurement circuit with multiple electrical resonances. The desired 500 MHz resonance frequency of the high frequency electrical measurement circuit and the additional series capacitance $C_1 = 500$ nF determines the inductance $L_1 = 150$ nH; the series capacitance C_1 is chosen to ensure that the high frequency measurement circuit is effectively an open circuit at 70 MHz.

Using these circuit values, I analyze the 70 MHz and 500 MHz measurement circuits separately to determine the minimum voltage V_{APC} across the APC that is required for the noise in each measurement to be dominated by shot noise. From equation 5.12, the noise in 70 MHz measurement using a dc voltage V_{APC} across the

APC will be dominated by shot noise when

$$|V_{APC}| \geq \frac{S_{Vamp2}}{2e\Xi\zeta_{dc}R_{APC}}\left|1+\frac{R_{APC}}{Z_{a2}(\omega)}\right|^2 \tag{5.65}$$

The noise of the effective amplifier S_{Vamp2} created by the 70 MHz measurement circuit is

$$S_{Vamp2} = S'_{Vamp2}\frac{Z_0^2+\omega^2L_2^2}{Z_0^2} \tag{5.66}$$

and $Z_{a2}(\omega)$ is the impedance of the 70 MHz measurement circuit

$$Z_{a2}(\omega) = \frac{Z_0+i\omega(L_2-\omega^2L_2^2C_s-C_sZ_0^2)}{(1-\omega^2L_2C_s)^2+(\omega C_sZ_0)^2} \tag{5.67}$$

where $S'_{Vamp2} = 2\times10^{-19}$ V^2/Hz is the noise and $Z_0 = 50\ \Omega$ is the input impedance of the 70 MHz amplifier. Similarly, the noise in the 500 MHz measurement using a microwave voltage V_{APC} across the APC will be shot noise limited when

$$|V_{APC}| \geq \frac{S_{Vamp1}}{2e\Xi\zeta_{ac}R_{APC}}\left|1+\frac{R_{APC}}{Z_{a1}(\omega)}\right|^2 \tag{5.68}$$

$$S_{Vamp1} = S'_{Vamp1}\frac{(\omega C_1Z_0)^2+\left(1-\omega^2C_1L_1\right)^2}{(\omega C_1Z_0)^2} \tag{5.69}$$

$$Z_{a1}(\omega) = \frac{1-\omega^2L_1C_1+i\omega C_1Z_0}{i\omega\left(C_1+C_s-\omega^2C_1C_sL_1+i\omega C_1C_sZ_0\right)} \tag{5.70}$$

where $S'_{Vamp1} = 5\times10^{-21}$ V^2/Hz is the noise and $Z_0 = 50\ \Omega$ is the input impedance of the low-noise cryogenic 500 MHz amplifier.

In the previous section I used this type of inequality to calculate a measurement bandwidth, however in this section I will calculate the frequency-dependent voltage $V_{APC}^{SN}(\omega)$ across the APC at which the amplifier noise and shot noise contribute equally to the measurement noise. In other words, V_{APC}^{SN} is the minimum APC voltage where either equation 5.65 or equation 5.68 is satisfied. Using the values for the circuit component describe above and various values of APC resistance R_{APC}, I plot V_{APC}^{SN} as a function of frequency ω for the 70 MHz and 500 MHz measurements (figure 5.17a,b). For comparison, I also plot V_{APC}^{SN} as a function of frequency ω for the original 500 MHz

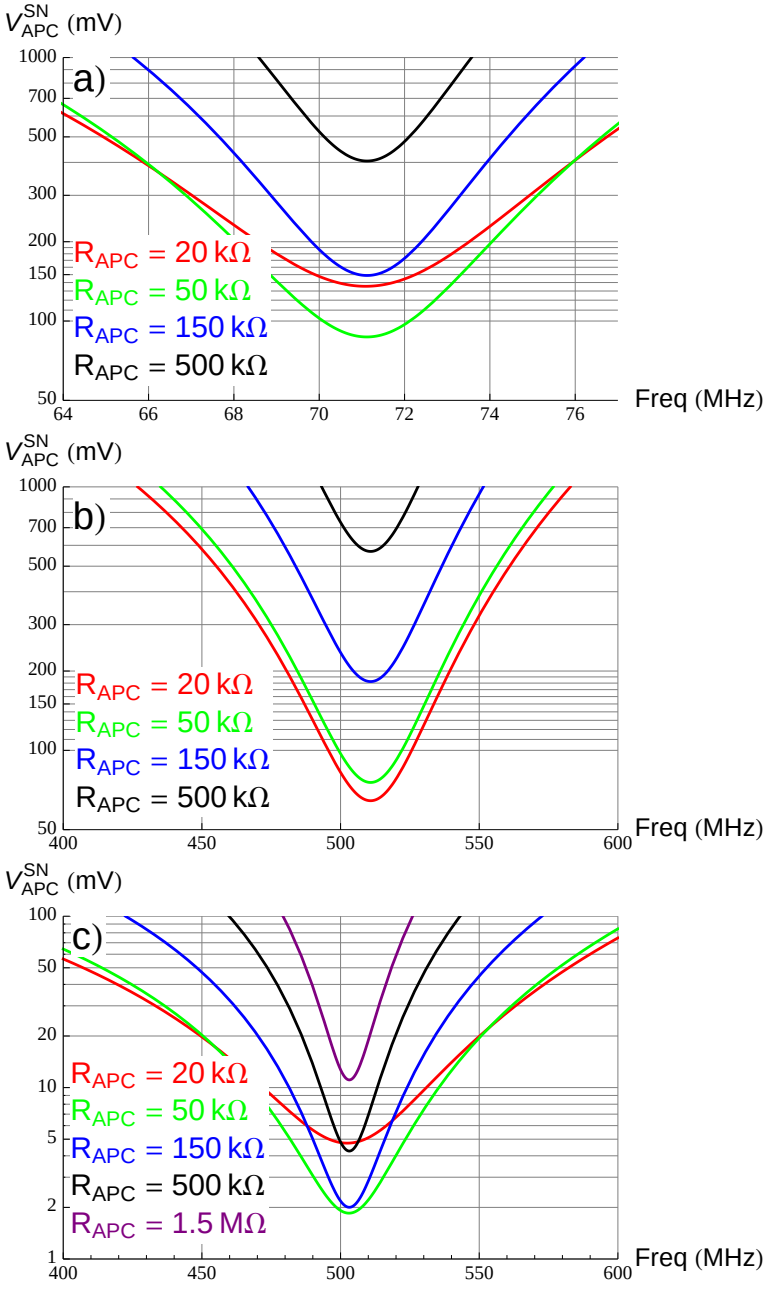

Figure 5.17: The voltage V_{APC}^{SN} is plotted plotted versus frequency for a range of APC resistances. When a voltage V_{APC}^{SN} is applied across the APC, the contribution of shot-noise and amplifier noise to the total measurement noise is equal; at APC voltages above the plotted line, the measurement noise is dominated by shot noise. Since V_{APC}^{SN} for the combined 70 MHz (a) and 500 MHz (b) measurement circuits (figure 5.16) is never less than the maximum stable APC voltage $V_{APC}^{max} = 50$ mV, there is no frequency at which the measurement noise is dominated by shot noise. On the other hand, the magnitude of V_{APC}^{SN} for the 500 MHz measurement described in the previous section (c) indicates that the measurement noise is dominated by shot noise over a wide bandwidth and at various APC resistances and voltages, as expected.

measurement analyzed in section 5.3 (figure 5.17c). In this figure, the measurement bandwidth over which the measurement noise is dominated by shot noise can be determined by observing the frequency range over which $V_{APC} \geq V_{APC}^{SN}$. Since the APC is unstable for $V_{APC} > V_{APC}^{max} = 50$ mV, the maximum measurement bandwidth is the frequency range over which $V_{APC}^{SN} \leq V_{APC}^{max} = 50$ mV.

As expected, it is possible to make a shot-noise limited measurement using the original 500 MHz measurement circuit (section 5.3, figure 5.17c), but there is no frequency range over which the measurement noise in the new 70 MHz measurement (figure 5.17a) or new 500 MHz measurement (figure 5.17b) is dominated by shot noise. The new 500 MHz measurement is less sensitive because of the larger stray capacitance, as expected. The large stray capacitance also decreases the sensitivity of the 70 MHz measurement, but the main problem is the large noise of the 70 MHz amplifier. The 70 MHz amplifier's voltage noise spectral density S'_{Vamp} used in figure 5.17a is about 30 times worse than that of the 500 MHz cryogenic amplifier. Since $V_{SN}^{APC} \propto S'_{Vamp}$, if I could use a 70 MHz amplifier that had the same noise as the 500 MHz cryogenic amplifier then V_{APC}^{SN} in figure 5.17a would be scaled down by a factor of 30 and the 70 MHz measurement would have a shot noise bandwidth > 1 MHz over a wide range of APC resistances.

In conclusion, while I can attempt to measure the correlations between shot noise at the nanomechanical resonance frequency and nanomechanical displacement using the measurement circuit in figure 5.16, the measurement noise will not be dominated by shot noise and therefore the results are disappointing (see chapter 7). This measurement could be improved in the future by using an amplifier that contributes less noise and a more complicated measurement circuit.

5.5 Using Shot Noise to Calibrate the Microwave Measurement

In this experiment, the shot noise of the atomic point contact is used to calibrate the microwave measurement circuit. There are three steps in this process. First, the shot noise is used to determine the frequency and APC resistance dependent gain $G(\omega, R_{APC})$ and noise $S_{Vamp}(\omega, R_{APC})$ of the measurement circuit. Second, a model for the measurement circuit, including the value of circuit components and a frequency-dependent amplifier gain, is determined by fitting the calculated gain of the model circuit to the measured gain $G(\omega, R_{APC})$. Finally, the magnitude of the microwave voltage across the APC created by a microwave voltage bias is calibrated by comparing the shot noise created by the microwave bias to the shot noise created by a known dc voltage bias.

The measurement circuit's gain $G(\omega, R_{APC})$ and noise $S_{Vamp}(\omega, R_{APC})$ are determined using the voltage dependence of the shot noise due to tunneling electrons. As

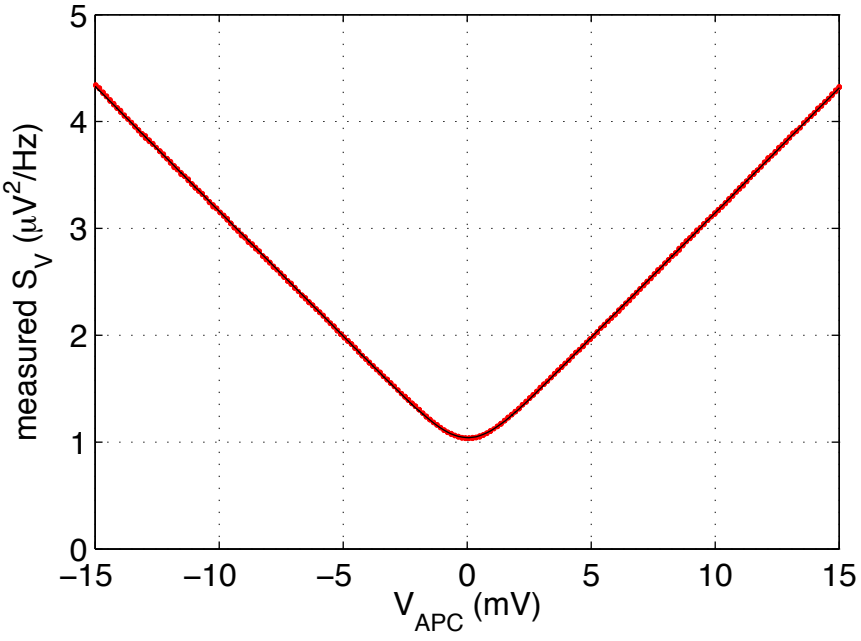

Figure 5.18: I plot the 500 MHz shot noise versus the dc voltage bias applied to the APC (red dots) and a fit of the data to equation 5.72 (black line).

shown in chapter 3, the shot noise of electrons tunneling across the APC creates voltage fluctuations with a spectral density

$$S_{Vsn}(V_{APC}) = 2\frac{2e^2}{h}\left[2k_BTD^2 + D(1-D)eV_{APC}\coth\left(\frac{eV_{APC}}{2k_BT}\right)\right]R_{APC}^2 \qquad (5.71)$$

when the APC is at temperature T with a dc voltage V_{APC} across the APC and electrons tunnel through a single spin-degenerate channel with probability D, that is, the APC resistance $R_{APC} = h/(2e^2D) > 13$ kΩ. The total measured noise S_V also includes the noise of the amplifiers in the measurement circuit and is scaled by the gain of the measurement circuit

$$S_V(V_{APC}) = G\left[S_{Vamp} + S_{Vsn}(V_{APC})\right] \qquad (5.72)$$

Since the shot-noise $S_{Vsn}(V_{APC})$ has a distinct V-shape as a function of V_{APC}, the gain and noise of the measurement circuit at a frequency ω can be determined by fitting equation 5.72 to the measured noise S_V at ω (figure 5.18).

An accurate circuit model for the measurement can be determined using the frequency and APC resistance dependent gain $G(\omega, R_{APC})$. The approximate measurement circuit (figure 5.19) is known, however the exact values of the capacitances, circuit components, and amplifier gain need to be determined. The shot noise S_{Vsn} will be amplified by this measurement circuit with a gain

$$|G| = \left|G_a(\omega)\frac{R_a'}{i\omega L + R_a'}\frac{Z_a(\omega)}{R_{APC} + Z_a(\omega)}\right| \qquad (5.73)$$

where $G_a(\omega)$ is the frequency dependent amplifier gain, $R_a' = 50\ \Omega$ is the amplifier impedance, $Z_a(\omega)$ is the impedance of the measurement circuit

$$Z_a(\omega) = \frac{i\omega L + R_a'}{1 - \omega^2 C_s L + i\omega C_s R_a'} \qquad (5.74)$$

and $i\omega L$ is the impedance of the inductor including an inductance L_i and shunting capacitance C_i

$$i\omega L = \frac{i\omega L_i}{1 - \omega^2 C_i L_i} \qquad (5.75)$$

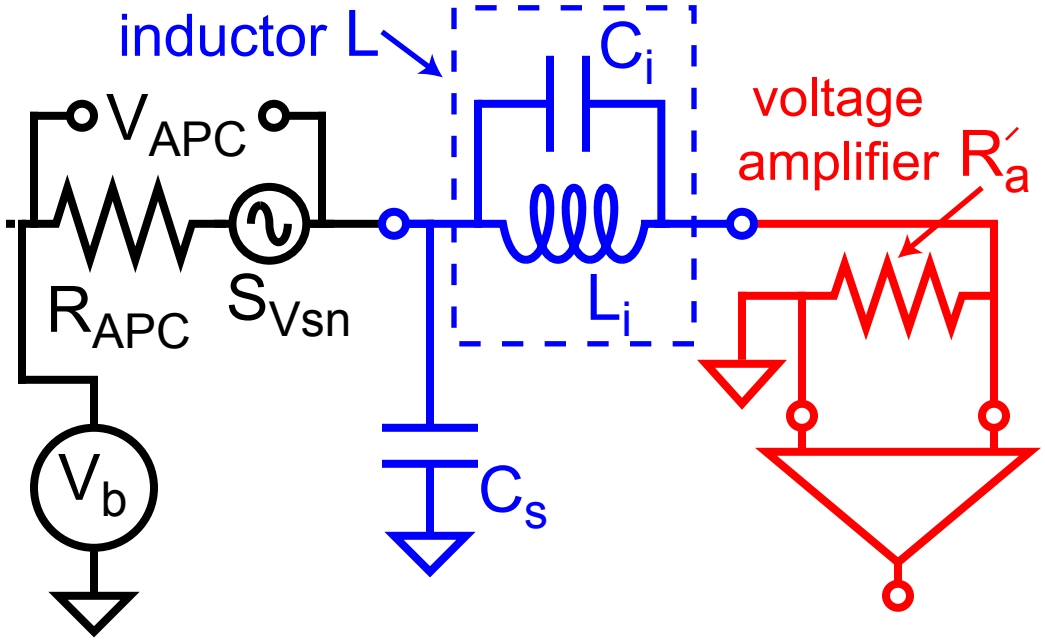

Figure 5.19: Approximate measurement circuit whose values L_i, C_i, C_s, and amplifier gain G_a are calibrated using shot noise.

Imperfections in this circuit model are included by making the amplifier gain $G_a(\omega, R_{APC})$ a function of APC resistance as well as frequency ω. This gain $G_a(\omega, R_{APC})$ and the value of L_i, C_i, and C_s are found by fitting equation 5.73 to the measured gain $G(\omega, R_{APC})$; the difference between the measured gain and the gain of the model circuit is less than 3% over a 15 MHz bandwidth and almost two decades in APC resistance (figure 5.20).

The shot noise of tunneling electrons can also be used to calibrate the voltage V_{APC}^{ac} across the APC created by a microwave voltage bias. In general, this quantity is difficult to calibrate because the attenuation of the microwave bias lines in the cryostat at cryogenic temperatures cannot be measured easily. As described in section 5.1.1, the shot noise S_{Vsn}^{dc} (equation 5.71) due to a dc voltage V_{APC} across the atomic point contact is related to the average shot noise S_{Vsn}^{ac} due to a microwave voltage $V_{APC}\cos(\omega_{ac}t)$

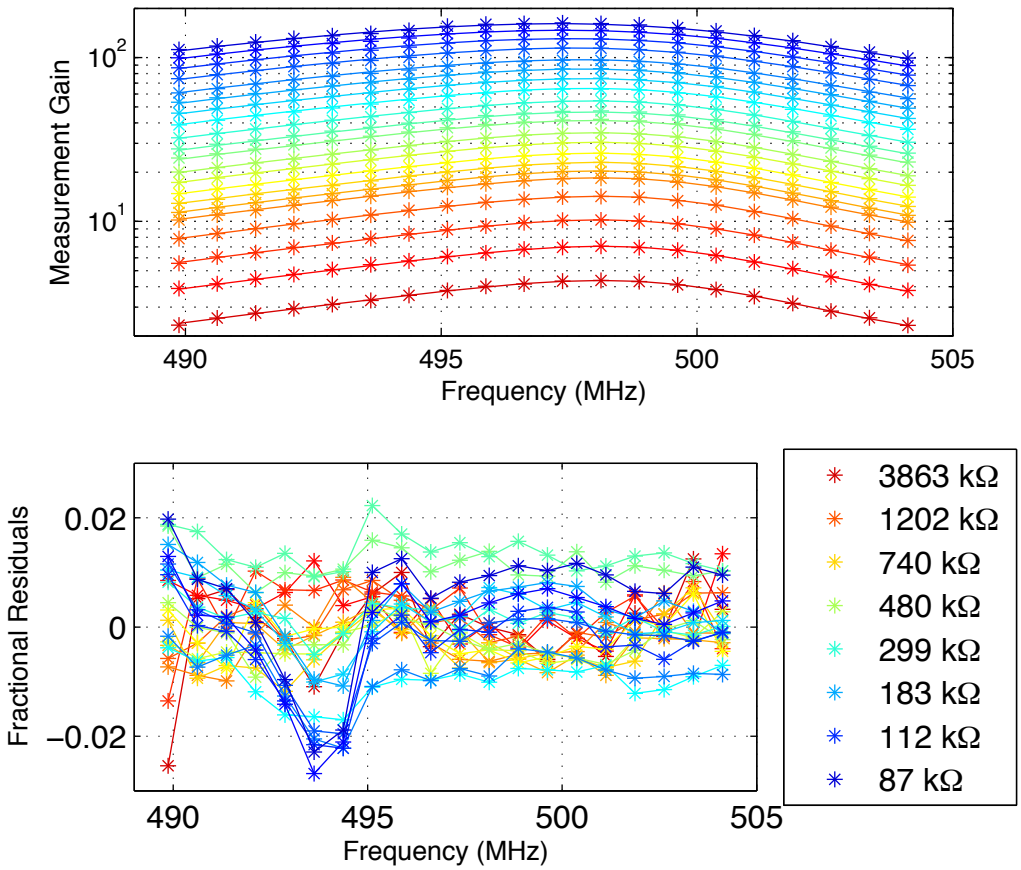

Figure 5.20: Calibrated measurement gain as a function of frequency at different APC resistances.

across the atomic point contact by

$$S^{ac}_{Vsn}(V_{APC}) = \frac{2}{\pi} S^{dc}_{Vsn}(V_{APC}) \tag{5.76}$$

when $eV_{APC} \gg k_B T$ and the measurement frequency $\omega \ll eV_{APC}/\hbar$ and $\omega \ll k_B T/\hbar$. Examining the case of a microwave voltage bias $V_T \cos(\omega_{ac} t)$ applied in transmission, the microwave voltage $V_{APC} \cos(\omega_{ac} t)$ across the APC due to this microwave bias is

$$V_{APC} = A V_T \frac{R_{APC}}{R_{APC} + Z_a(\omega_{ac})} \tag{5.77}$$

where A is the attenuation of the microwave lines and $Z_a(\omega_{ac})$ is the impedance of the measurement circuit at the frequency of the microwave bias ω_{ac}. Since the impedance

$Z_a(\omega)$ of the measurement circuit is known, the attenuation A can be found by comparing the shot noise due to a microwave bias V_T to the shot noise due to a known dc bias V_{APC} (equation 5.76, figure 5.21). A similar procedure can be used to calibrate a microwave voltage applied in reflection.

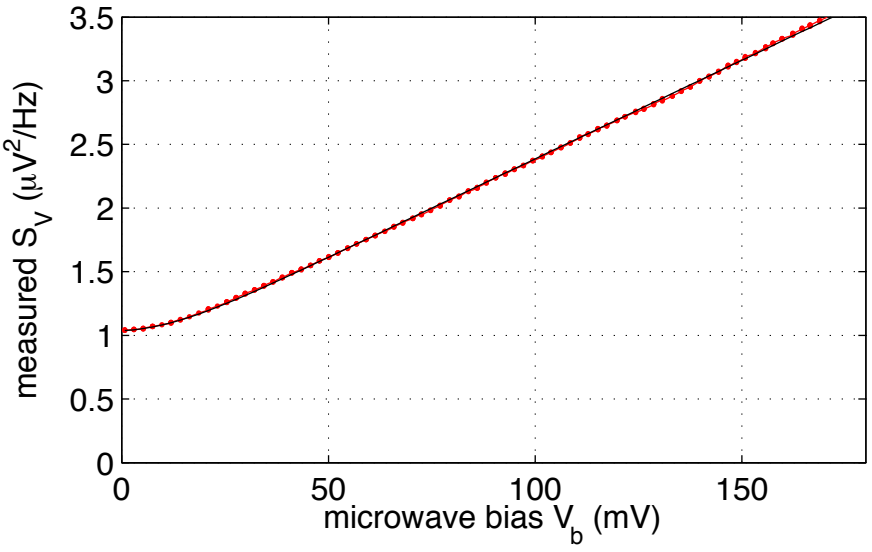

Figure 5.21: The 500 MHz shot noise is plotted versus the magnitude at the top of the cryostat of a 437 MHz microwave voltage bias V_b. Using this shot noise data, I determine that the microwave bias creates a voltage across the APC $V_{APC} = 0.10V_b$ which is consistent with the known attenuation in the cryostat.

Chapter 6

Sensitive Position Measurement using Electromigrated APC

In this chapter, I demonstrate a measurement of nanomechanical motion using an atomic point contact (APC) with shot-noise limited imprecision and an unexpectedly large backaction. I start by discussing the first measurements I made using an electromigrated APC. The resonance modes detected using this APC are compared to those detected using magnetomotive detection, confirming that the measured changes in APC resistance are due to nanomechanical motion. The sensitivity of the APC to nanomechanical motion is calibrated using the random thermal motion of the nanomechanical beam. The APC detector's backaction is also determined by measuring the thermal motion over a range of device temperatures. The properties of the APC displacement detectors are compared to the quantum limits. While the imprecision is limited by shot-noise which is the fundamental source of noise in the APC detector, the APC backaction is much larger than required by quantum mechanics.

I have also observed this unexpectedly large backaction in another electromigrated devices. Using a similar calibration based on thermal motion, I observe a large random backaction force that is proportional to shot noise and is not dependent upon whether the shot noise is created by a dc voltage or microwave voltage across the APC.

I finally compare these experimental APC detectors to the phenomenological model described in chapter 3 in which the backaction force is caused by momentum kicks from tunneling electrons. While the backaction force spectral density is propor-

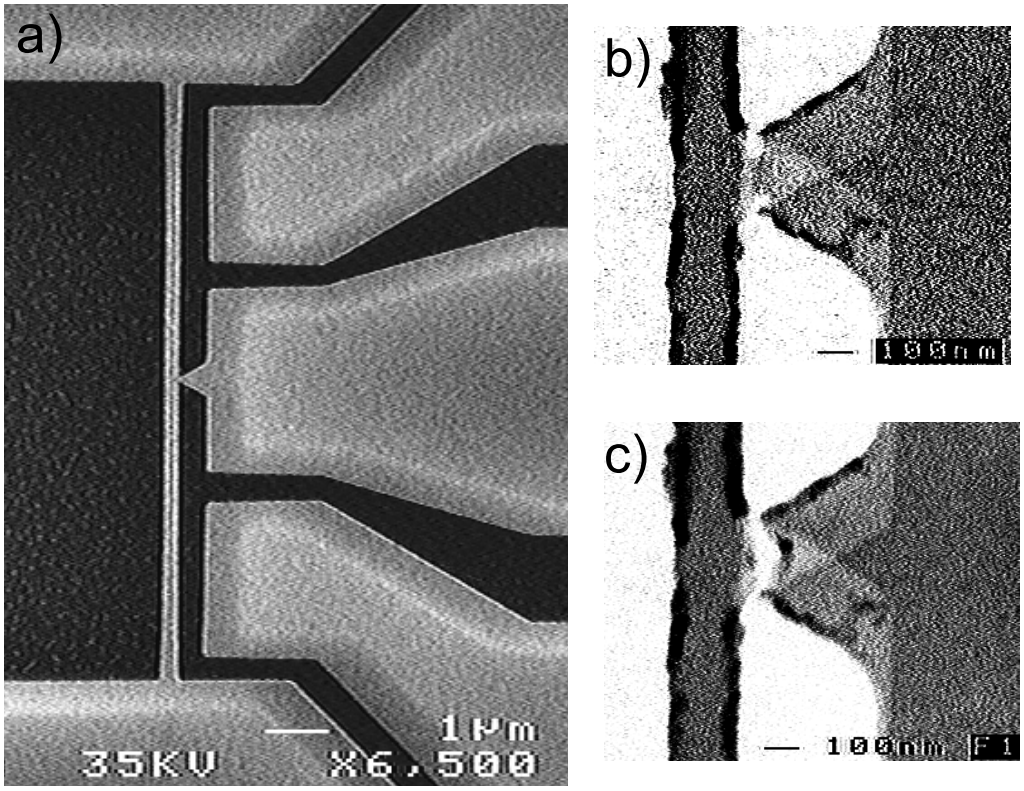

Figure 6.1: Scanning electron micrographs of nanomechanical structure prior to electromigration (a,b) and after electromigration (c). (a) large scale structure, with the gold nanostructure in grey/white and the GaAs substrate in black. The nanomechanical structure is suspended, and the white outline seen on the gold (grey) electrodes shows the extent of the undercut created by the etch. (b) prior to electromigration there is a thin, narrow gold contact (black) created using a triple angle evaporation (chapter 5). (c) after electromigration there is a clear gap between the triangular electrode and the nanomechanical beam. This APC was destroyed when a SMA connector broke at the top of the cryostat. The resulting spark and changes as the system warmed to room temperature caused a > 10 nm gap.

tional to the shot noise spectral density as in the model, the APC backaction is much larger than expected; each electron would have to deliver a momentum equal to about thirty times the Fermi momentum.

6.1 Initial Demonstration of the APC Displacement detector

I first demonstrated the use of an APC as a detector of nanomechanical motion using the nanomechanical structure in figure 6.1 and an electromigrated APC. The mechanical system is composed of a doubly clamped 5.6 μm long by 220 nm wide by 100 nm thick nanomechanical beam next to an atomically sharp point. The total mass of the nanostructure is about 2.3×10^{-15} kg. The fabrication of the device and APC creation using electromigration was described in chapter 4; in this case, the electromigration at cryogenic temperatures resulted in an APC with a resistance of 33 kΩ.

Nanomechanical motion is measured using a single sideband measurement, with

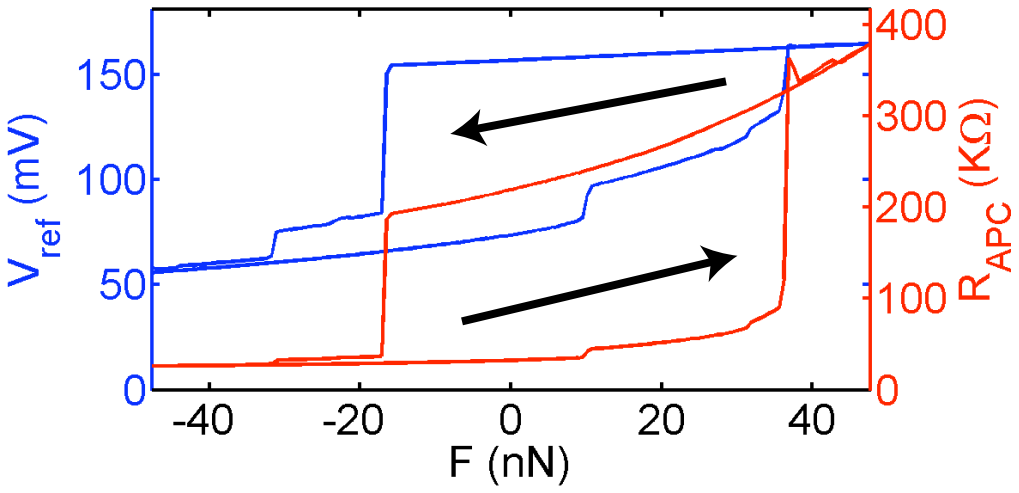

Figure 6.2: The average resistance of the APC, measured using a dc measurement (right axis, red) and a microwave reflectance measurement (left axis, blue) is plotted as a function of a Lorentz force (x-axis) applied by running a dc current through the nanomechanical beam. The resistance of the APC is varied from 3 kΩ to 380 kΩ and depends on the history of the applied force (black arrows indicate increasing force from low resistances and decreasing force from high resistances).

the bias voltage applied in reflection (see chapter 3 for details). All of the nanomechanical measurements were taken at the initial electromigrated resistance of 33 kΩ before the resistance of the APC was adjusted using a Lorentz force.

Unlike most electromigrated devices, the resistance of this electromigrated junction could be varied between 3 kΩ and 380 kΩ using a Lorentz force. A dc current is passed through the nanomechanical beam (figure 6.1) in a 9 T magnetic field which is perpendicular to the substrate. As the magnitude and orientation of the Lorentz force is varied betwen ±50 nN, the size of the APC gap and thus the resistance of the APC changes in a hysteretic loop (figure 6.2). This type of hysteretic loop is commonly seen in mechanically controllable break junctions (MCBJ, see chapter 4), where a mechanically applied strain is used to vary the APC resistance instead of a Lorentz force, however I am not usually able to control the resistance of electromigrated APCs. In all other electromigrated devices, the current passed through the nanomechanical beam melted the beam before the Lorentz force was large enough to appreciably change the resistance of the APC.

6.1.1 Comparison between APC detection and magnetomotive detection

In order to confirm that the APC detector is observing nanomechanical motion and not a different mesoscopic effect, the resonant modes observed with the APC detector can be compared to the modes observed using magnetomotive detection. Magnetomotive detection involves measuring changes in magnetic flux created by nanomechanical motion (figure 6.3, references [14, 190]). The nanomechanical structure is fabricated as part of a loop, and the loop is placed in a constant magnetic field. Nanomechanical motion changes the area of the loop which also changes the amount of flux enclosed by the loop; this creates a voltage signal which is equal to the rate of change in magnetic flux, $V_{sig} = d\Phi/dt$.

This magnetomotive technique is generally used to detect nanomechanical dis-

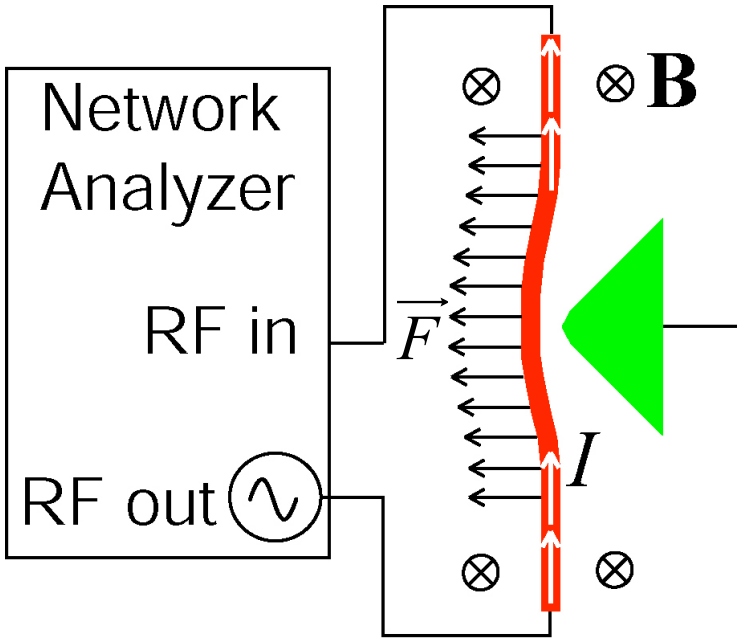

Figure 6.3: Representative circuit diagram used with magnetomotive drive and detection. The network analyzer is used to pass an ac current $\vec{I}$ at a frequency near a nanomechanical resonance through the nanomechanical beam (red) in a magnetic $\vec{B}$ field. The beam reacts to the Lorentz force per unit length $\vec{F}/l = \vec{B} \times \vec{I}$, and the motion creates an electromotive force $V_{sig} = d\Phi/dt$. This voltage signal mixes with the applied voltage and is detected using the network analyzer. The network analyzer is effectively measuring the transmission through a parallel RLC circuit, with a frequency and damping determined by the mechanical resonance.

placement due to a magnetomotive driving force (figure 6.3, references [14, 190]). This type of force is created by passing an ac current $\vec{I} = \vec{I}_{ac}\cos(\omega_{ac}t)$ through the nanomechanical structure in the presence of a magnetic field $\vec{B}$, creating a Lorentz force per unit length $\vec{F}/l = \vec{B} \times \vec{I}$. When using the combination of magnetomotive drive and detection, as in figure 6.3 and below, the nanomechanical structure has an electrical response that is equivalent to a parallel RLC circuit at frequencies near a mechanical resonance; the electrical RLC resonator has the same resonance frequency and width as the nanomechanical resonance [190].

The magnetomotive technique is not sensitive to the mesoscopic details of electron

transport in the APC. Both sides of the APC are at the same potential as ground, so there is no current flowing through the APC or voltage across the APC and the electrical current flowing through the beam is not affected by the presence of the APC (figure 6.3).

The shape of the nanomechanical modes, which is influenced by the mechanical properties of the APC (see chapter 3), affects the sensitivity of the magnetomotive and the APC measurements in different ways. The sensitivity of the magnetomotive measurement to a specific mechanical mode depends on the change in the magnetic flux enclosed by the measurement loop per unit motion. For example, if resonant motion does not change the amount of magnetic flux enclosed by the measurement loop then the resonant motion will not be detected by the magnetomotive measurement.

On the other hand, the APC measurement is coupled to those resonant modes which result in a strain at the APC; if the APC is located at a node of a mechanical resonance mode, then the APC measurement of displacement will not detect that resonant mode. Since the coupling of the APC and magnetomotive measurements to nanomechanical motion is very different, only one type of measurement can detect some nanomechanical modes.

The magnitude of the magnetomotive driving force also depends upon the mode shape. As discussed above, the magnetomotive drive is a Lorentz force per unit length $\vec{F}/l = \vec{B} \times \vec{I}$. The Lorentz force will couple strongly to a nanomechanical mode when the mode shape has a large average displacement in the same direction as the applied force (see [14, 190] for details). This implies that the modes which couple weakly to the magnetomotive detection will also couple weakly to the magnetomotive drive.

The APC and magnetomotive measurements detect similar resonance modes, confirming that the APC measurement is detecting nanomechanical motion. In figure 6.4 I plot the response to a magnetomotive drive at frequencies near the resonances observed at frequencies below 60 MHz; the response is detected using the magnetomotive

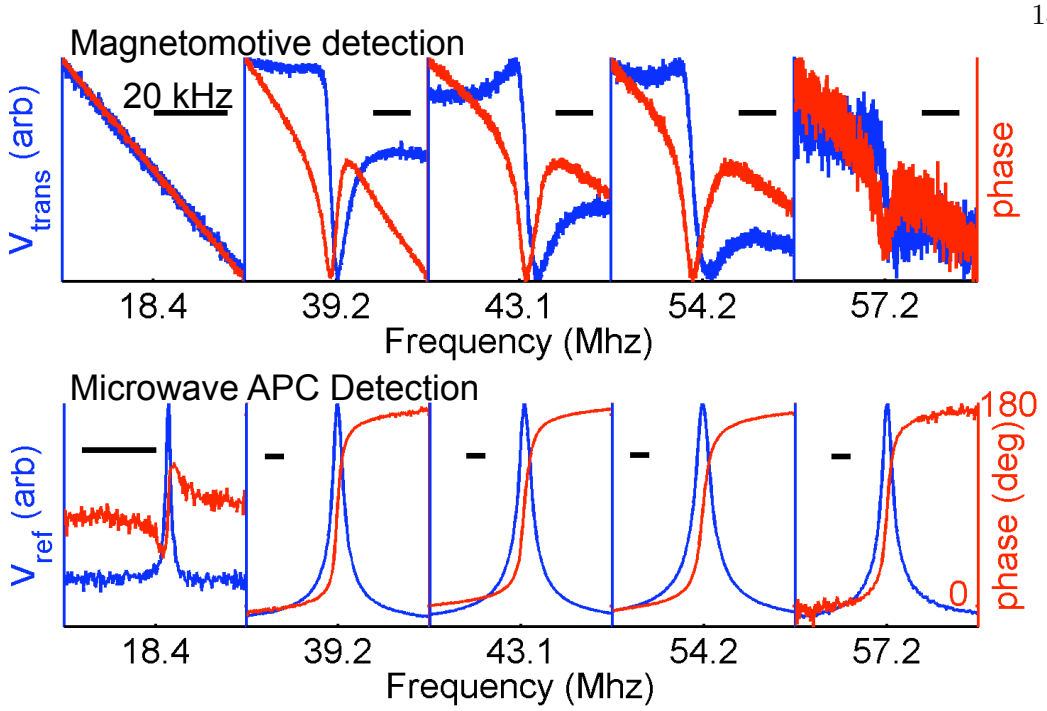

Figure 6.4: Measure response amplitude (blue) and phase (red) to a magnetomotive drive as a function of drive frequency for the observed resonance modes; the width of the black bar in each graph is 20 kHz. In the magnetomotive detection (top), the mechanical response is mixed with a background response resulting in a complicated line-shape. Using the APC detector (bottom), the background response is small enough that I generally observe the expected Lorentzian line-shape and 180° phase shift. The 18.4 Mhz mode is the only mode that is not detected by both the magnetomotive detection technique and the APC detector.

technique (figure 6.4, top) and APC technique (figure 6.4, bottom). Five resonances are observed using the APC technique at frequencies between 18.4 MHz and 57.2 MHz. The same four higher frequencies modes are also observed using magnetomotive detection, confirming that the resonances are due to nanomechanical motion.

The lowest frequency resonance detected using the APC measurement is not detected by the magnetomotive measurement; this can be explained by examining the mode shapes calculated using finite element modeling (figure 6.5, see chapter 3 for details). The magnetic field is applied in the vertical $\hat{z}$ direction so the magnetomotive measurement does not couple to nanomechanical motion in the $\hat{x}$ or $\hat{z}$ directions. Ex-

amining the mode shapes, the four higher frequency modes include motion in the $\hat{y}$ direction that couple to the magnetomotive measurement through a change in magnetic flux. On the other hand, the lowest frequency mode contains motion that is almost entirely in the $\hat{x}$ direction and is also reasonably symmetric. Such motion does not change the magnetic flux through the magnetomotive measurement loop, so it is not surprising that the magnetomotive measurement is unable to detect this lowest frequency mode.

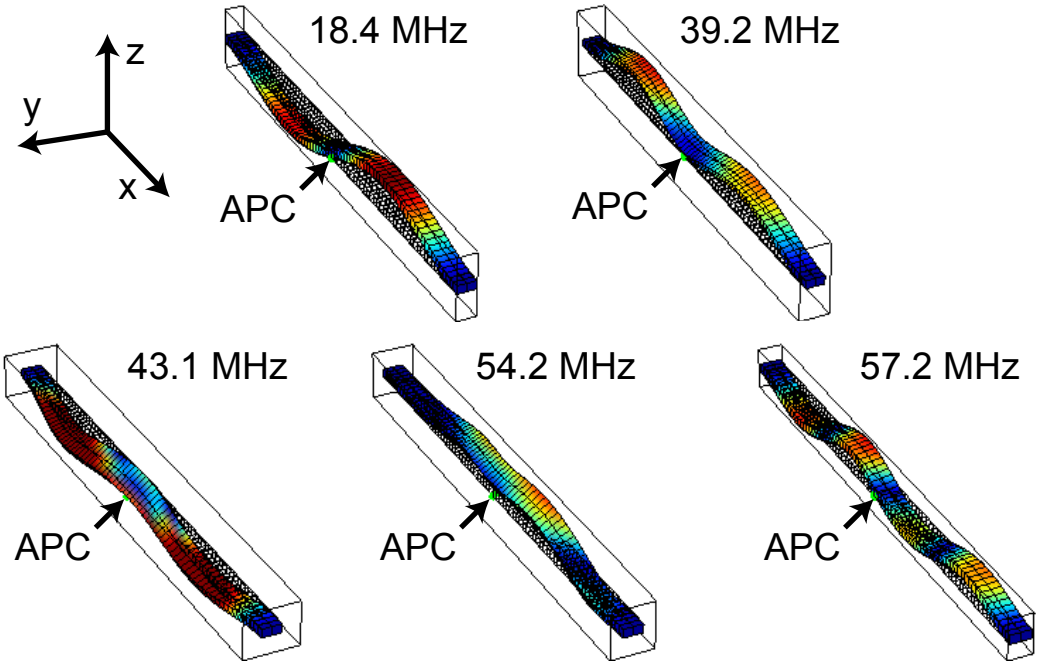

Figure 6.5: Finite element simulations of the five lowest frequency nanomechanical modes. The finite element model (FEM) was designed so that the FEM frequencies match the measured mode frequencies (figure 6.4). In the finite element model, the APC is represent by a spring attached at the green dot (labeled, in this orientation at the bottom left side of the middle of the beam). The APC detector is sensitive to motion that changes the length of the APC spring, that is, motion at the green dot. The magnetomotive detection technique is sensitive to average motion in the $\hat{y}$ direction.

6.1.2 APC detector calibration using thermal noise

I use the Brownian motion of the nanomechanical beam to calibrate the APC detector and determine the measurement backaction and imprecision. Nanomechani-

cal displacement is detected by applying a microwave voltage to the APC; changes in the APC resistance will then result in a voltage signal at the input of the microwave amplifier (see chapter 5). The frequency and magnitude of the nanomechanical motion are determined from this voltage signal. Relating the frequency of the voltage signal ω_s to the frequency of nanomechanical motion ω_x is simple; the frequency of the voltage signal is detuned from the microwave voltage frequency ω_b by the frequency of the nanomechanical motion, that is, $|\omega_x| = |\omega_b - \omega_s|$.

Determining the magnitude of nanomechanical displacement from the magnitude of the voltage signal is more difficult and requires a known displacement. As described in chapter 5, the calibration factor dx'/dV_s that relates a small voltage signal V_s to a small change in the APC gap x' is determined by the magnitude of the voltage bias V_{APC} across the APC, the resistance R_{APC} of the APC, the impedance Z_a of the measurement circuit, and the length scale λ that controls the probability of electrons tunneling across the APC

$$\frac{dx'}{dV_s} = -\frac{\lambda}{V_{APC}} \frac{R_{APC} + Z_a}{2Z_a} \frac{1}{G_{amp}\Lambda} \tag{6.1}$$

where G_{amp} is the gain of the amplifier chain used in the measurement and $\Lambda = 1/2$ for a single sideband measurement (see chapter 5). Each mode of the nanomechanical structure is effectively a simple harmonic oscillator (SHO) and the motion x of that SHO results in a change in the APC gap $x' = \chi x$, where the coupling χ is different for each mode and depends upon both the mode shape and the details of the APC (see chapter 3). Using this coupling χ, the voltage signal V_s is related to the motion x of a nanomechanical mode by

$$\frac{dx}{dV_s} = \frac{1}{\chi}\frac{dx'}{dV_s} = -\frac{\lambda}{\chi V_{APC}} \frac{R_{APC} + Z_a}{2Z_a} \frac{1}{G_{amp}\Lambda} \tag{6.2}$$

While it is possible to measure the resistance R_{APC} and both V_{APC} and Z_a using the shot noise calibration described in section 5.5, the length scale λ and coupling χ cannot

be directly measured. Instead, I measure the voltage signal due to a known displacement to calibrate the measurement and determine dx/dV_s.

The known displacement is provided by the Brownian motion of the beam. Because each nanomechanical mode is effectively a SHO coupled to a heat bath at temperature T_{beam}, each mode experiences a random force with a spectral density $S_F^T = 4m\gamma k_B T_{beam}$ where m is the effective mass of the SHO and γ is the SHO damping constant. This random force creates random displacement with a spectral density

$$S_x^T = \frac{S_F^T}{m^2} \frac{1}{(\omega_0^2 - \omega^2)^2 + \gamma^2\omega^2} \tag{6.3}$$

The integrated mean squared displacement due to the random force is

$$(\Delta x_T)^2 = \int_0^\infty S_x^T \frac{d\omega}{2\pi} = \int_0^\infty \frac{S_F^T}{m^2} \frac{1}{(\omega_0^2 - \omega^2)^2 + \gamma^2\omega^2} \frac{d\omega}{2\pi} = \frac{k_B T_{beam}}{m\omega_0^2} \tag{6.4}$$

This displacement is consistent with the equipartition theorem; since each mode is effectively a SHO with two degrees of freedom, the average potential energy is $m\omega_0^2 (\Delta x_T)^2 /2 = k_B T_{beam}/2$.

I use the known Brownian motion to determine the calibration factor dx/dV_s which is used to infer nanomechanical displacement from the measured voltage signal. Near a nanomechanical resonance, the amplifier noise and shot noise will contribute a white background with a spectral density S_{V_n} to the measured voltage spectral density S_{V_m} (figure 6.6). This white background of apparent motion is simply the imprecision in the measurement. The Brownian motion of the nanomechanical structure creates a signal which is added to the noise whose voltage spectral density S_{V_s} has a Lorentzian line shape

$$S_{V_s} = \left(\frac{dx}{dV_s}\right)^{-2} \frac{S_F^T}{m^2 \left[(\omega_0^2 - \omega^2)^2 + \gamma^2\omega^2\right]} \tag{6.5}$$

The integrated strength of the Lorentzian signal is

$$(\Delta V_s)^2 = \int_0^\infty S_{V_s} \frac{d\omega}{2\pi} = \left(\frac{dx}{dV_s}\right)^{-2} \frac{S_F^T}{4m^2\gamma\omega_0^2} \tag{6.6}$$

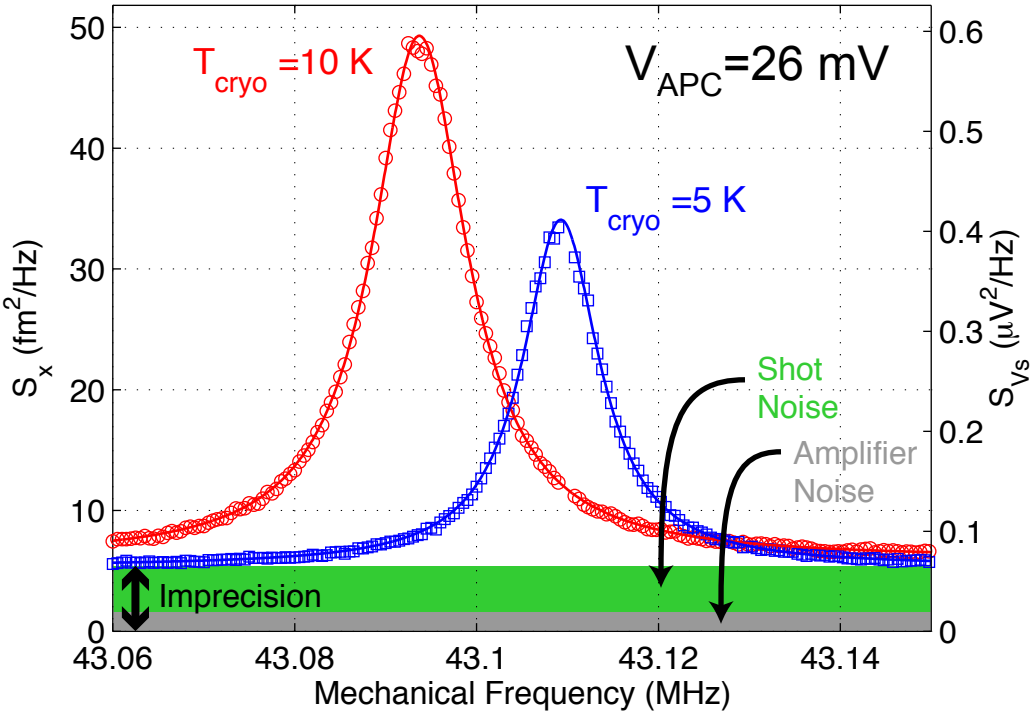

Figure 6.6: The spectral density of the fluctuations in the voltage signal (right axis) are plotted as a function of frequency near one of the nanostructure's mechanical resonances when the cryostat is at 10 K (red) and 5 K (blue). The Lorentzian peaks in the noise are due to the Brownian motion of the beam. Using the equipartition theorem and the integrated strength of the peaks, the y-axis can be calibrated in displacement units (left axis). The Lorentzian peaks are on top of a white background; this apparent motion is the measurement imprecision ($S_x = 5.3$ fm^2/Hz for $V_{APC} = 26$ mV) due to a combination of shot noise (green) and amplifier noise (grey).

In the simple case where there is no measurement backaction, the temperature T_{beam} of the nanostructure will be equal to temperature T_{cryo} of the cryostat and the calibration factor can be determined from T_{cryo} and the integrated mean squared $(\Delta V_s)^2$ voltage signal

$$\frac{dx}{dV_s} = \sqrt{\frac{k_B T_{cryo}}{m\omega_0^2 \left(\Delta V_s\right)^2}} \tag{6.7}$$

However, I need to include the measurement backaction to accurately describe the experimental system which complicates the calibration. The effect of the measurement on the nanomechanical system can be divided into two parts. First, the measurement

can effect the nanostructure by increasing the temperature of the bulk material. The microwave current passing through the APC dissipates power in the nanostructure. This power can raise the temperature of the nanostructure above the temperature of the cryostat by an unknown amount. Experimentally this effect spoils the calibration based on Brownian motion, but it is only a problem at low cryostat temperatures < 4 K, depending upon the dissipated power. This problem is avoided, as discussed in more detail below, by ignoring data taken at cryostat temperatures where the dissipated power has begun to effect the temperature of the nanostructure.

Second, the measurement will necessarily create a random force on the nanostructure which depends on the precision of the measurement (chapter 3). This type of backaction enforces the Heisenberg Uncertainty Principle, and, unlike the first effect, is interesting in the context of quantum limited displacement measurements. I use a phenomenological model for the measurement backaction (chapter 3) where the measurement backaction is a temperature independent, APC voltage bias dependent, random force with a white spectral density S_F^{BA}. This backaction can be parameterized in temperature units, $T_{BA} = S_F^{BA}/(4m\gamma k_B)$, and the mean squared Brownian motion will be the same as if the nanostructure was at a temperature $T_{beam} = T_{cryo} + T_{BA}$.

To determine both S_F^{BA} and the calibration factor dx/dV_s for a given bias V_{APC}, it is necessary to collect data at multiple cryostat temperatures T_{cryo}. Experimentally, I determine the calibration factor and backaction force of the nanomechanical measurement at four different microwave bias voltages V_{APC}, or gains, between 4 mV and 39 mV by measuring nanomechanical motion at cryostat temperatures between 300 mK and 10 K. At each temperature and bias voltage, I measure the fluctuating voltage signal near the mechanical resonance (figure 6.7) and determine the mechanical resonance frequency ω_0, damping constant γ, and integrated mean squared voltage signal $(\Delta V_s)^2$. In figure 6.7 I plot $(\Delta V_s)^2$ as a function of cryostat temperature T_{cryo} for four different APC bias voltages. For a given APC bias voltage, when the temperature of the

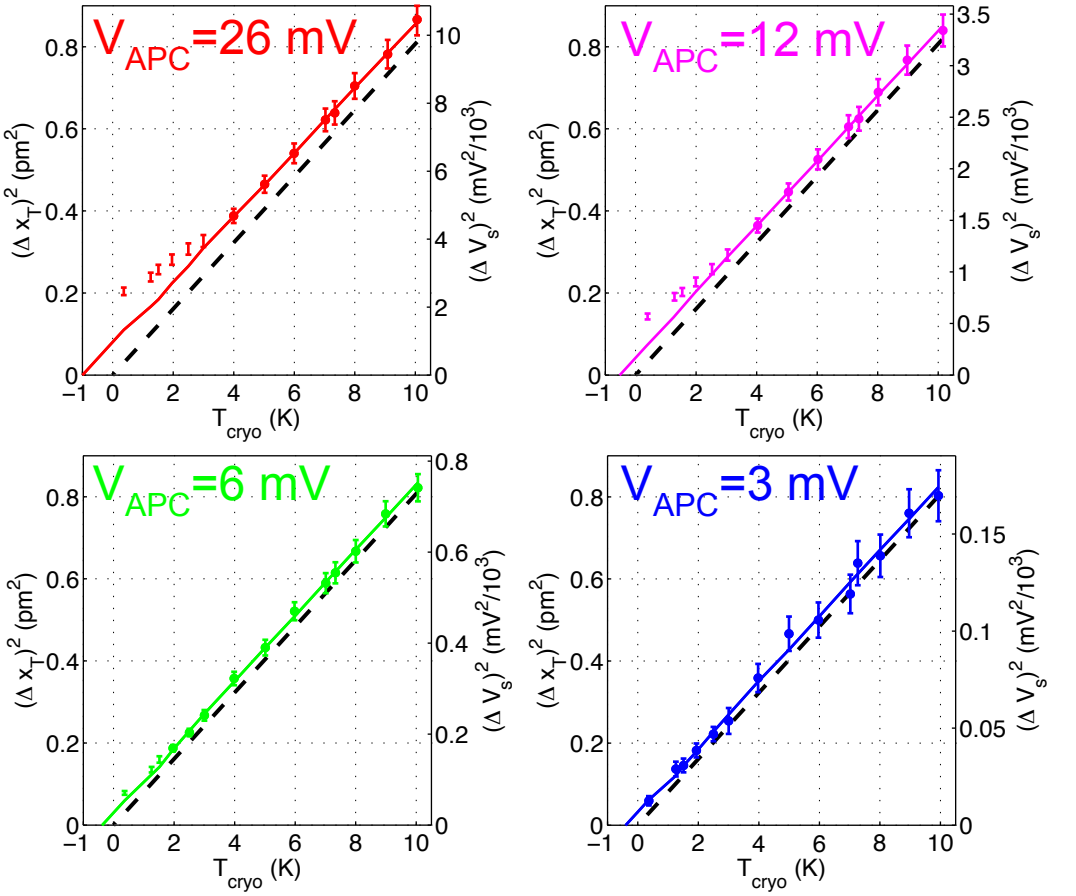

Figure 6.7: Integrated strength $(\Delta V_s)^2$ (data points) as a function of cryostat temperature T_{cryo} at four different microwave bias voltages. Each plot includes a fit line (solid line) to a phenomenological model which assumes a temperature-independent backaction force S_F^{BA}. The data clearly deviates from this model at low T_{cryo} and high V_{APC}, so only the solid data points are included in the fit. This line is not simply proportional to T_{cryo}, as expected from the equipartition theorem, because the width of the resonance γ changes by 30% between 10 K and 250 mK. Based on this fit the y-axis can be calibrated in displacement units (left axis) and I include a line (dashed black line) which shows the expected integrated strength based on the equipartition theorem in the absence of backaction.

nanostructure is equal to the temperature of the cryostat then

$$(\Delta V_s)^2 = \left(\frac{dx}{dV_s}\right)^{-2} \frac{k_B}{m\omega_0^2}\left(T_{cryo} + \frac{S_F^{BA}}{4m\gamma k_B}\right) \tag{6.8}$$

and the integrated strength $(\Delta V_s)^2$ can be fit using linear fit coefficients a and b

$$(\Delta V_s)^2 = a\frac{k_B T_{cryo}}{m\omega_0^2} + \frac{b}{4m^2\omega_0^2\gamma} \tag{6.9}$$

The fit variables are used to determine the calibration factor dx/dV_s and the backaction force S_F^{BA}

$$\frac{dx}{dV_s} = \sqrt{\frac{1}{a}} \tag{6.10}$$

$$S_F^{BA} = \frac{b}{a} \tag{6.11}$$

The observed backaction force S_F^{BA} at each of the four different APC voltage biases is given in table 6.1.

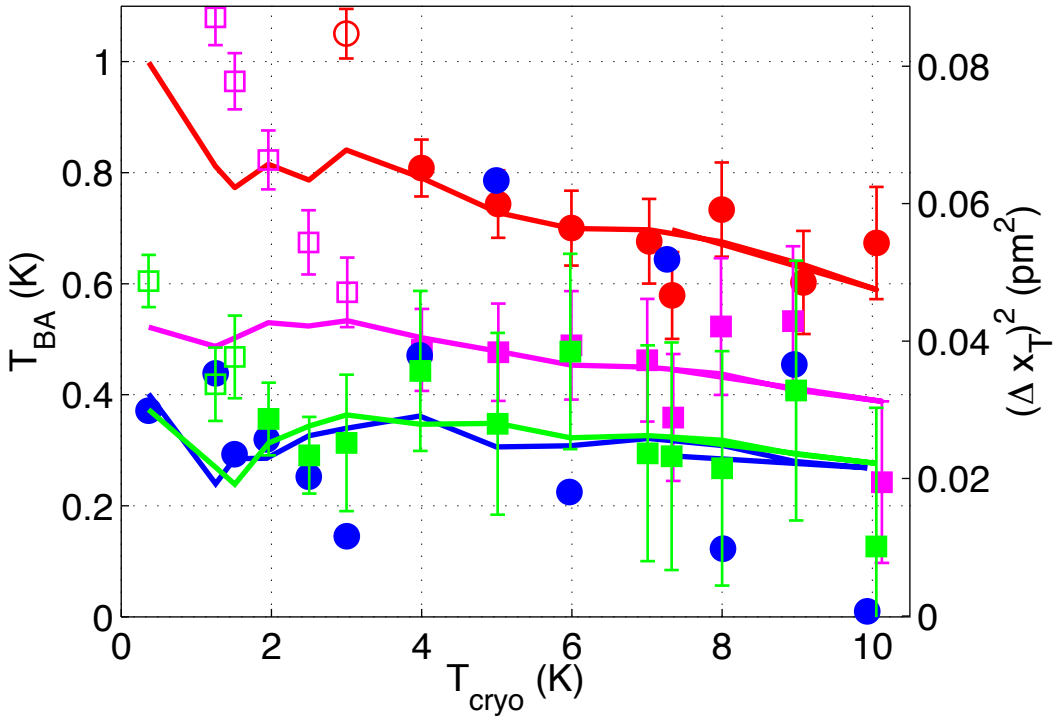

Figure 6.8: Backaction temperature $T_{BA} = S_F^{BA}/(4m\gamma k_B)$ (left axis) plotted versus cryostat temperature T_{cryo} at four different microwave voltage biases: 26 mV (red), 12 mV (magenta), 6 mV (green), and 3 mV (blue). The error bars for the 3 mV data (blue) are not shown, but are about twice the size of green error bars. The backaction temperature is proportional to the difference (right axis) between the expected integrated strength due to the equipartition theorem (dashed black lines in figure 6.7) and the measured integrated strength (data points and solid fit line in figure 6.7). The fit lines (solid lines) are dependent on temperature because the fit model assumes a constant backaction force S_F^{BA} and the width of the resonance γ changes by 30% between 10 K and 250 mK. The hollow data points are excluded from the fit because local heating causes the temperature of the nanostructure to deviate from the cryostat temperature.

In performing the fit to equation 6.9, I ignore the low temperature data points where the temperature of the nanostructure deviates from the temperature of the cryostat. As discussed above, the local temperature of the nanostructure is increased by the power dissipated in the APC. The effect of deviation of the local temperature from the cryostat temperature is observed in figure 6.7, where the measured values (dots) of the integrated strength deviate from the expected value based on the equipartition theorem and the cryostat temperature at large bias voltages and low temperatures. This deviation is even more apparent in figure 6.8, where the backaction temperature T_{BA}

$$T_{BA} = \frac{(\Delta V_s)^2}{a}\frac{m\omega_0^2}{k_B} - T_{cryo} = \frac{b}{4m\gamma k_B a} \tag{6.12}$$

is plotted as a function of the cryostat temperature. In this figure the solid data points are used in the fit to equation 6.9 (solid lines), while hollow data points are excluded from the fit because the temperature of the nanostructure deviates from the cryostat temperature. As expected, the temperature at which the dissipated power begins to have a measurable effect decreases as the microwave power decreases.

Having calibrated the detector and determined the backaction force, determining the detector imprecision S_x in displacement units is simple. I have already measured the detector imprecision in voltage units; this imprecision is the white background S_{V_n} observed when measuring the magnitude of voltage fluctuations near a nanomechanical resonances (figure 6.6) and is composed of contributions from the shot noise and the amplifier noise. The voltage fluctuations in figure 6.6 are calibrated in displacement units using dx/dV_s, and the displacement imprecision S_x is simply the magnitude of the white background noise in displacement units

$$S_x = S_{V_n}\left(\frac{dx}{dV_s}\right)^2 \tag{6.13}$$

The observed imprecision S_x at each APC voltage bias is shown in table 6.1.

I use the shot-noise contribution to the displacement imprecision $S_{x_{sn}}$ to determine the effective length scale λ/χ which sets the scale of the APC resistance's expo-

APC voltage bias	Displacement Imprecision S_x	Backaction Force S_F
2.6 mV	126.8 ± 5 fm^2/Hz	2800 ± 2000 aN^2/Hz
5.5 mV	36.1 ± 1 fm^2/Hz	2800 ± 2000 aN^2/Hz
12 mV	11.29 ± 0.5 fm^2/Hz	3900 ± 3000 aN^2/Hz
26 mV	5.33 ± 0.2 fm^2/Hz	6100 ± 3000 aN^2/Hz

Table 6.1: The observed imprecision and backaction of a displacement detector created using an electromigrated APC with resistance R_{APC}=33 kΩ and various APC bias voltages V_{APC}. This detector is used to measure the 43 MHz mode of the nanostructure shown in figure 6.1.

nential dependence on nanomechanical displacement x, $R_{APC} = R_0 \exp[\chi x/\lambda]$. For the same microwave bias and R_{APC}, a smaller length scale will result in a displacement measurement with a smaller imprecision. The length scale is calculated from the shot-noise contribution $S_{x_{sn}}$ to the displacement; from chapter 5,

$$S_{x_{sn}} = \left[S_{V_{sn}} \left(\frac{Z_a}{R_{APC} + Z_a} \right)^2 \right] \left(\frac{dx}{dV_s} \right)^2 \tag{6.14}$$

$$S_{x_{sn}} = \frac{e\zeta\Xi R_{APC}}{2|V_{APC}|\Lambda^2} \left(\frac{\lambda}{\chi} \right)^2 \tag{6.15}$$

For the 33 kΩ device and 43 MHz mode, $\zeta = 2/\pi$ because the shot noise is due to a microwave bias and $\Lambda = 1/2$ because the measurement is single sideband. Solving for the effective length scale,

$$\frac{\lambda}{\chi} = \sqrt{S_{x_{sn}} \frac{2|V_{APC}|\Lambda^2}{eR_{APC}\zeta\Xi}} = \sqrt{S_{x_{sn}} \frac{\pi|V_{APC}|}{4eR_{APC}\Xi}} \tag{6.16}$$

and for the 33 kΩ APC detector and 43 MHz mode the effective length scale $\lambda/\chi = 3$ nm

.

The effective length scale $\lambda/\chi = 3$ nm is larger than in a standard STM because the APC resistance is relatively small, $R_{APC} = 33$ kΩ, and χ, the coupling between motion at the APC gap and nanomechanical displacement, is less than 1. At large tunneling resistances, $R_{APC} > 100$ MΩ, the length scale in a standard STM is about $\lambda/\chi = 0.1$ nm. In a STM, $\chi = 1$ because the APC support structure is much stiffer than the effective spring constant of the APC so $\lambda = 0.1$ nm. This length scale is consistent

with electrons tunneling through a barrier equal to the work function of bulk gold $\phi = 5$ eV ($\lambda = \hbar/\sqrt{2m_e\phi}$, see chapter 3). However, as the resistance of the tunneling contact in an STM is decreased, the height of the tunneling barrier also decreases. This break-down in the apparent height of the tunnel barrier results in a larger length scale λ and contributes to the large observed $\lambda/\chi = 3$ nm in the $R_{APC} = 33$ kΩ APC.

The coupling constant $\chi = x'/x$ that relates displacement of the nanomechanical modal coordinate x to changes in the APC gap x' also contributes to the large observed $\lambda/\chi = 3$ nm. Based on a finite element simulation of the 43 MHz mode shape (see chapter 3) and assuming that the strain caused by nanomechanical motion on the atomic scale at the APC gap is equal to the macroscopic strain near the APC, I estimate $\chi \approx 0.5$ and therefore $\lambda \approx 1.5$ nm. This APC displacement detector is about an order of magnitude less sensitive to changes in the APC gap as is possible with a standard STM, assuming both measurement imprecisions are dominated by the shot noise of tunneling electrons.

6.1.3 The Heisenberg uncertainty principle and the standard quantum limit

The Heisenberg uncertainty principle limits both the product of the imprecision S_x and backaction S_F^{BA} and, for a harmonic oscillator, the minimum total imprecision in the measurement S_{xtot}. I consider the simple case of a continuous linear amplifier of position with uncorrelated imprecision and backaction. In this case, the Heisenberg constraint is

$$S_x S_F^{BA} \geq \hbar^2 \tag{6.17}$$

where I continue to use a one-sided spectral density; if a two-sided spectral density is used, then $S_x S_F^{BA} \geq \hbar^2/4$.

When measuring the position of a harmonic oscillator, the Heisenberg uncertainty

principle also limits the total displacement imprecision S_{xtot}; the minimum total imprecision is called the standard quantum limit. The random backaction force with spectral density S_F^{BA} results in random displacement with a spectral density at frequency ω

$$S_{xBA} = \frac{S_F^{BA}}{m^2} \frac{1}{\left(\omega_0^2 - \omega^2\right)^2 + \gamma^2\omega^2} \tag{6.18}$$

The total displacement imprecision S_{xtot} is due to the sum of the imprecision S_x and backaction S_{xBA}

$$S_{xtot} = S_x + S_{xBA} = S_x + \frac{S_F^{BA}}{m^2} \frac{1}{\left(\omega_0^2 - \omega^2\right)^2 + \gamma^2\omega^2} \tag{6.19}$$

To be clear, while both S_x and S_{xBA} cause displacement noise, S_x is due to voltage noise added by the measurement process and is not due to actual beam motion. The backaction contribution S_{xBA} is due to actual beam motion, and creates noise in the measurement that is very similar to the noise created by Brownian motion. Using the Heisenberg constraint 6.17, the total displacement noise is

$$S_{xtot}(\omega) \geq S_x + \frac{\hbar^2}{m^2 S_x} \frac{1}{\left(\omega_0^2 - \omega^2\right)^2 + \gamma^2\omega^2} \tag{6.20}$$

and at the mechanical resonance $\omega = \omega_0$

$$S_{xtot}(\omega_0) \geq S_x + \frac{1}{S_x} \frac{\hbar^2}{m^2\gamma^2\omega_0^2} \tag{6.21}$$

At the mechanical resonance $\omega = \omega_0$ the minimum total imprecision, also called the standard quantum limit (SQL)

$$S_{xtot}(\omega_0) \geq \frac{2\hbar}{m\gamma\omega_0} \tag{6.22}$$

occurs when the contributions to the total noise from the imprecision and backaction are equal

$$S_x = S_{xSQL} = \frac{\hbar}{m\gamma\omega_0} \tag{6.23}$$

$$S_F^{BA} = S_{FSQL}^{BA} = m\gamma\hbar\omega_0 \tag{6.24}$$

When comparing S_x and S_F^{BA} to each other and the standard quantum limit, it is convenient to express both quantities in terms of energy quanta. The backaction force S_F^{BA} increases the energy of the beam by an amount, in quanta,

$$N_F = \frac{S_F^{BA}}{4m\gamma\hbar\omega_0} \tag{6.25}$$

Similarly, at the mechanical resonance ω_0 the noise in the measurement results in an apparent increase in energy

$$N_x = \frac{S_x m\gamma\omega_0}{4\hbar} \tag{6.26}$$

In quanta, the Heisenberg constraint is

$$N_x N_F \geq \frac{1}{16} \tag{6.27}$$

and the total imprecision

$$N_{tot} = N_F + N_x \geq \frac{1}{2} \tag{6.28}$$

is minimized at the standard quantum limit where

$$N_x = N_F = N_{SQL} = \frac{1}{4} \tag{6.29}$$

6.1.4 The experimental APC detector compared to the quantum limits

In this subsection I compare the experimental results from the APC detector described at the beginning of this section to the the limits imposed by the Heisenberg uncertainty principle, as described in the previous subsection. In figure 6.9 I plot the measured imprecision N_x and backaction N_F as function of APC bias voltage. At the largest APC voltage bias, the imprecision is limited by shot noise, the fundamental source of noise in an APC detector, and the imprecision $\sqrt{N_x} = 45/2$ is 45 times the standard quantum limit. At the same voltage bias, the backaction force $\sqrt{N_F} = 38/2$ is 38 times the standard quantum limit.

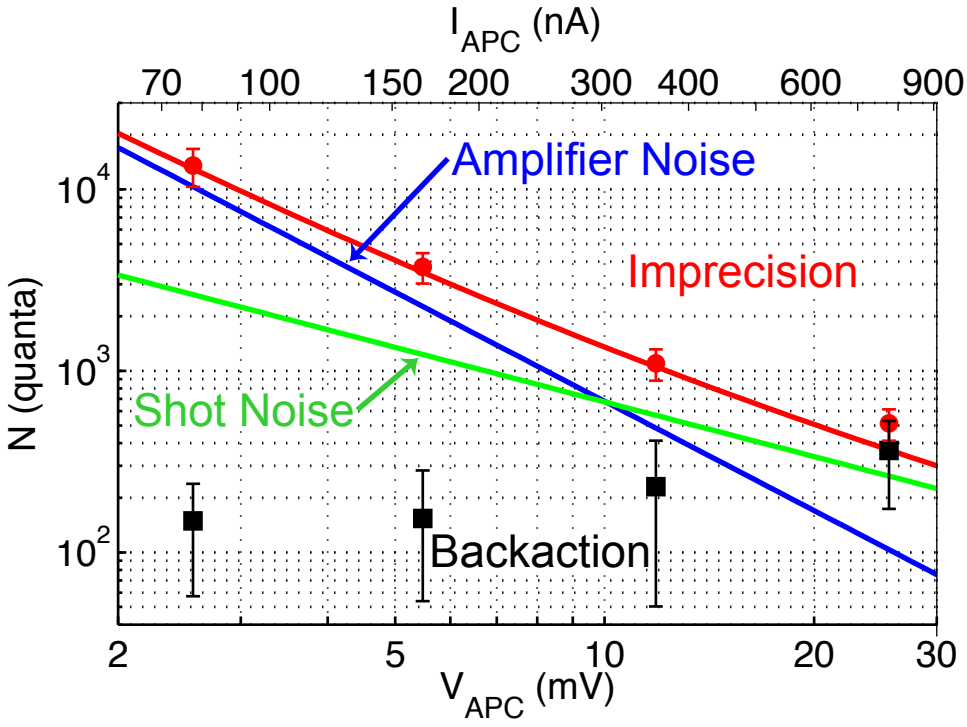

Figure 6.9: Measurement imprecision quanta N_x (red) and backaction quanta (black) as a function of APC voltage V_{APC} (top axis) or current I_{APC} (bottom axis). Both the amplifier noise (blue line) and shot noise (green line) contribute to the imprecision (red line), which is dominated by shot noise at the largest APC bias voltage. The total imprecision $N_x + N_F$ is approximately minimized at the largest APC bias voltage where $N_x \approx N_F$. The uncertainty (error bars) in the imprecision and backaction is dominated by the uncertainty in the local temperature of the nanostructure.

APC voltage bias	$\sqrt{S_x S_F^{BA}}$	imprecision N_x	backaction N_F	total N_{tot}
2.6 mV	$6000\hbar$	54000/4	600/4	27000/2
5.5 mV	$3000\hbar$	15000/4	600/4	8000/2
12 mV	$2000\hbar$	4400/4	900/4	2700/2
26 mV	$1700\hbar$	2050/4	1500/4	1800/2
detector at SQL	$\hbar$	1/4	1/4	1/2

Table 6.2: The observed imprecision-backaction product, imprecision quanta, backaction quanta, and total imprecision quanta of a displacement detector created using an electromigrated APC with resistance R_{APC}=33 kΩ and various APC bias voltages V_{APC}. This detector is used to measure the 43 MHz mode of the nanostructure shown in figure 6.1. The observed values can be compared to the values of a quantum-limited detector operated at the standard quantum limit (last line of the table).

The imprecision-backaction product at the highest APC bias voltage $\sqrt{N_x N_F} = 1700/4$ is 1700 times the minimum required by the Heisenberg uncertainty principle $\sqrt{N_x N_F} \geq 1/4$. Unlike an ideal detector, this product also becomes larger as the bias voltage is decreased (table 6.2) because the amplifier noise becomes significant (blue line, figure 6.9).

Since the noise in the APC detector at the highest APC bias voltage is limited by shot noise, the large imprecision-backaction product is due to a large backaction force. The APC detector is theoretically predicted to be an ideal, Heisenberg limited detector $\sqrt{N_x^{fund} N_F^{fund}} = 1/4$ (see chapter 3). Since the Heisenberg uncertainty principle does not individually constrain N_x or N_F, determining whether N_x, N_F, or both are non-ideal requires understanding the source of measurement imprecision or backaction. In the APC detector, the fundamental source of noise is the shot noise of tunneling electrons. At the highest APC voltage, the shot noise accounts for 70% of the measured N_x, so $\sqrt{N_x} = 1.2\sqrt{N_x^{fund}}$. Since the observed imprecision is close to the theoretical expectation, the observed backaction force is significantly larger than required by quantum mechanics, $\sqrt{N_F} = 1400\sqrt{N_x^{fund}}$. In the next section I will focus on this large backaction force, examining possible sources of the force in the context of the phenomenological model described in chapter 3.

Finally, I have operated the detector near the APC bias voltage which minimizes the total displacement imprecision $\sqrt{N_{tot}} = \sqrt{N_x + N_F}$. This minimum occurs when $N_x = N_F$, so the total displacement uncertainty at the highest APC voltage bias $\sqrt{N_{tot}} = 42/\sqrt{2}$ is close to the minimum achievable N_{tot}. The total imprecision at the highest APC voltage bias is 42 times the standard quantum limit, and this N_{tot} is near the minimum achievable N_{tot} and yet still significantly above the standard quantum limit because the backaction force is significantly larger than that required by quantum mechanics.

6.2 Another Similar Electromigrated Device

I have observed a similar large backaction force in another electromigrated APC. This APC had a resistance of 16 kΩ, and was created as part of the nanomechanical structure in figure 6.10, composed of a doubly-clamped nanomechanical beam (6.3 μm long by 200 nm wide by 90 nm thick) next to the APC. Nanomechanical motion is detected using a single sideband measurement with the bias voltage applied in transmission (see chapter 3 for details).

This device was initially electromigrated to a resistance of 71 kΩ and later jumped to 16 kΩ. Using a dc Lorentz force, as described in the previous section, it was possible to hysteretically modify the resistance between 75 kΩ and 90 kΩ using a force ±30 nN. Later, the device resistance irreversibly jumped to 16 kΩ while applying a driving force using a voltage across the APC. The measurements described in this section where taken while the APC resistance was 16 kΩ. The device was finally destroyed while attempting to modify the resistance.

I determine the frequencies of the nanomechanical modes by measuring the mechanical displacement in response to an electrostatic driving force. The electrostatic force F_C is created by applying a voltage V_g to the electrostatic gate (figure 6.10 and 6.11). The nanomechanical structure experiences a force

$$F_C = \frac{1}{2}\frac{dC_g}{dx}V_g^2 \tag{6.30}$$

where x is the displacement of one of the nanostructure's modal coordinates and C_g is the capacitance between the nanostructure and the electrostatic gate. I usually apply both a dc voltage and an ac voltage at frequency ω_g, $V_g = V_{gdc} + V_{gac}\cos(\omega_g t)$, to the gate.

Using this type of voltage bias, $V_g = V_{gdc} + V_{gac}\cos(\omega_g t)$, simplifies the displacement measurement in two different ways. First, it results in a force F_C and displacement

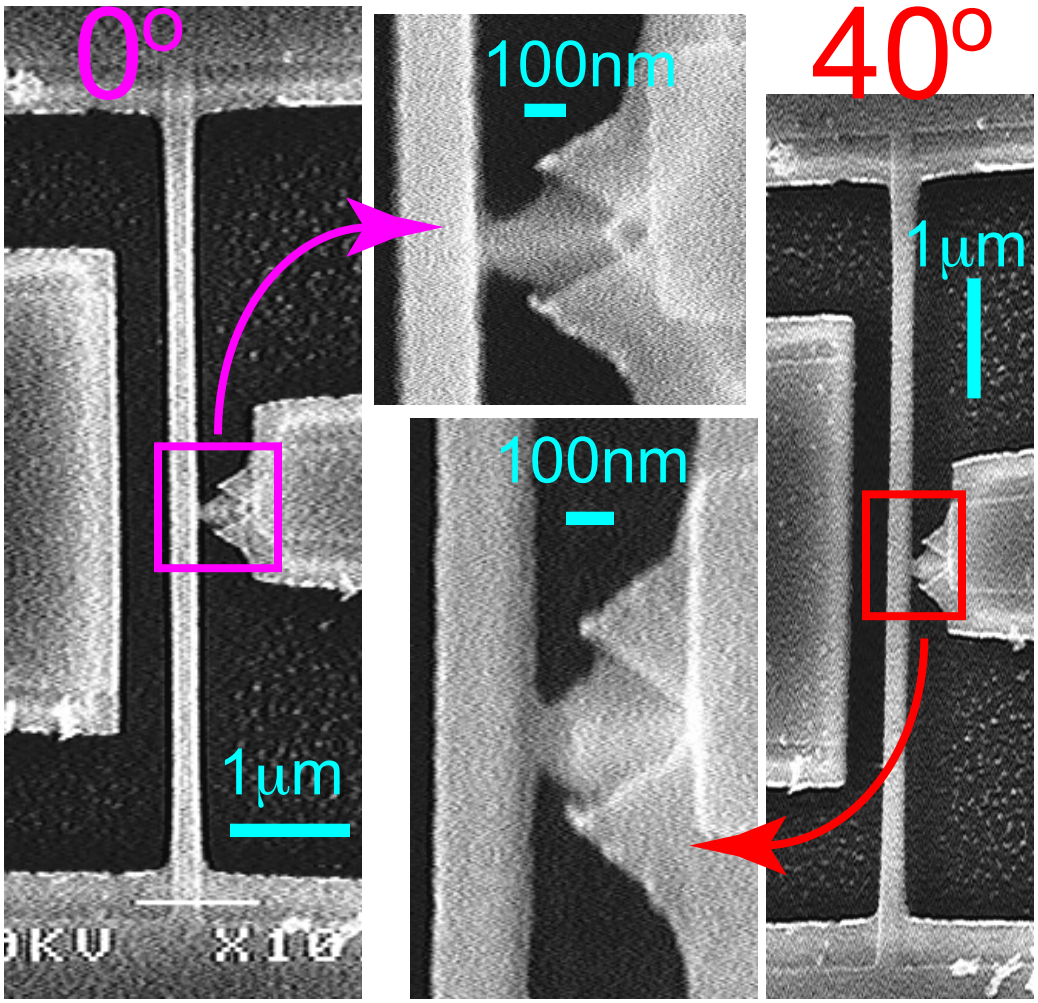

Figure 6.10: Scanning electron micrograph (SEM) of nanomechanical structure prior to electromigration, with the narrow gold structure in white/grey suspended over the GaAs substrate in black. The APC will be created at the thin narrow constriction between the nanomechanical beam and the triangular electrode shown in the middle SEMs. The constriction is created using a triple-angle evaporation (chapter 5). The two upper left SEMs are taken from directly above the nanostructure. The two lower right SEMS are taken at a 40° angle and show that nanomechanical beam is suspended above the substrate.

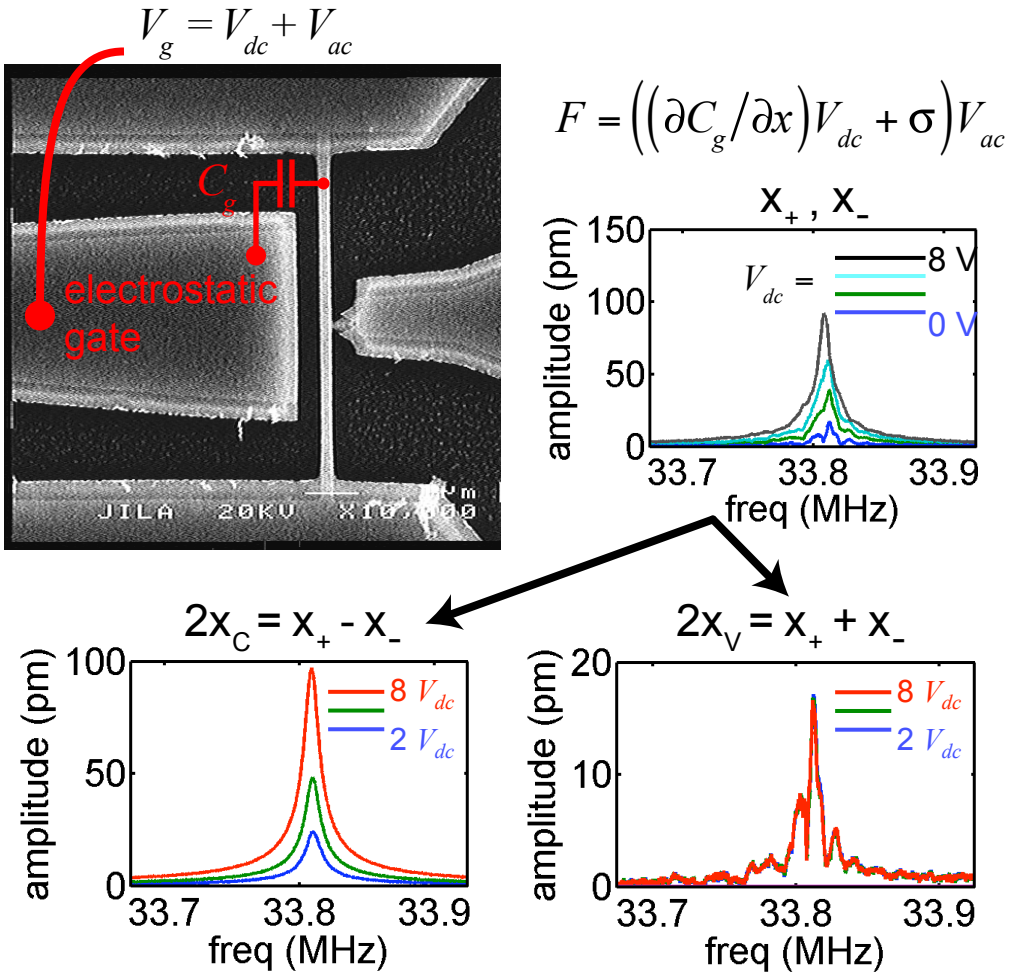

Figure 6.11: A gate electrode (top left, scanning electron micrograph) is voltage biased to create both an electrostatic force and a piezoelectric force. The electrostatic force is due to the change dC_g/dx in the capacitance C_g between the gate and the nanomechanical structure caused by nanomechanical motion x. Since the GaAs substrate is piezoelectric, a sinusoidal voltage applied to the gate electrode will launch surface acoustic waves onto the surface of the chip, shaking the nanomechanical supports and creating a detectable frequency dependent force $F = \sigma V_{ac}$. The complicated, frequency dependent response to a $V_{ac} + V_{dc}$ voltage applied to the gate electrode (upper right) can be split into an electrostatic response (lower left) and a piezoelectric response (lower right) by separately measuring the total response with both a positive dc voltage, x_+, and negative dc voltage, x_- and either subtracting (electrostatic response $x_C = (x_- - x_-)/2$) or adding (piezoelectric response $x_V = (x_+ + x_-)/2$) the two responses.

at the frequency ω_g of the ac voltage

$$F_C = \frac{dC_g}{dx} V_{gdc} V_{gac} \cos(\omega_g t) + \frac{1}{2}\frac{dC_g}{dx}\left[V_{gdc}^2 + \frac{V_{gac}^2}{2}\left(1 + \cos(2\omega_g t)^2\right)\right] \tag{6.31}$$

where the displacement due to the dc force and the force at $2\omega_g$ are usually negligible. This force at ω_g is an advantage, because a commercial network analyzer can be used to apply the ac voltage at ω_g and measure the magnitude and phase of the resulting mechanical displacement at ω_g. Measuring the magnitude and phase of the response at $2\omega_g$ due to an ac signal at ω_g is more difficult. Second, it is possible to separate the electrostatic force from any force that is proportional to voltage $F_V = \sigma V_g$ (such as a peizoelectric force) by measuring the mechanical response $x_\pm(\omega)$ to both a positive and negative dc voltage $\pm V_{gdc}$. Changing the sign of the dc voltage will change the phase of the electrostatic force F_C by 180° but will not affect the phase of F_V. Therefore, the electrostatic response to $+V_{gdc}$ is $x_C = (x_+ - x_-)/2$ and the response to F_V is $x_V = (x_+ + x_-)/2$ (see figure 6.11).

Using this electrostatic drive, I observed mechanical resonances at 10.46 MHz, 16.29 MHz, 33.82 MHz, 40.69 MHz, 40.93 MHz, 53.31 MHz, and 55.15 MHz. These resonance frequencies are lower frequency than those observed in the previous section. This frequency shift is expected, since the nanomechanical beam in this nanostructure is 20% longer. The 34 MHz mode was most strongly coupled to the APC measurement. In the rest of this section I will concentrate exclusively on this 34 MHz mode.

6.2.1 Improved thermal noise calibration

In order to determine the 16 kΩ APC detector's displacement sensitivity and backaction I use a calibration based on the thermal noise. The basic calibration technique is described and applied to the 33 kΩ APC detector in section 6.1 above. The calibration of the 16 kΩ detector is slightly more complicated. I make two modifications to the basic technique which improve the calibration by removing systematic errors.

First, I measure the displacement in response to an applied electrostatic force as well as the spectral density of the Brownian motion. The response measurement is used to compensate for changes in the measurement gain G_{amp}. Second, I use the temperature dependence of the mechanical resonance frequency to determine the effective temperature of the nanostructure. Using this effective temperature instead of the cryostat temperature compensates for the local heating caused by the power dissipated in the nanomechanical structure due to the measurement voltage bias.

I use the measured response to an electrostatic force to compensate for drifts in the measurement gain G_{amp}. As described in the previous subsection, the electrostatic gate is used to impose a force

$$F_C = \frac{1}{2}\frac{dC_g}{dx}V_g^2 \tag{6.32}$$

The measured voltage signal V_C due to the displacement x_C in response to the force F_C is

$$V_C = \left(\frac{dx}{dV_s}\right)^{-1} x_C = \left(\frac{dx}{dV_s}\right)^{-1} \frac{F_C}{m\left(\omega^2 - \omega_0^2 + i\omega\gamma\right)} \tag{6.33}$$

The voltage response V_C is going to depend on temperature because the width γ and resonance frequency ω_0 depend on temperature. On the other hand, I can define a quantity

$$A = \left(\frac{dx}{dV_s}\right)^{-1} \frac{F_C}{m} = \left(-\frac{\lambda}{\chi V_{APC}}\frac{R_{APC} + Z_a}{2Z_a}\frac{1}{G_{amp}\Lambda}\right)^{-1} \frac{F_C}{m} \tag{6.34}$$

which is frequency independent and only contains variables which should be constant as a function of temperature and time.

Unfortunately, the gain of the amplifier chain G_{amp} does drift during the >12 hours needed to complete a thermal calibration. This drift affects both A and the integrated strength of the measured voltage signal due to Brownian motion $(\Delta V_s)^2$, which results in a systematic error in the backaction force. However, if $(\Delta V_s)^2$ and A are measured

at approximately the same time then the fraction

$$\frac{(\Delta V_s)^2}{A^2} = \left(\frac{m}{F_C}\right)^2 \frac{S_F^T}{4m^2\gamma\omega_0^2} \tag{6.35}$$

is independent of the amplifier gain G_{amp}. Substituting $(\Delta V_s)^2 / A^2$ for $(\Delta V_s)^2$ in the basic thermal calibration (subsection 6.1.2) will results in a more accurate calibration and measurement of the backaction force S_F^{BA}.

Another source of systematic error in the thermal calibration is the difference between the temperature of the cryostat and the nanostructure. The microwave voltage V_{APC} used to measure nanomechanical motion also dissipates power $P_{APC} = V_{APC}^2/R_{APC}$ in the nanostructure. As discussed in the previous section, this dissipated power can heat nanostructure so that the local temperature of the nanostructure is higher than the temperature of the cryostat thermometer. In the 33 kΩ APC discussed in the previous section, this effect was obvious at $P_{APC} > 2$ nW and $T_{cryo} < 4$ K; I dealt with this problem by ignoring temperature and power data where there were clear deviations from the expected linear relationship between integrated strength $(\Delta V_s)^2$ and temperature T_{cryo}.

Instead of discarding data points, with the 16 kΩ device it is possible to use the temperature dependence of the mechanical resonance frequency as a local thermometer. The temperature dependence is determined by measuring the resonance frequency as a function of temperature using an electrostatic driving force and a small microwave voltage bias, $P_{APC} = 0.2$ nW (figure 6.12, thick blue line). At this small power, the local temperature T_{local} of the nanostructure and the temperature T_{cryo} of the cryostat are approximately equal. When a large microwave power is dissipated at the APC, the local temperature T_{local} of the nanostructure can be determined by measuring the frequency of the nanostructure (figure 6.12 and 6.13).

With these improvements, I use the Brownian motion of the nanostructure to calibrate the displacement measurement and determine both the measurement imprecision

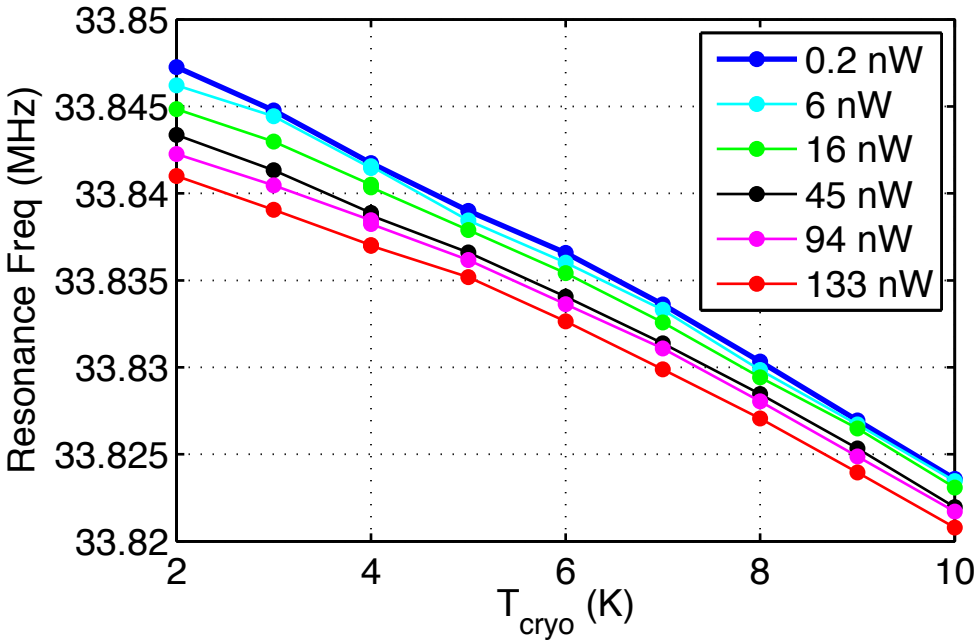

Figure 6.12: The nanomechanical resonance frequency is plotted as a function of cryostat temperature T_{cryo} with a variety of different powers dissipated in the APC due to a combination of microwave and dc voltages across the APC. The low power (blue) resonance frequency has a clear dependence on cryostat temperature T_{cryo}. Using this calibration curve, the resonance frequency is a local thermometer and can be used to determine the effect of the power dissipated at the APC on the temperature of the nanostructure.

and the backaction force. In figure 6.14 I plot the integrated mean squared displacement $(\Delta x_T)^2$ as a function of temperature, measured with various microwave voltage biases and dc voltage biases across the APC. The measured imprecision and backaction are given in table 6.3.

The effective length scale λ/χ of the 16 kΩ displacement detector (table 6.3) is about an order of magnitude larger than in the 33 kΩ detector discussed in the previous section. The best displacement imprecision obtained with the 16 kΩ device is worse than with the 33 kΩ device because of the larger effective length scale. The tunnel barrier is expected to become smaller at low resistances (chapter 3) and even the model of the APC as a high rectangular tunnel barrier becomes suspect at low resistances, so

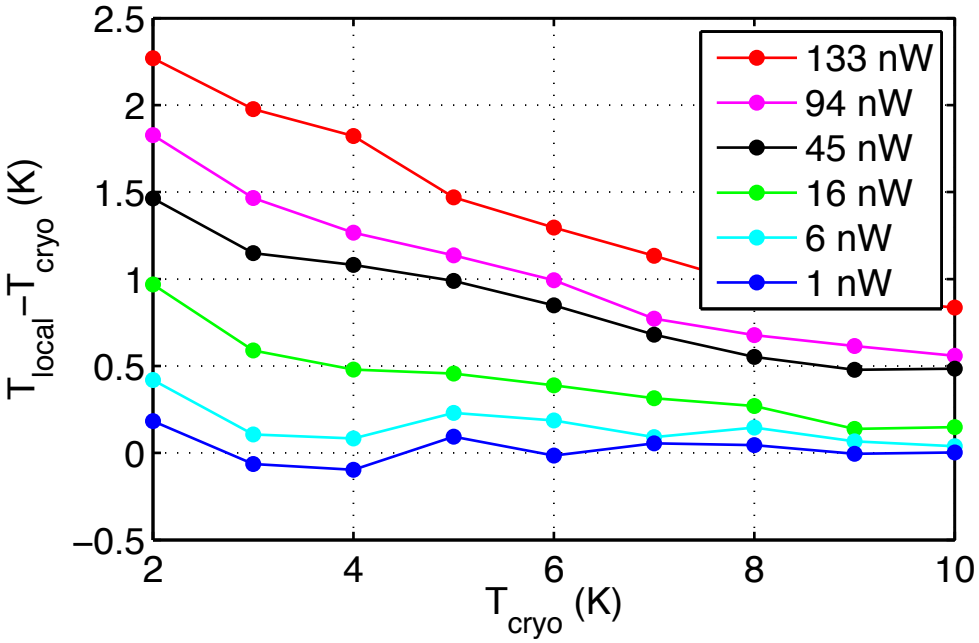

Figure 6.13: The difference between the local temperature T_{local} of the nanostructure, derived from the mechanical resonance frequency, and the cryostat temperature T_{cryo} is plotted as a function of cryostat temperature for different powers dissipated in the APC. The temperature shift is larger for large powers and low cryostat temperatures, as expected, and has an uncertainty less than 200 mK.

it is not surprising that the λ would be larger for a 16 kΩ junction. Based on a finite element simulation, I also expect the 34 MHz mode χ to be smaller than the χ of the 43 MHz mode. Qualitatively, this is because the mode shapes of the 34 MHz mode and the 43 MHz mode are similar, but the 34 MHz mode's nanomechanical beam is both longer and has a smaller cross-section than the 43 MHz mode's beam. Since the effective spring constant of the nanomechanical beam is smaller, less force is applied to the APC by nanomechanical motion and χ is smaller.

The effective length scale λ/χ of the 16 kΩ device also depends on the APC voltage (table 6.3). While the APC voltage is expected to effect λ by effecting the shape of the barrier (see chapter 3), in the simple case of a rectangular 5 eV barrier (with no applied voltage) the effect on λ is only significant when $|V_{APC}|$ is within an

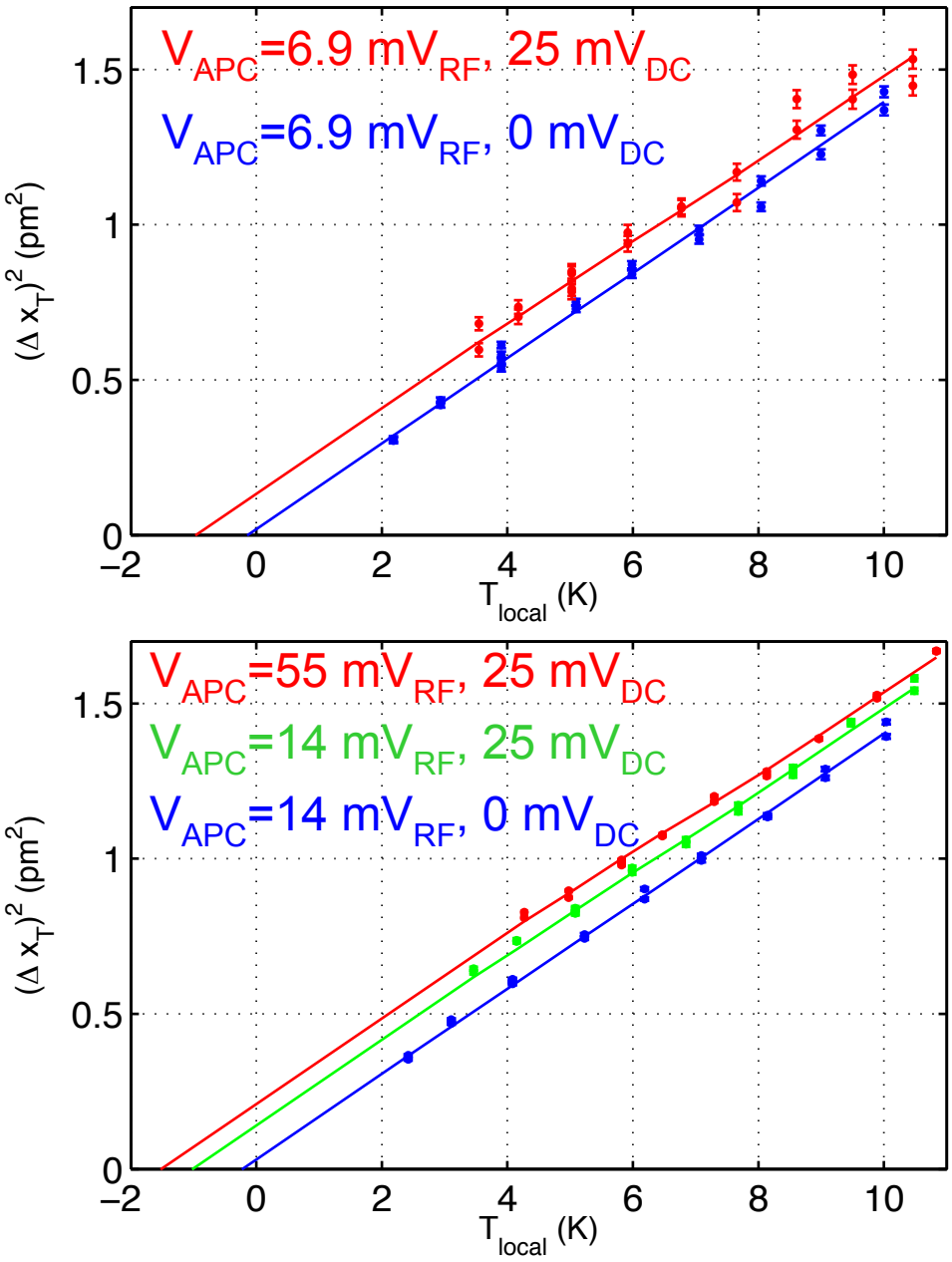

Figure 6.14: The integrated strength in displacement units $(\Delta x_T)^2$ is plotted versus the local temperature of the nanostructure T_{local} for various different microwave and dc voltages across the APC. The local temperature T_{local} is derived from the observed mechanical resonance frequency. In these plots, the y-axis has already been calibrated in displacement units using the integrated strength of the measured voltage signal and the magnitude of the capacitive response, as described in the main text. Each data set is fit to a model that assuming a constant backaction force S_F^{BA} (lines).

order of magnitude of 5 V. In this case, the effective length scale becomes significantly larger when $V_{APC} < -10$ mV; the dependence on the sign of V_{APC} and the small magnitude of the voltage scale implies that this APC should not be modeled as a simple rectangular 5 eV tunnel barrier. The dependence of this 16 kΩ APC's characteristics on APC voltage was not investigated in detail, but a similar dependence is discussed in chapter 7 in the context of a different nanomechanical system and a mechanically controllable break junction (MCBJ).

APC voltage bias	Imprecision S_x	Backaction S_F	λ/χ
V_{RF}=7 mV, V_{DC}=0 mV	621 ± 20 fm^2/Hz	1400 ± 500 aN^2/Hz	20 nm
V_{RF}=7 mV, V_{DC}=25 mV	1370 ± 60 fm^2/Hz	6400 ± 1000 aN^2/Hz	20 nm
V_{RF}=14 mV, V_{DC}=0 mV	278 ± 10 fm^2/Hz	1260 ± 600 aN^2/Hz	20 nm
V_{RF}=14 mV, V_{DC}=-13 mV	1940 ± 100 fm^2/Hz	5200 ± 1000 aN^2/Hz	50 nm
V_{RF}=14 mV, V_{DC}=25 mV	407 ± 20 fm^2/Hz	6100 ± 1000 aN^2/Hz	20 nm
V_{RF}=55 mV, V_{DC}=25 mV	247.8 ± 6 fm^2/Hz	9350 ± 800 aN^2/Hz	40 nm

Table 6.3: The observed imprecision, backaction, and length scale λ/χ of a displacement detector created using an electromigrated APC with resistance R_{APC}=16 kΩ and various dc and microwave APC bias voltages V_{APC}. This detector is used to measure the 34 MHz mode of the nanostructure shown in figure 6.10. The backaction force S_F is plotted as a function of the shot noise spectral density S_I in figure 6.15 (red).

6.2.2 Measurement backaction

I fit the observed backaction force to the phenomenological model of the APC detector described in chapter 3. In this model, the backaction of the APC detector is due to momentum kicks from tunneling electrons. The force is

$$F = \frac{I_{APC}}{e} p_e \tag{6.36}$$

equal to the momentum delivered by each electron p_e times the number of electrons that tunnel per unit time I_{APC}/e. The random backaction force due to the momentum of tunneling electrons is proportional the random number of electrons that tunnel per unit time and has a spectral density proportional to the shot noise spectral density

$$S_F^{BA} = S_{Isn} \frac{p_e^2}{e^2} \tag{6.37}$$

The magnitude of the observed backaction force S_F^{BA} is linearly proportional to the magnitude of the shot noise current $S_{Isn} = 2e\zeta\Xi V_{APC}/R_{APC}$. In figure 6.15 I plot the backaction force S_F^{BA} versus the shot noise S_{Isn} observed using the 16 kΩ APC described in the previous subsection (red) and the 33 kΩ APC describe in the previous section (blue). I fit each data set to a line through the origin, that is, fit to the phenomenological model described in the previous paragraph and equation 6.37. A linear fit to the shot noise current S_{Isn} is better than a fit to higher powers of S_{Isn} (for example, the black line is a fit to $(S_{Isn})^3$). It is possible that the 33 kΩ APC data has a systematic deviation from a line through the origin, though there are not enough data points to make a clear determination.

One possible explanation for such a deviation is a poor knowledge of the local temperature. In the analysis of the 33 kΩ APC data I simply ignored thermal data points where the local temperature appeared to deviate from the cryostat temperature. This technique will not compensate for a difference between the local temperature and the cryostat temperature that is approximately constant between 5 K and 10 K. An offset ΔT between the local temperature and the cryostat temperature will cause the measured backaction force to be incorrect by an amount $4m\gamma k_B\Delta T$.

While the linear dependence of the backaction force S_F^{BA} on shot noise S_{Isn} is consistent with a backaction force due to momentum kicks from tunneling electrons, each electron would have to deliver a momentum equal to about 30 times the Fermi momentum (figure 6.16) which is implausibly large. In the simple phenomenological model of backaction described in chapter 3, electrons tunnel from filled states near the top of the Fermi sea on one side of the barrier to unfilled states on the other side of the barrier. Since the applied voltage bias is small compared to the Fermi energy, the momentum of each tunneling electron is expected be on the order of the Fermi momentum p_F (for gold, $p_F = 1.2 \times 10^{-24}$ N sec).

There are other possible sources of backaction. While I have attempted to com-

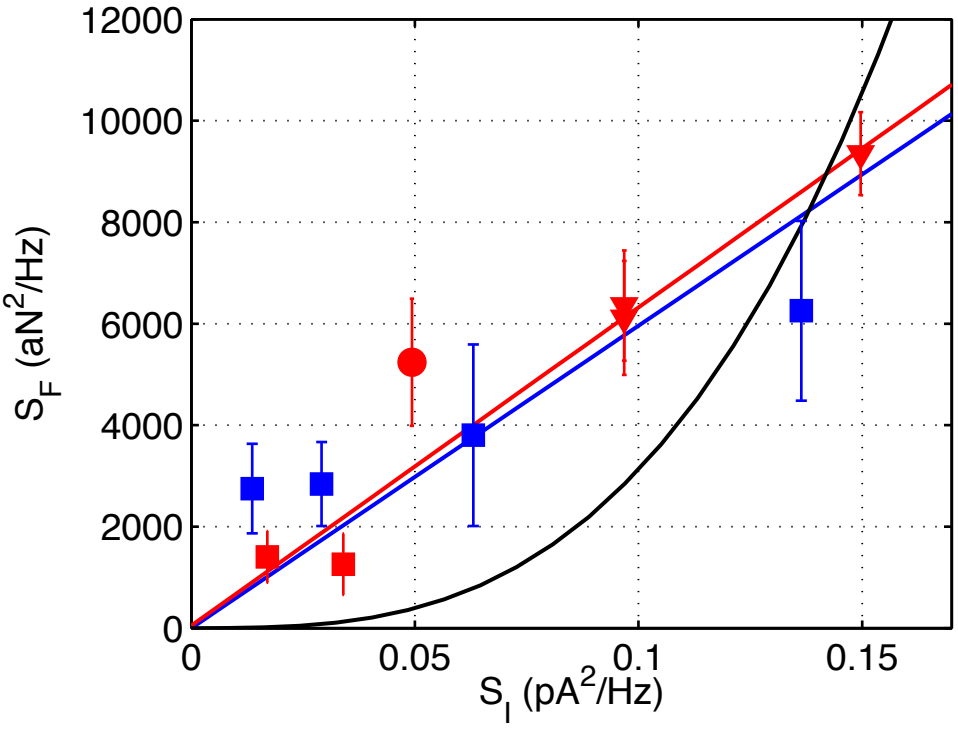

Figure 6.15: The backaction force S_F^{BA} observed when using the 33 kΩ APC detector (blue data) and when using the 16 kΩ APC detector (red data) is plotted versus the shot noise in the current S_I. The shot noise is due to just a microwave voltage (squares), a microwave voltage plus a dc voltage $V_{dc} = -12.5$ mV (circles), or a microwave voltage plus a dc voltage $V_{dc} = 25$ mV. Based on the phenomenological model where the backaction force is due to momentum kicks from tunneling electrons, each data set is fit to a line through the origin (red/blue lines). The red data set is also fit to $(S_I)^3$ (black line), the dependence expected from backaction due to an electrostatic force. This poor fit is one indication that the backaction force is not electrostatic.

pensate for differences between the local temperature and the cryostat temperature, it is still possible that heating due to power dissipated at the APC is responsible for the observed backaction force. As explained earlier, this explanation is unlikely because it is not consistent with the observed dependence on dc and microwave voltages. I also expect that there is an electrostatic backaction force due to dC_{APC}/dx, however this backaction force S_F^{BA} would be proportional to $(V_{APC})^3$ (black line in figure 6.15) which does not fit the data. I can also determine $dC_{APC}/dx < 10$ nF/m directly by measuring the calibrated mechanical response to a voltage applied across the APC. The resulting

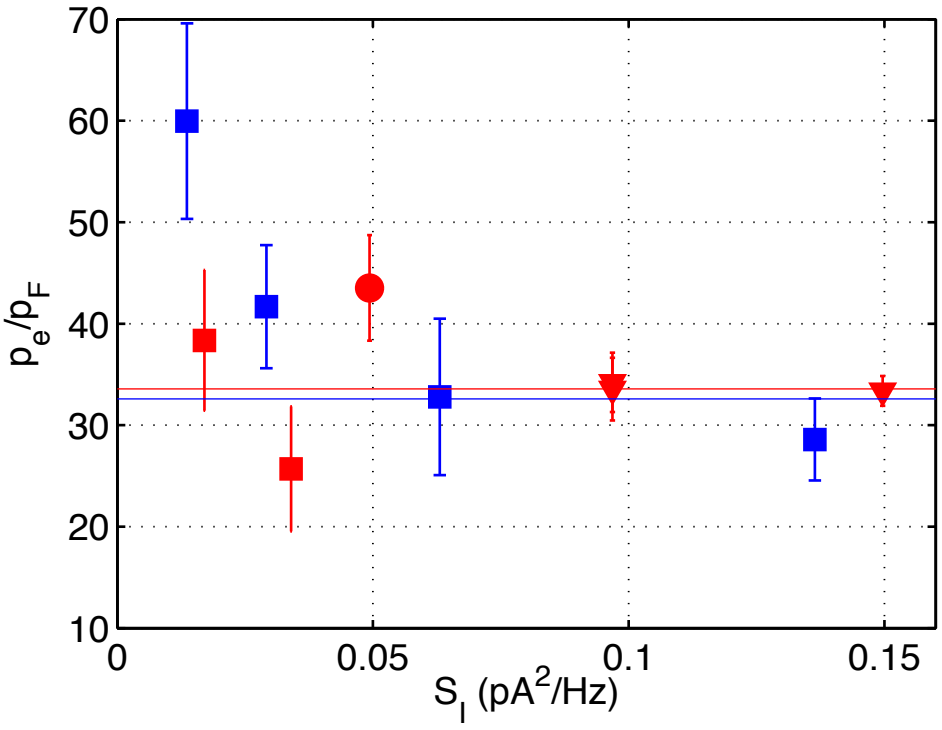

Figure 6.16: The electron momentum p_e needed to explain the observed backaction is plotted in units of the Fermi momentum (for gold, $p_F = 1.2 \times 10^{-24}$ N sec) as a function of the shot noise current S_I for the 33 kΩ APC detector (blue data) and for the 16 kΩ APC detector (red data). Fitting the observed backaction forces (figure 6.15) to the phenomenological model of a backaction force caused by the momentum kicks from tunneling electrons, the 33 kΩ APC detector backaction would require that each electron impart a momentum $p_e = p_F \times (32 \pm 3)$ (red line) and the 16 kΩ APC detector backaction would require $p_e = p_F \times (34 \pm 1)$ (blue line).

backaction force

$$S_F^{BA} = \left(\frac{dC_{APC}}{dx}\right)^2 S_{Isn} R_{APC}^2 \left(\frac{(V_{APC_{rf}})^2}{2} + (V_{APC_{dc}})^2\right) \tag{6.38}$$

is too small to account for the observed backaction.

It is also possible that the observed backaction force is due to the peizo-electric nature of the substrate or trapped charges near the APC. This type of force is proportional to the voltage across the APC, and thus the spectral density of the backaction force S_F^{BA} would proportional to the shot noise voltage across the APC

$$S_F^{BA} = \sigma^2 S_{Vsn} = \sigma^2 S_{Isn} R_{APC}^2 \tag{6.39}$$

where σ is the proportionality constant.

Using the data from the two electromigrated APCs (figure 6.15) it is difficult to determine whether the backaction force is due to a force proportional to current, such as momentum kicks from tunneling electrons, or a force proportional to voltage because the spectral density of both backaction forces is proportional to the shot noise. If the proportionality constant is not dependent on the APC resistance, then the type of backaction force can be determined using the resistance dependence of the backaction force.

Assuming the proportionality constant is not dependent on the APC resistance, the backaction force observed in these electromigrated junctions is due to a force proportional to current because this proportionality constant p_e/e is the same in the two devices while the voltage force proportionality constant σ changes by a factor of two. However, this assumption is suspect because these backaction forces are measured using different nanomechanical structures and different APCs with different characteristics. In chapter 7 I will discuss other ways of determining whether the backaction force is proportional to current or voltage.

Chapter 7

Results: Mechanically Controllable APC coupled to nanomechanical motion

In this chapter, I demonstrate that a mechanically controllable break junction can be used to create an atomic point contact (APC) and measure nanomechanical motion. I start by describing how the resistance of the junction can be reversibly changed between 40 Ω and open (> 10 GΩ). I use this controllable resistance to measure nanomechanical motion at different resistances. The nanomechanical resonance frequency and damping depend on resistance and generally decrease with increasing resistance.

I also measure the length scale λ that controls the probability of electron's tunneling at different junction resistances and, in general, observe an increase in λ at resistance $R_{APC} < 500$ kΩ. The best displacement measurement compared to the standard quantum limit $\sqrt{S_x} = 4.4\sqrt{S_{xSQL}}$ and the Heisenberg constraint $\sqrt{S_x S_F} = 168\hbar$ is obtained at a resistance $R_{APC} = 60$ kΩ.

Finally, I use the MCBJ to investigate the backaction force created by voltages or currents through the junction. In general, the magnitude of the backaction force is similar to that observed in electromigrated devices (chapter 6). The presence of unintentional feedback indicates that there exists a backaction force proportional to current. I attempt to measure correlations between the shot noise and the backaction, but the noise in the measurement is large enough that the data is consistent both with the absence of correlations and with correlations due to the expected backaction force. I

also observe an unexpected increase in the backaction at certain dc voltage biases which could be related to changes in the differential resistance R_{APC} at the same voltage biases.

7.1 Mechanically Controlling the APC Resistance

I use a mechanically controllable break junction (MCBJ) to create an atomic point contact (APC) and control the resistance of the APC. The resistance of the junction is changed by straining the suspended nanostructure (figure 7.1) using a mechanical plunger (chapter 4). By moving the plunger with a screw for coarse adjustments and a piezo crystal for fine control, the resistance R_{APC} of the junction can be increased from 40 Ω to open (> 10 GΩ) and then decreased back to about 40 Ω.

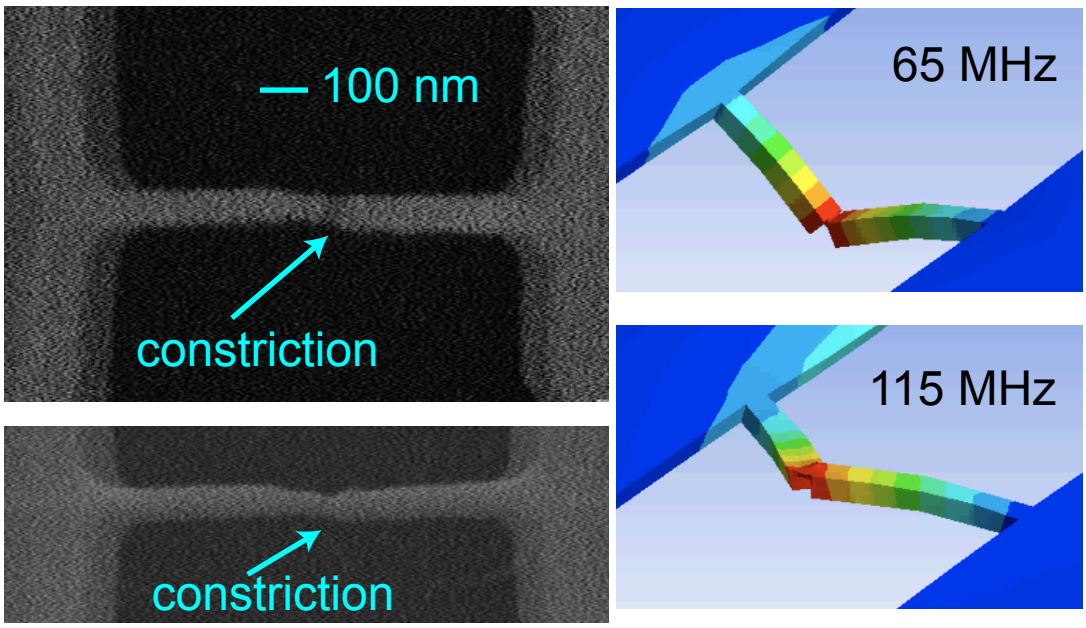

Figure 7.1: Scanning electron micrograph of nanostructure (left) composed of a gold nanomechanical beam (light gray) suspended above a polyimide layer (dark grey/black) on top of a phosphor bronze substrate. The mechanically controllable junction is created at the constriction by stretching the suspended beam (chapter 4). A finite element simulation (right) is used to determine the mode shape of the two lowest frequency nanomechanical modes (see chapter 3).

The hysteretic loops in resistance R_{APC} that occur when the strain is increased and decreased can be divided into three rough categories. First, the resistance R_{APC} can jump from about 100 Ω to greater than 10 GΩ under small increases in strain and then, as the strain is decreased, jump from greater than 10 GΩ to less than 100 Ω (figure 7.2). Second, in some cases the resistance R_{APC} could be adjusted almost continuously between about 10 kΩ and greater than 10 MΩ with only small ($< 10\%$) jumps in resistance (figure 7.3). In other MCBJ experiments, the ability to adjust the resistance in the regime between 15 kΩ and 100 kΩ is often associated with the presence of impurities near the junction [8–10]. Finally, in one case it was possible to adjust the the resistance from about 11 kΩ to 10 MΩ with a large, repeatable, jump in resistance between 11 kΩ and about 150 kΩ (figure 7.4). This type of repeatable jump in resistance is generally associated with an uncontaminated gold APC [9, 10].

In most cases, attempts to increase the junction resistance R_{APC} from below 100 Ω to above 20 kΩ by straining the junction results in a sudden jump in resistance from less than 1 kΩ to greater than 10 GΩ (figure 7.2). Decreasing the strain then results in a sudden jump from greater than 10 GΩ to about 100 Ω. In order to produce a device that I can use to sensitively detect nanomechanical motion (about 20 kΩ $< R_{APC} <$ 1 MΩ), I repeatedly open and close the junction. After many cycles, the the junction resistance eventually jumps from closed to less than 1 MΩ (instead of $>$ 10 GΩ) or the junction resistance decreases smoothly from open to a resistance less than 10 MΩ instead of jumping to $R_{APC} <$ 1 kΩ. In general, the number of times that I needed to cycle the junction before obtaining a useful resistance increased over time.

This behavior is in contrast to the expected behavior of a gold junction [8]. Straining a gold junction usually results in the formation of a chain of gold atoms with a resistance close to half the quantum of resistance, $R_Q/2 = h/(2e^2) = 12.9$ kΩ. When this chain breaks, the resistance of the junction usually jumps to $R_{APC} >$ 100 kΩ. At these higher resistances, gradually increasing the strain results in a gradually increasing

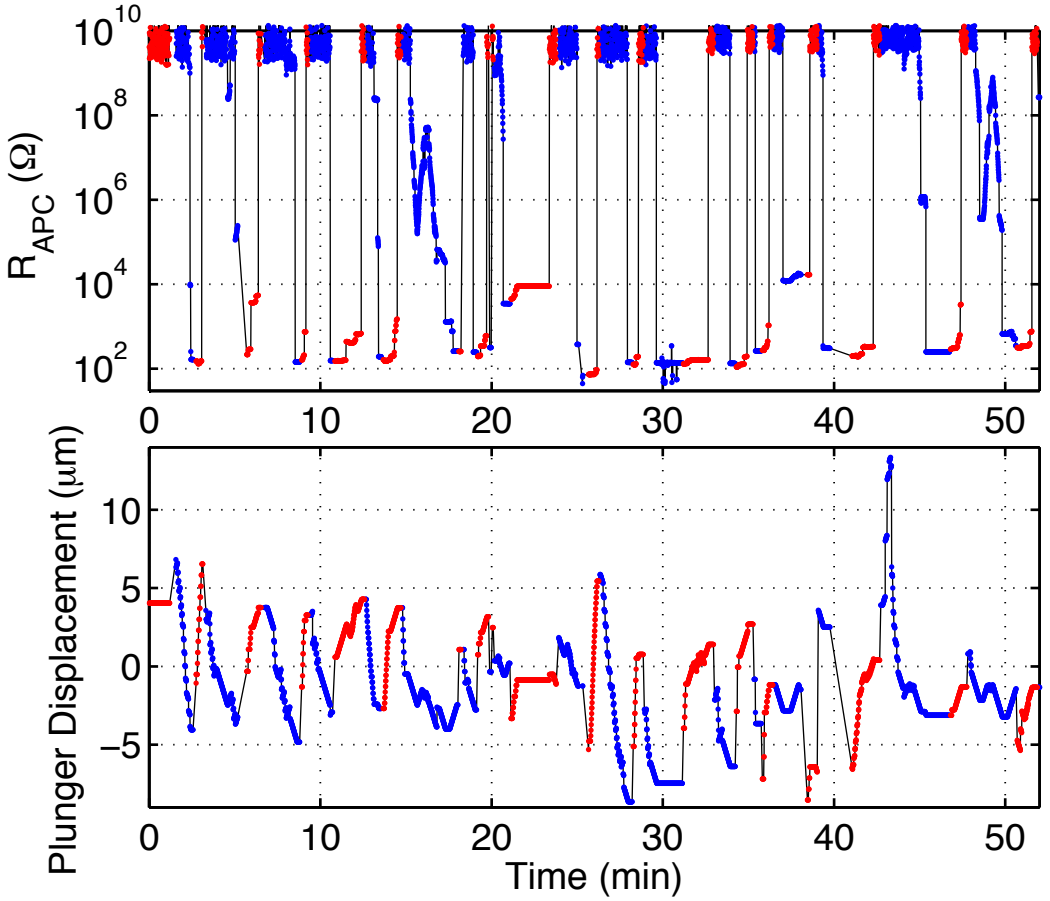

Figure 7.2: The junction resistance (top) and plunger displacement (bottom) as a function of time during a typical attempt to create a junction with a useable resistance 20 kΩ $< R_{APC} <$ 1 MΩ. Increasing strain typically causes a jump from low resistance $R_{APC} <$ 1 kΩ to high resistance $R_{APC} >$ 10 GΩ (red). The noise in the resistance measurement (chapter 5) places an upper limit of about 10 GΩ on the measurable junction resistance. After breaking the junction, decreasing the strain typically causes a jump from high resistance $R_{APC} >$ 10 GΩ to low resistance $R_{APC} <$ 1 kΩ (blue). Occasionally, the junction resistance will not jump suddenly to low resistance but instead will decrease controllably as the strain is decreased (at 17 min and 48 min). I use this behavior to create a junction that can be used to detect nanomechanical motion. More rarely, the junction resistance will jump from a low resistance to a useable resistance as the strain is increased.

resistance with only small discontinuities. The discontinuities are usually attributed to small rearrangements of the gold atoms near the junction. Similarly, decreasing the strain of a high resistance junction will decrease the resistance R_{APC} with only small dis-

continuities until, in a typical junction, the resistance jumps from from $R_{APC} > 100$ kΩ to close to half the quantum of resistance $R_Q/2$. Continuing to decrease the strain will typically cause the conductance $G_{APC} = 1/R_{APC}$ to increase in steps that are initially equal to about half the quantum of conductance $G_Q = 1/R_Q$. The decrease in resistance becomes continuous at lower resistances.

Two possible explanations for the deviation of the observed behavior from the expected behavior are the incorporation of other contaminants into the junction and differences between the nanostructure used to suspend and strain the junction in this experiment and previous experiments. The presence of contaminate atoms or molecules changes the mechanical properties of the junction [8, 49, 52–54, 57]. The junction described in this chapter (figure 7.1) was cycled between opened and closed hundreds of times in a cryogenic vacuum and also exposed to the atmosphere five times in order to adjust the electrical resonance circuit (chapter 5). While the junction was always closed $R_{APC} < 50$ Ω when not in vacuum, the exposure will still increase the contaminants around the junction. Contaminates (especially helium atoms) around a gold junction are generally believed to stabilize the junction and allow junction resistances between 20 kΩ and 100 kΩ [8–10]. However, different types of contaminates or the presence of a large number of contaminates incorporated into gold near the junction could lead to a brittle junction which breaks instead of forming a stable atomic contact. The expected increase in contamination over time can also explain the observed increase in the typical number of breaking and closing cycles needed before achieving a useful junction.

This atypical behavior could also be caused by the nanomechanical structure (figure 7.1). This structure is more mechanically pliant than most support structures [8] to create a lower mass mechanical system and achieve mechanical resonance frequencies around 100 MHz. This compliant structure enables more sensitive force detection, however it is also more difficult to concentrate the strain at the junction (chapter 4) when breaking a low resistance junction $R_{APC} < 100$ Ω. In general, any strain in the

structure is released when the junction breaks which increases the size of the junction gap after breaking. This process could result in an abrupt transition from a closed junction to an open junction with a large gap, as observed (figure 7.2), if the strain in the structure is large. After breaking the contact, decreasing the size of the junction's gap will eventually result in the atoms in the junction jumping into contact. A sufficiently complaint structure could have a small effect on the size of the gap at which the atoms jump into contact and could also effect the size of the contact after the jump. The nanomechanical structure will effect the junction's behavior under strain, however this effect should not change with time which makes it unlikely that the nanomechanical structure is the only cause of the observed breaking and closing cycles.

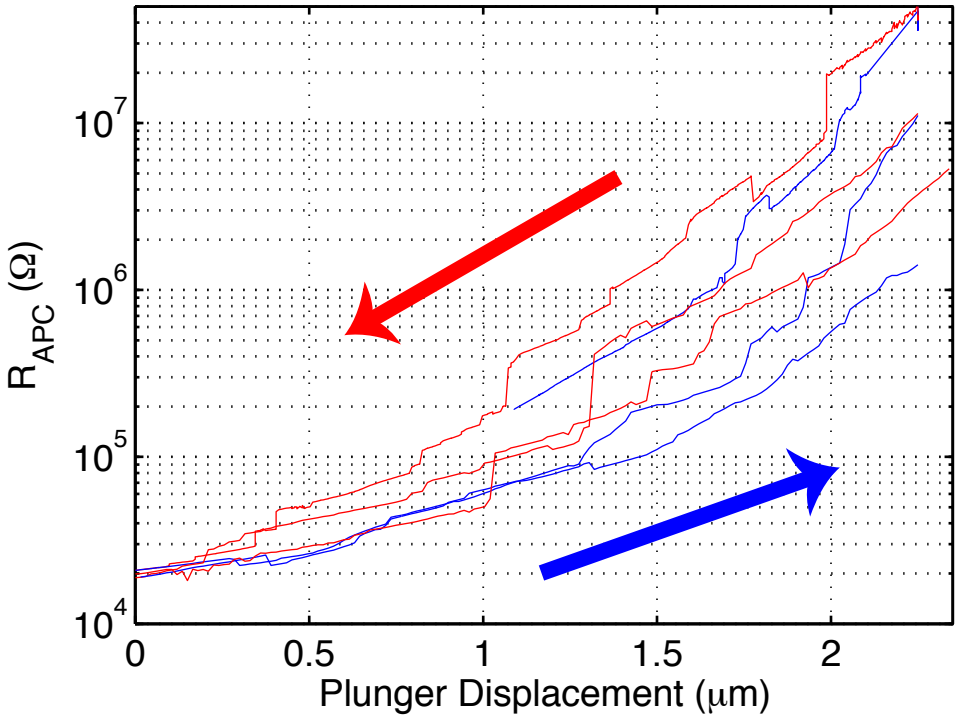

Figure 7.3: The junction resistance R_{APC} is plotted as a function of plunger displacement. The position of the plunger is increased (blue) and decreased (red) causing, in this case, the junction resistance to sweep between 20 kΩ and >1 MΩ with only small discontinuous jumps. The small jumps are due to the rearangment of atoms near the junction. The ability to control the resistance between 20 kΩ and 100 kΩ, as in this figure, is often thought to be a sign that there are contaminants near the junction.

When the junction resistance does not jump between less than 1 kΩ and greater than 1 GΩ, it is usually possible to continuously sweep the junction resistance between 20 kΩ and 10 MΩ by applying and removing mechanical strain (figure 7.3). There are usually only small, unrepeatable, jumps in resistance as a function of strain. This behavior is not expected in clean gold junctions, where the junction resistance is expected to jump between $R_{APC} = R_Q/2 = 12.9$ kΩ and $R_{APC} > 100$ kΩ. A common explanation for the ability to adjust the junction resistance between 20 kΩ and 100 kΩ is the presence of contaminants around the junction [8–10]. This explanation is consistent with the nonlinear I-V curves observed at resistances up to about 1 MΩ, which have features that could be due to the vibrational modes of contaminants. The features in these nonlinear I-V curves depend on the junction resistance and will be discussed in more detail in section 7.5.

In one case, I did observe the behavior expected from a clean junction. I observe a plateau in the junction resistance as a function of strain at $R_{APC} \approx R_Q/2$, likely due to the formation of a chain of gold atoms, and then an abrupt jump in resistance to greater than 1 MΩ as the chain breaks. As I reduce mechanical strain, the junction resistance decreases with small hysteretic features until the resistance jumps from about 100 kΩ to $R_Q/2$. Initially the dependence of the resistance on mechanical strain is different every time the resistance is swept from $R_Q/2$ to greater than 10 MΩ and back to $R_Q/2$. The dependence of resistance on strain becomes repeatable, though still hysteretic, after more than fifty cycles (figure 7.4). This type of "training" behavior has been analyzed in similar gold junctions [9, 10] and is associated with a clean, uncontaminated gold contact.

The junction resistance's dependence on plunger position can be used to determine the length scale λ that controls the probability of electrons tunneling across the junction. At large junction resistances where electrons tunnel across a gap, the resistance R_{APC}

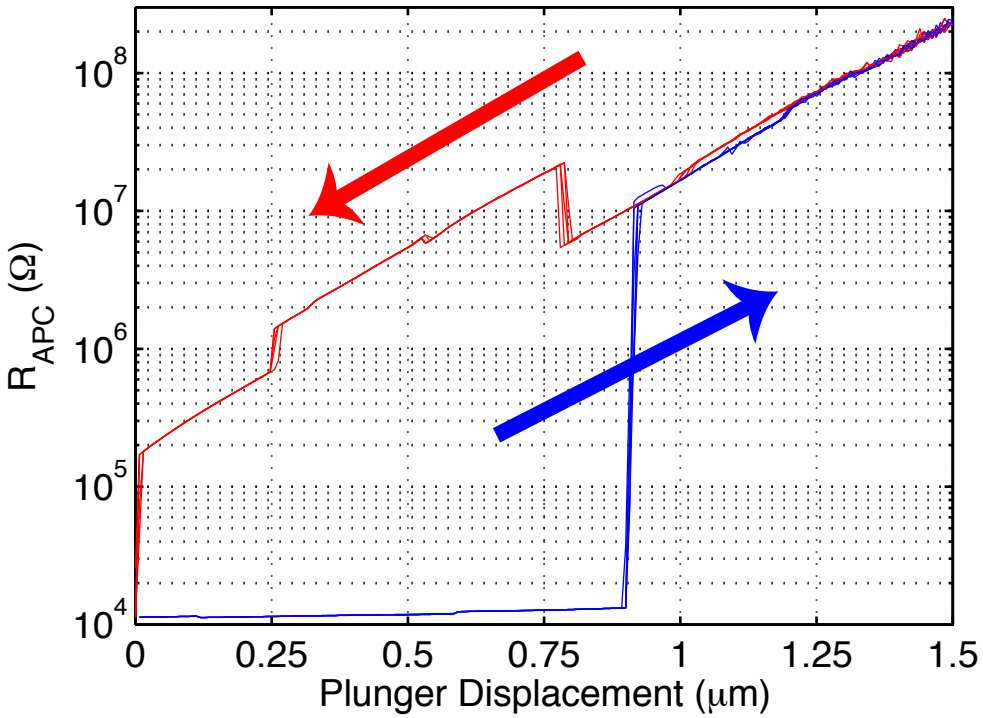

Figure 7.4: The junction resistance R_{APC} is plotted as a function of plunger displacement. After "training" the junction [9,10], sweeping the plunger over 1.5 μm results in a repeatable hysteretic loop in resistance between 11 kΩ and 200 MΩ. As the position of the plunger is increased from 0 μm (blue), there is a plateau where R_{APC} increases slightly from 11 kΩ to 13 kΩ which is likely due to the formation of a chain of gold atoms. There is an abrupt jump to 10 MΩ at 0.9 μm as the chain breaks, after which the resistance increases exponential due to plunger displacement. When decreasing the strain (red), the resistance decreases exponentially as the plunger is retracted until the atoms forming the junction jump to contact from 200 kΩ to 11 kΩ at 0 μm. There are two small, repeatable, discontinuities at 0.25 μm and 0.75 μm when the strain is decreased (red); these discontinuities do not significantly effect the exponential dependence of resistance on plunger displacement (the slope of the red line is constant). While ideally a "trained" junction would not have any discontinuities, the constant exponential dependence supports the idea that the discontinuities are due to the rearrangement of atoms away from the junction rather than a change in the atoms forming the junction or the presence of a contaminate. This repeatable hysteretic loop is not typical; I was only able to successfully train a junction one time (shown here).

of the junction depends exponentially on changes x in the size of the gap

$$R_{APC}(x) = R_0 \exp\left[\frac{2x}{\lambda}\right] \tag{7.1}$$

In the simple case where the strain at the top surface of the chip is homogeneous, the

size of the gap x is related to motion of the plunger u by

$$\frac{x}{u} = \frac{3tD}{L^2} \tag{7.2}$$

where t is the thickness of the chip, D is the length of the suspended nanostructure, and L is the distance between the supports holding the chip (chapter 4). The length scale λ is determined from the changes in junction resistance $R_{APC}(u)$ caused by plunger motion u

$$\lambda = 2\left(\frac{u}{\ln R_{APC}(u) - \ln R_0}\right)\left(\frac{3tD}{L^2}\right) \tag{7.3}$$

The length scale λ of the junctions discussed in this chapter cannot be determined from $R_{APC}(u)$ because the strain at the top surface of the chip is not homogenous. The chip has been permanently deformed and the strain is larger near the center of the chip, where the nanostructure is located, than near the supports. The ratio $x/u \neq 3tD/L^2$ is unknown, and so λ cannot be determined from equation 7.3.

If the gold junction is free of contaminates, then the dependence of R_{APC} on plunger displacement u can be used to determine the ratio x/u of changes in the gap x to plunger displacement u. When a gold junction has a large resistance $R_{APC} > 1$ MΩ and is free of impurities then the length scale is expected to be $\lambda = 0.1$ nm [8], consistent with the bulk work function of gold $\phi = 5$ eV ($\lambda = \hbar/\sqrt{2m_e\phi}$). By assuming $\lambda = 0.1$ nm, the actual ratio

$$\frac{x}{u} = \frac{\lambda}{2}\left(\frac{u}{\ln R_{APC}(u) - \ln R_0}\right)^{-1} \neq \frac{3tD}{L^2} \tag{7.4}$$

can be determined from $R_{APC}(u)$. If I assume that the junction is not contaminated when training behavior is observed (figure 7.4), then the ratio $x/u = 2.1 \times 10^{-4} = 5(3tD/L^2)$ is five times larger than would have been predicted assuming homogeneous strain. Since the chip has undergone plastic deformation and the strain is concentrated near the nanostructure, this increase in the ratio x/u is to be expected.

7.2 Changes in APC Resistance Effect Nanomechanical Modes

The nanomechanical resonance frequency and damping depend on the resistance of the junction and strain on the nanostructure. At many resistances, the resonance frequency is not stable and often jumps between two distinct states. The cryostat also needs to be mechanically isolated to avoid low frequency (100 Hz) changes in the mechanical resonance frequency.

As an example, I measure the mechanical resonance frequency and damping as the resistance of the APC is increased from 200 kΩ to 2 MΩ (figure 7.5). This junction had been "trained," as described in the previous section (figure 7.4). In general, increasing resistance and gap size results in a decreasing mechanical resonance frequency. This decrease is not surprising, since the elastic connection between the two sides of the junction is expected to become weaker as the size of the gap increases. Discontinuous changes in junction resistance, usually associated with the rearrangement of atoms in the junction, also cause discontinuous changes in the mechanical resonance frequency. In this case the damping constant also decreases with increasing resistance of the junction. This is consistent with a decreasing elastic connection, since any damping due to the junction should decrease when the elastic connection due to the junction decreases because the forces on the junction will be smaller. The mechanical resonance frequency and damping can also depend on the bias voltage across the junction and on the cryostat temperature (as discussed in chapter 6).

At some resistances and junction configurations, the resonance frequency and damping constant are not stable. Usually the resonance frequency jumps between two values, sometimes on the time scale of a second and sometimes much faster. Increasing the bias voltage can also make the resonance frequency unstable and, eventually, causes the junction resistance to fluctuate. In some cases the junction resistance is unstable even at low bias voltages; this is usually accompanied by fluctuations in the mechanical

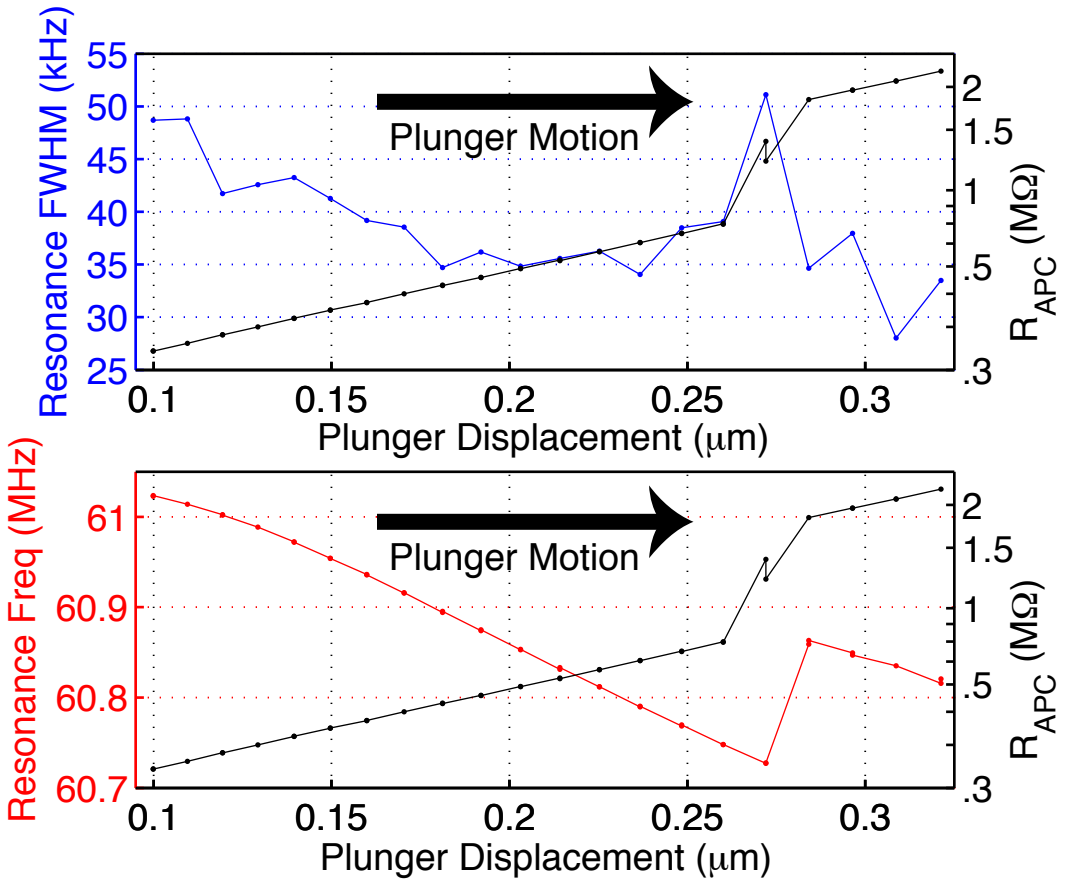

Figure 7.5: The mechanical damping, i.e., Full Width at Half Maximum (FWHM, top, blue), and mechanical resonance frequency (bottom, red) are plotted versus the plunger displacement. This data was taken using the "trained" junction (figure 7.4) while increasing the plunger displacement and junction resistance (black). In general, a junction with a larger gap is expected to have both a larger resistance and provide a weaker elastic connection. This expectation is consistent with both the smooth decrease in mechanical resonance frequency with smooth increase in junction resistance and the general trend of decreasing mechanical damping with increasing resisance. The mechanical resonance frequency is unstable at resistances below 300 kΩ and at the discontinuity $R_{APC} \approx 1.4$ MΩ; the instability causes the large FWHM at $R_{APC} \approx 1.4$ MΩ as well as a non-lorentzian line shape.

damping and mechanical resonance frequency.

It is also necessary to isolate the cryostat from vibrations in the floor and cables (figure 7.6). When the cryostat is not isolated, the nanomechanical resonance frequency oscillates at frequencies >50 Hz. This oscillation is damped by placing the dewar on

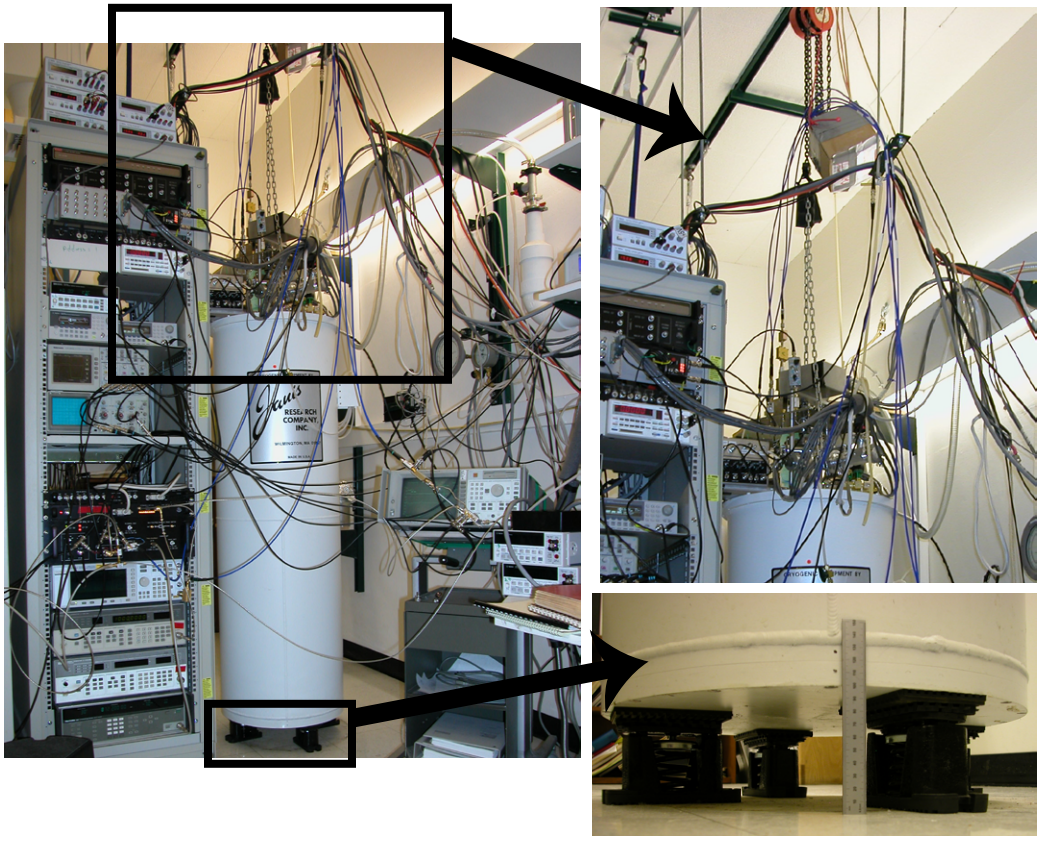

Figure 7.6: Pictures of the mechanically isolated cryostat. The weight of the cryostat is supported by four springs (bottom left, bottom right) which mechanically isolates the cryostat from most vibrations > 50 Hz. Additional damping material is placed on top of the springs. The cryostat is also attached to the ceiling (top right) as a precautionary measure. Finally, all of the cables connected to the cryostat are supported and damped by either bungee cord or surgical tubing (top left, top right.

springs and supporting any cables connected to the cryostat with surgical tubing or bungee cords. The springs compress by $l = 9$ mm when weighted by the cryostat, creating a mechanical resonance with a resonance frequency

$$f_0 = \frac{1}{2\pi}\sqrt{\frac{g}{l}} = 5 \text{ Hz} \tag{7.5}$$

Cryostat vibrations at frequencies much greater than $f_0 = 5$ Hz are damped by the presence of the springs and absorbent material on top of the springs. Using this mechanical isolation, it is possible to observe stable nanomechanical resonance frequencies.

7.3 APC Resistance Effects Displacement Sensitivity

The length scale λ/χ and the nanomechanical displacement sensitivity also depend on the junction resistance R_{APC}. At each junction resistance, I use the Brownian motion of the nanomechanical structure and the response to an electrostatic drive (chapter 6) to calibrate the displacement measurement and determine both λ/χ and the displacement sensitivity. I observe the expected increase in the length scale (chapter 6) at lower resistances $R_{APC} < 500$ kΩ and a length scale consistent with the work function of bulk gold at resistances $R_{APC} > 500$ kΩ. The best displacement sensitivity in comparison to the standard quantum limit, $\sqrt{S_x} = 4.4\sqrt{S_{xSQL}}$, is obtained at a resistance $R_{APC} = 60$ kΩ.

The displacement measurement is calibrated using the Brownian motion of the nanostructure at a single temperature and an electrostatic drive. It is not possible to use the Brownian motion at multiple temperatures, as described in chapter 6, because the needed > 10 K change in cryostat temperature also changes the junction resistance. Instead, I measure the 5 K Brownian motion of the nanostructure using a small microwave voltage across the junction. Because the measurement is weak, the backaction force and change in the local temperature due to power dissipated at the APC are small compared to 5 K and I can use the nanomechanical motion at this single temperature point to calibrate the displacement measurement (see chapter 5). I simultaneously calibrate the electrostatic force F_C applied to the nanostructure using a voltage V_C on a nearby electrostatic gate. The measured displacement in response to the calibrated electrostatic force is then used to determine the length scale λ/χ (see chapter 6), displacement sensitivity, and backaction of a displacement measurement which uses a large voltage across the APC.

Using this calibration, I measure the length scale λ/χ at junction resistances between 80 kΩ and 1 MΩ (figure 7.7). At large resistances $R_{APC} > 500$ kΩ, the length

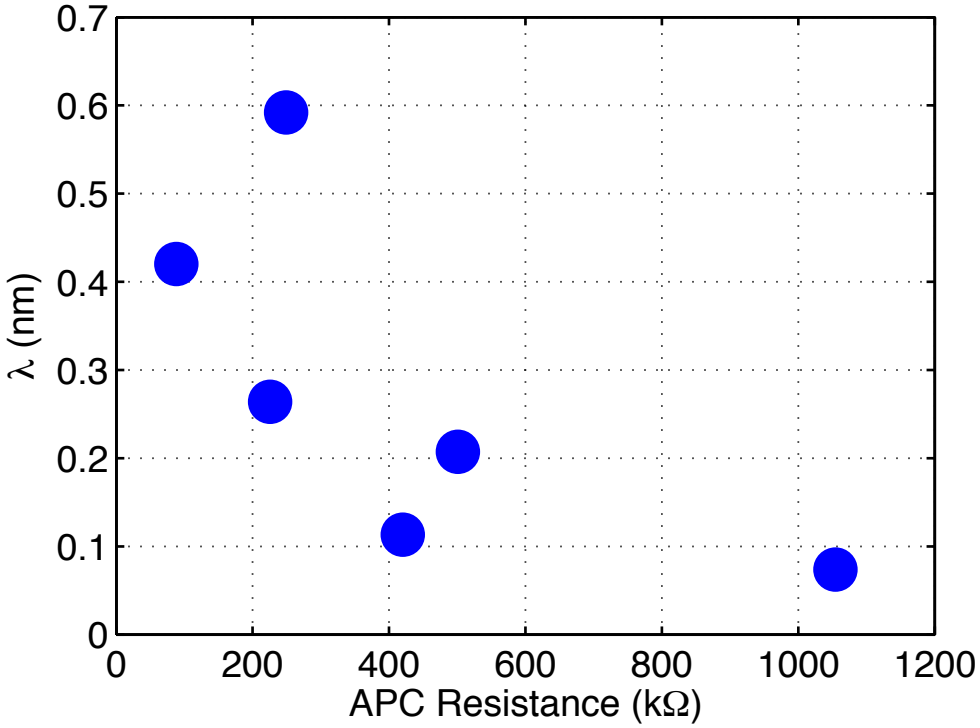

Figure 7.7: The length scale λ/χ for the 65 MHz mode is plotted as a function of APC resistance. As expected, the length scale increases from the expected value of 0.1 nm as the resistance of the junction is decreased. There is no data between 600 kΩ and 1 MΩ because the the resonance frequency was not stable. The different data points were also not taken as part of a continuous sweep in resistance, but instead were taken during multiple sweeps from 100 kΩ to above 1 MΩ while attempting to find resistances with stable mechanical resonance frequencies.

scale $\lambda/\chi \approx 0.1$ nm is consistent with electrons tunneling through a barrier equal to the work function of bulk gold $\phi = 5$ eV ($\lambda = \hbar/\sqrt{2m_e\phi}$, see chapter 3), as in a standard STM. As the resistance is decreased below 500 kΩ, the length scale increases to a maximum, in this case, of $\lambda/\chi = 0.6$ nm.

The best displacement sensitivity is achieved by optimizing the combination of a small length scale, large junction bias, and small contribution to the measurement noise from the amplifier (figure 7.8). When measuring the displacement of the nanostructure shown in figure 7.1, that optimum was achieved using a microwave bias voltage $V_{APC} =$ 47 mV and a junction with a resistance $R_{APC} = 61$ kΩ and length scale $\lambda = 0.5$ nm.

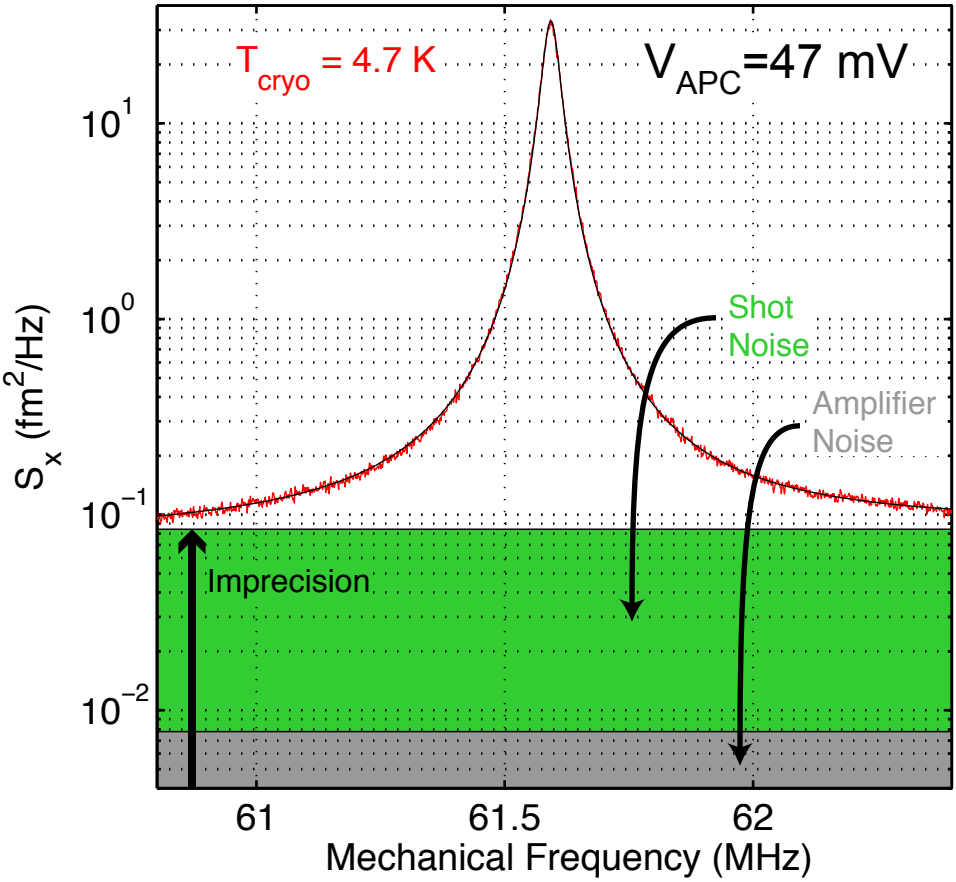

Figure 7.8: The spectral density of the fluctuations in the measured displacement (red) and a Lorentzian fit (black) are plotted as a function of frequency near one of the nanostructure's mechanical resonances. The Lorentzian peak in the noise is due to the Brownian motion of the beam at $T_{cryo} = 4.7$ K. The Lorentzian peak is on top of a white background; this apparent motion is the measurement imprecision ($S_x = 0.08$ fm^2/Hz $= 20S_{xSQL}$ for $V_{APC} = 47$ mV) due to a combination of shot noise (green) and amplifier noise (grey). This measurement has the best displacement sensitivity compared to the standard quantum limit achieved using an APC displacement detector. I use a single sideband measurement with a microwave bias voltage $V_{APC} = 47$ mV and a junction with a resistance $R_{APC} = 61$ kΩ and length scale $\lambda = 0.5$ nm.

Using a single-sideband measurement, the best displacement imprecision $S_x = 0.0841 \pm 0.0001$ fm^2/Hz is 20 times the imprecision at the standard quantum limit, $S_{xSQL} = \hbar/m\omega_0\gamma$. This imprecision is dominated by the shot noise of tunneling electrons, the fundamental source of noise in the measurement, but a single sideband measurement only collects half of the voltage signal (chapter 5). The imprecision S_x could be decreased

by a factor of two if it were possible to change the measurement electronics and perform a double sideband measurement.

I observe a backaction force much larger than required by quantum mechanics, $S_F = 3750 \pm 50$ aN^2/Hz. If the backaction force is caused by momentum kicks from tunneling electrons, each electron would have to deliver a momentum equal to 23 times the fermi momentum, $p_e = 23p_F$. The total imprecision, in quanta, is $N_{tot} = 365 \pm 5$ which is 730 times the total imprecision at the standard quantum limit (chapter 6). Finally, this displacement measurement can be compared to the Heisenberg constraint and the product of the imprecision and backaction $\sqrt{S_x S_F} = 168\hbar$ is 168 times larger than required by quantum mechanics.

The standard deviations in the previous two paragraphs are derived from statistical variations and do not include two important sources of systematic error. First, this analysis is sensitive to any differences between the measured temperature of the cryostat and the local temperature of the nanostructure at low voltage bias. This difference is expected to be less than 10% which would result in less than a 10% change in the value of S_x as well as a larger effect on S_F. Second, the quoted value of the backaction force S_F includes any increase in the local temperature of the beam caused by the large voltage bias. The actual value for S_F could therefore be smaller than stated above, though this effect is expected to be small because the increase in the local temperature observed at $T_{cryo} = 5$ K in chapter 6 was relatively small.

7.4 APC Detector Backaction

I attempt to understand the observed backaction force in more detail using three different methods. First, I measure the unintentional feedback caused by the backaction force. This feedback could be caused by a force proportional to voltage or current, but the observations are more consistent with a backaction force proportional to current. Second, I attempt to determine whether the backaction force is correlated with the shot

noise of tunneling electrons. I place an upper limit on the magnitude of any correlated backaction force consistent with electron momentum kicks $p_e < 50p_F$. The previously observed backaction is included within this limit, so more accurate measurements are needed to determine whether the backaction force is correlated with shot noise. Finally, I examine the dependence of the backaction force on the dc voltage across the junction. I observe increased backaction and peaks or dips in the differential resistance at approximately the same dc voltage. The peaks and dips in the differential resistance are thought to be caused by the vibrational modes of contaminates near the junction which suggests that the backaction could also be increased by the presence and influence of contaminates.

7.4.1 Unintentional feedback caused by the backaction force

Part of the backaction force can be proportional to nanomechanical displacement, creating a feedback loop. I use the observed effect of the feedback loop to distinguish between two phenomenological models for the backaction force: models where the force is proportional to either voltage $F_{BA_V} = \sigma_V V_{APC}$ or current $F_{BA_I} = \sigma_I I_{APC}$. The correct model of APC backaction should account for both the unintentional feedback and the directly observed backaction force. At all APC resistances, the data is best accounted for by a backaction force proportional to current. If this force were due to the momentum of tunneling electrons $p_e = e\sigma_I$, the momentum kick p_e delivered by each electron would be dependent on R_{APC} and would vary between 40 times the Fermi momentum p_F and the fermi momentum p_F. At some APC resistances, this momentum is consistent with the backaction force observed in electromigrated devices (chapter 6) where $p_e \approx 30p_F$.

The backaction force can create an unintentional feedback loop (figure 7.9). The measurement of nanomechanical displacement requires electrically biasing the APC which creates a current I_{APC} through the APC and a voltage V_{APC} across the APC,

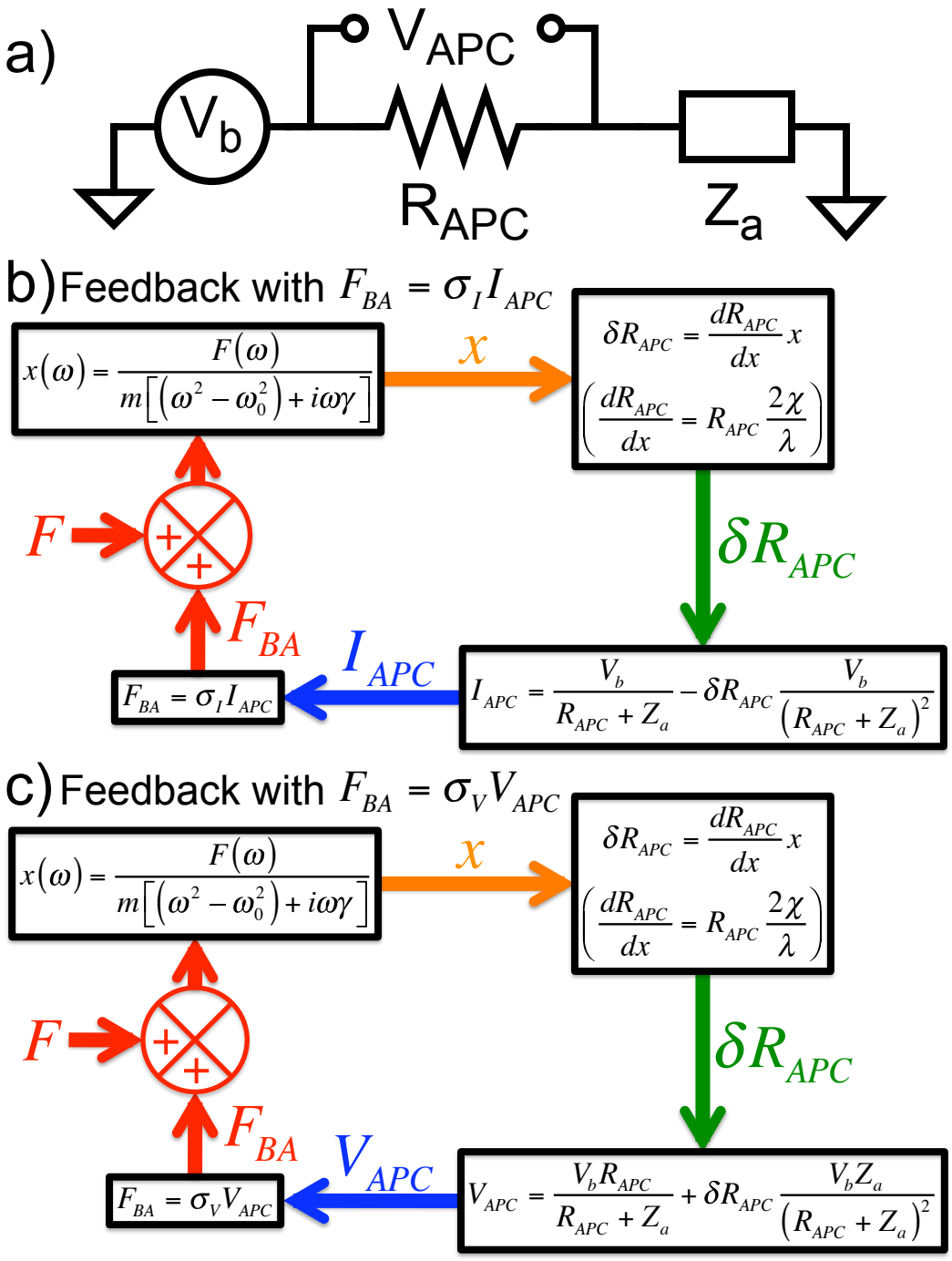

Figure 7.9: (a) circuit including a voltage bias V_b, junction resistance R_{APC}, and measurement circuit impedance Z_A. (b,c) Feedback loop assuming a backaction force proportional to either current (b) or voltage (c). Force (red) causes nanomechanical displacement (orange) which changes the resistance of the APC (green). The changing resistance also changes the current flowing through the junction (b, blue) and the voltage across the junction (c, blue) which closes the feedback loop by creating a change in the backaction force.

where $R_{APC} = V_{APC}/I_{APC}$. If the backaction force is proportional to I_{APC} or V_{APC}, then the applied bias will apply a force to the nanostructure. Because nanomechanical displacement changes R_{APC}, a portion of the backaction force can be proportional to displacement which creates a feedback loop. The magnitude of the feedback depends on both the electrical circuit surrounding the APC (figure 7.9a) and whether there is a backaction force proportional to I_{APC} or V_{APC} (figure 7.9c and d, respectively). For example, if the impedance Z_a of the electrical circuit at the mechanical resonance frequency goes to zero then the APC is voltage biased and V_{APC} is independent of R_{APC}. On the other hand, I_{APC} will change as nanomechanical motion changes R_{APC}. In this case, a backaction force proportional to current will create feedback and a backaction force which is proportional to voltage will not create feedback. In this experiment the resistance of the measurement circuit $Z_a < 30$ kΩ and is less than a third of the APC resistances considered in this subsection. It is possible for either a backaction force proportional to current or voltage to create feedback. I consider this feedback loop to be "unintentional" because I do not intentionally apply a force to the nanostructure which is proportional to the measured displacement.

Assuming a backaction force proportional to current $F_{BA_I} = \sigma_I I_{APC}$, the feedback due to a dc bias voltage V_b will shift the mechanical resonance frequency and a voltage bias near twice the mechanical resonance frequency will create parametric gain. From chapter 5 and the circuit diagram in figure 7.9, the current I_{APC} through the APC due to a voltage bias $V_b \cos(\omega_b t)$ at a frequency ω_b is

$$I_{APC}(t) = \frac{V_b \cos(\omega_b t)}{R_{APC} + Z_a} - V_b \cos(\omega_b t) x(t) \frac{2\chi}{\lambda} \frac{R_{APC}}{(R_{APC} + Z_a)^2} \tag{7.6}$$

If there is a force backaction force proportional to current, there will then be a force proportional to displacement. The effect of this backaction force is found by explicitly including it in the differential equation which describes the nanomechanical motion x

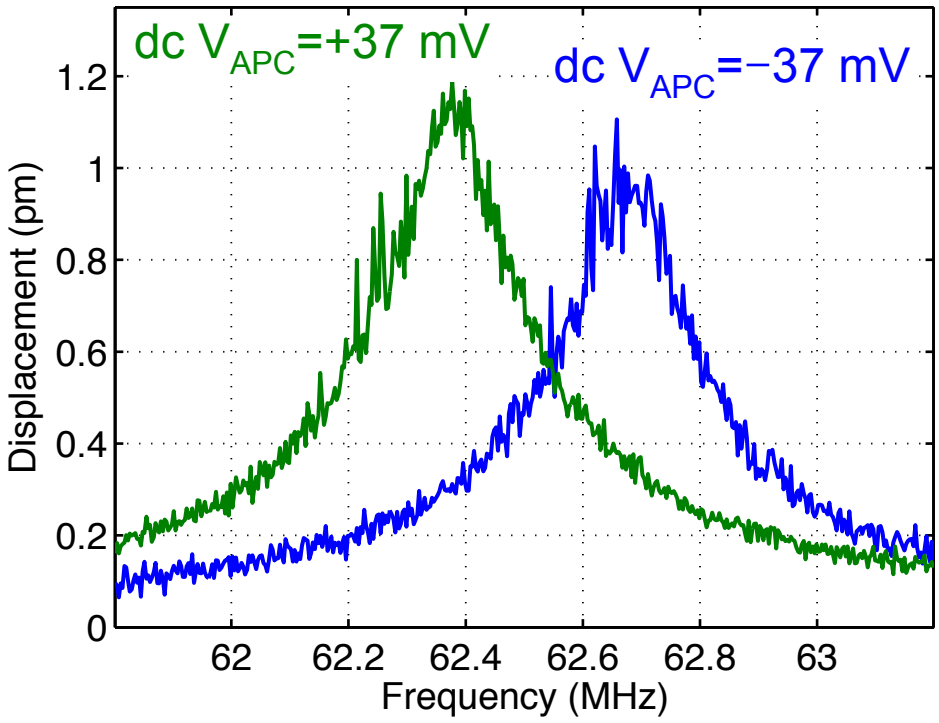

Figure 7.10: The nanomechanical displacement in response to a 1 mV bias voltage is plotted as a function of the frequency of the bias voltage when there is also a dc voltage $V_{APC} = 37$ mV (green) or $V_{APC} = -37$ mV (blue) across the junction. The feedback created by the backaction force shifts the frequency of the mechanical resonance. The change in the magnitude of the response is due to the presence of an electrostatic force (chapter 6), which interferes constructively (green) or destructively (blue) with the backaction force. The electrostatic force is proportional to $dC/dx = 0.5$ nF/m and is small compared to the backaction force.

in response to other forces F

$$F + \sigma_I \left(\frac{V_b \cos(\omega_b t)}{R_{APC} + Z_a} - x V_b \cos(\omega_b t) \frac{2\chi}{\lambda} \frac{R_{APC}}{(R_{APC} + Z_a)^2} \right) = m\omega_0^2 x + m\gamma\dot{x} + m\ddot{x} \quad (7.7)$$

$$F + \sigma_I \frac{V_b \cos(\omega_b t)}{R_{APC} + Z_a} = \left(m\omega_0^2 + \sigma_I V_b \cos(\omega_b t) \frac{2\chi}{\lambda} \frac{R_{APC}}{(R_{APC} + Z_a)^2} \right) x + m\gamma\dot{x} + m\ddot{x} \quad (7.8)$$

The feedback created by a dc voltage ($\omega_b = 0$) bias shifts the mechanical resonance frequency $\omega_0 \rightarrow \omega_0 + \Delta_I$

$$\Delta_I = \frac{\sigma_I V_b}{2\omega_0 m} \frac{2\chi}{\lambda} \frac{R_{APC}}{(R_{APC} + Z_a)^2} \quad (7.9)$$

when $\Delta_I \ll \omega_0$. An example of this shift in mechanical resonance frequency is shown

in figure 7.10).

A voltage bias $V_b \cos(\omega_b t)$ applied at about twice the mechanical resonance frequency ($\omega_b \approx 2\omega_0$) creates parametric gain and effectively decreases the width γ of the resonance (figure 7.11). The parametric gain is used to determine σ_I. As shown in equation 7.8, the voltage bias $V_b \cos(\omega_b t)$ will pump the mechanical spring constant $m\omega_0^2$ at about twice the mechanical resonance frequency when $\omega_b \approx 2\omega_0$. The solution to equation 7.8 when $\omega_b \approx 2\omega_0$ is complicated (see appendix D), but becomes simple when $\omega_b = 2\omega_0$ and the displacement $x(t)$ is due to a force applied at the mechanical resonance frequency $F(t) = F_0 \cos(\omega_0 t)$. In this case, the parametric gain results in

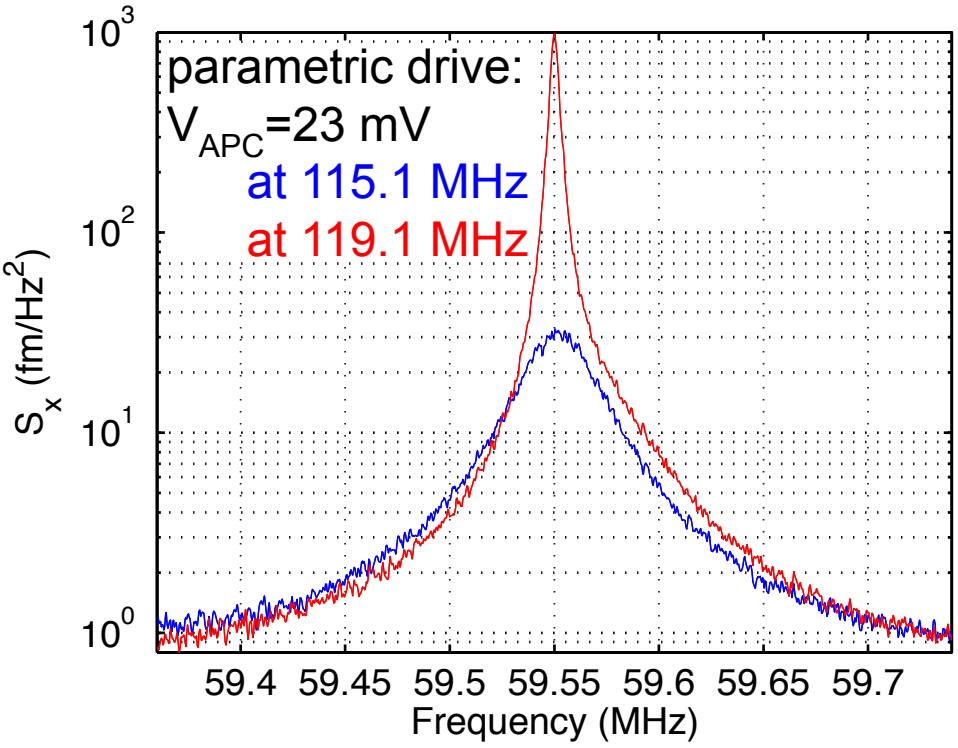

Figure 7.11: The spectral density S_x of the nanostructure's Brownian motion is plotted versus frequency with a $V_{APC} = 23$ mV pump applied at 115.1 MHz $\ll 2\omega_0/2\pi$ (blue) and 119.1 MHz $\approx 2\omega_0/2\pi$ (red). The 115.1 MHz pump has little effect on the nanomechanical motion (blue), however the feedback from the 119.1 MHz $\approx 2\omega_0/2\pi$ pump results in parametric gain and significantly increased displacement (red).

increased displacement

$$x(t) = \frac{-2F_0}{m}\left(2\gamma\omega_0 - \sigma_I V_b \frac{2\chi}{m\lambda}\frac{R_{APC}}{(R_{APC}+Z_a)^2}\right)^{-1}\sin(\omega_0 t) \tag{7.10}$$

when $2\gamma\omega_0 > \sigma_I V_b \frac{2\chi}{m\lambda}\frac{R_{APC}}{(R_{APC}+Z_a)^2}$. An example of this parametric gain is shown in figure 7.11. When $2\gamma\omega_0 \leq \sigma_I V_b \frac{2\chi}{m\lambda}\frac{R_{APC}}{(R_{APC}+Z_a)^2}$ the mechanical system will begin to regeneratively oscillate. The proportionality constant σ_I is determined from the threshold bias voltage V_b^R at which the mechanical oscillator begins to regeneratively oscillate

$$\sigma_I = \frac{2\gamma\omega_0}{V_b^R}\frac{m\lambda}{\chi}\frac{(R_{APC}+Z_a)^2}{2R_{APC}} \tag{7.11}$$

A backaction force $F_{BA_V} = \sigma_V V_{APC}$ proportional to voltage can also cause feedback. In comparison to the model above of $F_{BA} = \sigma_I I_{APC}$, the feedback due to this model has a very different dependence on the circuit impedance Z_a. From chapter 5 and the circuit diagram in figure 7.9, the voltage V_{APC} across the APC due to a voltage bias $V_b\cos(\omega_b t)$ is

$$V_{APC} = \frac{V_b\cos(\omega_b t)R_{APC}}{R_{APC}+Z_a} + V_b\cos(\omega_b t)x(t)\frac{2\chi}{\lambda}\frac{R_{APC}Z_a}{(R_{APC}+Z_a)^2} \tag{7.12}$$

A small part of V_{APC} is proportional to displacement $x(t)$ which, because of the backaction, causes a force proportional to displacement. This force can be explicitly included in the differential equation that describes the nanomechanical motion $x(t)$ in response to other forces F:

$$F + \sigma_V\left(\frac{V_b\cos(\omega_b t)R_{APC}}{R_{APC}+Z_a} + V_b\cos(\omega_b t)x(t)\frac{2\chi}{\lambda}\frac{R_{APC}Z_a}{(R_{APC}+Z_a)^2}\right) = m\omega_0^2 x + m\gamma\dot{x} + m\ddot{x} \tag{7.13}$$

$$F + \sigma_V\frac{V_b\cos(\omega_b t)R_{APC}}{R_{APC}+Z_a} = \left(m\omega_0^2 - \sigma_V V_b\cos(\omega_b t)\frac{2\chi}{\lambda}\frac{R_{APC}Z_a}{(R_{APC}+Z_a)^2}\right)x + m\gamma\dot{x} + m\ddot{x} \tag{7.14}$$

A dc voltage ($\omega_b = 0$) bias creates a feedback loop that shifts the mechanical resonance frequency $\omega_0 \rightarrow \omega_0 + \Delta_V$

$$\Delta_V = \frac{\sigma_V V_b}{2\omega_0 m}\frac{2\chi}{\lambda}\frac{R_{APC}Z_a}{(R_{APC}+Z_a)^2} \tag{7.15}$$

when $\Delta_V \ll \omega_0$. When the voltage bias is applied at twice the mechanical resonance frequency ($\omega_b = 2\omega_0$), this parametric drive will cause the nanomechanical oscillator to regeneratively oscillate when the bias voltage $V_b > V_b^R$. This voltage V_b^R can be used to calculate the proportionality constant

$$\sigma_V = \frac{2\gamma\omega_0}{V_b^R}\frac{m\lambda}{2\chi}\frac{(R_{APC}+Z_a)^2}{R_{APC}Z_a} \tag{7.16}$$

Given the bias voltage V_b^R at which regenerative oscillation begins, the two models make different predictions for the backaction force F_{BA} created by a voltage bias V_b applied near the mechanical resonance frequency. When $R_{APC} > Z_a$, the model of a backaction force proportional to current predicts a force F_{BA_I} on the nanostructure that is larger than the force F_{BA_V} predicted by a model of the backaction force proportional to voltage by a factor of Z_a/R_{APC}. If the backaction force is proportional to voltage then

$$F_{BA_V} = \sigma_V V_{APC} = \frac{2\gamma\omega_0 V_b}{V_b^R}\frac{m\lambda}{2\chi}\frac{R_{APC}+Z_a}{Z_a} \tag{7.17}$$

I infer the magnitude of the backaction force F_{BA_V} at different resistances (figure 7.12, red data) caused by a voltage bias $V_b = 1$ mV from the observed onset of regenerative oscillations at a pump voltage V_b^R. On the other hand, if the backaction force is proportional to current then

$$F_{BA_I} = \sigma_I I_{APC} = \frac{2\gamma\omega_0 V_b}{V_b^R}\frac{m\lambda}{2\chi}\frac{R_{APC}+Z_a}{R_{APC}} \tag{7.18}$$

I also infer the magnitude of the backaction force F_{BA_I} at different resistances (figure 7.12, green data) caused by a voltage bias $V_b = 1$ mV from V_b^R. These two models predict different backaction forces $F_{BA_V} \neq F_{BA_I}$.

The backaction force F_{BA} is directly determined by measuring the displacement in response to a voltage applied across the APC. A bias $V_b\cos(\omega t)$ applied at frequencies ω near the nanomechanical resonance frequency ω_0 creates a backaction force $F_{BA}\cos(\omega t)$

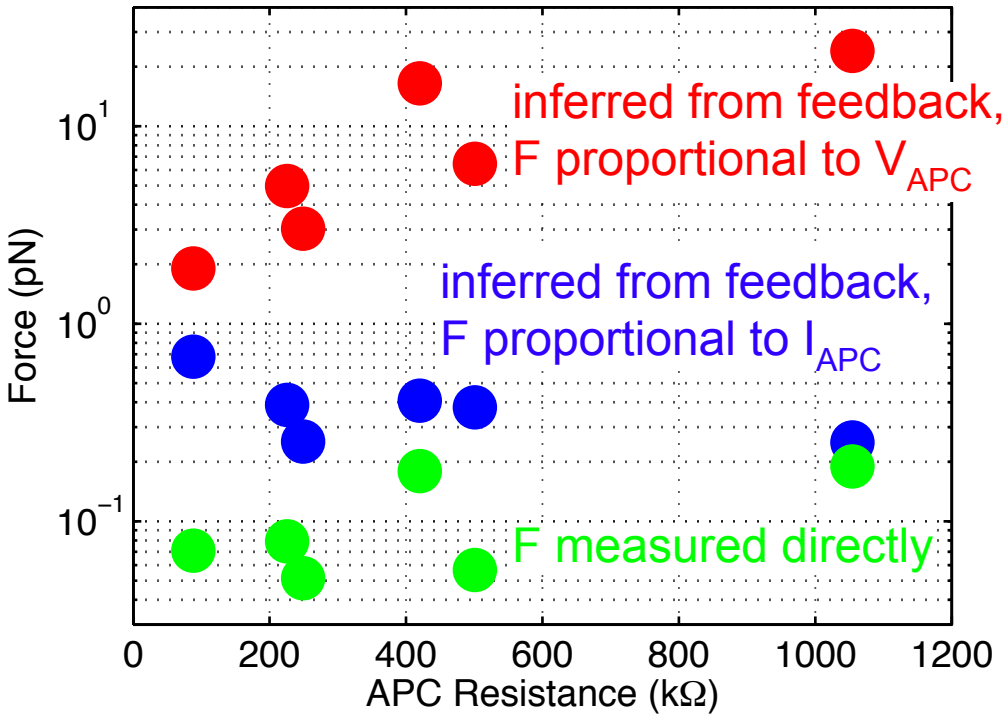

Figure 7.12: Backaction force due to a voltage bias $V_b = 1$ mV at different junction resistances. The backaction force is inferred from the onset of regenerative oscillations at a pump voltage V_b^R using a model $F_{BA_I} = \sigma_I I_{APC}$ (blue data) or using a model $F_{BA_V} = \sigma_V V_{APC}$ (red data). The backaction force is also determined directly by measuring the nanomechanical motion in response to V_b (green data). The model $F_{BA_I} = \sigma_I I_{APC}$ is a better explanation for the observed force and feedback at all junction resistances.

I determine the magnitude of F_{BA} by measuring the frequency-dependent displacement

$$x(\omega) = \frac{F_{BA}}{m\left[(\omega_0^2 - \omega^2) + i\gamma\omega\right]} \tag{7.19}$$

using the APC detector and the calibration described in section 7.3. I plot the directly observed backaction force F_{BA} created by a bias voltage $V_b = 1$ mV in figure 7.12 (green data).

The model of a backaction force proportional to current is a better explanation for the observed unintentional feedback and backaction force than a model of a backaction force proportional to voltage. In figure 7.12, the force inferred from feedback using these two models is compared to the directly observed backaction force (green data).

The model of a backaction force proportional to current (blue data) is more consistent with the observed force than the model than a model of a backaction force proportional to voltage (red data) at all junction resistances.

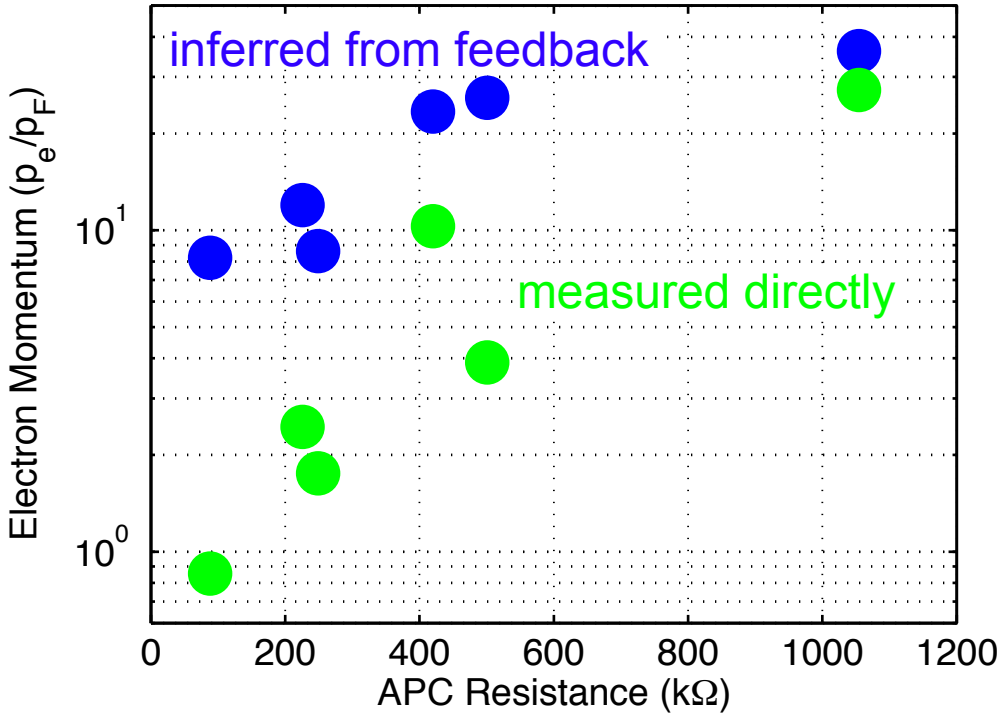

Figure 7.13: The electron momentum $p_e = \sigma_I/e$ needed to explain the directly measured backaction force (green) and the backaction force inferred from feedback (red) in units of the Fermi momentum p_F at different junction resistances. At large resistances $R_{APC} >$ 400 kΩ the inferred electron momentum is similar to the electron momentum $p_e \approx 30p_F$ needed to explain the backaction observed in electromigrated devices (chapter 6). However, the resistances R_{APC} of the devices measured in chapter 6 were $R_{APC} <$ 50 kΩ; the electron momentum inferred from the directly measured backaction (green) is significantly smaller than $30p_F$ when $R_{APC} <$ 400 kΩ.

This model of a backaction force proportional to current is phenomenological and the feedback data does not provide any insight into the microscopic origins of the force. However, if the backaction force proportional to current is caused by the momentum kicks of tunneling electrons then the momentum p_e of each tunneling electron is within an order of magnitude of the electron momentum needed to explain the backaction force observed in the electromigrated junctions (chapter 6). I plot the momentum p_e

in units of the Fermi momentum p_F as a function of junction resistance in figure 7.13. While the inferred electron momentum p_e is similar to the electron momentum needed to account for the previously observed backaction (chapter 6, $p_e \approx 30p_F$) at resistances $R_{APC} > 400\text{k}\Omega$, the electromigrated devices in chapter 6 had resistances $R_{APC} < 50\text{k}\Omega$. At more comparable resistances, the electron momentum inferred from the directly measured backaction force in the MCBJ device (green, figure 7.13) is less than a tenth of the momentum inferred in chapter 6. The devices in chapter 6 used different in APC creation techniques, nanomechanical structures, and measurement techniques.

7.4.2 Correlations between shot noise and nanomechanical motion

A backaction force may create correlations between shot noise and nanomechanical motion. If the backaction force is proportional to the either the current I_{APC} flowing through the junction $F_{BA_I} = \sigma_I I_{APC}$ or the voltage V_{APC} across the APC $F_{BA_V} = \sigma_V V_{APC}$ then nanomechanical motion caused by the backaction force will be correlated with the electrical shot noise at the nanomechanical resonance frequency. I do not observe correlations between shot noise and mechanical motion. This places an upper bound on the backaction proportional to current or voltage, expressed in units of electron momentum $p_e = \sigma_I/e = \sigma_V/R_{APC}e$, of $p_e < 50p_F$. This upper bound is not inconsistent with the previously measured backaction $p_e \approx 30p_F$ (chapter 6). In this measurement the noise is dominated by amplifier noise instead of the fundamental shot noise. A more precise measurement of the correlation would require reducing the 5 K Brownian motion by cooling the nanostructure and decreasing the amplifier noise.

Correlations between nanomechanical motion and electrical shot noise can be detected using the measured voltage spectral density. I simultaneously apply a dc voltage bias V_{APCdc} and a microwave voltage bias V_{APCrf} at ω_{rf} resulting in a voltage signal due to nanomechanical motion at the nanomechanical resonance frequency ω_0 and at $\omega_{rf} \pm \omega_0$. I use two electrical resonances to implement both a baseband measurement

of the signal at ω_0 and single-sideband measurement of the signal at $\omega_{rf}+\omega_0$ (chapter 5). The backaction $F_{BA}=\sigma_I I_{APC}$ due to shot noise $S_{Vsn}(\omega)$ will result in fluctuations in the displacement of the nanostructure with spectral density

$$S_{xBA}(\omega)=S_{Vsn}(\omega)\left(\frac{\sigma_I}{R_{APC}}\right)^2\frac{1}{m^2\left[(\omega_0^2-\omega^2)^2+\gamma^2\omega^2\right]} \tag{7.20}$$

Since the shot noise $S_{Vsn}(\omega)$ is equal to but not correlated with the shot noise in the single-sideband measurement $S_{Vsn}(\omega+\omega_{rf})$, the signal due to S_{xBA} adds incoherently with the shot noise S_{Vsn} and the measured microwave voltage spectral density $S'_{Vsn}(\omega+\omega_{rf})$ proportional to shot noise is

$$S'_{Vsn}(\omega+\omega_{rf})=S_{Vsn}\left[\frac{(\sigma_I/R_{APC})^2\left|\chi V_{APCrf}/\lambda\right|^2}{m^2\left[(\omega_0^2-\omega^2)^2+\gamma^2\omega^2\right]}+1\right]\left|\frac{Z_a(\omega+\omega_{rf})}{R_{APC}+Z_a(\omega+\omega_{rf})}\right|^2 \tag{7.21}$$

On the other hand, near the mechanical resonance frequency the shot noise $S_{Vsn}(\omega)$ and the displacement $S_{xBA}(\omega)$ due to the backaction force are correlated. The two noise sources interfere constructively on one side of the mechanical resonance and destructively on the other side resulting in a measured microwave voltage spectral density $S'_{Vsn}(\omega)$ proportional to shot noise

$$S'_{Vsn}(\omega)=S_{Vsn}\left|\frac{(\sigma_I/R_{APC})(2\chi V_{APCdc}/\lambda)}{m\left[(\omega_0^2-\omega^2)+i\gamma\omega\right]}+1\right|^2\left|\frac{Z_a(\omega)}{R_{APC}+Z_a(\omega)}\right|^2 \tag{7.22}$$

The correlations create a difference between the inferred displacement spectral density ΔS_x using the baseband measurement and the single-sideband measurement

$$\begin{aligned}\Delta S_x(\omega)=&\left(S'_{Vsn}(\omega)\left|\frac{R_{APC}+Z_a(\omega)}{Z_a(\omega)}\right|^2-S_{Vsn}\right)\left|\frac{\lambda}{2\chi V_{APCdc}}\right|^2-\\&\left(S'_{Vsn}(\omega+\omega_{rf})\left|\frac{R_{APC}+Z_a(\omega+\omega_{rf})}{Z_a(\omega+\omega_{rf})}\right|^2-S_{Vsn}\right)\left|\frac{\lambda}{\chi V_{APCrf}}\right|^2\end{aligned} \tag{7.23}$$

$$\Delta S_x(\omega)=\frac{\sigma_I S_{Vsn}}{V_{APCdc}R_{APC}}\frac{\lambda}{\chi}\frac{\omega_0^2-\omega^2}{m\left[(\omega_0^2-\omega^2)^2+\gamma^2\omega^2\right]} \tag{7.24}$$

explicitly removing the white background caused by the shot noise S_{Vsn}. The contribution from the amplifier, discussed below, is also subtracted.

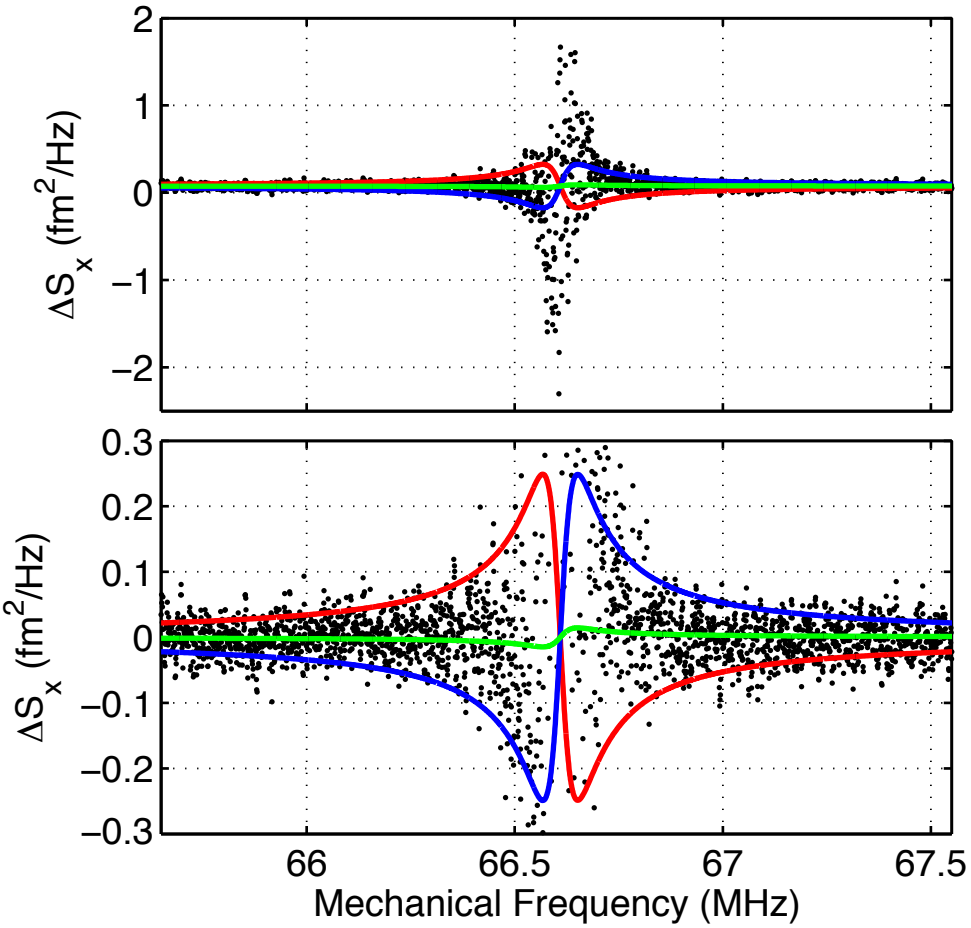

Figure 7.14: The difference $\Delta S_x(\omega)$ between the magnitude of the displacement fluctuations S_x inferred from a baseband measurement and the displacement fluctuations inferred from a single-sideband measurement as a function of mechanical frequency. The displacement fluctuations are measured using a junction with $R_{APC} = 80$ kΩ and a length scale $\lambda/\chi = 0.2$ nm. A dc voltage $V_{APCdc} = 42$ mV and a microwave voltage $V_{APCrf} = 50$ mV are simultaneously applied to the junction and used to perform the baseband and single-sideband measurements, respectively. If there is a backaction force proportional to voltage or current, then the correlation between shot noise and and the backaction force caused by shot noise will create interference in the baseband measurement but not in the single-sideband measurement performed at microwave frequencies. Parameterizing the backaction force proportional to current in terms of the electron momentum $F_{BA_I} = (p_e/e)I_{APC}$, I plot the expected signal $\Delta S_x(\omega)$ (equation 7.24) when $p_e = 50p_F$ (red) and $p_e = -50p_F$ (blue); the sign of p_e is dependent on the definition of a positive current I_{APC}. The observed $\Delta S_x(\omega)$ (black dots) is inconsistent with $|p_e| > 50p_F$. I also fit the observed data to equation 7.24 (green) and infer $p_e = (-3 \pm 7)p_F$ not including sources of systematic error. The error in this measurement is large enough that it cannot distinguish between a correlated backaction force and an uncorrelated backaction force; in this data, the on-resonance noise is dominated by the nanostructure's Brownian motion and the off-resonance noise is dominated by amplifier noise (see figure 7.15).

I plot $\Delta S_x(\omega)$ in figure 7.14; due to the additional noise added by the amplifier and the Brownian motion of the nanostructure, this measurement can only place an upper limit on the size of any correlated backaction which is consistent with each electron delivering a momentum kick $p_e < 50p_F$ (red line). This measurement is performed using a junction with resistance $R_{APC} = 80$ kΩ and length scale $\lambda/\chi = 0.2$ nm. I attempt to detect a backaction force that is correlated with the shot noise due to a dc voltage $V_{APCdc} = 42$ mV and a microwave voltage $V_{APCrf} = 50$ mV. The backaction of previous measurements can also be explained by electron momentums less than $50p_F$, so this measurement of $\Delta S_x(\omega)$ is not able to distinguish between a backaction correlated with shot noise from an uncorrelated backaction.

The amplifier and the Brownian motion of the nanostructure add additional noise terms to $S'_{Vsn}(\omega)$ and $S'_{Vsn}(\omega_{rf} + \omega)$. In figure 7.15 I plot the voltage spectral density as a function of the frequency of the nanomechanical displacement. At frequencies away from the mechanical resonance, the noise in the measurement is dominated by the amplifier noise (see chapter 5 for details). Near the mechanical resonance frequency the noise in the measurement is dominated by the $T_{cryo} = 5$ K Brownian motion of the beam. These noise sources dominate the noise in the measurement of $\Delta S_x(\omega)$, so a more precise measurement of the correlated backaction can be made by reducing the contribution of the amplifier noise relative to the shot noise or reducing the temperature of the nanostructure.

Two sources of systematic error in this measurement are the determination of the length scale λ/χ and the unstable mechanical resonance frequency. The measurement of λ/χ was discussed in 7.3 and any systematic error will scale the inferred magnitude of the backaction (equation 7.24). Small changes in the mechanical resonance frequency could also create an effect on $\Delta S_x(\omega)$ that is similar to the effect of correlations between backaction and shot noise. My measurement of $S'_{Vsn}(\omega)$ and $S'_{Vsn}(\omega_{rf}+\omega)$ are separated by minutes, so any shift in resonance frequency in that time would result in a $\Delta S_x(\omega)$

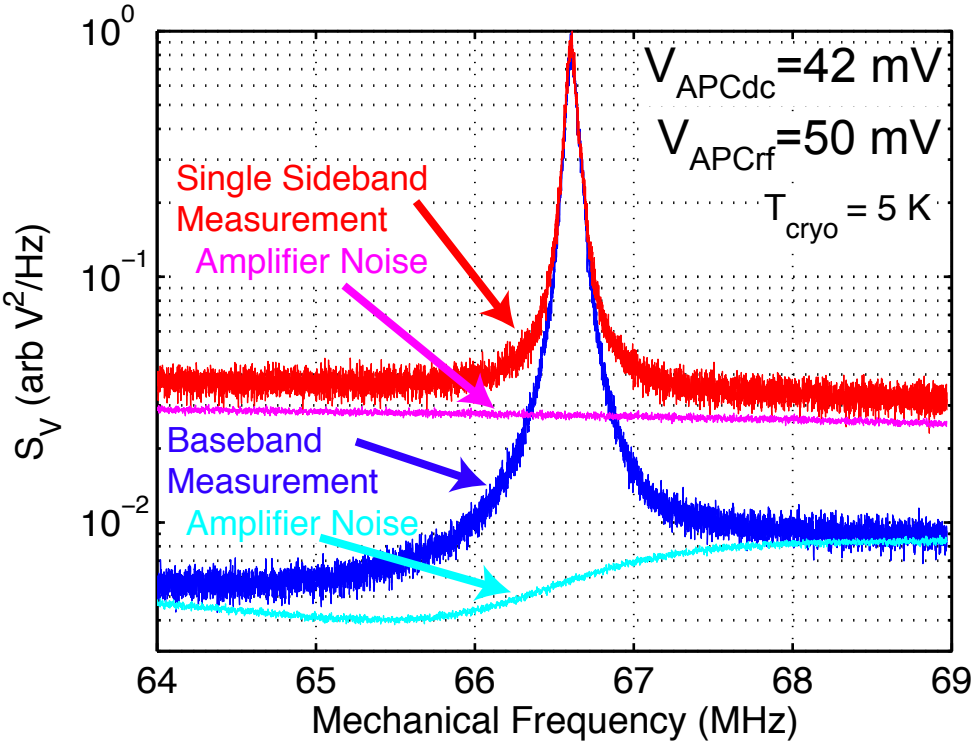

Figure 7.15: The voltage spectral density S_V observed using both a baseband measurement (blue, cyan) and single-sideband measurement (red, magenta) are plotted versus the inferred mechanical frequency. The voltage spectral densities are scaled so that the voltage noise spectral density due to on-resonance Brownian motion of the mechanical structure is equal to one. The junction has a resistance $R_{APC} = 80$ kΩ and a length scale $\lambda/\chi = 0.2$ nm. A dc voltage $V_{APCdc} = 42$ mV and a microwave voltage $V_{APCrf} = 50$ mV are simultaneously applied to the junction and used to perform the baseband(blue) and single-sideband (red) measurements, respectively. In both measurements, the total noise is dominated by the $T_{cryo} = 5$ K Brownian motion on-resonance. Off-resonance, the noise is dominated by amplifier noise (cyan/magenta). The shot noise contribution to the noise is equal to the difference between the amplifier noise (cyan/magenta), i.e., the observed spectral density when $V_{APCdc} = V_{APCrf} = 0$ mV, and the measurement noise (blue/red) off-resonance. In the single-sideband measurement, the amplifier noise (magenta) and the shot noise are not dependent on frequency, because the microwave amplifier noise is flat and the microwave electrical resonance frequency is broad > 50 MHz. On the other hand, the baseband amplifier noise is frequency dependent around 66 MHz and the observed voltage fluctuations due to shot noise are frequency dependent because the 66 MHz electrical resonance is only 2 MHz wide. This electrical resonance filters the shot noise and signal due to nanomechanical displacement. The measurement of $\Delta S_x(\omega)$ can be improved by improving the electrical measurement so that the measurement noise is dominated by shot noise (see chapter 5) and by reducing the temperature of the nanostructure.

which changes sign at the average resonance frequency and decreases away from the resonance frequency; this is similar to the $\Delta S_x(\omega)$ created by correlations. I attempt to identify changes in the resonance frequency by alternating between measuring $S'_{Vsn}(\omega)$ and $S'_{Vsn}(\omega_{rf}+\omega)$ multiple times.

7.5 APC Backaction and Tunneling Spectroscopy

I finally examine the effect of dc bias on the backaction force. In molecular electronics experiments, changes in differential resistance as a function of dc bias voltage have been used to observe the vibrational modes of atoms and molecules in atomic point contacts (APCs) [8, 10, 40, 49, 50, 52–54, 57]. I observe similar changes in differential resistance at bias voltages $|V_{APC}|$ between 15 mV and 50 mV. At the same bias voltage, I also observe increased backaction. One possible explanation for this increased backaction is interaction between the nanomechanical mode and the vibration, created by tunneling electrons, of nearby atoms or molecules.

Inelastic scattering by electrons can create additional channels for electron tunneling, changing the resistance of the APC. This discussion follows a more detailed review of inelastic scattering in the context of experimental APCs contained in M.L. Trouwborst's thesis [10]. In this inelastic process, an electron scatters off of an impurity exciting a vibration at frequency ω_v. An energy $\hbar\omega_v$ is transferred from the electron to the impurity, so this process only occurs when the electron energy $e|V_{APC}| \geq \hbar\omega_v$ or when $k_BT \geq \hbar\omega_v$. At large resistances where the expected tunneling channel is mostly closed ($R_{APC} \gg R_Q/2 = h/(2e^2) = 12.9$ kΩ) the presence of an additional channel decreases the resistance of the APC. This effect will only appear when $|V_{APC}| > \hbar\omega_v/e$ creating a step in the differential resistance R_{APC} as a function of dc bias V_{APC} at a voltage bias $\pm\hbar\omega_v/e$. The observation of this type of symmetric step is called inelastic tunneling spectroscopy (IETS).

At small resistances where the expected tunneling channel is mostly open ($R_{APC} \approx$

$R_Q/2 = h/(2e^2) = 12.9$ kΩ), electrons scattering off of an impurity will increase the resistance of the APC. After interacting with the impurity and losing an energy $\hbar\omega_v$, the electron scatters into a lower energy state. The low momentum states in the forward direction on the far side of the APC are filled, so the electron will backscatter into the low momentum states in the reverse direction on the near side of the APC. The backscatter increases the resistance of the junction, and the observation of this effect is called point contact spectroscopy (PCS).

Experimentally, the step in differential resistance due to vibrational levels is often accompanied by a larger peak or dip in differential resistance R_{APC} at $|V_{APCv}| = \hbar\omega_v/e$ [10, 40, 52]. In gold chains, vibration modes have been observed at voltages $|V_{APCv}| = 10$ mV and 18 mV thought to be due to the transversal and longitudinal vibrational modes in gold [152]. Some evidence of the vibrational modes of helium, a likely contaminate, have been observed at $|V_{APCv}| \approx$ 15-20 mV [182] and the vibrational modes of other materials have also been observed [10, 191–194]. In many cases, peaks and dips are observed at $|V_{APCv}|$ which are much larger than the step in resistance. The microscopic mechanism that results in a peak or dip in resistance is unknown, but most models posit an impurity that fluctuates between two positions with different conductances [191–193].

Using the MCBJ shown in figure 7.1, I sometimes observe clear, symmetric peaks and dips in the differential resistance R_{APC} as a function of dc voltage bias V_{APC} as well as overall steps in R_{APC}. In figures 7.16 and 7.17 I plot the differential resistance as a function of the voltage across the APC $R_{APC}(V_{APC})$ at different plunger positions. I change the plunger position over 600 nm and increase the zero bias resistance $R_{APC}(0$ mV) from 270 kΩ to 2.2 MΩ.

At resistances $R_{APC}(0$ mV) $<$ 500 kΩ I observe a dip in resistance and a step to smaller resistance with increasing voltage bias $|V_{APC}|$. At the lowest measured R_{APC} =270 kΩ the dip and step occur at a dc bias voltage $|V_{APC}| = 25$ mV. As the

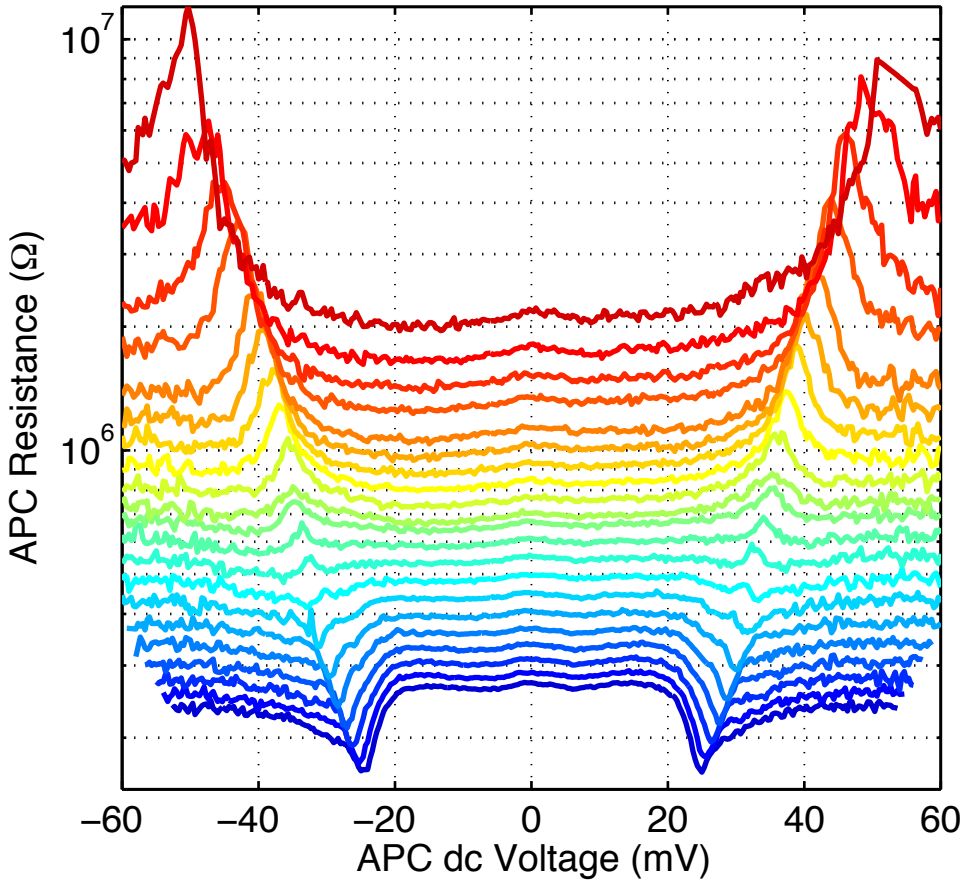

Figure 7.16: Differential resistance R_{APC} versus dc voltage V_{APC} across the junction as the position of plunger is stepped in 30 nm increments over 600 nm. Also see figure 7.17 for a different representation of the same data. At low resistances there is a symmetric dip in $R_{APC}\,[V_{APC}]$. As the junction is strained, increasing the resistance, the dip appears at larger $|V_{APC}|$ and the magnitude of the effect decreases. Simultaneously, a peak begins to appear in R_{APC} at a voltage $|V_{APC}|$ that is slightly smaller than the dip. The $|V_{APC}|$ location of the peak and the fractional size of the peak both increase with increasing resistance. When there is a distinct dip or peak, there is also a small change in the resistance across the feature. At low resistances with a dip at V^d_{APC}, there is a small decrease in resistance $R_{APC}\left[|V_{APC}| \gg |V^d_{APC}|\right] < R_{APC}\left[|V_{APC}| \ll |V^d_{APC}|\right]$ when comparing the resistance at voltages $|V_{APC}|$ significantly greater than and less than V^d_{APC}. Similarly, at higher resistances there is a small increase in resistance. There is a smooth transition with increasing strain between a decrease in resistance at large voltages $|V_{APC}|$ and an increase in resistance at large voltages which is similar to the transition of the feature from a dip to a peak. There is also a small peak in R_{APC} at zero bias.

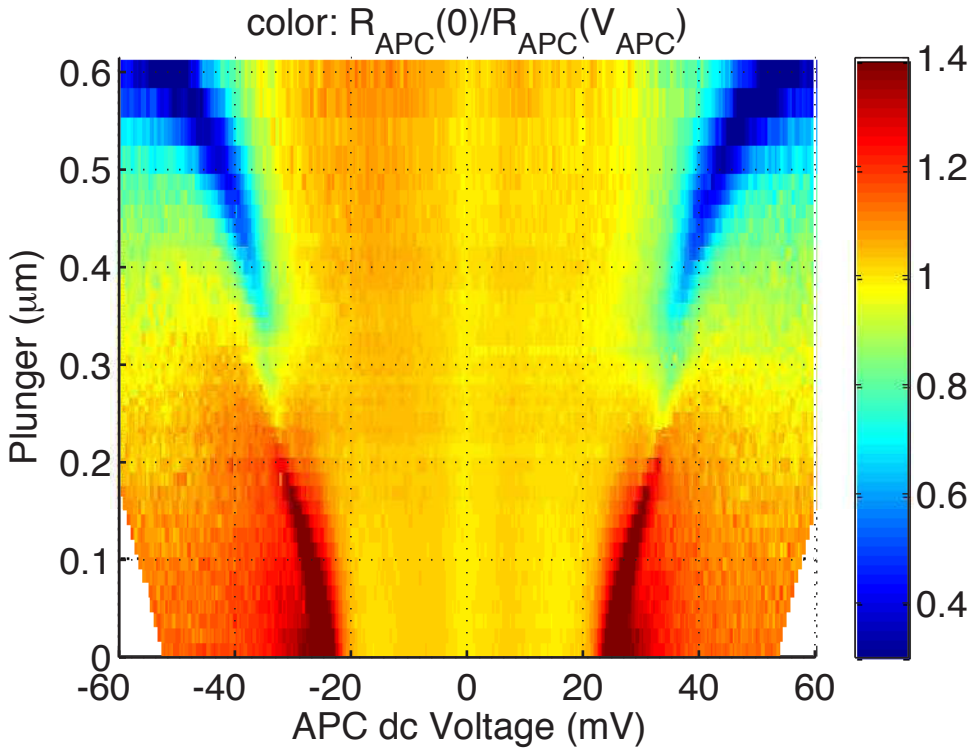

Figure 7.17: The differential conductance scaled by the conductance at zero bias, $R_{APC}(0)/R_{APC}(V_{APC})$, versus plunger position and dc voltage V_{APC} across the junction. See figure 7.16 for a more detailed discussion of the same data.

plunger is used to increase the zero bias resistance $R_{APC}(0\text{ mV})$, the magnitude of the dip and the step become smaller and they occur at larger voltage biases $|V_{APC}|$. When the APC resistance has reached 500 kΩ, the dip and step appear at $|V_{APC}| = 33$ mV and have almost disappeared. The step to lower resistance is consistent with the model of inelastic scattering and the energy scale $e\times 25$ mV is consistent with the vibrational frequency of possible contaminants as discussed above.

At resistances $R_{APC}(0\text{ mV}) > 450$ kΩ I observe a peak in resistance and a step to larger resistance with increasing voltage bias $|V_{APC}|$. A small peak in resistance can be observed at $R_{APC}(0\text{ mV}) > 450$ kΩ and inside the broader dip described in the previous paragraph. At resistances $R_{APC}(0\text{ mV}) > 750$ kΩ the peak in resistance is accompanied by a step to larger resistances. The magnitude of both the peak and the step grow with

increasing strain. The location $|V_{APC}|$ of the peak and step also increases as the strain increases to 50 mV when $R_{APC}(0\text{ mV}) > 2.2\text{ M}\Omega$. This step to lower resistance is not consistent with the model of inelastic scattering described above, which predicts a step to lower resistance due to an additional channel for electron conductance.

Based on this measurement, it is difficult to determine whether the peak and dip are due to a single inelastic channel which is modified by strain or due to two interfering channels. The smooth change in the location V_{APC} of the feature is suggestive of a single channel. However, a closer examination of the data when $R_{APC}(0\text{ mV}) \approx 500\text{ k}\Omega$ indicates that the dip and peak in resistance appear simultaneously at slightly different voltages. In spite of this interesting behavior, I was unable to study this behavior in more detail and determine the microscopic origin of the spectrum.

I also measure the backaction force as a function of dc voltage bias V_{APCdc} and observe peaks in the backaction and features (peaks or dips) in the differential resistance at the same V_{APCdc}. I measure the backaction force using APCs with three different atomic configurations; that is, the junction was closed with a resistance $< 100\ \Omega$ and then a new useable resistance was obtained after opening and closing the junction multiple times (section 7.1). In figures 7.18, 7.19 and 7.20 I plot the characteristics of the APC displacement measurement and the nanomechanical resonance as a function of dc voltage V_{APCdc} along with the different resistance R_{APC}. In figure 7.18 I observe that the differential resistance does not have peaks or dips indicating scattering and the magnitude of the backaction, parameterized in units of the electron momentum p_e where $F_{BA} = (p_e/e)I_{APC}$, does not depend on the dc voltage bias V_{APCdc}. On the other hand, in figures 7.19 and 7.20 I observe peaks and dips, respectively, in the differential resistance and an increase in the magnitude of the backaction force p_e at the same dc voltage bias V_{APCdc}.

Finally, I measure the length scale λ/χ and the nanomechanical resonance characteristics as a function of V_{APCdc}. I observe a clear change in the length scale λ/χ at

the same voltages V_{APCdc} where there is a peak in the resistance (figure 7.19) and a small peak in the length scale at the voltages V_{APCdc} where there is a dip in the resistance (figure 7.20). The length scale λ/χ is constant when the differential resistance is featureless (figure 7.18). There is a small increase in the nanomechanical damping when there is a dip the resistance (figure 7.20); in the other two cases the damping depends smoothly on dc voltage $|V_{APCdc}|$. In the data where there is a peak in resistance the damping increases (figure 7.19), while the damping decreases when the resistance is featureless (figure 7.18).

In all three data sets, I observe changes in the resonance frequency due to the dc bias voltage. Because of the unintentional feedback discussed in section 7.4.1, the dc voltage bias can create antisymmetric changes in the mechanical resonance frequency, that is, changes proportional to voltage V_{APCdc}. In these measurements, the dc voltage creates a significant symmetric change (proportional to $|V_{APCdc}|$) in the mechanical resonance frequency which makes it difficult to detect feedback and can also cause systematic errors. It is not possible to determine whether the asymmetric dependence of the frequency on V_{APCdc} is due to feedback or small asymmetries in the microscopic processes which create the symmetric frequency shifts. However, in some cases the symmetric frequency shift is small in comparison to the antisymmetric frequency shift; in this case, the shift is likely due to feedback.

A possible explanation for the increase in backaction is the motion of an impurity. The features in the differential resistance are commonly associated with vibrational modes of impurities, and any increase in that vibration due to an increase in the effective temperature of the impurity [10, 195, 196] could create a random force which acts on the beam creating backaction. Random motion of an impurity between two different positions could also create a force on the beam and lead to a backaction force. Such a backaction force could be larger than that expected from the momentum kicks of tunneling electrons. The data in figures 7.18, 7.19, and 7.20 suggests that the presence

of impurities and atomic motion could play a role in the backaction but further study is necessary to understand that role.

One possible source of systematic error is a change in the temperature of the nanostructure caused by the increasing dc voltage bias. Since I am not using a thermal sweep to calibrate the measurement, any increase in the local temperature of the nanostructure compared to the cryostat temperature will create the appearance of an increase in the backaction force. I observe this heating at large voltage bias (for example, figure 7.20 when $|V_{APC}| > 30$ mV), however the local temperature of the nanostructure should monotonically increase with increasing voltage bias $|V_{APC}|$. Local heating of the nanostructure cannot explain both the increase and the decrease in the magnitude of the observed backaction force.

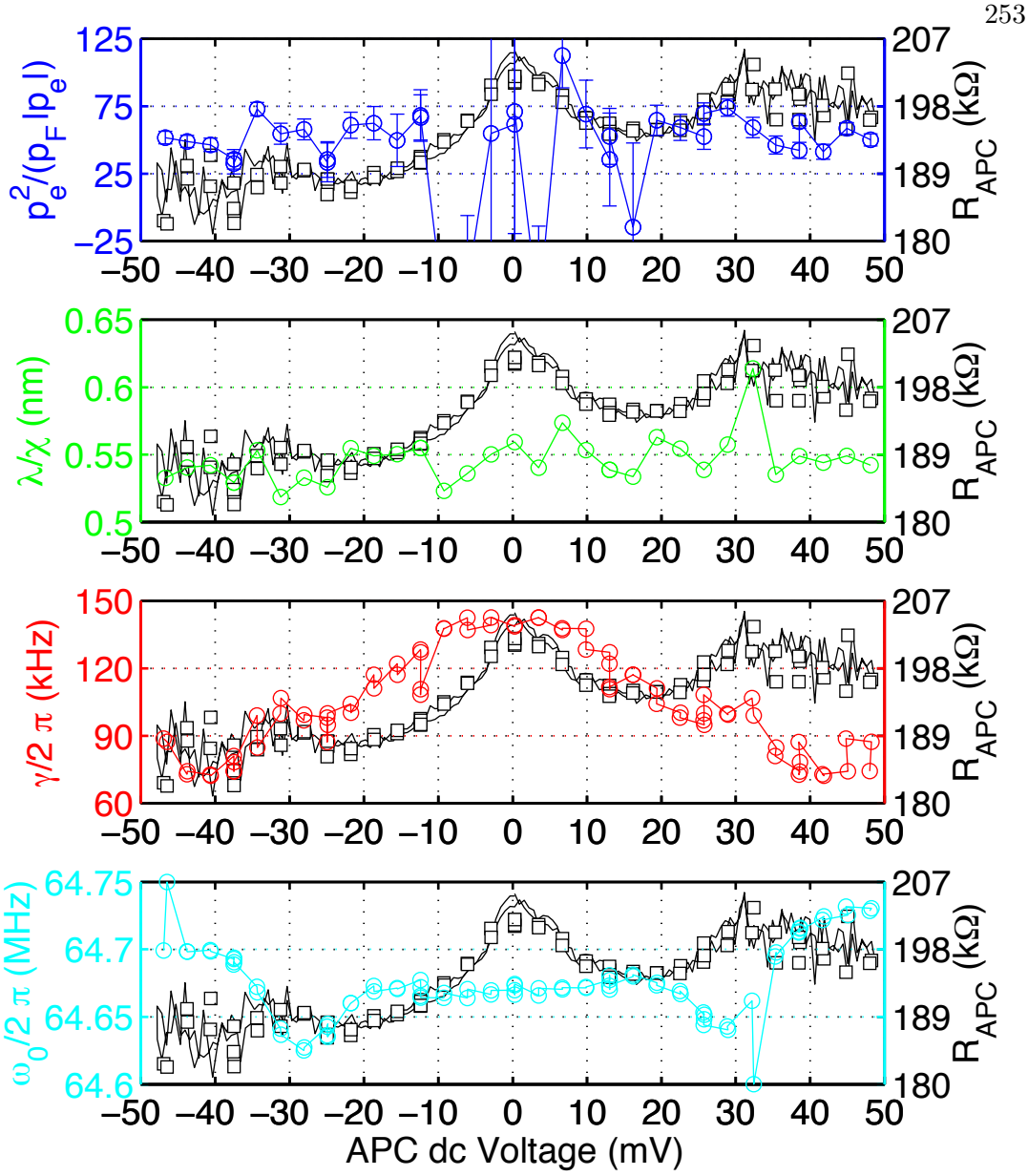

Figure 7.18: As a function of dc voltage V_{APCdc} across the junction, I plot the backaction force parameterized in terms of electron momentum p_e/p_F (blue, left axis), the inferred length scale λ/χ (green, left axis), the nanomechanical damping γ (red, left axis), and the nanomechanical resonance frequency ω_0 (cyan, left axis). I also plot the differential resistance R_{APC} of the junction on each axis (right axis, black). The resistance R_{APC} is determined both during the displacement measurement (black squares) with a 4 mV microwave bias voltage and separately without an applied microwave bias (black lines). The microwave voltage bias effectively averages these measurements over V_{APCdc}±4 mV (see chapter 5). The differential resistance R_{APC} does not contain any large peaks or dips, and both the effective electron momentum p_e/p_F and length scale λ/χ also have little dependence on V_{APCdc}. Contrary to most expectations, in this case the damping γ decreases with increasing voltage. There is also a small feature in the resonance frequency as a function of V_{APCdc}.

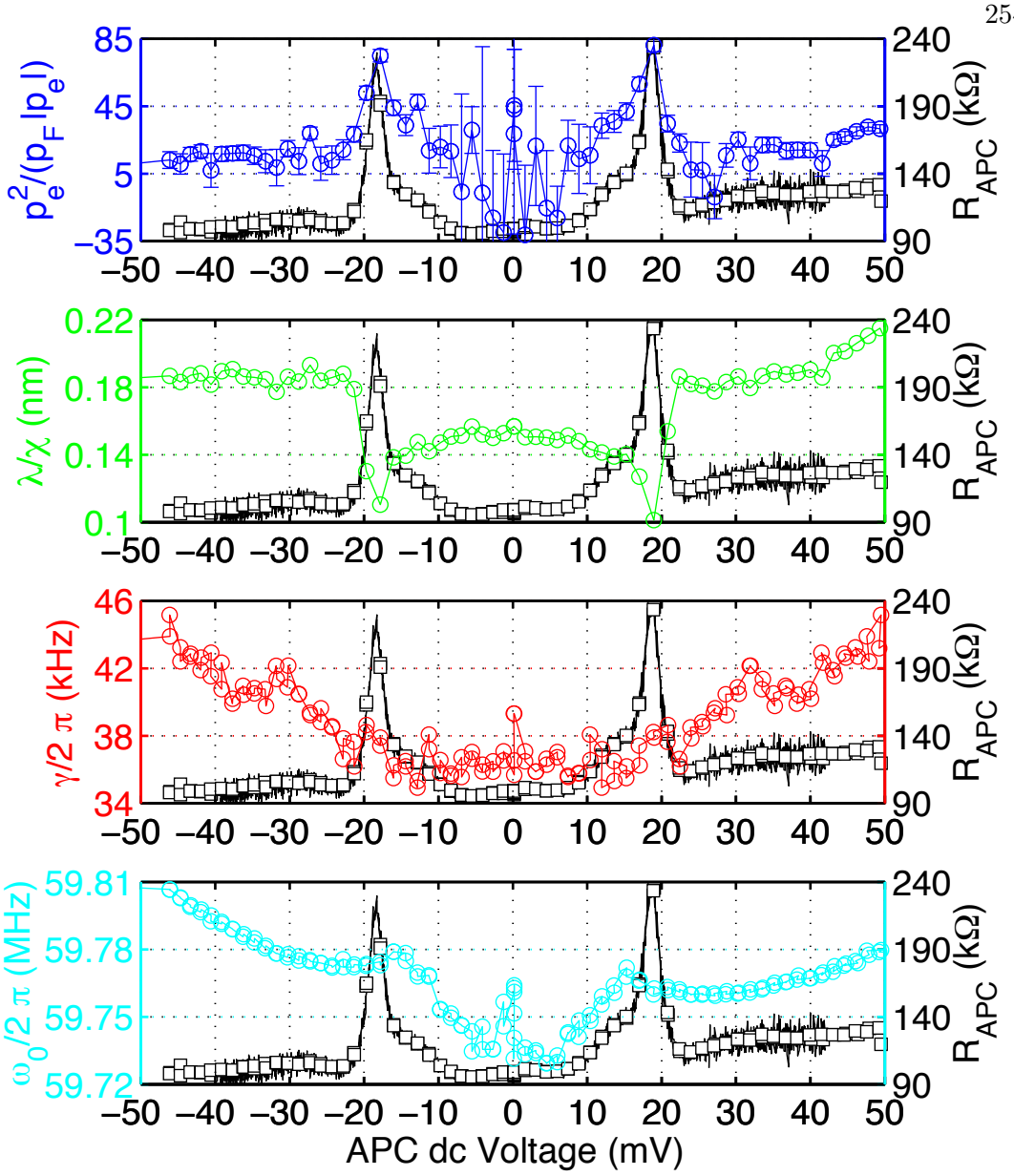

Figure 7.19: As a function of dc voltage V_{APCdc} across the junction, I plot the back-action force parameterized in terms of electron momentum p_e/p_F (blue, left axis), the inferred length scale λ/χ (green, left axis), the nanomechanical damping γ (red, left axis), and the nanomechanical resonance frequency ω_0 (cyan, left axis). I also plot the differential resistance R_{APC} of the junction on each axis (right axis, black). The resistance R_{APC} is determined both during the displacement measurement (black squares) with a 2 mV microwave bias voltage and separately without an applied microwave bias (black lines). The microwave voltage bias effectively averages these measurements over V_{APCdc}±2 mV (see chapter 5). The differential resistance R_{APC} contains a large peak at $V_{APCdc} = \pm 18$ mV, and both the effective electron momentum p_e/p_F and length scale λ/χ also have sharp features at $V_{APCdc} = \pm 18$ mV. The damping γ increases slightly with increasing voltage. There are also small features and an overall increase in the resonance frequency as a function of V_{APCdc}.

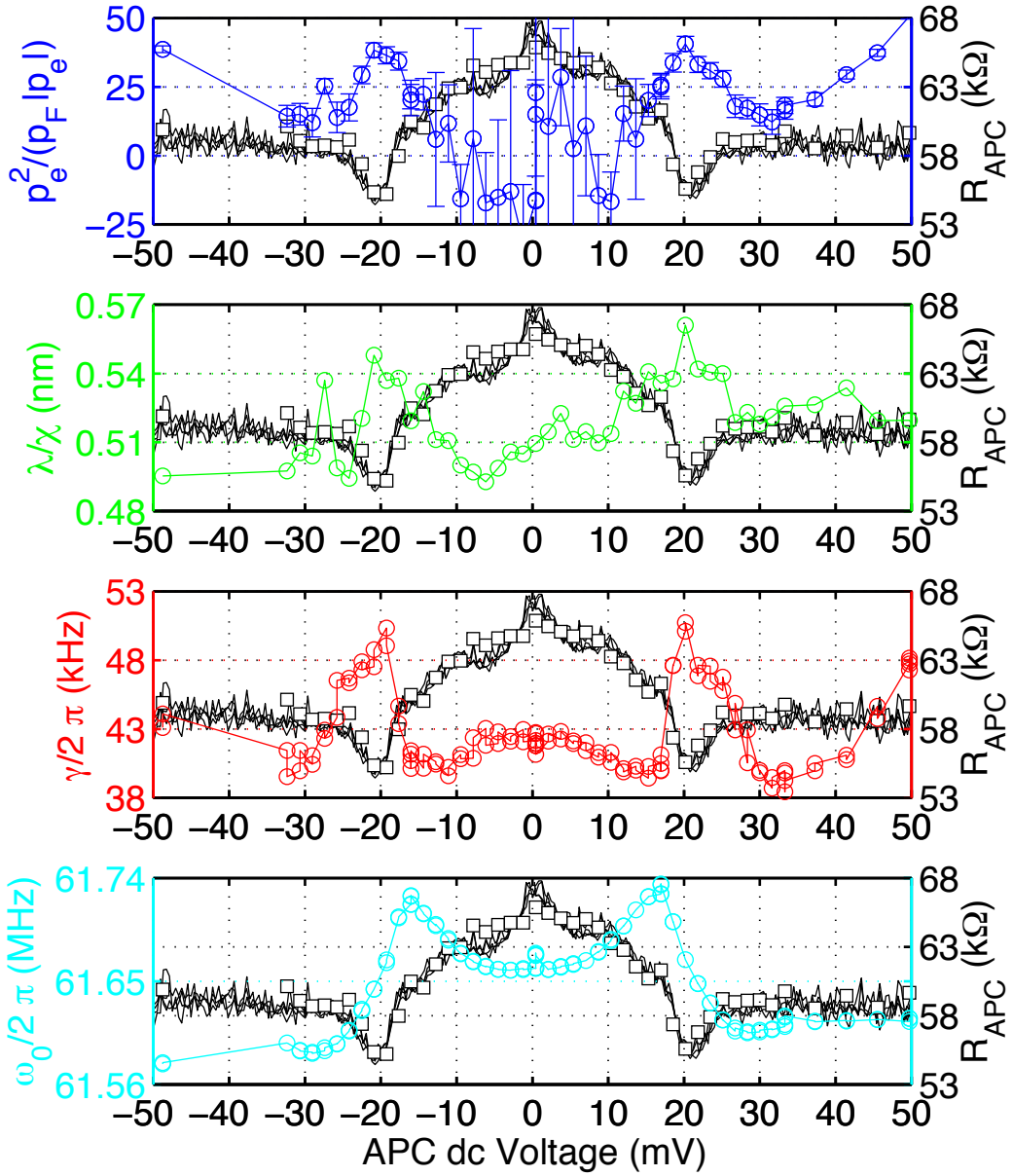

Figure 7.20: As a function of dc voltage V_{APCdc} across the junction, I plot the backaction force parameterized in terms of electron momentum p_e/p_F (blue, left axis), the inferred length scale λ/χ (green, left axis), the nanomechanical damping γ (red, left axis), and the nanomechanical resonance frequency ω_0 (cyan, left axis). I also plot the differential resistance R_{APC} of the junction on each axis (right axis, black). The resistance R_{APC} is determined both during the displacement measurement (black squares) with a 4 mV microwave bias voltage and separately without an applied microwave bias (black lines). The microwave voltage bias effectively averages these measurements over V_{APCdc}±4 mV (see chapter 5). The differential resistance R_{APC} has a dip at $V_{APCdc} = \pm 21$ mV, and both the effective electron momentum p_e/p_F and damping γ have features at $V_{APCdc} = \pm 21$ mV. The resonance frequency ω_0 also depends on V_{APCdc} with a larger rate of change near $V_{APCdc} = \pm 21$ mV and the length scale λ/χ has a small feature near $V_{APCdc} = \pm 21$ mV.

Chapter 8

Conclusions and Future Directions

8.1 Conclusions

In conclusion, I have demonstrated a sensitive measurement of nanomechanical displacement using an atomic point contact (APC). Two techniques were used to create an APC which was coupled to a nanostructure. In both cases, the standard tools of nanolithography were used to create a suspended gold nanostructure with a constriction which was thin and narrow in comparison to the rest of the nanostructure. The device was placed in the ultrahigh vacuum of a 4 K cryogenic system. In the first technique, electromigration, I passed a large current through the constriction and the large current density effectively forced atoms away from the constriction. Eventually, all except two atoms where removed and the flow of electrons through the constriction was dominated by electrons tunneling through a vacuum gap between the two atoms. This technique has the advantage that it is relatively easy to implement, but it is not possible to control the resistance of the APC, that is, the width of the gap. The second technique used mechanical strain to control the resistance of the constriction, creating a mechanically controllable break junction (MCBJ). The applied strain caused the metal constriction to become thinner and fracture on the atomic scale, creating an atomic point contact. This technique required additional infrastructure to create strain by bending the substrate beneath the suspended nanostructure, but had the advantage that the width of the APC gap was controllable and the configuration of atoms in the APC could

be changed, though not with microscopic control. I used this technique to measure the APC properties as a function of APC resistance. In both cases, the motion of the nanostructure created additional strain on the APC because the APC was in the middle of the suspended nanostructure. The changing width of the APC gap created a change in the resistance of the APC which I used to infer the nanomechanical displacement.

Having created an APC coupled to a nanomechanical structure, I used a microwave resonant circuit to increase the speed of the APC measurement. The filter created by the combination of the APC, a high impedance device $R_{APC} > 10$ kΩ, and the stray capacitance in the measurement circuit limited the bandwidth of earlier APC measurements to less than 100 kHz. I used the same microwave technique that was used to create the radio-frequency single electron transistor (RF-SET) to overcome this bandwidth limitation. The high impedance device was embedded in an LC resonant circuit. Near the electrical resonance frequency, the LC circuit matched the APC resistance to the resistance of the 50 Ω measurement circuit. The bandwidth of the measurement is controlled by the quality factor of the resonant circuit. Using a 500 MHz resonant circuit, I increased the bandwidth of the APC measurement to more than 30 MHz. Kemiktarak *et al* [140] recently used this technique, which I described in reference [11], to create an RF-STM with the goals of decreasing STM image acquisition time, using the STM tip as a local thermometer, and sensing nanomechanical motion.

Because of the large bandwidth of the microwave measurement and the low noise of 50 Ω cryogenic microwave amplifiers, the noise in the APC displacement measurement was dominated by the shot noise of tunneling electrons. The shot noise of tunneling electrons is the fundamental source of noise in an APC measurement. Minimizing the effect of other, less interesting, sources of noise is important because it is a prerequisite for performing a quantum limited measurement. In this thesis, the displacement measurement was calibrated using the Brownian motion of the nanostructure at cryogenic temperatures. I measured displacement with a shot-noise limited imprecision

$\sqrt{S_x} = 0.29$ fm/$\sqrt{\text{Hz}}$; this is equal to 4 times the imprecision $\sqrt{S_{xSQL}} = \sqrt{\hbar/m\omega_0\gamma}$ at the standard quantum limit where m is the effective mass of the nanostructure, ω_0 the resonance frequency, and γ the damping.

I compared the APC displacement detector to a quantum limited detector by simultaneously measuring the backaction force of the APC detector. The APC measurement created a noisy backaction force with a spectral density $\sqrt{S_F} = 61$ aN/$\sqrt{\text{Hz}}$; this is equal to 40 times the backaction $\sqrt{S_{FSQL}} = \sqrt{\hbar m\omega_0\gamma}$ at the standard quantum limit. The combination of the measurement imprecision S_x and the random motion caused by the backaction force resulted in a total measurement uncertainty that is 27 times the standard quantum limit $\sqrt{2\hbar/m\omega_0\gamma}$. A quantum limited detector would operate at the limit imposed by the Heisenberg uncertainty principle $\sqrt{S_xS_F} \geq \hbar$. In comparison, the imprecision-backaction product of the APC detector $\sqrt{S_xS_F} = 168\hbar$ is larger than required by quantum mechanics. Because the measurement imprecision S_x was dominated by the fundamental source of noise in an APC measurement, the shot noise of tunneling electrons, the non-ideality of the APC detector is likely due to a backaction force S_F in excess of that required by quantum mechanics.

The excess backaction force created by the APC measurement could have many possible origins. For example, the mutual capacitance C between the APC electrodes depends on the electrode separation x which results in an electrostatic backaction force $F_C = (\partial C/\partial x)(V_{APC}^2/2)$ where V_{APC} is the voltage across the APC. The presence of trapped charge near the APC would result in a backaction force $F_V = \sigma_V V_{APC}$ where the proportionality constant σ_V depends on the magnitude and location of the trapped charge. As a final example, each tunneling electron imparts a momentum kick p_e to the nanostructure resulting in a backaction force $F_I = (p_e/e)I_{APC}$. In a phenomenological model of the APC displacement detector it is the uncertainty in the magnitude of the momentum kick p_e which enforces the Heisenberg constraint.

While I cannot unambiguously determine the origin of this excess backaction force,

I was able to eliminate certain possible origins by investigating the properties of the backaction force in more detail. In two electromigrated APCs I observe a linear dependence between the spectral density of the current fluctuations $S_I = S_V/R_{APC}^2 \approx 2eI_{APC}$ and the backaction force S_F. This linear dependence is consistent with a backaction force due to trapped charge F_V or the momentum kicks of tunneling electrons F_I, but inconsistent with an electrostatic backaction F_C. To account for the observed backaction force, each electron would have to deliver a momentum impulse of $p_e = p_F \times (32 \pm 3)$, for the first electromigrated device, or $p_e = p_F \times (34 \pm 1)$ for the second electromigrated device, where p_F is the Fermi momentum of electrons in bulk gold. A simple phenomenological model of the backaction created by momentum kicks predicts that each electron should deliver a momentum kick approximately equal to the Fermi momentum. In this context, the momentum impulse $p_e \approx 30p_F$ required to account for the APC backaction seems implausibly large.

Using an MCBJ, I controlled the width of the vacuum gap between atoms that form the APC and measured the backaction force at different APC resistances. I measured the unintentional feedback created by the APC backaction and directly measured the magnitude of the backaction force. The combination of the APC and the measurement circuit formed an unintentional feedback loop. Nanomechanical motion changed the resistance R_{APC} of the APC. The changing resistance modified the current I_{APC} flowing through the APC and the voltage V_{APC} across the APC. The details of this effect depends on the measurement circuit; in this case, the impedance of the measurement circuit was smaller than R_{APC} so nanomechanical motion had a larger effect on the current I_{APC} than on the voltage V_{APC}. A backaction force proportional to current I_{APC} or voltage V_{APC} closed the feedback loop, creating a force on the nanomechanical structure that was proportional to displacement. At the same time, I directly measured the magnitude of the backaction force by observing the nanomechanical response to a voltage $V_{APC} = I_{APC}R_{APC}$ across the APC at frequencies near the nanomechanical

resonance frequency. The combination of the observed unintentional feedback and directly measured backaction force was better explained by a backaction force proportional to current than a backaction force proportional to voltage F_V at all APC resistances. While these observations did not directly address the origin of the backaction force, I can parameterize this backaction force proportional to current F_I in terms of the momentum kick p_e delivered by tunneling electrons. At different APC resistances, each electron would have to deliver a momentum impulse between p_F and $40p_F$ to account for the observed backaction force.

I also attempted to determine whether the noisy backaction force and the shot noise of tunneling electrons were correlated. If the backaction force was due to the average momentum impulse p_e delivered by each tunneling electron, then the shot noise and backaction force would be correlated. This correlation measurement could only place an upper limit on the size of any correlated backaction which is consistent with each electron delivering a momentum kick $p_e < 50p_F$. The upper bound is so large because in these measurements the amplifier regrettably contributed much more noise than the electrical shot noise due to tunneling electrons.

Finally, I observed evidence of molecular vibrations in the APC using inelastic electron tunneling spectroscopy and simultaneously measured the backaction force. Molecular vibrations can increase or decrease the differential resistance R_{APC} of the APC when the vibrational energy $\hbar\omega_0$ is equal to the bias energy $e|V_{APC}|$. When I observed peaks or dips in R_{APC} at a bias V_{APC}, indicative of molecular vibrations, I also observed a resonant increase in the backaction force at the same bias V_{APC}. This observation suggests that the excess backaction may have been caused by the interaction of tunneling electrons with molecular vibrations.

8.2 Future Directions

There are a number of different questions that future experiments involving APC displacement detectors can explore. An improved correlation measurement could conclusively demonstrate whether the backaction force is due to the effect of single electrons. In addition, a simultaneous measurement of the directly applied backaction force, the unintentional feedback created by the backaction force, and the correlations between the noisy backaction force and the shot noise of tunneling electrons would place additional constraints on the possible physical origins of the backaction force.

An improved correlation measurement would require a lower noise measurement circuit. There are three main approaches to improving the measurement circuit. First, the measurement could be improved by using an amplifier which adds less noise. Second, the bandwidth and noise characteristics of the measurement circuit could be improved by using a more complicated matching circuit with multiple stages instead of a single capacitance and inductance. Finally, the APC could be coupled to a nanomechanical structure with a larger mechanical resonance frequency ω_0. This change in frequency could help the measurement circuit because it is easier to create low noise 50 Ω amplifiers at higher frequencies. It could also improve the stability of the APC and potentially push the mechanical structure towards the interesting quantum regime where $\hbar\omega_0 \approx k_B T$. However increasing the resonance frequency would usually also increase the stiffness $k = m\omega_0^2$ of the structure and decrease the displacement caused by applied forces which would make it more difficult to observe correlations. This undesirable scaling could be mitigated if the increase in resonance frequency was accomplished by decreasing the mass of the nanomechanical structure using, for example, novel fabrication techniques and nanotubes or nanowires.

Future experiments involving APC displacement detectors could also explore the differences between gold APCs and APCs made out of other materials. The static me-

chanical and electrical properties of APCs are material dependent, so other materials could result in a more stable atomic point contact. More interestingly, measuring the backaction force in different materials could help to differentiate between the fundamental backaction due to the momentum impulse delivered by tunneling electrons and the material-specific properties. In addition, a material that is lighter than gold could be used to create a more compliant mechanical system which is more sensitive to applied forces.

Finally, future experiments could study in detail the interaction between trapped molecules, tunneling electrons, and nanomechanical structures. The observations of the inelastic electron tunneling spectrum and backaction force I performed indicated a possible link between molecular vibrations and the backaction force. However, I did not purposefully trap a specific molecular species or study in detail the link between trapped molecules and tunneling electrons. Such an investigation could lead to valuable insight into the properties of trapped molecules and the backaction force. If the excess backaction is due to molecular vibrations, this insight could be used to improve the APC displacement detector by decreasing the excess backaction force.

Bibliography

[1] D. Rugar, C. Yannoni, and J. Sidles, "Mechanical detection of magnetic resonance," Nature, vol. 360, no. 6404, pp. 563–566, Dec 1992.

[2] Y. Sugimoto, P. Pou, M. Abe, P. Jelinek, R. Perez, S. Morita, and O. Custance, "Chemical identification of individual surface atoms by atomic force microscopy," Nature, vol. 446, no. 7131, pp. 64–67, Mar 2007.

[3] R. Knobel and A. Cleland, "Nanometre-scale displacement sensing using a single electron transistor," Nature, vol. 424, no. 6946, pp. 291–293, Jul 2003.

[4] S. Etaki, M. Poot, I. Mahboob, K. Onomitsu, H. Yamaguchi, and H. van der Zant, "Motion detection of a micromechanical resonator embedded in a d.c. squid," Nat Phys, vol. 4, no. 10, pp. 785–788, Aug 2008.

[5] M. Poggio, M. P. Jura, C. L. Degen, M. A. Topinka, H. J. Mamin, D. Goldhaber-Gordon, and D. Rugar, "An off-board quantum point contact as a sensitive detector of cantilever motion," Nature Physics, vol. 4, no. 8, pp. 635–638, Jun 2008.

[6] V. Sazonova, Y. Yaish, H. Ustunel, D. Roundy, T. Arias, and P. McEuen, "A tunable carbon nanotube electromechanical oscillator," Nature, vol. 431, no. 7006, pp. 284–287, Sep 2004.

[7] G. Binnig and H. Rohrer, "Scanning tunneling microscopy¯from birth to adolescence," Rev. Mod. Phys., vol. 59, no. 3, pp. 615–625, Jul 1987.

[8] N. Agrait, A. Yeyati, and J. van Ruitenbeek, "Quantum properties of atomic-sized conductors," Physics Reports, vol. 377, no. 2-3, pp. 81–279, Feb 2003.

[9] M. L. Trouwborst, E. H. Huisman, F. L. Bakker, S. J. van der Molen, and B. J. van Wees, "Single atom adhesion in optimized gold nanojunctions," Physical Review Letters, vol. 100, no. 17, p. 175502, Apr 2008.

[10] M. Trouwborst, "Electron transport through single gold atoms and hydrogen molecules switching on the atomic scale electron transport through single gold electron transport through single gold atoms and hydrogen moleculs," Ph.D. dissertation, Zernike Institute for Advanced Materials at the University of Groningen, the Netherlands, 2009.

[11] N. E. Flowers-Jacobs, D. R. Schmidt, and K. W. Lehnert, "Intrinsic noise properties of atomic point contact displacement detectors," Phys Rev Lett, vol. 98, p. 096804, Mar 2007.

[12] R. P. Feynman, "There's plenty of room at the bottom," Caltech's Engineering and Science, 1960.

[13] K. E. Drexler, Engines of Creation: The Coming Era of Nanotechnology. Anchor Books, 1986.

[14] A. N. Cleland, Foundations of Nanomechanics. Springer, 2003.

[15] K. Ekinci and M. Roukes, "Nanoelectromechanical systems," Review of Scientific Instruments, vol. 76, no. 6, p. 061101, May 2005.

[16] A. Cleland and M. Roukes, "Nanoscale mechanics," Proceedings of 24th International Conference on the Physics of Semiconductors, 2-7 Aug. 1998, pp. 261–8, Aug 1999.

[17] S. Datta, Electronic transport in mesoscopic systems. Cambridge University Press, 1997.

[18] Y. Imry, Introduction to mesoscopic physics. Oxford University Press, 2002.

[19] M. J. M. Jong and C. W. J. Beenakker, "Shot noise in mesoscopic systems," arxiv:cond-mat, p. 9611140, Nov 1996.

[20] D. K. Ferry and S. M. Goodnick, Transport in Nanostructures. Cambridge University Press, 1997.

[21] F. Giessibl, "Advances in atomic force microscopy," Reviews of Modern Physics, vol. 75, no. 3, p. 949, Jul 2003.

[22] G. Binnig and H. Rohrer, "In touch with atoms," Reviews of Modern Physics, vol. 71, no. 2, p. S324, Mar 1999.

[23] G. Binnig, C. Quate, and C. Gerber, "Atomic force microscope," Physical Review Letters, vol. 56, no. 9, p. 930, Mar 1986.

[24] C. Caves, K. Thorne, R. Drever, V. Sandberg, and M. Zimmermann, "On the measurement of a weak classical force coupled to a quantum-mechanical oscillator. i. issues of principle," Rev. Mod. Phys., vol. 52, no. 2, pp. 341–392, Apr 1980.

[25] K. Thorne, "Gravitational-wave research: Current status and future prospects," Reviews of Modern Physics, vol. 52, no. 2, p. 285, Apr 1980.

[26] H. Paik, "Superconducting tunable-diaphragm transducer for sensitive acceleration measurements," Journal of Applied Physics, vol. 47, no. 3, pp. 1168–1178, Mar 1976.

[27] J. Weber, "Observation of the thermal fluctuations of a gravitational-wave detector," Physical Review Letters, vol. 17, no. 24, p. 1228, Dec 1966.

[28] ——, "Detection and generation of gravitational waves," Phys. Rev., vol. 117, no. 1, p. 306, Jan 1960.

[29] A. A. Clerk, M. H. Devoret, S. M. Girvin, F. Marquardt, and R. J. Schoelkopf, "Introduction to quantum noise, measurement and amplification," arXiv, vol. cond-mat.mes-hall, Oct 2008.

[30] M. Aspelmeyer and K. Schwab, "Focus on mechanical systems at the quantum limit," New Journal of Physics, vol. 10, no. 9, p. 095001, Sep 2008.

[31] A. Naik, O. Buu, M. LaHaye, A. Armour, A. Clerk, M. Blencowe, and K. Schwab, "Cooling a nanomechanical resonator with quantum back-action," Nature, vol. 443, no. 7108, pp. 193–196, Sep 2006.

[32] M. LaHaye, O. Buu, B. Camarota, and K. Schwab, "Approaching the quantum limit of a nanomechanical resonator," Science, vol. 304, no. 5667, pp. 74–77, Apr 2004.

[33] A. Cleland, J. Aldridge, D. Driscoll, and A. Gossard, "Nanomechanical displacement sensing using a quantum point contact," Applied Physics Letters, vol. 81, no. 9, pp. 1699–1701, Aug 2002.

[34] M. Bocko and R. Onofrio, "On the measurement of a weak classical force coupled to a harmonic oscillator: experimental progress," Rev. Mod. Phys., vol. 68, no. 3, pp. 755–799, Jul 1996.

[35] G. Steele, A. Huttel, B. Witkamp, M. Poot, H. Meerwaldt, L. Kouwenhoven, and H. van der Zant, "Strong coupling between single-electron tunneling and nanomechanical motion," Science, vol. 325, no. 5944, pp. 1103–1107, Aug 2009.

[36] A. K. Hüttel, M. Poot, B. Witkamp, and H. S. J. van der Zant, "Nanoelectromechanics of suspended carbon nanotubes," New Journal of Physics, vol. 10, no. 9, p. 095003 (13pp), Sep 2008.

[37] D. Garcia-Sanchez, A. Paulo, M. Esplandiu, F. Perez-Murano, L. Forro, A. Aguasca, and A. Bachtold, "Mechanical detection of carbon nanotube resonator vibrations," Physical Review Letters, vol. 99, no. 8, pp. 085 501–4, Aug 2007.

[38] Binnig, H. Rohrer, C. Gerber, and E. Weibel, "Surface studies by scanning tunneling microscopy," Phys. Rev. Lett., vol. 49, no. 1, pp. 57–61, Jul 1982.

[39] G. Binnig, H. Rohrer, C. Gerber, and E. Weibel, "Tunneling through a controllable vacuum gap," Applied Physics Letters, vol. 40, no. 2, pp. 178–180, Jan 1982.

[40] H. Park, J. Park, A. Lim, E. Anderson, A. Alivisatos, and P. McEuen, "Nanomechanical oscillations in a single-c60 transistor," Nature, vol. 407, no. 6800, pp. 57–60, Sep 2000.

[41] H. Park, A. Lim, A. Alivisatos, J. Park, and P. McEuen, "Fabrication of metallic electrodes with nanometer separation by electromigration," Applied Physics Letters, vol. 75, no. 2, pp. 301–303, Jul 1999.

[42] A. Morpurgo, C. Marcus, and D. Robinson, "Controlled fabrication of metallic electrodes with atomic separation," Applied Physics Letters, vol. 74, no. 14, pp. 2084–2086, Apr 1999.

[43] A. Bezryadin and C. Dekker, "Nanofabrication of electrodes with sub-5 nm spacing for transport experiments on single molecules and metal clusters," Journal of Vacuum Science & Technology B: Microelectronics and Nanometer Structures, vol. 15, no. 4, pp. 793–799, Jul 1997.

[44] J. Ruitenbeek, A. Alvarez, I. Pineyro, C. Grahmann, P. Joyez, M. Devoret, D. Esteve, and C. Urbina, "Adjustable nanofabricated atomic size contacts," Review of Scientific Instruments, vol. 67, no. 1, pp. 108–111, Oct 1996.

[45] C. Zhou, C. Muller, M. Deshpande, J. Sleight, and M. Reed, "Microfabrication of a mechanically controllable break junction in silicon," Applied Physics Letters, vol. 67, no. 8, pp. 1160–1162, Aug 1995.

[46] C. Muller and R. Ouboter, "Fabrication of inherently stable and adjustable contacts of atomic size," Journal of Applied Physics, vol. 77, no. 10, pp. 5231–5236, May 1995.

[47] C. Muller, J. van Ruitenbeek, and L. de Jongh, "Conductance and supercurrent discontinuities in atomic-scale metallic constrictions of variable width," Phys. Rev. Lett., vol. 69, no. 1, pp. 140–143, Jul 1992.

[48] J. Moreland and J. Ekin, "Electron tunneling experiments using nb-sn "break" junctions," Journal of Applied Physics, vol. 58, no. 10, pp. 3888–3895, Nov 1985.

[49] M. Kiguchi, O. Tal, S. Wohlthat, F. Pauly, M. Krieger, D. Djukic, J. C. Cuevas, and J. M. van Ruitenbeek, "Highly conductive molecular junctions based on direct binding of benzene to platinum electrodes," Physical Review Letters, vol. 101, no. 4, p. 046801, Jul 2008.

[50] O. Tal, M. Krieger, B. Leerink, and J. M. van Ruitenbeek, "Electron-vibration interaction in single-molecule junctions: From contact to tunneling regimes," Physical Review Letters, vol. 100, no. 19, p. 196804, May 2008.

[51] J. Parks, A. Champagne, G. Hutchison, S. Flores-Torres, H. Abruna, and D. Ralph, "Tuning the kondo effect with a mechanically controllable break junction," Physical Review Letters, vol. 99, no. 2, p. 026601, Jul 2007.

[52] A. Pasupathy, J. Park, C. Chang, A. Soldatov, S. Lebedkin, R. Bialczak, J. Grose, L. Donev, J. Sethna, D. Ralph, and P. McEuen, "Vibration-assisted electron tunneling in c¡sub¿140¡/sub¿ transistors," Nano Letters, vol. 5, no. 2, pp. 203–207, Feb 2005.

[53] A. Champagne, A. Pasupathy, and D. Ralph, "Mechanically adjustable and electrically gated single-molecule transistors," Nano Letters, vol. 5, no. 2, pp. 305–308, Jan 2005.

[54] R. Smit, Y. Noat, C. Untiedt, N. Lang, M. van Hemert, and J. van Ruitenbeek, "Measurement of the conductance of a hydrogen molecule," Nature, vol. 419, no. 6910, pp. 906–909, Oct 2002.

[55] W. Liang, M. Shores, M. Bockrath, J. Long, and H. Park, "Kondo resonance in a single-molecule transistor," Nature, vol. 417, no. 6890, pp. 725–729, Jun 2002.

[56] J. Park, A. Pasupathy, J. Goldsmith, C. Chang, Y. Yaish, J. Petta, M. Rinkoski, J. Sethna, H. Abruna, P. McEuen, and D. Ralph, "Coulomb blockade and the kondo effect in single-atom transistors," Nature, vol. 417, no. 6890, pp. 722–725, Jun 2002.

[57] M. Reed, C. Zhou, C. Muller, T. Burgin, and J. Tour, "Conductance of a molecular junction," Science, vol. 278, no. 5336, pp. 252–254, Oct 1997.

[58] M. Bocko and K. Stephenson, "Tunneling transducers: Quantum limited displacement monitors at the nanometer scale," Journal of Vacuum Science & Technology B: Microelectronics and Nanometer Structures, vol. 9, no. 2, pp. 1363–1366, Mar 1991.

[59] M. Bocko, "The scanning tunneling microscope as a high-gain, low-noise displacement sensor," Review of Scientific Instruments, vol. 61, no. 12, pp. 3763–3768, Dec 1990.

[60] F. Bordoni, M. Karim, M. Bocko, and T. Mengxi, "Proposed room-temperature detector for gravitational radiation from galactic sources," Phys. Rev. D, vol. 42, no. 8, pp. 2952–2955, Oct 1990.

[61] K. Stephenson, M. Bocko, and R. Koch, "Reduced-noise nonreciprocal transducer based upon vacuum tunneling," Phys. Rev. A, vol. 40, no. 11, pp. 6615–6625, Dec 1989.

[62] M. Bocko, K. Stephenson, and R. Koch, "Vacuum tunneling probe: A nonreciprocal, reduced-back-action transducer," Phys. Rev. Lett., vol. 61, no. 6, pp. 726–729, Aug 1988.

[63] M. Niksch and G. Binnig, "Proposal for a novel gravitational-wave sensor," Journal of Vacuum Science & Technology A: Vacuum, Surfaces, and Films, vol. 6, no. 2, pp. 470–471, Mar 1988.

[64] R. Onofrio and C. Presilla, "Quantum limit in resonant vacuum tunnelling transducers," Europhysics Letters, vol. 22, no. 5, p. 333, May 1993.

[65] C. Presilla, R. Onofrio, and M. Bocko, "Uncertainty-principle noise in vacuum-tunneling transducers," Phys. Rev. B, vol. 45, no. 7, pp. 3735–3743, Feb 1992.

[66] B. Yurke and G. Kochanski, "Momentum noise in vacuum tunneling transducers," Phys. Rev. B, vol. 41, no. 12, pp. 8184–8194, Apr 1990.

[67] S. D. Bennett and A. A. Clerk, "Full counting statistics and conditional evolution in a nanoelectromechanical system," Physical Review B (Condensed Matter and Materials Physics), vol. 78, no. 16, p. 165328, Oct 2008.

[68] C. B. Doiron, B. Trauzettel, and C. Bruder, "Measuring the momentum of a nanomechanical oscillator through the use of two tunnel junctions," Physical Review Letters, vol. 100, no. 2, p. 027202, Jan 2008.

[69] C. Doiron, B. Trauzettel, and C. Bruder, "Improved position measurement of nanoelectromechanical systems using cross correlations," Physical Review B (Condensed Matter and Materials Physics), vol. 76, no. 19, p. 195312, Nov 2007.

[70] J. Wabnig, J. Rammer, and A. Shelankov, "Noise spectrum of a tunnel junction coupled to a nanomechanical oscillator," Physical Review B (Condensed Matter and Materials Physics), vol. 75, no. 20, p. 205319, May 2007.

[71] J. Wabnig, D. Khomitsky, J. Rammer, and A. Shelankov, "Statistics of charge transfer in a tunnel junction coupled to an oscillator," Physical Review B (Condensed Matter and Materials Physics), vol. 72, no. 16, p. 165347, Oct 2005.

[72] A. Clerk, "Quantum-limited position detection and amplification: A linear response perspective," Physical Review B (Condensed Matter and Materials Physics), vol. 70, no. 24, p. 245306, Dec 2004.

[73] J. Rammer, A. Shelankov, and J. Wabnig, "Quantum measurement in charge representation," Physical Review B (Condensed Matter and Materials Physics), vol. 70, no. 11, p. 115327, Sep 2004.

[74] L. Levitov and M. Reznikov, "Counting statistics of tunneling current," Physical Review B (Condensed Matter and Materials Physics), vol. 70, no. 11, p. 115305, Sep 2004.

[75] A. Clerk and S. Girvin, "Shot noise of a tunnel junction displacement detector," Physical Review B (Condensed Matter and Materials Physics), vol. 70, no. 12, p. 121303, Sep 2004.

[76] A. Tajic, M. Kindermann, and C. Beenakker, "Momentum noise in a quantum point contact," Phys. Rev. B, vol. 66, no. 24, p. 241301, Dec 2002.

[77] D. Mozyrsky and I. Martin, "Quantum-classical transition induced by electrical measurement," Phys. Rev. Lett., vol. 89, no. 1, p. 018301, Jun 2002.

[78] D. Rugar, R. Budakian, H. Mamin, and B. Chui, "Single spin detection by magnetic resonance force microscopy," Nature, vol. 430, no. 6997, pp. 329–332, Jul 2004.

[79] J. Sidles, J. Garbini, K. Bruland, D. Rugar, O. Züger, S. Hoen, and C. Yannoni, "Magnetic resonance force microscopy," Rev. Mod. Phys., vol. 67, no. 1, pp. 249–265, Jan 1995.

[80] J. Sidles and D. Rugar, "Signal-to-noise ratios in inductive and mechanical detection of magnetic resonance," Phys. Rev. Lett., vol. 70, no. 22, pp. 3506–3509, May 1993.

[81] C. Degen, M. Poggio, H. Mamin, C. Rettner, and D. Rugar, "Nanoscale magnetic resonance imaging," Proceedings of the National Academy of Sciences, vol. 106, no. 5, pp. 1313–1317, Feb 2009.

[82] M. Poggio, C. Degen, C. Rettner, H. Mamin, and D. Rugar, "Nuclear magnetic resonance force microscopy with a microwire rf source," Applied Physics Letters, vol. 90, no. 26, pp. 263 111–1, Jun 2007.

[83] H. J. Mamin, M. Poggio, C. L. Degen, and D. Rugar, "Nuclear magnetic resonance imaging with 90-nm resolution," Nat Nano, vol. 2, no. 5, pp. 301–306, Apr 2007.

[84] R. Budakian, H. Mamin, and D. Rugar, "Spin manipulation using fast cantilever phase reversals," Applied Physics Letters, vol. 89, no. 11, pp. 113 113–1, Sep 1120.

[85] S. hui Chao, W. Dougherty, J. Garbini, and J. Sidles, "Nanometer-scale magnetic resonance imaging," Review of Scientific Instruments, vol. 75, no. 5, pp. 1175–1181, May 2004.

[86] D. Rugar, R. Budakian, H. Mamin, and B. Chui, "Manipulation and detection of electron spins by magnetic resonance force microscopy, 12th international conference on scanning tunneling microscopy / spectroscopy and related techniques, 21-25 july 2003," AIP Conference Proceedings, no. 696, pp. 45–52, Dec 2003.

[87] H. Mamin, R. Budakian, B. Chui, and D. Rugar, "Detection and manipulation of statistical polarization in small spin ensembles," Physical Review Letters, vol. 91, no. 20, pp. 207 604–1, Nov 2003.

[88] D. Rugar, O. Zuger, S. Hoen, C. Yannoni, H.-M. Vieth, and R. Kendrick, "Force detection of nuclear magnetic resonance," Science, vol. 264, no. 5165, pp. 1560–1563, Jun 1994.

[89] F. Giessibl, "Atomic resolution of the silicon (111)-(7x7) surface by atomic force microscopy," Science, vol. 267, no. 5194, pp. 68–71, Jan 1995.

[90] G. Meyer and N. Amer, "Optical-beam-deflection atomic force microscopy: The nacl (001) surface," Applied Physics Letters, vol. 56, no. 21, pp. 2100–2101, May 1990.

[91] E. Meyer, H. Heinzelmann, H. Rudin, and H. Güntherodt, "Atomic resolution on lif (001) by atomic force microscopy," Zeitschrift für Physik B Condensed Matter, vol. 79, no. 1, pp. 3–4, Feb 1990.

[92] F. Giessibl and G. Binnig, "Investigation of the (001) cleavage plane of potassium bromide with an atomic force microscope at 4.2 k in ultra-high vacuum," Ultramicroscopy, vol. 42-44, no. Part 1, pp. 281–289, 1992.

[93] K. Jensen, K. Kim, and A. Zettl, "An atomic-resolution nanomechanical mass sensor," Nat Nano, vol. 3, no. 9, pp. 533–537, Jul 2008.

[94] Y. Yang, C. Callegari, X. Feng, K. Ekinci, and M. Roukes, "Zeptogram-scale nanomechanical mass sensing," Nano Letters, vol. 6, no. 4, pp. 583–586, Apr 2006.

[95] K. Ekinci, X. Huang, and M. Roukes, "Ultrasensitive nanoelectromechanical mass detection," Applied Physics Letters, vol. 84, no. 22, pp. 4469–4471, May 2004.

[96] K. Ekinci, Y. Yang, and M. Roukes, "Ultimate limits to inertial mass sensing based upon nanoelectromechanical systems," Journal of Applied Physics, vol. 95, no. 5, pp. 2682–2689, Mar 2004.

[97] A. K. Naik, M. S. Hanay, W. K. Hiebert, X. L. Feng, and M. Roukes, "Towards single-molecule nanomechanical mass spectrometry," Nat Nano, vol. 4, no. 7, pp. 445–450, Jun 2009.

[98] J. Arlett, M. Paul, J. Solomon, M. Cross, S. Fraser, and M. Roukes, "Bionems: Nanomechanical systems for single-molecule biophysics," Controlled Nanoscale Motion, pp. 241–270, Apr 2007.

[99] C. Hagleitner, A. Hierlemann, D. Lange, A. Kummer, N. Kerness, O. Brand, and H. Baltes, "Smart single-chip gas sensor microsystem," Nature, vol. 414, no. 6861, pp. 293–296, Nov 2001.

[100] M. L. Roukes, "Nanoelectromechanical systems," arXiv, vol. cond-mat.mes-hall, Jan 2000.

[101] D. Baselt, G. Lee, K. Hansen, L. Chrisey, and R. Colton, "A high-sensitivity micromachined biosensor," Proceedings of the IEEE, vol. 85, no. 4, pp. 672–680, Apr 1997.

[102] T. Burg, M. Godin, S. Knudsen, W. Shen, G. Carlson, J. Foster, K. Babcock, and S. Manalis, "Weighing of biomolecules, single cells and single nanoparticles in fluid," Nature, vol. 446, no. 7139, pp. 1066–1069, Apr 2007.

[103] B. Ilic, Y. Yang, and H. Craighead, "Virus detection using nanoelectromechanical devices," Applied Physics Letters, vol. 85, no. 13, pp. 2604–2606, Sep 2004.

[104] T. Burg and S. Manalis, "Suspended microchannel resonators for biomolecular detection," Applied Physics Letters, vol. 83, no. 13, pp. 2698–2700, Sep 2003.

[105] D. Eddy and D. Sparks, "Application of mems technology in automotive sensors and actuators," Proceedings of the IEEE, vol. 86, no. 8, pp. 1747–1755, Aug 1998.

[106] M. Esashi, S. Sugiyama, K. Ikeda, Y. Wang, and H. Miyashita, "Vacuum-sealed silicon micromachined pressure sensors," Proceedings of the IEEE, vol. 86, no. 8, pp. 1627–1639, Aug 1998.

[107] H. Fujita, "Microactuators and micromachines," Proceedings of the IEEE, vol. 86, no. 8, pp. 1721–1732, Aug 1998.

[108] K. Gabriel, "Microelectromechanical systems," Proceedings of the IEEE, vol. 86, no. 8, pp. 1534–1535, Aug 1998.

[109] A. Mason, N. Yazdi, A. Chavan, K. Najafi, and K. Wise, "A generic multielement microsystem for portable wireless applications," Proceedings of the IEEE, vol. 86, no. 8, pp. 1733–1746, Aug 1998.

[110] C. Mastrangelo, M. Burns, and D. Burke, "Microfabricated devices for genetic diagnostics," Proceedings of the IEEE, vol. 86, no. 8, pp. 1769–1787, Aug 1998.

[111] R. Muller and K. Lau, "Surface-micromachined microoptical elements and systems," Proceedings of the IEEE, vol. 86, no. 8, pp. 1705–1720, Aug 1998.

[112] C.-C. Nguyen, L. Katehi, and G. Rebeiz, "Micromachined devices for wireless communications," Proceedings of the IEEE, vol. 86, no. 8, pp. 1756–1768, Aug 1998.

[113] P. V. Kessel, L. Hornbeck, R. Meier, and M. Douglass, "A mems-based projection display," Proceedings of the IEEE, vol. 86, no. 8, pp. 1687–1704, Aug 1998.

[114] N. Yazdi, F. Ayazi, and K. Najafi, "Micromachined inertial sensors," Proceedings of the IEEE, vol. 86, no. 8, pp. 1640–1659, Aug 1998.

[115] V. B. Braginsky and F. Y. Khalili, Quantum Measurement. Cambridge University Press, 1992.

[116] C. Caves, "Quantum limits on noise in linear amplifiers," Phys. Rev. D, vol. 26, no. 8, pp. 1817–1839, Oct 1982.

[117] W. Heisenberg, "Über den anschulichen inhalt der quantentheoretischen kinematik und mechanik," Z. Phys., vol. 43, pp. 172–198, 1927.

[118] ——, "Über quantentheoretishe umdeutung kinematisher und mechanischer beziehungen," Zeitschrift für Physik, vol. 33, pp. 879–893, 1925.

[119] LIGO and Virgo, "An upper limit on the stochastic gravitational-wave background of cosmological origin," Nature, vol. 460, no. 7258, pp. 990–994, Aug 2009.

[120] B. P. A. et al, "Ligo: the laser interferometer gravitational-wave observatory," Reports on Progress in Physics, vol. 72, no. 7, p. 076901, Jun 2009.

[121] O. D. A. et al, "The schenberg spherical gravitational wave detector: the first commissioning runs," Classical and Quantum Gravity, vol. 25, no. 11, p. 114042, May 2008.

[122] L. Gottardi, A. de Waard, O. Usenko, G. Frossati, M. Podt, J. Flokstra, M. Bassan, V. Fafone, Y. Minenkov, and A. Rocchi, "Sensitivity of the spherical gravitational wave detector minigrail operating at 5 k," Physical Review D (Particles, Fields, Gravitation, and Cosmology), vol. 76, no. 10, pp. 102 005–10, Nov 2007.

[123] A. V. (for the AURIGA Collaboration), "Present performance and future upgrades of the auriga capacitive readout," Classical and Quantum Gravity, vol. 23, no. 8, p. S103, Mar 2006.

[124] L. Baggio, M. Bignotto, M. Bonaldi, M. Cerdonio, L. Conti, P. Falferi, N. Liguori, A. Marin, R. Mezzena, A. Ortolan, S. Poggi, G. Prodi, F. Salemi, G. Soranzo, L. Taffarello, G. Vedovato, A. Vinante, S. Vitale, and J. Zendri, "3-mode detection for widening the bandwidth of resonant gravitational wave detectors," Physical Review Letters, vol. 94, no. 24, p. 241101, Jun 2005.

[125] I. G. E. Collaboration), Z. Allen, P. Astone, L. Baggio, D. Busby, M. Bassan, D. Blair, M. Bonaldi, P. Bonifazi, P. Carelli, M. Cerdonio, E. Coccia, L. Conti, C. Cosmelli, V. C. Visconti, S. D'Antonio, V. Fafone, P. Falferi, P. Fortini, S. Frasca, W. Hamilton, I. Heng, E. Ivanov, W. Johnson, M. Kingham, C. Locke, A. Marini, and V. Martinucci, "First search for gravitational wave bursts with a network of detectors," Physical Review Letters, vol. 85, no. 24, p. 5046, Dec 2000.

[126] G. Harry, I. Jin, H. Paik, T. Stevenson, and F. Wellstood, "Two-stage superconducting-quantum-interference-device amplifier in a high-q gravitational wave transducer," Applied Physics Letters, vol. 76, no. 11, pp. 1446–1448, Mar 2000.

[127] P. Falferi, M. Bonaldi, M. Cerdonio, R. Mezzena, G. Prodi, A. Vinante, and S. Vitale, "10 [h-bar] superconducting quantum interference device amplifier for acoustic gravitational wave detectors," Applied Physics Letters, vol. 93, no. 17, pp. 172 506–3, Oct 2008.

[128] R. Schoelkopf, P. Wahlgren, A. Kozhevnikov, P. Delsing, and D. Prober, "The radio-frequency single-electron transistor (rf-set): A fast and ultrasensitive electrometer," Science, vol. 280, no. 5367, pp. 1238–1242, May 1998.

[129] T. Fulton and G. Dolan, "Observation of single-electron charging effects in small tunnel junctions," Physical Review Letters, vol. 59, no. 1, p. 109, Jul 1987.

[130] M. Devoret and R. Schoelkopf, "Amplifying quantum signals with the single-electron transistor," Nature, vol. 406, no. 6799, pp. 1039–1046, Aug 2000.

[131] J. Clarke and A. I. Braginsky, The SQUID Handbook: Volume 1, Fundamentals and Technology of SQUIDs and SQUID Systems. Wiley-VCH, 2004.

[132] A. Vinante, M. Bignotto, M. Bonaldi, M. Cerdonio, L. Conti, P. Falferi, N. Liguori, S. Longo, R. Mezzena, A. Ortolan, G. Prodi, F. Salemi, L. Taffarello, G. Vedovato, S. Vitale, and J.-P. Zendri, "Feedback cooling of the normal modes of a massive electromechanical system to submillikelvin temperature," Physical Review Letters, vol. 101, no. 3, pp. 033 601–4, Jul 2008.

[133] A. Clerk, "Backaction noise in strongly interacting systems: The dc squid and the interacting quantum point contact," Physical Review Letters, vol. 96, no. 5, p. 056801, Feb 2006.

[134] R. Koch, D. V. Harlingen, and J. Clarke, "Quantum noise theory for the dc squid," Applied Physics Letters, vol. 38, no. 5, pp. 380–382, Mar 1981.

[135] H. van Houten and C. Beenakker, "Quantum point contacts," Phys. Today, vol. 49, no. 7, pp. 22–27, Jul 1996.

[136] E. Buks, R. Schuster, M. Heiblum, D. Mahalu, and V. Umansky, "Dephasing in electron interference by a /'which-path/' detector," Nature, vol. 391, no. 6670, pp. 871–874, Feb 1998.

[137] K. Jensen, J. Weldon, H. Garcia, and A. Zettl, "Nanotube radio," Nano Letters, vol. 7, no. 11, pp. 3508–3511, Oct 2007.

[138] S. Perisanu, P. Vincent, A. Ayari, M. Choueib, D. Guillot, M. Bechelany, D. Cornu, P. Miele, and S. T. Purcell, "Ultra high sensitive detection of mechanical resonances of nanowires by field emission microscopy," physica status solidi (a), vol. 204, no. 6, pp. 1645–1652, May 2007.

[139] H. S. K. et al, "Field emission from a single nanomechanical pillar," Nanotechnology, vol. 18, no. 6, p. 065201, Jan 2007.

[140] U. Kemiktarak, T. Ndukum, K. Schwab, and K. Ekinci, "Radio-frequency scanning tunnelling microscopy," Nature, vol. 450, no. 7166, pp. 85–88, Nov 2007.

[141] M. Rost, L. Crama, P. Schakel, E. van Tol, G. van Velzen-Williams, C. Overgauw, H. ter Horst, H. Dekker, B. Okhuijsen, M. Seynen, A. Vijftigschild, P. Han, A. Katan, K. Schoots, R. Schumm, W. van Loo, T. Oosterkamp, and J. Frenken, "Scanning probe microscopes go video rate and beyond," Review of Scientific Instruments, vol. 76, no. 5, pp. 053 710–9, May 2005.

[142] H. Mamin, H. Birk, P. Wimmer, and D. Rugar, "High-speed scanning tunneling microscopy: Principles and applications," Journal of Applied Physics, vol. 75, no. 1, pp. 161–168, Jan 1994.

[143] Y. Manassen, R. Hamers, J. Demuth, and A. C. Jr, "Direct observation of the precession of individual paramagnetic spins on oxidized silicon surfaces," Phys. Rev. Lett., vol. 62, no. 21, pp. 2531–2534, May 1989.

[144] C. Durkan and M. Welland, "Electronic spin detection in molecules using scanning-tunneling- microscopy-assisted electron-spin resonance," Applied Physics Letters, vol. 80, no. 3, pp. 458–460, Jan 2002.

[145] K. W. Hipps, Handbook of Applied Solid State Spectroscopy. Springer, 2006, ch. 7, pp. 305–350.

[146] Y. Zhang, V. Brar, C. Girit, A. Zettl, and M. Crommie, "Origin of spatial charge inhomogeneity in graphene," Nat Phys, vol. 5, no. 10, pp. 722–726, Aug 2009.

[147] R. H. M. Smit, R. Grande, B. Lasanta, J. J. Riquelme, G. Rubio-Bollinger, and N. Agrait, "A low temperature scanning tunneling microscope for electronic and force spectroscopy," Review of Scientific Instruments, vol. 78, no. 11, p. 113705, Nov 2007.

[148] Y. Sun, H. Mortensen, S. Schar, A.-S. Lucier, Y. Miyahara, P. Grutter, and W. Hofer, "From tunneling to point contact: Correlation between forces and current," Physical Review B (Condensed Matter and Materials Physics), vol. 71, no. 19, p. 193407, May 2005.

[149] J. Stroscio and D. Eigler, "Atomic and molecular manipulation with the scanning tunneling microscope," Science, vol. 254, no. 5036, pp. 1319–1326, Nov 1991.

[150] D. Eigler and E. Schweizer, "Positioning single atoms with a scanning tunnelling microscope," Nature, vol. 344, no. 6266, pp. 524–526, Apr 1990.

[151] A. Yanson, G. Bollinger, H. van den Brom, N. Agrait, and J. van Ruitenbeek, "Formation and manipulation of a metallic wire of single gold atoms," Nature, vol. 395, no. 6704, pp. 783–785, Oct 1998.

[152] N. Agraït, C. Untiedt, G. Rubio-Bollinger, and S. Vieira, "Onset of energy dissipation in ballistic atomic wires," Physical Review Letters, vol. 88, no. 21, p. 216803, May 2002.

[153] M. P. Marder, Condensed Matter Physics. John Wiley and Sons, Inc, 2000.

[154] Y. Blanter and M. Buttiker, "Shot noise in mesoscopic conductors," Phys. Rep. (Netherlands), vol. 336, no. 1-2, pp. 1 – 166, Aug 2000.

[155] M. de Jong and C. Beenakker, "Semiclassical theory of shot noise in mesoscopic conductors," Physica A: Statistical and Theoretical Physics, vol. 230, no. 1-2, pp. 219–248, Aug 1996.

[156] E. Merzbacher, Quantum Mechanics. John Wiley and Sons, Inc, 1998.

[157] R. L. Liboff, Introductory Quantum Mechanics. Addison-Wesley, 1998.

[158] J. J. Sakurai, Modern Quantum Mechanics Revised Edition, S. F. Tuan, Ed. Addison-Wesley Publishing Company, 1994.

[159] S. Timoshenko, D. H. Young, and W. Weaver, Vibration Problems in Engineering, 4th ed. John Wiley and Sons, Inc, 1974.

[160] S. G. Kelly, Fundamentals of Mechanical Vibration. McGraw-Hill, 2000.

[161] G. Rubio, N. Agrait, and S. Vieira, "Atomic-sized metallic contacts: Mechanical properties and electronic transport," Phys. Rev. Lett., vol. 76, no. 13, pp. 2302–2305, Mar 1996.

[162] P. S. Ho and T. Kwok, "Electromigration in metals," Reports on Progress in Physics, vol. 52, no. 3, p. 301, Mar 1989.

[163] R. Hesketh, "Electromigration: The electron wind," Phys. Rev. B, vol. 19, no. 4, pp. 1727–1733, Feb 1979.

[164] A. Verbruggen, "Fundamental questions in the theory of electromigration," IBM Journal of Research and Development, vol. 32, no. 1, pp. 93–8, Jan 1988.

[165] D. Malone and R. Hummel, "Electromigration in integrated circuits," Critical Reviews in Solid State and Materials Sciences, vol. 22, no. 3, pp. 199–238, Sep 1997.

[166] H. Yasuda and A. Sakai, "Conductance of atomic-scale gold contacts under high-bias voltages," Phys. Rev. B, vol. 56, no. 3, pp. 1069–1072, Jul 1997.

[167] R. Sorbello, "Electromigration and the local transport field in mesoscopic systems," Phys. Rev. B, vol. 39, no. 8, pp. 4984–4996, Mar 1989.

[168] R. S. Sorbello, "Theory of electromigration," Solid State Physics, vol. 51, pp. 159 – 231, Jan 1997.

[169] M. Trouwborst, S. Molen, and B. Wees, "The role of joule heating in the formation of nanogaps by electromigration," Journal of Applied Physics, vol. 99, no. 11, p. 114316, Jun 2006.

[170] S. van der Molen, M. Welling, and R. Griessen, "Correlated electromigration of h in the switchable mirror yh3- delta," Physical Review Letters, vol. 85, no. 18, p. 3882, Oct 2000.

[171] D. Strachan, D. Smith, D. Johnston, T.-H. Park, M. Therien, D. Bonnell, and A. Johnson, "Controlled fabrication of nanogaps in ambient environment for molecular electronics," Applied Physics Letters, vol. 86, no. 4, p. 043109, Jan 2005.

[172] R. Hoffmann, D. Weissenberger, J. Hawecker, and D. Stoffler, "Conductance of gold nanojunctions thinned by electromigration," Applied Physics Letters, vol. 93, no. 4, p. 043118, Jul 2008.

[173] P. Horowitz and W. Hill, The Art of Electronics. Cambridge University Press, 1989.

[174] F. Hadeed and C. Durkan, "Controlled fabrication of 1–2 nm nanogaps by electromigration in gold and gold-palladium nanowires," Applied Physics Letters, vol. 91, no. 12, p. 123120, Sep 2007.

[175] K. Bolotin, F. Kuemmeth, A. Pasupathy, and D. Ralph, "From ballistic transport to tunneling in electromigrated ferromagnetic breakjunctions," Nano Letters, vol. 6, no. 1, pp. 123–127, Jan 2006.

[176] G. Esen and M. Fuhrer, "Temperature control of electromigration to form gold nanogap junctions," Applied Physics Letters, vol. 87, no. 26, p. 263101, Dec 2005.

[177] A. Houck, J. Labaziewicz, E. Chan, J. Folk, and I. Chuang, "Kondo effect in electromigrated gold break junctions," Nano Letters, vol. 5, no. 9, pp. 1685–1688, Jul 2005.

[178] O. Kolesnychenko, O. Shklyarevskii, and H. van Kempen, "Giant influence of adsorbed helium on field emission resonance measurements," Phys. Rev. Lett., vol. 83, no. 11, pp. 2242–2245, Sep 1999.

[179] O. Y. Kolesnychenko, O. I. Shklyarevskii, and H. van Kempen, "Anomalous increase of the work function in metals due to adsorbed helium," Physica B (Netherlands), vol. 284 (III), pp. 1257 – 1258, Oct 2000.

[180] K. Hansen, S. Nielsen, M. Brandbyge, E. Laegsgaard, I. Stensgaard, and F. Besenbacher, "Current-voltage curves of gold quantum point contacts revisited," Applied Physics Letters, vol. 77, no. 5, pp. 708–710, Jul 2000.

[181] J. Gimzewski and R. Möller, "Transition from the tunneling regime to point contact studied using scanning tunneling microscopy," Phys. Rev. B, vol. 36, no. 2, p. 1284, Jul 1987.

[182] R. J. P. Keijsers, O. I. Shklyarevskii, and H. van Kempen, "Spectroscopic study of the tunnel-current reduction due to adsorbed helium," Phys. Rev. B, vol. 61, no. 11, pp. 7328–7331, Mar 2000.

[183] C. Muller, J. van Ruitenbeek, and L. de Jongh, "Experimental observation of the transition from weak link to tunnel junction," Physica C: Superconductivity, vol. 191, no. 3-4, pp. 485–504, Feb 1992.

[184] R. Keijsers, O. Shklyarevskii, J. Hermsen, and H. Kempen, "Thin film mechanically controllable break junctions," Review of Scientific Instruments, vol. 67, no. 8, pp. 2863–2866, Aug 1996.

[185] F. Tavazza, L. Levine, and A. Chaka, "Elongation and breaking mechanisms of gold nanowires under a wide range of tensile conditions," Journal of Applied Physics, vol. 106, no. 4, pp. 043 522–10, Aug 2009.

[186] E. da Silva, A. da Silva, and A. Fazzio, "How do gold nanowires break?" Physical Review Letters, vol. 87, no. 25, p. 256102, Nov 2001.

[187] G. Rubio-Bollinger, S. R. Bahn, N. Agraït, K. W. Jacobsen, and S. Vieira, "Mechanical properties and formation mechanisms of a wire of single gold atoms," Phys. Rev. Lett., vol. 87, no. 2, p. 026101, Jun 2001.

[188] R. D. Blandford and K. S. Thorne, "Applications of classical physics," unpublished textbook, Caltech Ph136.

[189] D. M. Pozar, Microwave engineering, 2nd ed. Wiley, 1997.

[190] A. Cleland and M. Roukes, "External control of dissipation in a nanometer-scale radiofrequency mechanical resonator," Sensors and Actuators A: Physical, vol. 72, no. 3, pp. 256–261, Feb 1999.

[191] A. Halbritter, P. Makk, S. Csonka, and G. Mihály, "Huge negative differential conductance in au- h2 molecular nanojunctions," Physical Review B, vol. 77, no. 7, p. 075402, Feb 2008.

[192] W. Thijssen, D. Djukic, A. Otte, R. Bremmer, and J. van Ruitenbeek, "Vibrationally induced two-level systems in single-molecule junctions," Physical Review Letters, vol. 97, no. 22, p. 226806, Dec 2006.

[193] J. Gupta, C. Lutz, A. Heinrich, and D. Eigler, "Strongly coverage-dependent excitations of adsorbed molecular hydrogen," Physical Review B, vol. 71, no. 11, p. 115416, Mar 2005.

[194] J. Gaudioso, L. Lauhon, and W. Ho, "Vibrationally mediated negative differential resistance in a single molecule," Physical Review Letters, vol. 85, no. 9, p. 1918, Aug 2000.

[195] M. Galperin, M. A. Ratner, and A. Nitzan, "Molecular transport junctions: vibrational effects," Journal of Physics: Condensed Matter, vol. 19, no. 10, p. 103201, Feb 2007.

[196] G. Schulze, K. Franke, A. Gagliardi, G. Romano, C. Lin, A. Rosa, T. Niehaus, T. Frauenheim, A. D. Carlo, A. Pecchia, and J. Pascual, "Resonant electron heating and molecular phonon cooling in single c60 junctions," Physical Review Letters, vol. 100, no. 13, p. 136801, Apr 2008.

Appendix A

Fabrication of Nanostructures on Gallium Arsenide Substrates

• cleave gallium arsenide wafer into approximately 5 mm by 5 mm squares

• Clean by rinsing with acetone, then isopropanol (IPA), then blow dry with dry nitrogen

Fabricate Bondpads

• spin a layer of resist on top of the chip: 950K PMMA A7 (7% anisole) at 4 krpm for 30 sec

• bake on a hot plate at 180° C for 5 minutes

• Expose resist using NPGS on a JOEL6400 SEM with beam set to 35 kV (figure A.1a); small orange alignment marks at a magnification of ×1000, beam current of 10 pA, and exposure of 450 μC/cm^2; yellow bond pads at a magnification of ×100, beam current of 1600 pA, and exposure of 375 μC/cm^2; large orange alignment marks at a magnification of ×100, beam current of 1600 pA, and exposure of 350 μC/cm^2.

• develop by shaking chip using tweezers in developer (1 part MIBK to 3 parts IPA) for 60 seconds then rinsing with IPA and blow dry with dry nitrogen

• evaporate 10 nm of titanium then 95 nm of gold at 0° (that is, vertically)

• liftoff by letting the chip sit in acetone for between 1 and 12 hours; at the end of the 12 hours and while chip is submerged in acetone, use a syringe to spray chip with acetone. In some cases, it is necessary to gently use the ultrasonic bath to remove all of

the material that was not deposited on GaAs. Then rinse with acetone, IPA, blow dry with dry nitrogen

Fabricate Devices

• spin a layer of resist on top of the chip: 950K PMMA A7 (7% anisole) at 4 krpm for 30 sec

• bake on a hot plate at 180° C for 5 minutes

• Expose resist using NPGS on a JOEL6400 SEM with beam set to 35 kV at a magnification of ×1000 and beam current of 10 pA (figure A.1b); beam (red) at exposure of 300 μC/cm^2; point (pink) at exposure of 260 μC/cm^2; electrostatic gate (green) at exposure of 350 μC/cm^2; support structure (cyan) at exposure of 400 μC/cm^2;

• develop by shaking chip using tweezers in developer (1 part MIBK to 3 parts IPA) for 60 seconds then rinsing with IPA and blow dry with dry nitrogen

• using an electron gun evaporator at a pressure of about 6×10^{-6} Torr, evaporate 40 nm of gold at 0° (that is, vertically), 180 nm of gold at −27° from vertical, and 180 nm of gold at 27° from vertical.

• liftoff by letting the chip sit in acetone for between 1 and 12 hours; at the end of the 12 hours and while chip is submerged in acetone, use a syringe to spray chip with acetone. In some cases, it is necessary to gently use the ultrasonic bath to remove all of the material that was not deposited on GaAs. Then rinse with acetone, IPA, blow dry with dry nitrogen

• etch in a solution composed of 5 parts 1 M citric acid to 1 part 70% H_20_2 for 150 seconds. In order to properly etch the GaAs that was exposed to the electron beam, I need to use a magnetic stir bar to stir the etch solution and hold the GaAs chip in the moving etch solution. Then rinse with acetone, IPA, blow dry with dry nitrogen. These nanostructures are stiff enough that critical point drying is unnecessary.

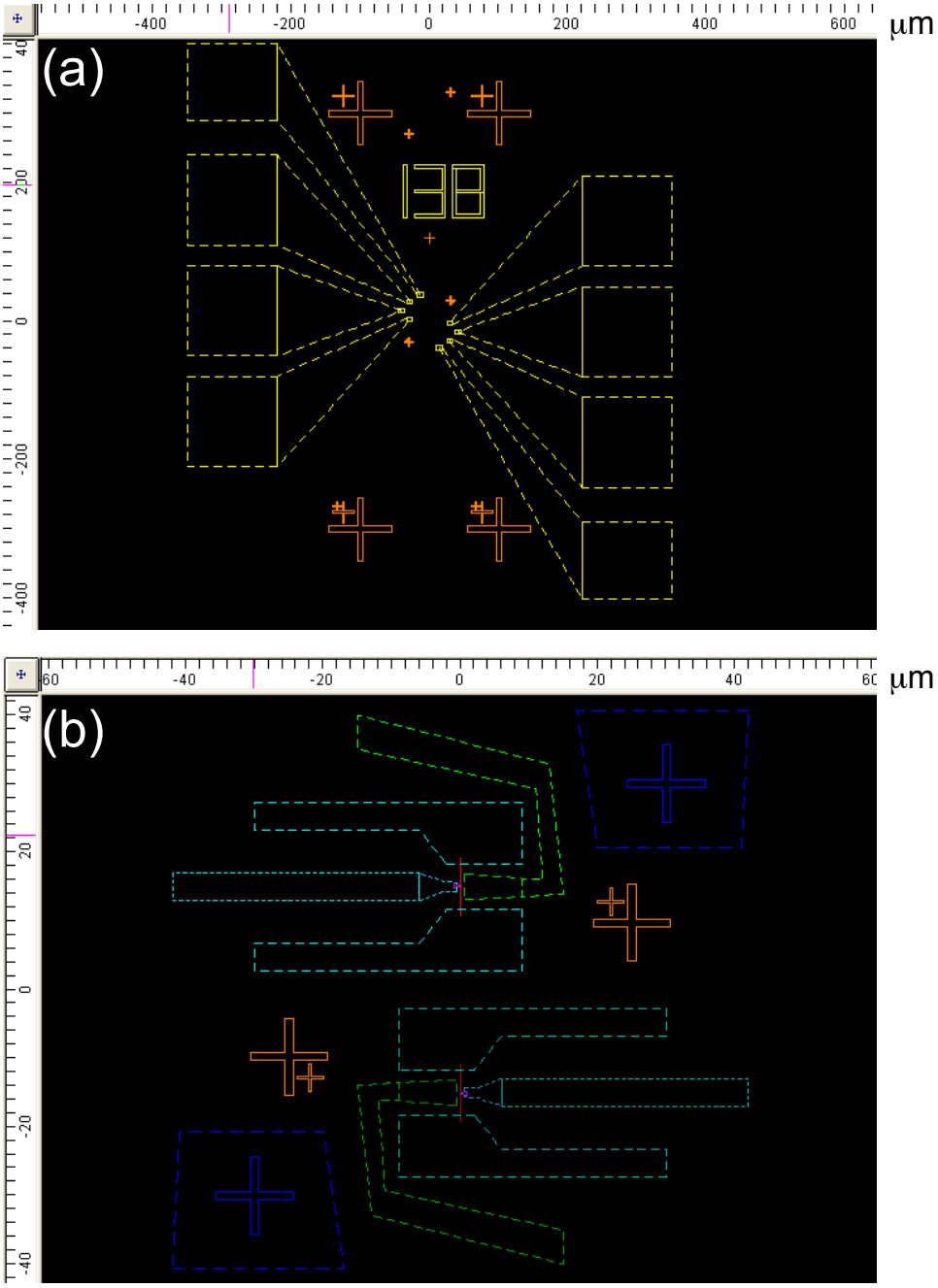

Figure A.1: (a) NPGS pattern used to create bond pads (yellow) and alignment marks (orange). (b) NPGS pattern used to create a device with a nanomechanical beam (red) and constriction (between pink and red).

Appendix B

Fabrication of Nanostructures on Silicon Substrates

• at NIST-Boulder: an approximately 100 nm thick layer of silicon oxide is thermally grown on a high-resistivity silicon wafer. Alignment marks (and large bond pads which are not used with these devices) are created using the standard tools of optical lithography and the silicon wafer is cut into 5 mm by 5 mm squares using a dicing saw.

Fabricate Holes in Silicon Oxide

• spin a layer of resist on top of the chip: 950K PMMA A7 (7% anisole) at 4 krpm for 30 sec

• bake on a hot plate at 180° C for 5 minutes

• Expose resist using NPGS on a JOEL6400 SEM with beam set to 35 kV; expose holes in silicon oxide at a magnification of ×1000, beam current of 10 pA, and exposure of 500 μC/cm^2 (figure B.1a).

• develop by shaking chip using tweezers in developer (1 part MIBK to 3 parts IPA) for 60 seconds then rinsing with IPA and blow dry with dry nitrogen

• etch the exposed silicon oxide using a buffered oxide etch (BOE). The chip is held using plastic tongs and is shook in the BOE for 2 minutes. Then dipped in one beaker of de-ionized (DI) water, dipped in another beaker of DI water, rinsed in ISO, and blown dry with dry nitrogen.

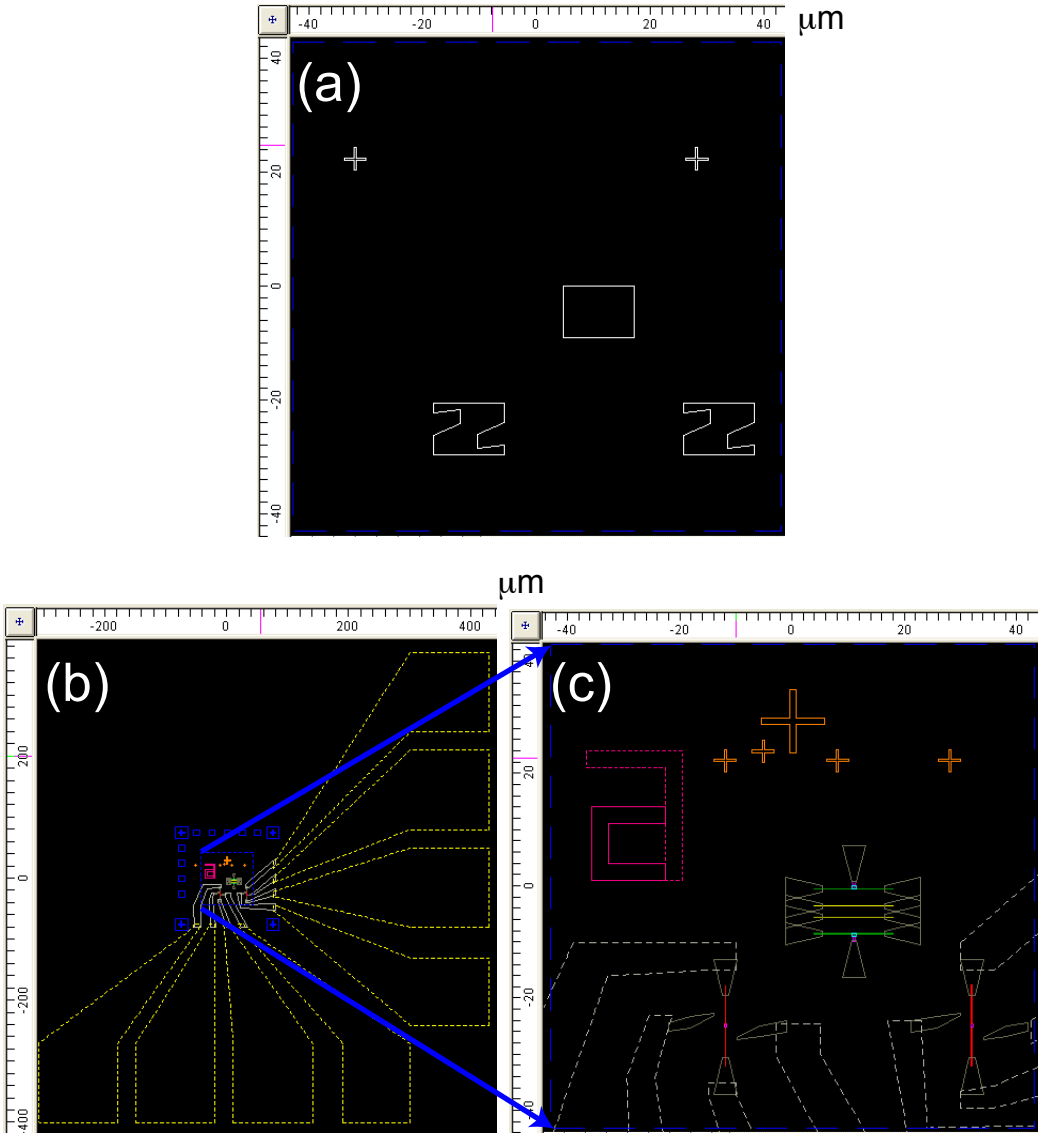

Figure B.1: (a) NPGS pattern used to create a mask to etch the silicon oxide; the area inside the white lines will be exposed and etched. (b & c) NPGS pattern used to bond pads (b, entire writing field) and device with a nanomechanical beam (c, close up). This structure is a nanomechanical beam (red) interrupted by a constriction (pink); the yellow and green beams/devices are used to test exposures.

Fabricate Devices

• spin layer of resist on top of the chip: PMGI SF9 at 3 krpm for 40 sec

• bake on a hot plate at 180° C for 10 minutes; let cool for 5 min

• spin another layer of resist on top of the chip: 950K PMMA A7 (7% anisole) at 4 krpm for 30 sec

• bake on a hot plate at 180° C for 10 minutes

• Expose resist using NPGS on a JOEL6400 SEM with beam set to 35 kV (figure B.1b,c); nanomechanical beam (red) at a magnification of ×1000, beam current of 10 pA, and exposure of 250 μC/cm^2; location of constriction in beam (pink) at a magnification of ×1000, beam current of 10 pA, and exposure of 50 μC/cm^2; beam supports (white) at a magnification of ×1000, beam current of 10 pA, and exposure of 450 μC/cm^2; larger electrodes (white) at a magnification of ×500, beam current of 135 pA, and exposure of 425 μC/cm^2; large bond pads (yellow) at a magnification of ×100, beam current of 1320 pA, and exposure of 400 μC/cm^2.

• develop PMMA by shaking chip using tweezers in developer (1 part MIBK to 3 parts IPA) for 60 seconds then rinsing with IPA and blow dry with dry nitrogen

• develop PMGI by shaking chip using tweezers in PMGI101 developer for 3 minutes, shake in beaker of DI water, then rinse with IPA and blow dry with dry nitrogen

• briefly clean exposed surface of chip using oxygen plasma in the reactive ion etcher (RIE): 20 seconds with 50 sccm 0_2 and 300 W of power; these setting result in a chamber at about 105 mT and a potential of 150 V.

• using an electron gun evaporator at a pressure of about 1×10^{-6} Torr, evaporate 400 nm of gold at 0° (that is, vertically), 30 nm of gold at −30° from vertical, and 30 nm of gold at −30° from vertical.

• liftoff by letting the chip sit in PG Remover at 70° C for 20 minutes. While the chip is submerged in acetone, use a syringe to spray chip with PG Remover. In some

cases, it is necessary to repeat these steps to remove all of the material that was not deposited on silicon or silicon oxide. Then rinse with acetone, IPA, blow dry with dry nitrogen

- etch using SF_6 gas in the RIE: 90 seconds with 20 sccm SF_6 and 500 W of power; these setting result in a chamber at about 50 mT and a potential of 40 V.
- clean surface of chip using oxygen plasma in the RIE: 60 seconds with 50 sccm 0_2 and 500 W of power; these setting result in a chamber at about 105 mT and a potential of 200 V.

Appendix C

Fabrication of Nanostructures on Phosphor Bronze/Polyimide Substrates

Prepare Phosphor Bronze/Polyimide substrate

• JILA machine shop: NIST-Boulder: an approximately 5 cm diameter circular piece (wafer) of phosphor bronze 0.016" thick shim stock was polished for about 24 hours using a solution of colloidal silicon that are about 50-70 nm in size.

• clean wafer by rinsing with acetone, IPA, the blow dry with dry nitrogen

• clean wafer by rinsing with acetone, IPA, the blow dry with dry nitrogen

• spin a layer of adhesion promoter on wafer: place wafer on spinner, relatively quickly drip about 3 mL of adhesion promoter VM-652 onto wafer, wait 20 seconds, take about 2 seconds to turn up speed of spinner to 2 krpm, spin for 30 seconds

• bake on a hot plate at 100° C for 1 minutes; wait for wafer to cool (about 2 minutes)

• spin a layer of polyimide on wafer: place wafer on spinner, cover wafer with polyimide PI-2611, make sure to remove any bubbles, slowly (taking about 90sec) turn up speed of spinner to 2 krpm, spin for 30 seconds, turn down speed of spinner over about 2 seconds

• pre-bake on a hot plate at 100° C for 1 minutes then on a hot plate at 180° C for 1 minutes; wait for wafer to cool (about 2 minutes)

• spin a layer of polyimide on wafer: place wafer on spinner, cover wafer with

polyimide PI-2611, make sure to remove any bubbles, slowly (taking about 90sec) turn up speed of spinner to 2 krpm, spin for 30 seconds, turn down speed of spinner over about 2 seconds

• pre-bake on a hot plate at 100° C for 1 minutes then on a hot plate at 180° C for 1 minutes;

• bake in a tube furnace: ramp up to 200° C, bake for 20 minutes, ramp down to room temperature (total process takes 2.25 hours, though the furnace was still at 84° C when the wafer was removed).

• bake/cure in a vacuum furnace (at less than 5×10^{-5} torr): ramp up to 350° C over 85 minutes, cure at 350° C for 30 minutes, ramp down over 3 hours

• spin a protective (not used for patterning chip) layer of resist on top of the chip: PMGI SF9 at 2.5 krpm for 40 sec

• bake on a hot plate at 180° C for 10 minutes; let cool for 5 min

Fabricate bond pads using optical lithography

• cut an approximately 5 mm by 5 mm square from the phosphor bronze/polyimide wafer using bench shears in the machine shop (carefully to avoid bending, rather than cutting, the phosphor bronze).

• remove protective layer of PMGI by placing chip in PG remover at 70° C for 10 minutes; rinse with acetone, IPA, blow dry with dry nitrogen

• spin layer of resist on top of the chip: PMGI SF9 at 3 krpm for 45 seconds

• bake on a hot plate at 180° C for 10 minutes.

• PMGI layer sometimes has large bubbles at the corner of the chips; if so, cut/scrape off bubbles with a razor blade

• dehydration bake on a hot plate at 115° C for 1 minutes; let cool for 1 min

• spin another layer of resist on top of the chip: S1813 at 4 krpm for 45 seconds

• bake on a hot plate at 115° C for 2 minutes.

• Expose in mask aligner for 8 seconds

• develop by shaking chip using tweezers in RD6 developer for 45 seconds, shake in beaker of DI water for 20 seconds, blow dry with dry nitrogen

• bake on a hot plate at 130° C for 5 minutes; let cool for 1 minute

• develop placing chip in RD6 developer for 2.5 minutes, shake in beaker of DI water for 20 seconds, blow dry with dry nitrogen

• briefly clean and rough (supposed to make evaporated metal stick to polyimide) exposed surface of chip using oxygen plasma in the reactive ion etcher (RIE): 90 seconds with 50 sccm 0_2 and 300 W of power; these setting result in a chamber at about 115 mT and a potential of 180 V.

• using an electron gun evaporator at a pressure of about $< 3 \times 10^{-6}$ Torr, evaporate 750 nm of titanium at 0° (that is, vertically), rotating wafer about the vertical axis by 90° every 50 nm. Evaporate 750 nm of gold at 0° (that is, vertically), rotating wafer about the vertical axis by 90° every 50 nm.

• liftoff by letting the chip sit in PG Remover at 70° C for 35 minutes. While the chip is submerged in acetone, use a syringe to spray chip with PG Remover. In some cases, it is necessary to use the ultrasonic bath to remove additional material that was not deposited on polyimide. Then rinse with acetone, IPA, blow dry with dry nitrogen

Fabricate Devices

• spin layer of resist on top of the chip: PMGI SF9 at 3 krpm for 40 sec

• bake on a hot plate at 180° C for 10 minutes; let cool for 10 min

• spin another layer of resist on top of the chip: 950K PMMA A7 (7% anisole) at 4 krpm for 30 sec

• bake on a hot plate at 180° C for 10 minutes

• Expose resist using NPGS on a JOEL6400 SEM with beam set to 35 kV (figure C.1); nanomechanical beam (red) at a magnification of ×1000, beam current of 10 pA,

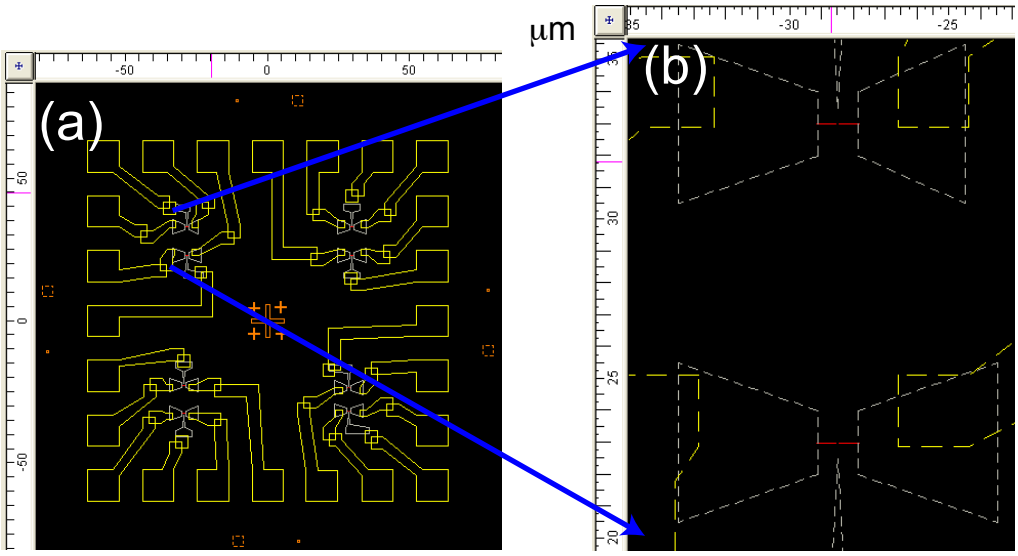

Figure C.1: (a & b) NPGS pattern used to connect to bond pads (a, entire writing field) and create device with a nanomechanical beam (b, close up). This structure is a nanomechanical beam (red) interrupted by a constriction with supports (white) and connections to bond pads (yellow).

and exposure of 1.5 nC/cm; beam supports (white) at a magnification of $\times$1000, beam current of 10 pA, and exposure of 500 μC/cm^2; connection to bond pads (yellow) at a magnification of $\times$500, beam current of 130 pA, and exposure of 550 μC/cm^2.

• develop PMMA by shaking chip using tweezers in developer (1 part MIBK to 3 parts IPA) for 50 seconds then rinsing with IPA and blow dry with dry nitrogen

• develop PMGI by shaking chip using tweezers in XP101A developer for 2 minutes, shake in beaker of DI water, then rinse with IPA and blow dry with dry nitrogen

• briefly clean and rough (supposed to make evaporated metal stick to polyimide) exposed surface of chip using oxygen plasma in the reactive ion etcher (RIE): 40 seconds with 50 sccm 0_2 and 400 W of power; these setting result in a chamber at about 110 mT and a potential of 180 V.

• using an electron gun evaporator at a pressure of about 2×10^{-6} Torr, evaporate 80 nm of gold at $+5^\circ$ from vertical, 80 nm of gold at -5° from vertical, and 2400 nm of

gold at 0° (that is, vertically).

• liftoff by letting the chip sit in PG Remover at 70° C for 65 minutes. While the chip is submerged in acetone, use a syringe to spray chip with PG Remover. In some cases, it is necessary to repeat these steps to remove all of the material that was not deposited on polyimide. Then rinse with acetone, IPA, blow dry with dry nitrogen

• etch using SF_6 and O_2 gas in the RIE: 11 minutes with 10 sccm SF_6 , 90 sccm O_2, and 200 W of power; these setting result in a chamber at about 200 mT and a potential of 28 V.

Appendix D

Algebra Related to Unintentional Feedback

I am going to try and find an approximate solution for a parametric oscillator

$$\ddot{x} + \gamma\dot{x} + \omega_0^2\left(1 + h_1 e^{i2\omega_1 t} + h_2 e^{-i2\omega_1 t}\right) = a_1 e^{i\omega_2 t} + a_2 e^{-i\omega_2 t} \tag{D.1}$$

and assume experimentally relevant conditions $\omega_0 \approx \omega_1 \approx \omega_2$. That is, I have a formula for a parametric oscillator where the parameter is oscillating at about twice the mechanical resonance frequency and there is a drive force at about the mechanical resonance frequency. I am now going to make the simplifying assumption that the mechanical oscillator is high Q (that is, $\omega_0/\gamma \gg 1$) which implies that the response to the force is going to be small at frequencies away from ω_0. Therefore I am going to try a solution

$$x = A_1 e^{i\omega_2 t} + A_2 e^{-i\omega_2 t} + B_1 e^{-i(2\omega_1 - \omega_2)t} + B_2 e^{i(2\omega_1 - \omega_2)t} \tag{D.2}$$

and solve for A_1, A_2, B_1, and B_2 while ignoring any term which is oscillating at a frequency far from ω_0. In this case, that means dropping terms at frequencies $(4\omega_1 - \omega_2)$ and $(2\omega_1 + \omega_2)$. So plugging the trial solution into the differential equation and dropping

frequency terms as described results in:

$$\begin{aligned}
&-\omega_2^2 A_1 e^{i\omega_2 t} - \omega_2^2 A_2 e^{-i\omega_2 t} \qquad \text{(D.3)}\\
&-(2\omega_1-\omega_2)^2 B_1 e^{-i(2\omega_1-\omega_2)t} - (2\omega_1-\omega_2)^2 B_2 e^{i(2\omega_1-\omega_2)t}\\
&+i\omega_2\gamma A_1 e^{i\omega_2 t} - i\omega_2\gamma A_2 e^{-i\omega_2 t}\\
&-i(2\omega_1-\omega_2)\gamma B_1 e^{-i(2\omega_1-\omega_2)t} + i(2\omega_1-\omega_2)\gamma B_2 e^{i(2\omega_1-\omega_2)t}\\
&+\omega_0^2 A_1 e^{i\omega_2 t} + \omega_0^2 A_2 e^{-i\omega_2 t} + \omega_0^2 B_1 e^{-i(2\omega_1-\omega_2)t} + \omega_2^2 B_2 e^{i(2\omega_1-\omega_2)t}\\
&+\omega_0^2 h_2 A_1 e^{-i(2\omega_1-\omega_2)t} + \omega_0^2 h_1 A_2 e^{i(2\omega_1-\omega_2)t} + \omega_0^2 h_1 B_1 e^{i\omega_2 t} + \omega_2^2 h_2 B_2 e^{-i\omega_2 t}\\
&= a_1 e^{i\omega_2 t} + a_2 e^{-i\omega_2 t}
\end{aligned}$$

collecting terms at the same frequency results in four coupled equations

$$\left(\omega_0^2 - \omega_2^2 + i\omega_2\gamma\right) A_1 + \omega_0^2 h_1 B_1 = a_1 \qquad \text{(D.4)}$$

$$\left(\omega_0^2 - \omega_2^2 - i\omega_2\gamma\right) A_2 + \omega_0^2 h_2 B_2 = a_2 \qquad \text{(D.5)}$$

$$\left(\omega_0^2 - (2\omega_1-\omega_2)^2 - i(2\omega_1-\omega_2)\gamma\right) B_1 + \omega_0^2 h_2 A_1 = 0 \qquad \text{(D.6)}$$

$$\left(\omega_0^2 - (2\omega_1-\omega_2)^2 + i(2\omega_1-\omega_2)\gamma\right) B_2 + \omega_0^2 h_1 A_2 = 0 \qquad \text{(D.7)}$$

now define

$$a_\pm = \omega_0^2 - \omega_2^2 \pm i\omega_2\gamma \qquad \text{(D.8)}$$

$$b_\pm = \omega_0^2 - (2\omega_1-\omega_2)^2 \pm i(2\omega_1-\omega_2)\gamma \qquad \text{(D.9)}$$

$$h_+ = \omega_0^2 h_1 \qquad \text{(D.10)}$$

$$h_- = \omega_0^2 h_2 \qquad \text{(D.11)}$$

resulting in the solutions

$$A_1 = \frac{a_1}{a_+ - \frac{h_+ h_-}{b_-}} \tag{D.12}$$

$$B_1 = \frac{-a_1 h_-}{a_+ b_- - h_+ h_-} \tag{D.13}$$

$$A_2 = \frac{a_2}{a_- - \frac{h_+ h_-}{b_+}} \tag{D.14}$$

$$B_2 = \frac{-a_2 h_+}{a_- b_+ - h_+ h_-} \tag{D.15}$$

I am now going to decide that the parametric oscillation is going to take the form of $h_0 \sin(2\omega_1 t) = h_1 e^{i2\omega_1 t} + h_2 e^{-i2\omega_1 t}$ and therefore $h_1 = h_0/2i$ and $h_2 = -h_0/2i$ and if I define $h = h_0\omega_0^2$ then I can rewrite my solutions as

$$A_1 = \frac{a_1}{a_+ - (h^2/4b_-)} \tag{D.16}$$

$$B_1 = \left(\frac{-ih}{2b_-}\right) \frac{a_1}{a_+ - (h^2/4b_-)} \tag{D.17}$$

$$A_2 = \frac{a_2}{a_- - (h^2/4b_+)} \tag{D.18}$$

$$B_2 = \left(\frac{ih}{2b_+}\right) \frac{a_2}{a_- - (h^2/4b_+)} \tag{D.19}$$

Now to check this with the results of other people's calculations, let's assume a drive $a \sin(\omega_2 t) = a_1 e^{i\omega_2 t} + a_2 e^{-i\omega_2 t}$ and therefore $a_1 = a/2i$ and $a_2 = -a/2i$ and equations

$$A_1 = \frac{-ia/2}{a_+ - (h^2/4b_-)} \tag{D.20}$$

$$B_1 = \left(\frac{-ih}{2b_-}\right) \frac{-ia/2}{a_+ - (h^2/4b_-)} \tag{D.21}$$

$$A_2 = \frac{ia/2}{a_- - (h^2/4b_+)} \tag{D.22}$$

$$B_2 = \left(\frac{ih}{2b_+}\right) \frac{ia/2}{a_- - (h^2/4b_+)} \tag{D.23}$$

and if $\omega_1 = \omega_0$ and $\omega_2 = \omega_0$ then the solution to the differential equation is

$$x = (A_1 + B_1)e^{i\omega_0 t} + (A_2 + B_2)e^{-i\omega_0 t} \tag{D.24}$$

where

$$A_1 + B_1 = \left(1 - \frac{ih}{2b_-}\right) \frac{-ia/2}{a_+ - (h^2/4b_-)} \tag{D.25}$$

$$A_1 + B_1 = \left(1 - \frac{ih}{2(-i\gamma\omega_0)}\right) \frac{-ia/2}{(i\gamma\omega_0) - (h^2/4(-i\gamma\omega_0))} \tag{D.26}$$

$$A_1 + B_1 = \left(1 + \frac{h}{2\gamma\omega_0}\right) \frac{-a/2}{\gamma\omega_0 - (h^2/4\gamma\omega_0)} \tag{D.27}$$

$$A_1 + B_1 = (2\gamma\omega_0 + h) \frac{-a}{4(\gamma\omega_0)^2 - h^2} \tag{D.28}$$

$$A_1 + B_1 = \frac{-a}{2\gamma\omega_0 - h} \tag{D.29}$$

and

$$A_2 + B_2 = \left(1 + \frac{ih}{2b_+}\right) \frac{ia/2}{a_- - (h^2/4b_+)} \tag{D.30}$$

$$A_2 + B_2 = \left(1 + \frac{ih}{2(i\gamma\omega_0)}\right) \frac{ia/2}{(-i\gamma\omega_0) - (h^2/4(i\gamma\omega_0))} \tag{D.31}$$

$$A_2 + B_2 = \left(1 + \frac{h}{2\gamma\omega_0}\right) \frac{-a/2}{\gamma\omega_0 - (h^2/4\gamma\omega_0)} \tag{D.32}$$

$$A_2 + B_2 = \frac{-a}{2\gamma\omega_0 - h} \tag{D.33}$$

and therefore

$$x = \frac{-2a}{2\gamma\omega_0 - h} \cos(\omega_0 t) \tag{D.34}$$

which diverges when $h = 2\gamma\omega_0$ as expected.